UNIVERSITATEA „ALEXANDRU IOAN CUZA" din IAŞI

Université de Lille 1 SCIENCES ET TECHNOLOGIES

<u>**Thèse en Cotutelle**</u>

between

Université Lille 1 - Sciences et Technologies, France

Doctoral school: Science of Matter, Radiation and Environment

Discipline: Optics and Lasers, Physical Chemistry, Atmosphere

and

"Alexandru Ioan Cuza" University of Iaşi, Romania

Doctoral school: Physics

Discipline: Exact Sciences, Physics

Dissertation

Experimental and theoretical studies on the dynamics of transient plasma plumes generated by laser ablation in various temporal regimes

by

Ștefan-Andrei IRIMICIUC

Reviewers:	**Diana MARDARE**	**Professor**	**"Alexandru Ioan Cuza" University of Iaşi, Romania**
	Philippe DELAPORTE	**Research Director**	**CNRS, Aix-Marseille Université, France**
	Stéphane PELLERIN	**Professor**	**Université d'Orléans, France**
	Cristina STAN	**Professor**	**Politehnica University of Bucharest, Romania**
	Valentin CRĂCIUN	**Senior Scientist**	**National Institute for Laser, Plasma and Radiation Physics, Romania**
Thesis Supervisors:	**Cristian FOCȘA**	**Professor**	**Université Lille 1, France**
	Maricel AGOP	**Professor**	**"Alexandru Ioan Cuza" University of Iaşi, Romania**

20 October 2017

Contents

Chapter I   Introduction

I.1   Context

This thesis was developed in cotutelle between the Université Lille 1 - Sciences et Technologies, France and the "Alexandru Ioan Cuza" University of Iasi, Romania in the framework of a **Bourse du Gouvernement Français** (BGF) awarded by the French Embassy in Romania in 2014. Between the two groups involved there is a strong and long collaboration of over 15 years, which has been concretized in several international projects (ARCUS, ECO-NET and PHC BRANCUSI) and more than 30 scientific papers published together. The ANATRAC (Trace Analysis) research group from the PhLAM Laboratory (UMR8523 – Physique des Lasers, Atomes et Molécules) acquired international recognition in optical and electrical diagnostics of laser-produced plasmas (ICCD fast camera imaging, Optical Emission Spectroscopy and Langmuir Probe method), while the group from the Romanian University has strong theoretical background which translated in the development of the first fractal model for the study of laser-produced plasmas. The originality of the thesis is two-fold, primarily the experimental investigations and the use of complementary techniques implemented for the study of laser-produced plasmas on various metallic and complex targets in different ablation regimes (nanosecond, picosecond, femtosecond) led to propose the first empirical laws connecting the properties of the plasma and those of the targets, secondarily the fractal theoretical model was extended for the temporal and spatial evolution of laser ablation plasmas. This led to the first straightforward correlations between the fractal parameters generated by the model and the physical parameters of the plasma. From a technical perspective, the thesis was divided in 18 months spent at the University of Lille, during which all the experimental investigations were performed, and 18 months at the University of Iasi, where the theoretical model was developed and the simulations were performed.

The work performed in the framework of this thesis overlapped with the development of the Romanian national project POSDRU 187/1.5/S/155397 "Doctoral Scholarships for a new generation of elite scientists", under the tutelage of the "Alexandru Ioan Cuza" University of Iasi. Part of the work was also performed in the framework of another Romanian project "Extreme Light Induced Ablation Plasma Jet And Nanopatterning" (ELIAN E03 /21.05.2014). This project was developed in collaboration between the LOA-SL laboratory from the "Alexandru Ioan Cuza" University of Iasi and the National Institute for Laser, Plasma and Radiation Physics (INFLPR) from Bucharest. From a personal point of view, this highly collaborative environment has allowed me to interact with researchers specialized in various experimental and theoretical approaches, which has clearly given me access to specific knowledge towards an overview of the laser ablation field.

I.2 Aim and scope of the thesis

The improvement of the modern technological applications of laser ablation can be achieved only through fundamental studies. By looking back at the main achievements in laser ablation, we learned that throughout its history fundamental research has been the main driving force behind the significant development of the technological applications based on laser ablation. Even nowadays when applications like pulsed laser deposition are being presented as ready for industrial use, there still are a significant number of books, papers and PhD theses dedicated to the fundamental investigations on laser-produced plasmas (LPP) and how their properties can affect the overall deposition process. In the laser ablation community, fundamental studies still are a common language used to express new developments of the topic.

In this thesis, the focus was on fundamental investigations of transient plasmas generated by laser ablation in various temporal regimes on several metallic and complex targets and the development of a fractal approach for modeling the dynamics of the laser-produced plasmas. This is part of the continuous work done by both research groups (Lille and Iasi) to understand the main aspects of laser ablation that relate directly to the improvement of the Pulsed Laser Deposition (PLD) technique. The studies are based on optical and electrical investigations performed simultaneously and in a systematic manner, in order to map the space-time evolution of the main plasma parameters (density, temperature, velocity). The optical investigations involved ICCD fast camera imaging and space- and time-resolved Optical Emission Spectroscopy (OES), while the electrical investigations were based on the Langmuir Probe (LP) method. The techniques were implemented for the study of a series of pure metallic targets (Al, Ni, Cu, Ti, Mn, Zn, In, Te, W) in three ablation regimes (ns, ps, fs) in similar experimental conditions regarding the background pressure and laser fluence. The final aim was two-fold, firstly to understand and compare the dynamics of laser-produced plasmas in different ablation regimes, and how their dynamics can be related to the fundamental ablation mechanism involved; secondly, to find empirical correlations between the properties of the laser-produced plasmas and the physical properties of the targets and to associate this to each specific ablation regime.

The same investigation techniques were further applied for the investigations of laser-produced plasmas on chalcogenide ($(GeSe_2)_{100-x}(Sb_2Se_3)_x$, with $x = 0 - 60$) targets. The main aspect explored here was how the structural changes in the target can affect the dynamics of the plasma plume generated by laser ablation. Using similar experimental conditions as the ones used for PLD, we investigated the global dynamics of the plasmas and the internal energy of the plume expressed through the excitation temperatures of the individual species of the plasmas. By analyzing the structure of the plasma through ICCD fast camera imaging, we were able to showcase the presence of clusters and nanoparticles which can be detrimental in the deposition process. The importance of the results obtained here relies on the direct connections made between the small changes in the structure and properties of the targets and the kinetic properties of the expanding plasmas.

Some experimental investigations were performed on plasmas generated by laser ablation on Aluminum target in PLD conditions. The results obtained here directly affect the deposition process. Here we observed how the PLD configuration can affect the dynamics of the LPP as well as the main plume dynamics in the vicinity of the substrate. The kinetics of the ejected ions was investigated by the LP method, where we evidenced an oscillatory regime overlapping the "classical" behavior, confirming the peculiar observations reported in the last decade by our groups.

The theoretical studies performed in this thesis are based on the fractal model developed by both groups during the last decade. The dynamics of the ejected particles are described in the framework of a fractal hydrodynamic model. The developments of the theoretical model presented in this thesis mainly concern the spatial and temporal evolution of the plasma parameters in a fractal representation. By performing simulation in the approximation of a stationary case, the model offered important information about the connection between some fractal parameters and the experimental ones, like laser pulse duration or background gas pressure. The experimental data were further used as template for the model in order to confirm results given by this non-conventional approach. The simulations preformed, besides confirming the experimental findings, offer valuable information about the physical meaning of the fractal parameters used to describe the laser-produced plasmas. Moreover, we proved the versatility of the model, as it was successfully applied for all three ablation regimes.

I.3   Short history of laser ablation

Laser ablation is defining a series of processes that are the results of a laser beam impinge onto a solid surface. The effects of "photonic ablation" (or the interaction of photons with the matter) have been tentatively known for centuries. Some example can be found even in the Greek literature, when in 303 B.C. are presented the properties of a globe filled with water that can light fire, regardless of the environmental conditions. Also, the concept of "photonic ablation" is even mentioned by Archimedes, who proposed in 203 B.C. to reflect and focus the sunlight on the Phoenicians attacking the city using an array of mirrors [*Miller*, 1994].

The "modern" history of the laser ablation started with a series of conference papers and talks from the 1960's. The results reported in those papers covered a series of fundamental aspects that are considered as the pillars of laser ablation and laser-produced plasmas which led to the development of an entirely new research direction. The first recorded "regular" paper was a theoretical study of Askar'yan and Moroz [*Askar'yan and Moroz*, 1963], where they made some calculations regarding the recoil pressure during the laser ablation of a solid target and discussed the acceleration of small particles or droplets in the framework of an "one-sided evaporation" model. They also predicted the presence of ultrasonic and hypersonic oscillations produced by modulated laser ablation. Following, in a similar pioneering experimental drive, Honig and Woolston [*Honig and Woolston*, 1963] reported some results from the investigation of laser

ablation of various targets (metals, semiconductors and dielectrics). They reported for the first time a quantitative measurement of the ejected particles (3 x 10^{16} electrons and 10^8 positive ions per m^3). The published paper presented the first detailed study of the electron emission and its temporal profile. They analyzed the mass distribution with a modified commercial, double-focusing mass spectrometer, thus demonstrating the first use of the ion microprobe analysis. This study will further be the basis for ion mass spectrometry and paved the way for electrical investigations of LPPs. In later papers Lichtman and Ready [*Lichtman and Ready*, 1963]*,* using a simple assumption of thermionic emission, derived the temperature of the surface during laser-target interaction, finding values of about 3300 K for a ruby laser interaction with a tungsten target. Ready [*Ready*, 1963] proved for the first time the implementation of high-speed photography as a viable method to study the temporal and spatial profiles of the plume of ejected material. The paper reported on a carbon laser ablation plasma. One of the main results presented in that paper was that the emitted light from the plasma reached its maximum at about 120 ns after the start of the laser pulse and had an estimated life-time of a few microseconds. From here, the expansion velocity of the plume was estimated as being of 20 km/s. Follow-up studies on carbon-based targets were performed by Howe [*Howe*, 1963], who reported on the energy of the ejected particles by means of the vibrational (0.86 - 1.72 eV) and rotational (0.38 eV) temperatures extracted form fluorescence spectra of CN and C_2. This represents one of the first mentioning of possible non-equilibrium conditions that were attributed to the cooling of the ejected particles during an adiabatic expansion. This subject was further investigated by Berkowitz and Chupka [*Berkowitz and Chupka*, 1964], who observed, after post-ionization of the ablated plume, cluster ions of carbon (*n* ~ 14), boron (*n* ~ 5) and manganese (*n* ~ 2). Exploring the production of large structures during laser ablation, there have been reports [*Neuman*, 1964] of large "blobs of molten material" and "fragments of material" suggested by the first momentum transfer measurements. This short period of time is characterized by a fast expansion of laser-matter interaction and related topics, during which the first reported papers concentrated on the study of various properties of the ejected particles (electrons, ions, neutrals, clusters and emitted photons). This, coupled with the first estimations of plasma temperatures, velocities and densities, led to the formation of a coherent image of the complex processes involved in the laser-matter interaction.

In the following years there was a "boom" of articles focused on fundamental investigations of laser produced plasmas performed over a wide range of laser characteristics (beam power, pulse width, repetition rate etc.). The development of the laser technology and the measurement techniques led to more sophisticated experiments and more comprehensive theoretical models. Exciting results began to arise due to the new means of study, such as visible, ultra-violet and X-ray emission measurements [*Ehler and Weissler*, 1966; *Benavides et al.*, 2016], coupled with the findings of multiply-charged ions [*Archbold and Hughes*, 1964] and two- and three-photon emission [*Sonnenberg et al.*, 1964]. All these achievements and findings led to the development of new applications that were proposed as alternatives to the already existing ones.

In 1964, Berkowitz and Chupka [*Berkowitz and Chupka*, 1964] proposed for the first time the laser ablation technique as an alternative to fusion, thus arose the idea of laser confinement fusion. Another spectacular application that was born was the Pulsed Laser Deposition (PLD), as a response to the already existing sputtering techniques. Smith and Turner [*Smith and Turner*, 1965] reported the first representative experiment of PLD. Although the authors experimented on a variety of materials using a ruby laser, the quality of the resulted thin films was secondary to the ones produced by sputtering. Not until the 80's was laser film growth able to compete with the other well established deposition techniques, when Dijkkamp et al. [*Dijkkamp et al.*, 1987] deposited a high quality thin film of $YBa_2Cu_3O_7$. Since then, the PLD technique has been used to successfully produce thin films with a wide variety of properties, amongst which a series of thin films with high crystallinity (ceramic oxides, nitrides, metallic multilayers) *[Eason,* 2007; *Craciun et al.,*1994, 2005; *Perriere et al.*, 1994]. The main advantages of PLD are the relatively low costs, with respect to molecular beam epitaxy (MBE) or metal-organic chemical vapor deposition (MOCVD), and the better control over stoichiometry and phase composition, which is very beneficial regarding the growth of complex materials, including high-quality nanomaterials that are impossible to synthesize otherwise. Some of the main successes of the technique can be summed up by the type of complex target resulted (nanowires of Si and Ge [*Morales and Lieber*, 1998], binary (In_2O_3 [*Li et al.*, 2003], SnO_2 [*Liu et al.*, 2003], ZnO [*Yang et al.*, 2006]) and ternary systems ($GaAs_{0.6}P_{0.4}$, $InAs_{0.5}P_{0.5}$, CdS_xSe_{1-x}, indium tin oxide [*Savu and Joanni*, 2006]), and more complex materials [*Eisenhawer et al.*, 2011].

As the thin-film deposition technology flourished, the growing reliability and stability of commercial lasers, particularly Q-switched YAG lasers, improved the uniformity of film growth and the reproducibility of microprobe measurements. Significant progress was made, simultaneously, on the fundamentals aspects of the deposition process. This was achieved through plume diagnostics and the development of theoretical models. The pulsed laser deposition process is a complex one. This complexity comes also from the correlations between a series of variables like: target composition, laser characteristics as fluence, wavelength or pulse width, background gas species, substrate's physical properties, overall PLD geometry etc. Changing one parameter often shifts the ideal settings for others. The effects of changing a single variable can be identified by keeping all other variables constant, and variables are generally kept constant for simplicity. Due to this network of inter-relationships, the control of the deposition process becomes complicated, as well as the overall understanding of the LPP dynamics and how the properties of the plume can influence the final product. This image can be somehow simplified. Let us observe the deposition process from three different perspectives based on the possible influencing factors. One perspective covers the interactions between the laser beam and the target, governed by the physical properties of the target (reflectivity, thermal/electrical conductivity, heat of vaporization, etc.) and those of the laser beam (wavelength, pulse width, shape, etc.) [*Zavestovskaya et al.*, 2008; *Benavides et al.*, 2016]. A second perspective will describe the relationships between the physical properties of the target and the properties of the laser produced plasmas [*Williams et al.*, 2008; *Hermann et al.*, 2012] and the third one the influence of the ejected particles on the properties of

the resulted thin film. In order to achieve some knowledge on any of these dependences it is imperative to use well-established investigation techniques (OES, ICCD fast camera imaging, Langmuir probe method, mass spectrometry, etc.) in order to find a unification relationship between all these "variables".

The benefits of the proper use of the investigation techniques further led to the discovery of other spectacular results. Splitting of the plume is one of them and it was first reported by Geohegan's group [*Geohegan and Puretzky*, 1995, 1996], when investigating the dynamics of LPP in an ambient gas. This group also proposed a theoretical description based on multiple-scattering and hydrodynamic approaches [*Leboeuf et al.*, 1996]. The plume splitting has been further confirmed and studied by other groups [*Harilal et al.*, 2002, 2003; *Wu et al.*, 2013]. All these results were obtained in typical PLD experimental conditions, i.e. fluence in the range of 1 J/cm^2 and background gas pressure of 1-100 mbar. We emphasize that similar results were also reported for laser ablation in vacuum (background pressure $< 10^{-5}$ mbar) and at fluences typically higher than 10 J/cm^2 [*Amoruso et al.*, 2005; *Ursu et al.*, 2009]. From a theoretical perspective the plume splitting is seen at the results of two distinct mechanisms for the particle ejection *[Peterlongo et al.*, 1994; *Yoo et al.*, 2000; *Ursu et al.*, 2009]: the ions would be ejected on a very short time scale through a Coulomb process in the very intense field left by the electrons laser excitation and detachment, while the neutrals would come from a subsequent thermal process (phase explosion [*Kelly and Miotello*, 1998]) which needs more time to establish [*Yoo et al.*, 2000].

Besides the overall dynamics of the plume, looking closely to the individual dynamics of the ejected charged particles, an oscillatory behavior was observed. The first reports of plasma oscillations were published in the 1980's. Borowitz et al. [*Borowitz et al.*, 1987] recorded a fast oscillation structure on the target current of about 100 ps period when irradiating with an 100 J, ns laser beam (fluence up to 10^5 J/cm^2). The first attempts for the comprehension of this "peculiar" behavior were based on the formation of single or multiple double-layers in the very vicinity of the target. This picture was the main focus to a long series of papers reporting on charge separation in laser-produced plasma, mainly from the 1970 – 1980 [*Pearlman and Dahlbacka*, 1977; *Ludmirsky et al.*, 1984, 1985]. Eliezer and Hora [*Eliezer and Hora*, 1989] gathered in a very comprehensive manner the state of the art regarding the double and multiple layers in laser-produced plasmas. One of the remarkable results reported are experimental proof with double-layer electric fields of $10^5 – 10^6$ V/cm and widths of 10-100 Debye lengths [*Eliezer and Ludmirsky*, 1983].

The study of ionic and electronic oscillations in laser-produced plasmas had a recurrence in the recent years when we can find reports on the presence of an oscillatory regime in the ionic current during the early stages of ablation (< 1 μs). Our groups were at the forefront of this movement, having reported on "peculiar" effects in LPP, double and multiple layer formation, or oscillations as results of systematic experimental studies of plasma plumes generated by laser ablation in various temporal regimes (ns, ps, fs) on materials spanning from simple metals (Cu,

Al, Mn, Ni, W, Te, In, Zn, Ti, etc.) to more complex compounds (ceramics, chalcogenide glasses, ferrites) [*Gurlui et al.*, 2006, *Nica et al.*, 2009, 2010; *Ursu et al.*, 2010; *Pompilian et al.*, 2014; *Irimiciuc et al.*, 2017; *Focsa et al.*, 2017]. Beside these experimental studies, three theoretical approaches where proposed. One based on the fractal model developed in [*Gurlui et al.*, 2008] as the interaction between two fractal structures, and their corresponding interface (generally, this interface delineates the double layer) [*Nica et al.*, 2009], with the second ones being on differential physics (a collisional model based on the plasma ion frequency and electron-ion collision rate [*Nica et al.*, 2010] in the context of the Lieberman's model for plasma immersion ion implantation [*Lieberman*, 1989]), and finally one based on the AC Josephson effect [*Gurlui et al.*, 2008]).

In this short introduction, it was attempted to review a few "firsts". All the results are building blocks as the techniques implemented in the 60's led to the development of new theoretical models and new aspects of the laser-produced plasmas never seen before. The history of laser ablation is full of "firsts": the first optical emission spectroscopy measuring led to the development of the Laser-Induced Breakdown Spectroscopy (LIBS) technique, the first measurements of the ionic energy distribution led to the further development of mass spectrometry or the first picture of the ejected material foreshadowing the development of the ICCD fast camera imagining method. These are pillars on which was built the image that we have today of laser ablation process as a whole. Now we can see the effects of all these great moments in laser ablation history, the rise of fast camera photography paved the way for the plume splitting effects while the probing of the charged particles led to the observation of plasma oscillations.

As a way of moving forward, in this thesis we attempted to use what history thought us in order to achieve another "first". Optical Emission Spectroscopy and ICCD imaging coupled with Langmuir Probe methods were implemented in a systematic way for the investigations of nanosecond, femtosecond and picosecond laser ablation plasmas generated on a series of simple (*Al, Cu, Mn, Ti, Zn, Ni, In, Te, W*) and complex (*$(GeSe_2)_{100-x}(Sb_2Se_3)_x$*) targets with the aim of investigating the link between the properties of the target and those of the laser-produced plasmas. We found for the first time empirical relationships between the physical properties of the targets (atomic mass, electrical conductivity, heat of vaporization, melting temperature) and those of the laser-produced plasmas (expansion velocity, excitation temperature, ionic density, electron temperature, electron temperature) in all three ablation regimes. From a theoretical perspective, we expanded the unique fractal approach proposed in [*Gurlui et al.*, 2008] in order to simulate the spatial and temporal evolution of plasma parameters and draw for the first time a direct relationship between the fractal fluid and its specific parameters and the properties of the plasmas as they are recorded through investigation techniques.

I.4   Various laser ablation regimes

With the aim of reaching the enthusiastic objectives presented above, we have to understand what can connect the data provided by the typical LPP measurements with the physical properties of the targets. All the available techniques study the ejected particle during expansion [*Geohegan*, 1992; *Lunney et al.*, 2007; *Ursu et al.*, 2010], thus all the investigations will be performed post laser - target interaction. Henceforth, our main goal becomes to look at the plasma during its expansion and then relate that to the *initio* properties of the electrons and ions in the target. This aspect becomes essential, as in order to understand the connection between the target and the LPP it is imperative to assume that the ejected particles and the information that they carry contain the "memory" embedded with the properties of the target. The memory of the ejected particles is mediated through the ablation mechanisms involved with respect to each ablation regime. Since the thesis is focused on the study of laser-produced plasmas in various ablation regimes (ns, ps, fs), we will attempt in the following to present the main mechanisms that manifest at various temporal regimes. In *Figure I.1* [*Rethfeld et al.*, 2004] there are presented as examples different processes that take place after the laser energy is absorbed by the lattice of the target. We notice some considerable differences between the ablation regimes used in this thesis. For the fs regime (fs ~ 1 ps) there are mainly non-thermal processes involved which end with the Coulomb explosion as the main ejection mechanism [*Shirk and Molian*, 1998]. For the ps regime, if the pulse width is higher than ~ 10 ps, the thermal mechanisms are becoming predominant, starting with the thermal damage of the lattice (homogeneous melting), if the pulse is shorter, there is defined a transition area between pure non-thermal and thermal effect where Coulomb explosion [*Bulgakova et al.*, 2005] is still the main ablation mechanism and the thermal effects are reduced. In the ns regime, the longer pulse width leads to strong thermal effects followed by the subsequent laser beam absorption by the ejected particles [*Mao et al.*, 2013]. Here, mechanisms like Coulomb explosion are secondary to the thermal ones.
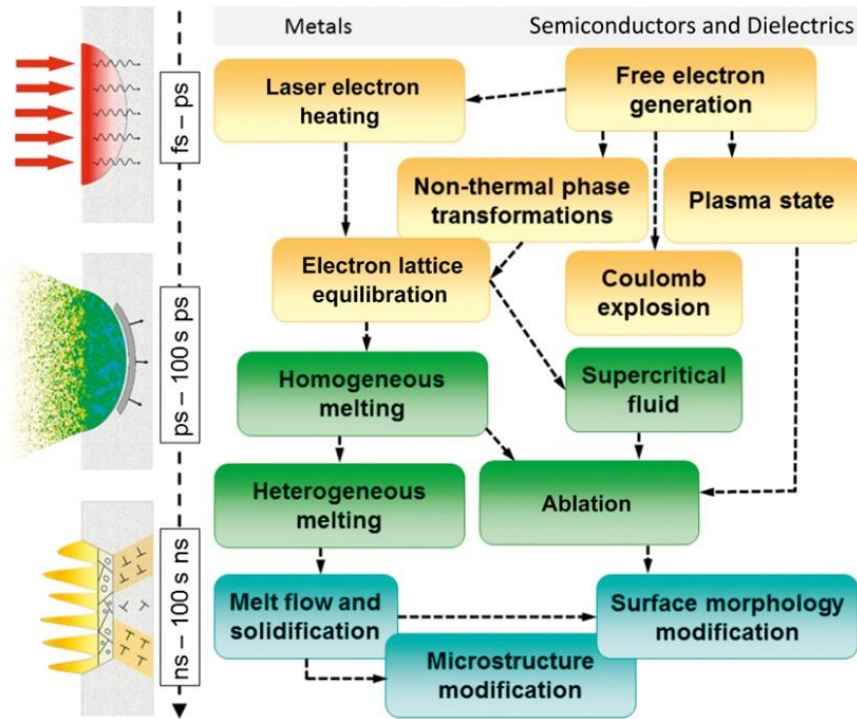
Figure I.1   Mechanisms involved in various laser ablation regimes [*Rethfeld et al.*, 2004].

The simplest way to describe the ablation process is to divide it into four stages. In the first stage are included all the laser-target interactions such as laser absorption by the target electrons or target heating (*Figure I.1*). Here we can see the manifestation of the ablation mechanisms. In the second stage, the particles are ejected from the target and the plume forms. During this stage, in the ns ablation regime and for the ps regime (if the pulse width is higher than 10 ps) the plume absorbs a part of the laser energy (the absorption of the laser radiation is done through single-photon processes [*Tokarev et al.*, 1995], mainly by Inverse Bremsstrahlung (IB) effect [*Mao et al.*, 1996]). Also, at this stage, the laser-plasma interactions are dominant. For the fs and ps (1 - 10 ps) regimes this stage does not exist because the plume expansion occurs after the laser pulse has ended. The third stage occurs after the laser pulse has ended. At this stage, in vacuum conditions, the plume is expanding adiabatically [*Doggett and Lunney*, 2011]. The expansion of the plume differs with respect to the background gas conditions, which leads to the fourth stage that describes the plume dynamics if the ablation takes place in a background gas. After the development of the three stages the plume expansion is dictated by the interactions between the plume particles (ions, atoms, electrons, clusters) and the background gas particles.

Understanding the main processes involved in laser-matter interaction is important for their fundamental relevance and also for comprehending the capabilities and limitations of laser-based applications and technologies. The last ablation stages are used for the diagnosis purposes and where the main "bulk" of information is extracted from the plasma, but before we can delve into studies related to the dynamics of the ejected particles it is essential to emphasize some

fundamental aspects of the first stage. Generally, when a laser beam impinges on the material, laser energy is first absorbed by free electrons [*Mao et al.*, 2013]. The absorbed energy then propagates through the electron system and is transferred to the lattice [*Mao et al.*, 2013]. In literature are identified three characteristic time scales: T_e – the electron cooling time, which is on the order of 1 ps; T_i – the lattice heating time ($\sim$ 10 ps); and T_l – the duration of laser pulse.

Let us first consider a general case covering a range of pulse widths from continuous wave (cw) laser to ms pulsed laser, T_l ($\sim$ ms) $>> T_i >> T_e$. The typical time scale is much larger than the electron-lattice energy coupling time, and thus the main processes involved will be the melting and the subsequent ejection of the molten material assisted by the particle gas [*Phipps*, 2007]. This ablation regime is completely described by the classical heat transfer laws which are often used for the modeling of the laser ablation process in the ms regime. Due to the particularities of the ablation mechanism, this regime is often used in applications like laser cutting, which covers a wide range of materials (steel, nonferrous metals, and nonmetals). For shorter ablation regimes ($\sim$ ns) a second case arises: T_l ($\sim$ ns) $>> T_i >> T_e$. In this case, electron absorbed laser energy has enough time to be transferred to the lattice, electrons and lattice can reach thermal equilibrium, and the main energy loss is the heat conduction into the solid target. Therefore, the target is melted, followed by evaporation occurring from the liquid state [*Kelly and Miotello*, 1998]. Usually, the heat affected zone is smaller than that of the cw laser processing. These properties make ns-laser ablation a powerful tool for technological applications like laser drilling [*Lawrence*, 2010], grooving, marking, or scribing. Nevertheless, the presence of a melted layer makes precise material removal rather difficult. In this time scale, the typical lasers used are Q-switched solid state lasers, such as the Nd:YAG laser (1024 nm - 266 nm). Another case corresponds to the ultra-fast laser ablation, $T_l << T_e << T_i$, where T_l is on the femtosecond scale, and laser pulse duration is shorter than the electron cooling time. The electrons in the surface layer undergo cooling by heat diffusion and by heat transfer to the lattice ions. This stage continues for several picoseconds. The picture changes in the case of a semiconductor target that is heated by an ultrashort pulse. The laser energy is deposited into the solid by creating a "bath" of hot electrons and holes [*Shirk and Molian*, 1998]. Hot carriers subsequently transfer energy to the lattice by creating optical and acoustic phonons. In the case of both metals and semiconductors, the thermalization of laser energy in the hot carrier bath takes place within a few femtoseconds ($\approx$ 10 fs), while the typical time-scale for lattice heating falls within the 1–10 ps range, where thermal conduction is totally negligible [*Leitz et al.*, 2011].

So far, in the literature the majority of the experimental investigations have been carried by Ti:Sapphire laser systems with variable pulse widths. The same systems are often used for the case of ps laser ablation. There, although the pulse width is much shorter than the typical thermal conduction time (hundreds of ns), the laser pulse duration is of the same order as the hot carriers-lattice relaxation time (few ps).

If we analyze in depth the particularities of the short and ultra-short laser ablation we can differentiate between several ablation regimes. The differences are schematically represented in *Figure I.2*.
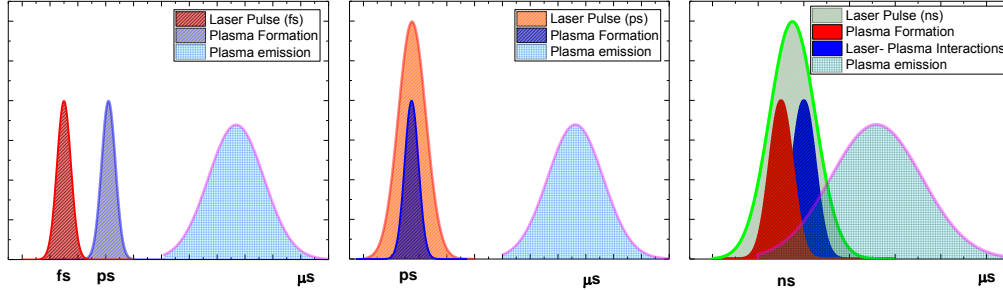
Figure I.2   Time-scales of laser-matter interactions and LPP expansion time for the three ablation regimes (ns, ps, fs).

Considering the strong differences between the various temporal regimes (ns, ps, fs), it is of the utmost interest to investigate the laser-produced plasmas in those regimes and try to comprehend how the fundamental mechanism affects the properties of the ablation plasmas. Moreover, the comparative study amongst different targets with different physical properties could allow us to understand the connections that can be made in each specific ablation regime and try to correlate with the physical processes involved in the material removal.

I.5   Laser ablation mechanisms

In the literature [*Miller*, 1994; *Phipps*, 2007; *Lawrence*, 2010; *Stafe et al.*, 2014] the mechanisms are generally divided into two main categories. There are the primary mechanisms that are involved only in the removal of the target material (*Normal Vaporization*, *Normal Boiling*, *Phase Explosion* and *Coulomb Explosion*) and the secondary mechanisms meant to describe the behavior of the expelled particles after the interaction between the laser beam and the target surface took place (*Knudsen-Layer Processes*, *Effusion-Like Release* and *Normal Outflow*). A better way we can differentiate between the ablation mechanisms is by the type of processes involved. Using these criteria, we can attribute mechanisms for each ablation regime. Thus, we find thermal (Normal Vaporization, Normal Boiling and Phase Explosion) and electrical (Electronic Processes, Coulomb Explosion) mechanisms. For the nanosecond or longer pulse lasers the thermal mechanisms are dominant and for the picosecond or shorter the electrical ones are dominant (*Figure I.2*). Also, for the ultrafast lasers the interaction time between the laser beam and the target is shorter and as a result the mechanisms involved in the removal of the target particles can be different from the ones involved in the nanosecond laser ablation.

I.5.1 Normal vaporization and normal boiling

Normal vaporization is a term which describes a group of processes having in common a thermal origin. This mechanism does not have a dependence on the laser fluence or pulse length, thus the main dependence is on the properties of the target. The term "thermal" is not accurate enough to describe this process, as it was reported by [*Mele et al.*, 1997], due to the fact that the temperature (which is usually a measure of a system at equilibrium) is transient, they suggested that a more accurate term would be "thermal spike". As a result of laser-matter interactions, the atoms, electron, ions, etc. are ejected from the outer layer of the surface. Due to the short interaction time vapor bubbles do not form at the surface, nor from layer beneath the surface. In this scenario, the particle flux emitted can be described by the Hertz-Knudsen equation:

$$Particle\ flux = \alpha(p_{sv} - p_v)(2\pi m k_b T)^{-\frac{1}{2}}(particles\,/\,s\ cm^2),$$ Eq. (I.1)

where α is the vaporization coefficient [*Anisimov et al.*, 1974], p_{sv} is the saturated vapor pressure, p_v is the vapor pressure, m is the particle mass, T is the surface temperature and k_B is the Boltzmann constant. By multiplying *Eq. (I.1)* by $m/\rho(\equiv \lambda^3)$, where ρ is the mass density and λ is the length of the atomic bond, then it will define the velocity of the surface recession in a 1-D situation:

$$\left.\frac{\partial x}{\partial t}\right|_{x=0} = \alpha(p_{sv} - p_v)(2\pi m k_B T)^{-\frac{1}{2}}\lambda^3\ (cm\,/\,s),$$ Eq. (I.2)

$$= \alpha\left[p_b e^{\frac{\Delta H_v m}{k_B}\left(\frac{1}{T_b}-\frac{1}{T}\right)} - p_v\right](2\pi m k_B T)^{-1/2}\lambda^3,$$ Eq. (I.3)

where ΔH_v is the heat of vaporization, assuming there is no re-condensation [*Yoo et al.*, 2000], p_b is the boiling pressure and T_b the boiling temperature. A second type of thermal spike often reported in the literature requires a longer pulse length, long enough for the heterogeneous nucleation of the vapor bubble [*Dell'Aglio et al.*, 2015] to occur. If p_v is higher than p_b the "normal boiling" will occur. However, the density of nucleation sites is rather low [*Yoo et al.*, 2000], this means that although the necessary conditions are met, the main ablation mechanism still remains normal vaporization.

I.5.2 Phase Explosion

In order for the phase explosion to manifest itself, it requires high laser fluences and relatively short pulse widths (ns, ps, fs) [*Schittenhelm et al.*, 1996]. In literature are reported some specific thresholds for this ablation mechanism, related to the laser beam properties and the physical properties of the target (mainly the laser wavelength and the binding energy of the target

lattice ions) [*Russo et al.*, 2000; *Yoo et al.*, 2000]. The main result that can be quantified using phase explosion as an ablation mechanism is the overall quantity of the ablated mass per pulse. From an experimental point of view the quantity of ablated mass can be also correlated to the depth of the crater made by the laser beam (*Figure I.3*).
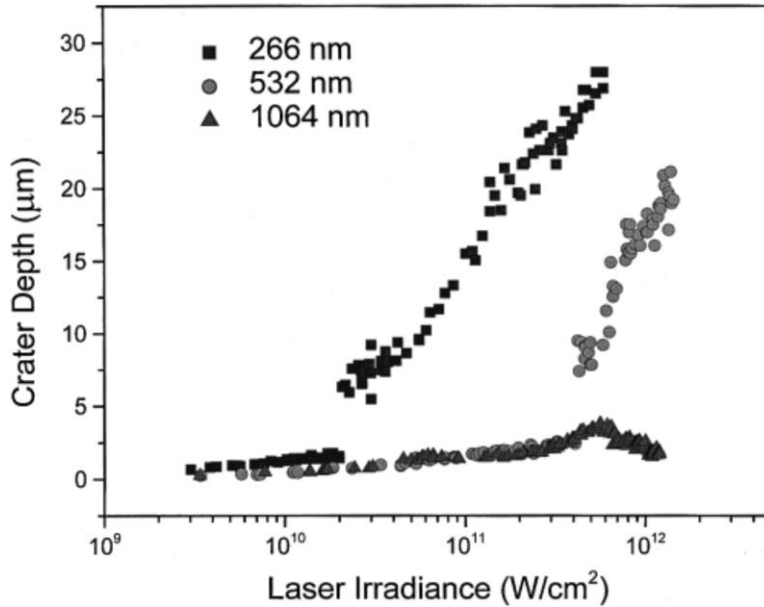
Figure I.3   Dependence of the crater depth on the incident laser wavelength and irradiance [*Schittenhelm et al.*, 1996].

If the laser beam fluence is high enough, above the threshold, the surface will reach a temperature of ~ $0.9 \cdot T_c$ (T_c is the thermodynamic critical temperature). Close to the thermodynamic critical temperature the vapor nucleation rate raises [*Martynyuk*, 1977], because the necessity of the nuclei formation is no longer a kinetic obstacle. It was shown that the formation rate of nuclei has a big variation from 10^{-25} $cm^{-3}s^{-1}$ to 10^{25} $cm^{-3}s^{-1}$ when the temperature increases from 0.88 T/T_c to 0.92 T/T_c [*Yoo et al.*, 2000]. Also, due to the high temperature, the nucleation of the homogenous vapor bubbles occurs and these vapor bubbles reach a critical size. The size of the bubbles is characterized by the critical radius, with the bubbles having a lower radius most probably collapsing. Generally speaking, the target changes its state from superheated liquid to mixture of liquid droplets and vapors. In the end, the bubbles explode and the particles and the clusters are ejected. The presence of the phase explosion is followed by an increase in the quantity of mass removed, as it was reported by Yoo et al. [*Yoo et al.*, 2000]. The increase in the mass removed will lead to an increase of the crater [*Yoo et al.*, 2000] created by the laser pulse as it is shown in *Figure I.4*.
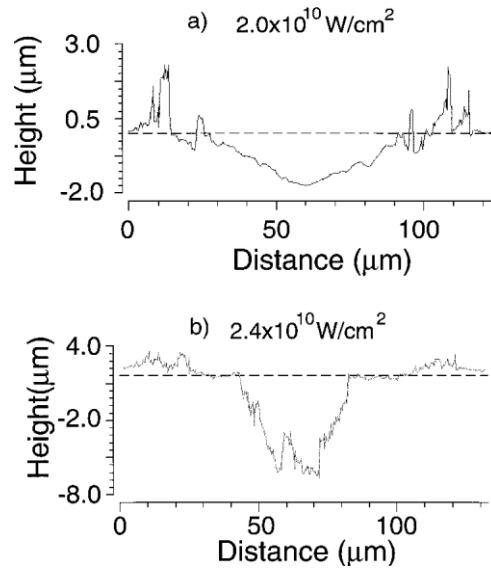
Figure I.4   Cross-sectional images of the crater for (a) laser irradiance slightly below the phase explosion threshold (20 GW/cm^2) and (b) laser irradiance slightly above the threshold (24 GW/cm^2) [*Schittenhelm et al.*, 1996].

Further studies have shown also that the ejected vapors and the liquid droplets are separated in time. Therefore, due to the difference in their mass, the vapors are reported to be detectable at *t < 500ns,* while the droplets at *t > 25μs* [*Schittenhelm et al.*, 1996; *Kelly and Miotello*, 1997; *Yoo et al.*, 2000]. These conclusions where further used to understand results related to the structure and overall dynamics of the ejected cloud obtained by ICCD fast camera imaging and Langmuir probe measurements [*Harilal et al.*, 2003; *Ursu et al.*, 2009; *Irimiciuc et al.*, 2014, 2017; *Focsa et al.*, 2017].

I.5.3   Coulomb Explosion

The *Coulomb explosion* is one of the electrostatic mechanisms of the laser ablation [*Bulgakova et al.*, 2005]. This mechanism has been discussed in many papers over the last years [*Jiang and Tsai*, 2003; *Dachraoui et al.*, 2006; *Werner and Hashimoto*, 2011; *Lin et al.*, 2012; *Focsa et al.*, 2017]. Coulomb explosion plays an important role in different applications such as surface nanostructuring [*Rapp et al.*, 2016] or nanoparticle formation [*De Giacomo et al.*, 2013]. Coulomb explosion has been observed first on dielectric materials, while for semiconductors and metals the subject remained controversial [*Gamaly et al.*, 2002]. It was however proven that for higher fluences of the laser beam, the generated electric field can be high enough for the disintegration of the surface even for semiconductors and metals [*Bulgakova et al.*, 2004].

One of the important results was the reporting of the energetic ions of several species having the same momenta but different energies [*Stoian et al.*, 2000]. Other reports [*Ursu et al.*, 2009, 2010; *Pompilian et al.*, 2013; *Irimiciuc et al.*, 2017] based on investigation of the overall

dynamics of the plume and individual kinetics of the ejected particles through optical methods revealed that doubly-charged ions had the velocities almost twice as high as the single-charged ions. The difference indicates that the ions are accelerated in the same electric field. The electric field is generated by intensive electron photoemission and by the separation between the fast escaping electrons and the ions left on the surface (or in the plume, but behind the electrons). Usually the repulsive force between ions is higher than the binding energy, which results in the disintegration of the surface (*Figure I.5*).
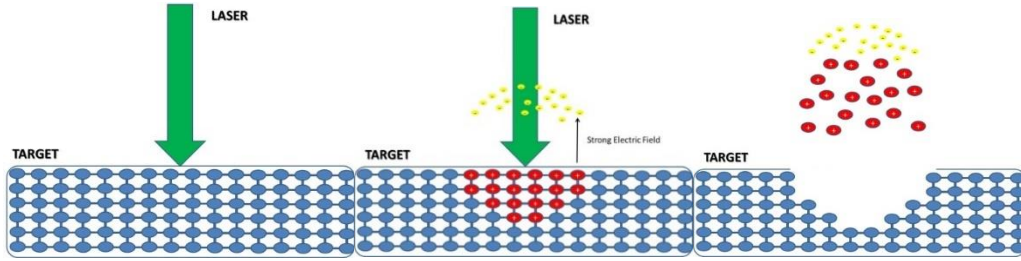
Figure I.5   The stages of the Coulomb Explosion.

If the electric field, generated by photoemission, is higher than the atomic bonding energy, the density of the electrostatic energy per atom has to exceed the value of the sublimation energy per atom. For an ultra-short laser (fs, ps), where the thermal mechanisms do not play an important part, the threshold electric field can be approximated as:

$$E_{C_f}\Big|_{x=0} = \sqrt{\frac{2\Lambda n_0}{\varepsilon\varepsilon_0}} ,$$
Eq. (I.4)

where Λ (kJ/mol) is the sublimation energy per atom, n_0 (cm^{-3}) is the lattice density, and ε is the dielectric permittivity. For longer pulses (ns, ps) it has to be taken into account the heating of the lattice. Due to the heating, the vibrational energy of the atoms increases and the probability of the atoms to escape from the target due to thermal effects increases. That being said, *Eq. (I.4)* further becomes:

$$E_{C_n}\Big|_{x=0} = \sqrt{\frac{2(\Lambda - 3k_B T_s)n_0}{\varepsilon\varepsilon_0}} .$$
Eq. (I.5)

I.5.4   Theoretical model for the Coulomb Explosion

In order to understand the implications of this mechanism to different types of materials, a unified theoretic model is necessary. Such a model was proposed by Bulgakova et al. [*Bulgakova et al.*, 2005]. The model is compact, containing a relatively small number of equations (*Eq. (I.6) – Eq. (I.11)* below), which are used to describe the laser-matter interactions and the ejected particle

16

dynamics for any type of material. There are two important assumptions that have to be made: the laser electric field causes oscillations of the electrons but this motion does not influence their drift motion; the electronic flow caused by the quasi-neutrality breaking at the target surface is a result of the electron photoemission, high density and presence of temperature gradients.

The first equation is the continuity equation for the evolution of the particles generated by the laser:

$$\frac{\partial n_{e,i}}{\partial t} + \frac{1}{e}\frac{\partial J_{e,i}}{\partial x} = S_{e,i} + L_{e,i}, \qquad \text{Eq. (I.6)}$$

where J is the current density and includes the drift and diffusion terms, S and L are terms which are describing the free charge carrier population (S is the source term and L are the losses), n is the charge carrier number density. The relation for the electric current density can be used as the motion equation:

$$J_{e,i} = |e|n_{e,i}\mu E - eD_{e,i}\nabla n_{e,i}. \qquad \text{Eq. (I.7)}$$

The diffusion coefficient is determined from Einstein's relation $D = k_B T_\mu / e$, where T is the temperature corresponding to each type of charge and μ is the charge carrier mobility. Taking into account the assumption made earlier related to the quasi-neutrality breaking, the electrical field generated by the laser can be described by the Poisson equation:

$$\frac{\partial E}{\partial y} = \frac{e}{\varepsilon\varepsilon_0}(n_i - n_e). \qquad \text{Eq. (I.8)}$$

In order to write the energy conservation equations for the electrostatic mechanisms and lattice heating it is necessary to make another assumption. The targets will be considered as dense plasmas so the two-temperature model [*Anisimov et al.*, 1999; *Wellershoff et al.*, 1999] can be used to describe the energy balance:

$$C_e\left(\frac{\partial T_e}{\partial t} + \frac{J}{en_e}\frac{\partial T_e}{\partial x}\right) = \frac{\partial}{\partial x}K_e\frac{\partial T_e}{\partial x} - g(T_e - T_i) + \sum(x,t) \qquad \text{Eq. (I.9)}$$

$$(C_l + L_m\delta(T_l - T_m))\frac{\partial T_l}{\partial t} = \frac{\partial}{\partial x}K_e\frac{\partial T_e}{\partial x} - g(T_e - T_i) \qquad \text{Eq. (I.10)}$$

In Equations (I.9) and (I.10) $C_{e,l}$ and $K_{e,l}$ are the heat capacity and thermal conductivity, g is the electron coupling constant, $\sum(x,t)$ is the energy source term. Also the indexes e,l are corresponding to the electrons and lattice parameters, respectively. For the determination of the term which allows

calculation of the liquid-solid interface ($L_m\delta(T_l\text{-}T_m$) [*Zhvavyi and Ivlev*, 1996]), an approximate form of the delta function is used:

$$\delta(T_l - T_m) = \frac{1}{\sqrt{2\pi}\Delta} e^{\left[-\frac{(T-T_m)^2}{2\Delta^2}\right]},$$

Eq. (I.11)

with Δ between 10 and 100K, depending on the temperature gradient; L_m is the latent heat and T_m is the lattice temperature. The equation system can be solved numerically if the characteristics of the laser beam are known. One important aspect of these equations is their generality. It can be applied for different types of materials and thus it will be the main point of our discussion that connects the properties of the target (conductivity, atomic mass, electron mobility) and the ones of the laser-produced plasmas. Moreover, a broader overview on several other modeling approaches will be given in the introductive part of *Chapter IV*.

I.6   Structure of the manuscript

We presented in the previous sections the complexity of the laser ablation mechanisms and the difficulty in reaching a unified (universal) view when dealing with various materials and laser sources. We tried in this thesis (work) to contribute to the efforts devoted to unveiling this complexity. The main experimental and theoretical developments performed during these three years are presented in the next chapters of this manuscript, which is structured as follows.

Chapter II presents in detail the experimental set-up used during the preparation of the thesis and the investigation techniques implemented for the laser-produced plasmas studies. The focus will be firstly on the equipment available at University of Lille in France, in terms of the lasers that were used, the particularities of the experimental chamber and all its annexes. Secondly, the methodology of each technique is presented coupled with some theoretical background in order to have an overview of the investigation techniques and the information that could be subtracted from a qualitative and quantitative point of view.

Chapter III presents the main experimental results of this thesis. The experimental investigations were focused on optical and electrical investigations of laser-produced plasmas in various ablation regimes. We present here the work on six metallic targets (Mn, Ti, Zn, Al, Ni, Cu) investigated in all three ablation regimes (nanosecond, picosecond, femtosecond). The experiments were performed in similar conditions (background pressure and laser fluence). There we will first discuss the general spatial and temporal evolution of their respective plasma parameters (temperature, velocity, density). Also, some correlations between the properties of the LPP and those of the targets are reported here. For the first time, an empirical correlation was showcased between the electron temperature, drift and thermal velocities and the electrical conductivity. The study was further focused on the peculiar behavior of an Al LPP in PLD conditions. For this study, a stainless steel substrate with a small orifice was placed in front of the

target at various distances. The experiments were performed at different background pressures in order to observe the effect on the plume dynamics. The results obtained here evidenced the presence of supplementary excitations in the substrate area and a strong relationship between the expansion velocity of the plasma and the PLD conditions (background pressure and target-substrate distance). In the same configuration, the oscillatory behavior of the ejected particles is discussed. Moreover, the optical emission spectroscopy reveals an oscillatory behavior of the excited species and a spatial mapping of the frequency of these oscillations was also performed. Finally some optical investigations were performed on chalcogenide targets. The aim here was to be able to investigate how the structural changes of the target, induced by the addition of $SeSb_2$, influence the overall dynamics of the plasma. Some discussion will be made about the influence of the physical properties of the target and the values of the expansion velocities of the plasma and its excitation temperature.

Chapter IV presents the fractal approach used for the modeling of laser-produced plasmas dynamics. The chapter first addresses the general basis for a non-differential theoretical model, its implications and the main advantages of the approach. The model is further used for the investigation of laser produced plasma dynamics. In the framework of the theoretical model the dynamics of each plasma particle (ions, electron, and atoms) are replaced by their respective geodesics (trajectories) and plasma, as a whole, is identified with a fractal fluid. For the first time we report some direct correlations between the properties of the fractal fluid and those of the plasma. The model is then discussed in two different cases: time-dependent and time-independent solutions. The time-independent solution was used to obtain bi-dimensional evolution of the fractal fluid in the expansion plane. The changes on the shape of the plume is discussed with respect to the fractal parameters used to perform the simulation. The time-dependent solution is used to follow the general evolution of all major plasma parameters (temperature, density, velocity), the results of the model following closely the experimental data presented in *Chapter III*. The implications of these similarities are also discussed alongside the importance of the fractalization degree as a main parameter of the model. Finally the model is confronted by all the experimental data (ns, ps, fs regimes) and the viability of such an approach is discussed.

In *Chapter V* are presented the general conclusions of the manuscript along with a few perspectives opened by these studies.

References for Chapter I

Agop, M., P. E. Nica, S. Gurlui, C. Focsa, V. P. Paun, and M. Colotin (2009), Implications of an extended fractal hydrodynamic model, *Eur. Phys. J. D*, *56(3)*, 405–419.

Agop, M., P. Nica, S. Gurlui, and C. Focsa (2010), Fractal hydrodynamic model of high-fluence laser ablation plasma expansion, *AIP Conf. Pr*oc., *1728(64)*, 482–491.

Anisimov, S. I., B. L. Kapeliovich, T. L. Perel 'man, and L. D. Landau (1974), Electron emission from metal surfaces exposed to ultrashort laser pulses, *Sov. Phys. JETP*, *39(2)*, 375-377.

Anisimov, S. I., and K.h. Rakhamatulina. (1973), The dynamics of the expansion of a vapor when evaporated into a vacuum, *Zh. Eksp. Teor. Fiz.*, *37(3)*, 441-444.

Archbold, E., and T. P. Hughes (1964), Electron Temperature in a Laser-heated Plasma, *Nature*, *204(4959)*, 670–670.

Askar'yan, G. A., and E. M. Moroz (1963), Pressure on Evaporation of Matter in a Radiation Beam, *Sov. Phys. JETP*, *13*, 1638–1639.

Benavides, O., L. de la Cruz, E.B. Meja, J.A. Ruz Hernandez, and A. Flores Gil. (2016), Laser wavelength effect on nanosecond laser light reflection in ablation of metals, *Laser Phys.*, *26(12)*, 126101.

Berkowitz, J., and W. A. Chupka (1964), Mass Spectrometric Study of Vapor Ejected from Graphite and Other Solids by Focused Laser Beams, *J. Chem. Phys.*, *40(9)*, 2735–2736.

Borowitz, J. L., S. Eliezer, Y. Gazit, M. Givon, S. Jackel, A. Ludmirsky, D. Salzmann, E. Yarkoni, A. Zigler, and B. Arad (1987), Temporally resolved target potential measurements in laser-target interactions, *J. Phys. D. Appl. Phys., 20(2),* 210–214.

Bulgakova, N. M., R. Stoian, A. Rosenfeld, I. V. Hertel, and E. E. B. Campbell (2004), Electronic transport and consequences for material removal in ultrafast pulsed laser ablation of materials, *Phys. Rev. B*, *69(5)*, 54102.

Bulgakova, N. M., R. Stoian, A. Rosenfeld, I. V. Hertel, W. Marine, and E. E. B. Campbell (2005), A general continuum approach to describe fast electronic transport in pulsed laser irradiated materials: The problem of Coulomb explosion, *Appl. Phys. A Mater. Sci. Process., 81(2), 345–356.*

Craciun, V., J. Elders, J. G. E. Gardeniers, and I. W. Boyd (1994), Characteristics of high quality ZnO thin films deposited by pulsed laser deposition, *Appl. Phys. Lett., 65(23)*, 2963-2965.

Craciun, V., and D. Craciun (2005), Pulsed laser deposition of crystalline LaB_6 thin films, *Appl. Surf. Sci.*, *247(1-4)*, 384-389.

Dachraoui, H., W. Husinsky, and G. Betz (2006), Ultra-short laser ablation of metals and semiconductors: Evidence of ultra-fast Coulomb explosion, *Appl. Phys. A Mater. Sci. Process., 83(2),* 333–336.

Dell'Aglio, M., R. Gaudiuso, O. De Pascale, and A. De Giacomo (2015), Mechanisms and processes of pulsed laser ablation in liquids during nanoparticle production, *Appl. Surf. Sci., 348,* 4-9.

Doggett, B., and J. G. Lunney (2011), Expansion dynamics of laser produced plasma, *J. Appl. Phys.*, *109(9)*, 093304.

Dijkkamp, D., T. Venkatesan., X. D Wu, S. A. Shaheen, N. Jisrawi, Y. H. Min-Lee, and W. L. McLean (1987), Preparation of Y-Ba-Cu oxide superconductor thin films using pulsed laser evaporation from high T_c bulk material, *Appl. Phys. Lett.*, *51 (8)*, 619-621.

Eason, R. (2007), *Pulsed laser deposition of thin films: applications-led growth of functional materials*, Wiley-Interscience, New Jersey.

Ehler, A. W., and G. L. Weissler (1966), Vacuum ultraviolet radiation from plasmas formed by a laser on metal surfaces, *Appl. Phys. Lett., 8(4),* 89-91.

Eisenhawer, B., D. Zhang, R. Clavel, A. Berger, J. Michler, and S. Christiansen (2011), Growth of doped silicon nanowires by pulsed laser deposition and their analysis by electron beam induced current imaging, *Nanotechnology*, *22(7)*, 75706.

Eliezer, S. (1989), Double layers in laser-produced plasmas, *Phys. Rep.*, *172(6)*, 339–407.

Eliezer, S., and A. Ludmirsky (1983), Double layer (DL) formation in laser-produced plasma, *Laser Part. Beams*, *1(3)*, 251–269.

Focsa, C., S. Gurlui, P. Nica, M. Agop, and M. Ziskind (2017), Plume splitting and oscillatory behavior in transient plasmas generated by high-fluence laser ablation in vacuum, *Appl. Surf. Sci.*, (in press).

Gamaly, E. G., A. V. Rode, B. Luther-Davies, and V. T. Tikhonchuk (2002), Ablation of solids by femtosecond lasers: Ablation mechanism and ablation thresholds for metals and dielectrics, *Phys. Plasmas*, *9(3)*, 949-957.

Geohegan, D. B. (1992), Fast-Iccd Photography and Gated Photon Counting Measurements of Blackbody Emission from Particulates Generated in The KrF-Laser Ablation of BN and YBCO, *MRS Proc.*, *285*, 27-32.

Geohegan, D. B., and A. a. Puretzky (1996), Laser ablation plume thermalization dynamics in background gases: combined imaging, optical absorption and emission spectroscopy, and ion probe measurements, *Appl. Surf. Sci.*, *96–98*, 131–138.

Geohegan, D. B., and A. A. Puretzky (1995), Dynamics of laser ablation plume penetration through low pressure background gases, *Appl. Phys. Lett.*, *67(2)*, 197-199.

De Giacomo, A., R. Gaudiuso, C. Koral, M. Dell'Aglio, and O. De Pascale (2013), Nanoparticle-enhanced laser-induced breakdown spectroscopy of metallic samples, *Anal. Chem.*, *85(21)*, 10180–10187.

Gurlui, S., M. Sanduloviciu, M. Strat, G. Strat, C. Mihesan, M. Ziskind, and C. Focsa (2006), Dynamic space charge structures in high fluence laser ablation plumes, *J. Optoelectron. Adv. Mater.*, *8(1)*, 148–151.

Gurlui S., M. Agop, P. Nica, M. Ziskind, and C. Focsa (2008), *E*xperimental and Theoretical Investigations of a Laser Produced Aluminum Plasma , *Phys. Rev. E, 78*, 026405.

Gurlui, S., M. Sanduloviciu, C. Mihesan, M. Ziskind, and C. Focsa (2009), Periodic Phenomena In Laser-Ablation Plasma Plumes: A Self-Organization Scenario, *AIP Conf. Proc.*, *812(1)*, 279–282.

Harilal, S. S., C. V Bindhu, M. S. Tillack, F. Najmabadi, and A. C. Gaeris (2002), Plume splitting and sharpening in laser-produced aluminium plasma, *J. Phys. D. Appl. Phys.*, *35(22)*, 2935–2938.

Hermann, J., L. Mercadier, E. Axente, and S. Noël (2012), Properties of plasmas produced by short double pulse laser ablation of metals, *J. Phys. Conf. Ser.*, *399*, 12006.

Honig, R. E., and J. R. Woolston (1963), Laser-Induced Emission of Electrons, Ions, and Neutral Atoms From Solid Surfaces, *Appl. Phys. Lett.*, *2*, 138.

Howe, J. A. (1963), Observations on the Maser Induced Graphite Jet, *J. Chem. Phys.*, *39(5)*, 1362–1363.

Irimiciuc, S., R. Boidin, G. Bulai, S. Gurlui, P. Nemec, V. Nazabal, and C. Focsa (2017), Laser ablation of

(GeSe $_2$)$_{100-x}$(Sb$_2$Se$_3$)$_x$ chalcogenide glasses: Influence of the target composition on the plasma plume dynamics, *Appl. Surf. Sci., 418(B),* 594-600.

Irimiciuc, S. A., I. Mihăilă, and M. Agop (2014), Experimental and theoretical aspects of a laser produced plasma, *Phys. Plasmas*, *21*(9), 093509.

Jiang, L., and H. L. Tsai (2003), Femtosecond Lasers Ablation : Challenges and Opportunities, *Aerosp. Eng.*, *1(1)*, 51–53.

Kelly, R., and A. Miotello (1997), On the mechanisms of target modification by ion beams and laser pulses, *Nucl. Intrum. Meth. B*, *122(3)*, 374–400.

Kelly, R., and A. Miotello (1998), On the role of thermal processes in sputtering and composition changes due to ions or laser pulses, *Nucl. Intrum. Meth. B*, *141(1–4)*, 49–60.

Lawrence, J. (2010), *Advances in laser materials processing: technology, research and applications*, Woodhead Publishing, Cambridge.

Leboeuf, J. N., K. R. Chen, J. M. Donato, D. B. Geohegan, C. L. Liu, A. A. Puretzky, and R. F. Wood (1996), Modeling of dynamical processes in laser ablation, *Appl. Surf. Sci.*, *96–98*, 14–23.

Leitz, K.-H., B. Redlingshöfer, Y. Reg, A. Otto, and M. Schmidt (2011), Metal Ablation with Short and Ultrashort Laser Pulses, *Phys. Proc.*, *12*, 230–238.

Li, C., D. Zhang, S. Han, X. Liu, T. Tang, and C. Zhou (2003), Diameter-Controlled Growth of Single-Crystalline In2O3 Nanowires and Their Electronic Properties, *Adv. Mater.*, *15(2)*, 143–146.

Lichtman, D., and J. F. Ready (1963), Laser Beam Induced Electron Emission, *Phys. Rev. Lett.*, *10(8)*, 342–345.

Lin, X., H. Chen, S. Jiang, and C. Zhang (2012), A Coulomb explosion theoretical model of femtosecond laser ablation materials, *Sci. China Technol. Sc.*, *55(3)*, 694–701.

Liu, Z., D. Zhang, S. Han, C. Li, T. Tang, W. Jin, X. Liu, B. Lei, and C. Zhou (2003), Laser Ablation Synthesis and Electron Transport Studies of Tin Oxide Nanowires, *Adv. Mater.*, *15(20)*, 1754–1757.

Ludmirsky, A., M. Givon, S. Eliezer, Y. Gazit, S. Jackel, A. Krumbein, and H. Szichman (1984), Electro-optical measurements of high potentials in laser produced plasmas with fast time resolution, *Laser Part. Beams*, *2(2)*, 245–250.

Ludmirsky, A., S. Eliezer, B. Arad, A. Borowitz, Y. Gazit, S. Jackel, A. D. Krumbein, D. Salzmann, and H. Szichman (1985), Experimental Evidence of Charge Separation (Double Layer) in Laser-Produced Plasmas, *IEEE Trans. Plasma Sci.*, *13(3)*, 132–134.

Lunney, J. G., B. Doggett, and Y. Kaufman (2007), Langmuir probe diagnosis of laser ablation plasmas, *J. Phys. Conf. Ser.*, *59*, 470–474.

Mao, X., W. T. Chan, M. Caetano, M. A. Shannon, and R. E. Russo (1996), Preferential vaporization and plasma shielding during nano-second laser ablation, *Appl. Surf. Sci.*, *96–98*, 126–130.

Mao, X., J. Yoo, J. J. Gonzalez, and R. E. Russo (2013), Femtosecond vs. Nanosecond Laser Pulse Duration for Laser Ablation Chemical Analysis, *Spectroscop*y, *28,* 6162-6177.

Martynyuk, M. M. (1977), Phase explosion of a metastable fluid, *Combust. Explo. Shock+*, *13(2)*, 178–191.

Mele, A., A. Giardini, R. Kelly, C. Flamini, and S. Orlando (1997), Laser ablation of metals: Analysis of surface-

heating and plume-expansion experiments, *Appl. Surf. Sci.*, *109–110*, 584–590.

Miller, C. J. (1994), *Laser Ablation: Principles and Applications,* Springer, Berlin.

Morales, A. M., and Lieber C. M. (1998), A laser ablation method for the synthesis of crystalline semiconductor nanowires, *Science*, *279(5348)*, 208–11.

Neuman, F. (1964), Momentum transfer and cratering effects produced by giant laser pulses, *Appl. Phys. Lett.*, *4*(9), 167–169.

Nica, P., P. Vizureanu, M. Agop, S. Gurlui, C. Focsa, N. Forna, P. D. Ioannou, and Z. Borsos (2009), Experimental and theoretical aspects of aluminum expanding laser plasma, *Jpn. J. Appl. Phys.*, *48*, 1–7.

Nica, P., M. Agop, S. Gurlui, and C. Focsa (2010), Oscillatory Langmuir probe ion current in laser-produced plasma expansion, *Europhys. Lett.*, *89(6)*, 65001.

Pearlman, J. S., and G. H. Dahlbacka (1977), Charge separation and target voltages in laser-produced plasmas, *Appl. Phys. Lett.*, *31(7)*, 414–417.

Perrière, J., E. Millon, W. Seiler, C. Boulmer-Leborgne, V. Craciun, O. Albert, J.C. Loulergue, and J. Etchepare (2002), Comparison between ZnO films grown by femtosecond and nanosecond laser ablation, *J. Appl. Phys., 91(2)*, 690-696.

Phipps, C. R. (2007), *Laser Ablation and its Applications*, Springer US, Boston.

Pompilian, O. G., S. Gurlui, P. Nemec, V. Nazabal, M. Ziskind, and C. Focsa (2013), Plasma diagnostics in pulsed laser deposition of GaLaS chalcogenides, *Appl. Surf. Sci.*, *278*, 352–356.

Pompilian, O. G., G. Dascalu, I. Mihaila, S. Gurlui, M. Olivier, P. Nemec, V. Nazabal, N. Cimpoesu, and C. Focsa (2014), Pulsed laser deposition of rare-earth-doped gallium lanthanum sulphide chalcogenide glass thin films, *Appl. Phys. A-Mater.*, *117(1)*, 197–205.

Rapp, S., M. Schmidt, and H. P. Huber (2016), Selective femtosecond laser structuring of dielectric thin films with different band gaps: a time-resolved study of ablation mechanisms, *Appl. Phys. A*, *122(12)*, 1035.

Ready, J. F. (1963), Development of plume of material vaporized by giant-pulse laser, *Appl. Phys. Lett.*, *3(1)*, 11-13.

Rethfeld, B., K. Sokolowski-Tinten, D. von der Linde, and S. I. Anisimov (2004), Timescales in the response of materials to femtosecond laser excitation, *Appl. Phys. A*, *79(4–6)*, 767–769.

Yang R., Yu. L. Chueh, J. R. Morber, R. Snyder, L.-J. Chou, and Z. L. Wang (2006), Single-Crystalline Branched Zinc Phosphide Nanostructures: Synthesis, Properties and Optoelectronic Devices, *Nano.-Micro. Lett., 7(2),* 269–275.

Russo, R. E., X. L. Mao, O. V. Borisov, and H. Liu (2000), Influence of wavelength on fractionation in laser ablation ICP-MS, *J. Anal. Atom. Spectrom.*, *15(9)*, 1115–1120.

Savu, R., and E. Joanni (2006), Low-temperature, self-nucleated growth of indium–tin oxide nanostructures by pulsed laser deposition on amorphous substrates, *Scripta Mater.*, *55(11),* 979-981.

Schittenhelm, H., G. Callies, P. Berger, and H. Hügel (1996), Investigations of extinction coefficients during excimer laser ablation and their interpretation in terms of Rayleigh scattering, *J. Phys. D. Appl. Phys.*, *29(6)*, 1564–1575.

Shirk, M. D., and P. A. Molian (1998), A review of ultrashort pulsed laser ablation of materials, *J. Laser Appl.*, *10(1)*,

18-28.

Smith, H. M., and A. F. Turner (1965), Vacuum Deposited Thin Films Using a Ruby Laser, *Appl. Opt.*, *4(1)*, 147.

Sonnenberg, H., H. Heffner, and W. Spicer (1964), Two-photon photoelectric effect in $Cs_3 Sb_1$, *Appl. Phys. Lett.*, *5(5)*, 95–96.

Stafe, M., A. Marcu, and N. N. Puscas (2014), *Pulsed Laser Ablation of Solids*: Basics, Theory and Applications, Springer-Verlag, Berlin..

Stoian, R., D. Ashkenasi, A. Rosenfeld, and E. E. B. Campbell (2000), Coulomb explosion in ultrashort pulsed laser ablation of $Al_2 O_3$, *Phys. Rev. B*, *62(19)*, 13167–13173.

Tokarev, V. N., J. G. Lunney, W. Marine, and M. Sentis (1995), Analytical thermal model of ultraviolet laser ablation with single-photon absorption in the plume, *J. Appl. Phys.*, *78(2)*, 1241-1246.

Ursu, C., S. Gurlui, C. Focsa, and G. Popa (2009), Space- and time-resolved optical diagnosis for the study of laser ablation plasma dynamics, *Nucl. Intrum. Meth. B*, *267(2)*, 446–450.

Ursu, C., O. G. Pompilian, S. Gurlui, P. Nica, M. Agop, M. Dudeck, and C. Focsa (2010), Al_2O_3 ceramics under high-fluence irradiation: plasma plume dynamics through space- and time-resolved optical emission spectroscopy, *Appl. Phys. A*, *101(1)*, 153–159.

Wellershoff, S.-S., J. Hohlfeld, J. Güdde, and E. Matthias (1999), The role of electron–phonon coupling in femtosecond laser damage of metals, *Appl. Phys. A-Mater.*, *69(S1)*, S99–S107.

Werner, D., and S. Hashimoto (2011), Improved working model for interpreting the excitation wavelength- and fluence-dependent response in pulsed laser-induced size reduction of aqueous gold nanoparticles, *J. Phys. Chem. C*, *115*(12), 5063–5072.

Williams, G. O., G. M. O'Connor, P. T. Mannion, and T. J. Glynn (2008), Langmuir probe investigation of surface contamination effects on metals during femtosecond laser ablation, *Appl. Surf. Sci.*, *254*, 5921–5926.

Wu, J., X. Li, W. Wei, S. Jia, and A. Qiu (2013), Understanding plume splitting of laser ablated plasma: A view from ion distribution dynamics, *Phys. Plasmas*, *20(11)*, 113512.

Yoo, J. H., S. H. Jeong, X. L. Mao, R. Greif, and R. E. Russo (2000), Evidence for phase-explosion and generation of large particles during high power nanosecond laser ablation of silicon, *Appl. Phys. Lett.*, *76(6)*, 783-785.

Zavestovskaya, I. N., O. A. Glazov, and N. N. Demchenko (2008), Threshold Characteristics of Ultrashort Laser Pulse Ablation of Metals., *Proc. 3rd Int. Conf. Front. Plasma Phys. Technol.*, *3*, 10–18.

Zhvavyi, S. P., and G. D. Ivlev (1996), Influence of the initial temperature of silicon on crystallization of a layer melted by nanosecond laser heating, *J. Eng. Phys. Thermophys.*, *69(5)*, 608–611.

Chapter II   Investigation techniques and experimental apparatus

II.1   Introduction

In the previous chapter we presented briefly the fundamental processes that take place when a pulsed laser beam interacts with a solid target. The complexity of those phenomena and the strong dependence on the beam properties (wavelength, pulse width, repetition rate) [*Yao et al.*, 2005; *Hussein et al.*, 2013; *Craciun et al.,* 1995] and external conditions (background pressure, target bias and target physical properties) [*Liu. et al.*, 1997; *Amoruso et al.*, 2010; *Donnelly et al.*, 2010; *Harilal et al.*, 2014] make it somehow difficult to have a profound understanding of the *laser beam – target – plasma* relationships, that transcends one set of experimental conditions and relates to all ablation regimes and different types of targets. In order to shed some light to either of these relations (*laser - target, target – plasma* or *laser – plasma*), over the time various investigation techniques were implemented and adapted for the study of laser-produced plasmas [*Geohegan et al.,* 1992; *Harilal et al.,* 2003; *Doggett et al.*, 2009; *Dzierga et al.*, 2006, 2010].

Regarding the diagnosis of laser-produced plasma, the aim is to gather knowledge about the chemical composition of the plasma plume (atoms, molecules, nanoparticles, clusters etc.), the electrical composition (ionization degree of the ejection particles, electron number density etc.), the plasma plume dynamics (overall plasma dynamics or the dynamics of the individual plasma species) and plasma energy (in terms of electronic, excitation, vibrational or rotational temperatures). We stress out that, due to the particularities of laser-produced plasmas, there is a requirement for all these plasma parameters to be space- and time-resolved. The current available plasma diagnostic methods ca be divided in two categories: optical (fast camera photography [*Harilal et al.,* 2003], interferometry [*Donnely et al.*, 2010], shadowgraphy [*Feinaeugle et al.,* 2012], optical emission spectroscopy [*Geohegan et al.,* 1992; *Briand et al.,* 2011;], laser induced fluorescence [*Sappey et al.*, 1991], Thomson scattering [*Dzierga et al.*, 2006, 2010; *Travaillé et al.,* 2011] etc.) and electrical methods (mass spectrometry [*Chen et al.*, 2014], electrostatic analyzers [*Ursu and Nica*, 2013], Langmuir probes [*Doggett et al.,* 2009], Faraday cups [*Doria et al.*, 2004]). The task of obtaining a complete description of the laser-produced plasmas is difficult/laborious due to their transient character. The typical life-time of the plume is on the tens of μs scale, although faster phenomena can occur even in the sub nanosecond time-scale [*Eliezer and Hora*, 1989; *Gurlui et al.,* 2008]. Accordingly, the investigation methods have to be selected carefully and adjusted to the "requirements" of the experimental configuration, depending on the analyzed phenomena (e.g. the Langmuir probe method is usually adapted for the space-time fast expansion of the plume in what it is known in literature as the "sweeping" approach [*Koopman*, 1971], which will be presented at large in *Section II.2.3*). In addition, one has to take into account the intrinsic limitations of each technique, as all of them are usually not applicable throughout the whole spatial and temporal evolution of the plasma plume. For example, the Thomson scattering technique requires higher electron densities than the ones required by the Langmuir probe technique. In *Figure II.1* we represented the coverage, in terms of space-time coordinates, of some of the mentioned techniques. It can easily be seen that the there is no "perfect" or "best" technique, but only the right method for the purpose of the experiment.
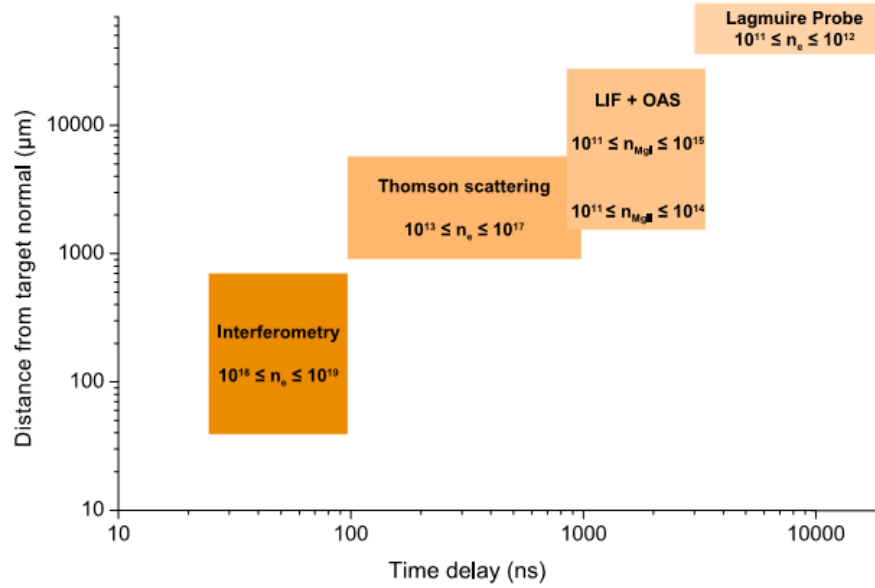
Figure II.1   A schematic representation of the main investigation techniques with respect to their spatial and temporal applicability related to the typical range of detection limits (number densities in m^{-3}).

Each technique reveals a unique facet of the plasma dynamics and provides important information that can be translated into diverse applications. For the deposition of thin films by laser ablation, parameters like angular distribution, particle density, particle velocity or spatial distribution are relevant to the properties and the quality of the deposited film [*Schou*, 2009]. On the other hand, the study of plasma phenomena, such as plume reflection, can help the development of PLD as a deposition technique by understanding some of its drawbacks in terms of changes in film stoichiometry and uniformity. Thus, we believe that a better understanding of the fundamental aspects regarding the LPP dynamics could allow us to control and improve the deposition process, for the tailoring of new thin films with desirable properties.

In general, a given study presents results from only one technique (either optical or electrical). The idea of complementary methods used in tandem or simultaneously is rather rarely seen. In the first part of this chapter we focus on the theoretical background of the main investigation techniques used during the preparation of this thesis, which fall into two categories: optical techniques (space-and time-resolved optical emission spectroscopy, ICCD fast camera imaging) and electrical techniques (space- and time-resolved Langmuir probe measurements). In the second part of the chapter we will describe the details of the experimental set-up from the University of Lille 1, which was used for the preparation of the thesis.

II.2   Investigation methods
II.2.1   ICCD fast camera imaging

The ICCD (Intensified Coupled Charge Device) fast camera photography technique [*Janesick*, 2013] is used to acquire bi-dimensional images of the global (i.e. not spectrally dispersed) optical emission of the LPP. The recording of the images is usually performed using short integration times (the gate width of the ICCD camera), on the order of a few nanoseconds during the early stages of expansion up to tens or hundreds of nanoseconds at later stages. This particular technique allows the recording of LPP emission at various moments in time during its expansion and offers information about the global dynamics of the plasma, the spatial distribution and the structure of the ablated cloud. By automatically incrementing the image recording moment with respect to the ablation laser pulse, one can build a "movie" of the plasma emission evolution in time. We note however that each recorded image will contain only the projection of the plume emission on the CCD detector plane (e.g. *xOy* from *Figure II.2*).
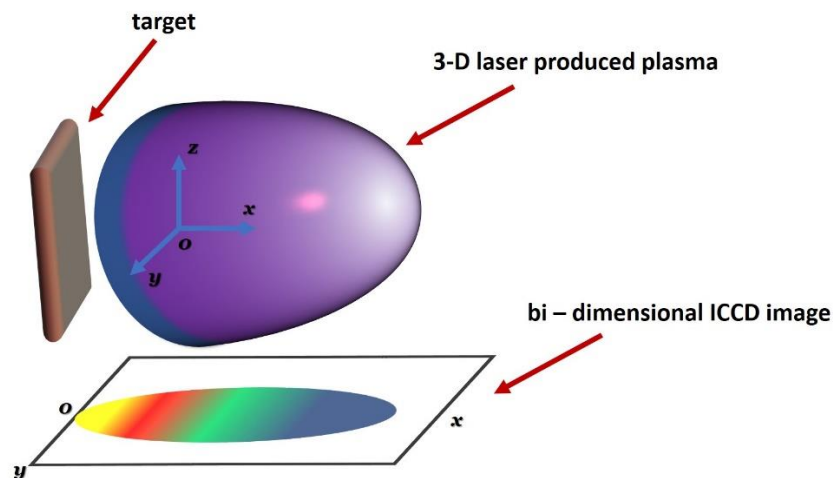
Figure II.2   Conceptual representation of bi-dimensional images recording using ICCD fast camera photography technique.

A CCD device usually contains a photoactive region and a shift register for the transfer of the collected data. While exposed to photons, each pixel (n-type semiconductor) will generate an electric current proportional with the intensity of the light shed on it. The current collected by the CCD array will then be converted to a voltage, which is then digitized and stored. The intensifier attached to the CCD detector has the role to significantly amplify the signal and thus improve the detection limit (up to 10^6-fold). The main components of the intensifier (placed in front of the CCD detector) are: a photocathode, a microchannel and a phosphor screen. The microchannel plate (MCP) usually consist of a thin sheet of glass tubes ($\sim 100\ \mu m$ in diameter) with length to diameter ratios of ~100. Gating is provided by applying a high voltage ~15 kV between the front and back sides of the MCP. When the voltage is applied and a photon strikes on the photocathode, the

extracted electron will further travel via multiple reflections down a thin channel in the MCP. Each tube has basically a continuous dynode structure resembling a photomultiplier. Because the electron is accelerated by the applied voltage, it gains enough kinetic energy, and frees other electrons from the channel wall as it travels along it. The result of a single electron passing through the channels is ~ 10^3 electrons. In the end the electrons are striking a luminescent phosphorous screen which is placed at the back end of the system. The result is a significantly amplified optical signal which will be detected by the CCD and further transferred to the PC for analysis. The ICCD technique has met a rapid development in the last few years and nowadays there are available systems with a high resolution of 2048 x 2048 pixels, high frame rate up to 8 MHz and a good signal to noise ratio. We note that despite the high frame rates available, a good temporal resolution of our "movie" mentioned above can be achieved only by recording each snapshot on successive ablation laser pulses. This requires a good pulse-to-pulse stability of the laser ablation/plasma formation process.

The fast camera imaging is suitable for the investigation of transient phenomena. In the case of laser produced plasmas, it is necessary to have an adequate triggering system and LPP generally have a life time of a few μs. Each recorded image is generally described by a series of parameters: resolution (which is given by the CCD detector and the optical system), time-delay (the moment of time, with respect to the trigger signal, at which acquiring starts), and the "gate width" (or integration time). In our case the initial moment (t = 0) is considered to be the "laser beam - target interaction moment". In order to have a good temporal resolution the gate width is usually of a few ns and it can increase towards longer evolution time where the plume is more rarefied and the emission is weak. An example of a typical Mn plasma produced by ns laser ablation in vacuum is given in *Figure II.3*.
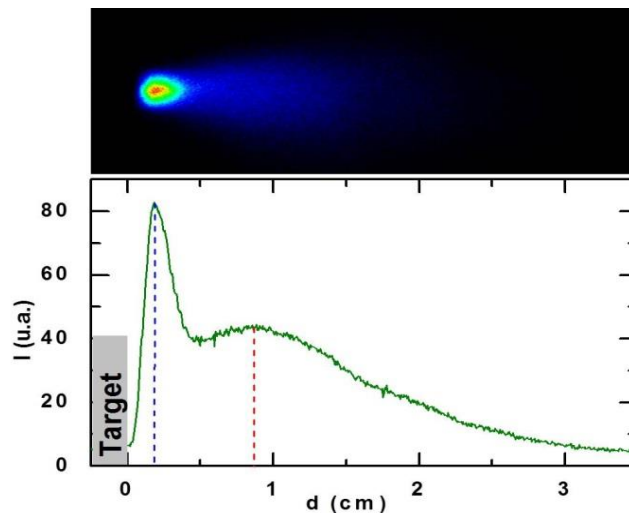
Figure II.3   ICCD image of a ns-laser ablation Mn plasma (gate width – 10 ns, gate delay – 200 ns) and the corresponding cross section on the plume expansion axis *Ox*.

After the images are recorded they are transferred to the computer where they can be further analyzed. The first step is a "pixel to cm" conversion that is based on simple calculations of the optical system used to image the plume on the ICCD detector. The second step is to perform a cross section on the main expansion axis (*Ox*), this allowing us to perform studies regarding the structure of the plasma. Each maximum in the emission cross-section describes a plasma component [*Harilal et al.,* 2003; *Geohegan et al.*, 1992].

By recording successive images of the plasma and representing the displacement of the emission maxima as a function of the moment of time at which the image was recorded (i.e. the delay), we can estimate the expansion velocity for each plasma component. An example from literature [*Ursu et al.*, 2010] is given in *Figure II.4*. Here we can observe the increase in the volume of the plume, as well as a decrease of the emitted light as the plume expands. From the evolution of the optical signals recorded by ICCD imaging, one can define and calculate various velocities (front, center-of-mass, radial) of the plasma structures [*Ursu et al.*, 2010].
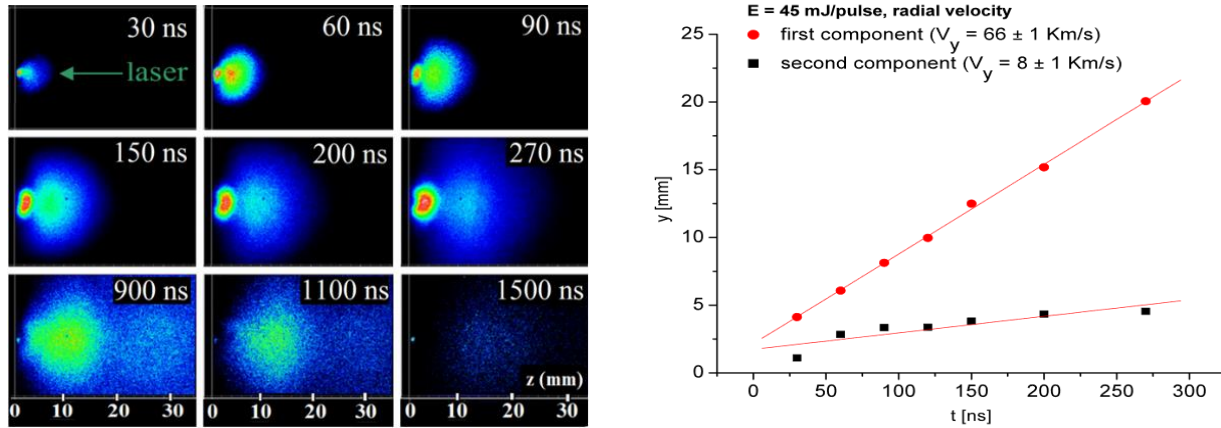
Figure II.4   Temporal evolution of the global emission of a ns laser-produced plasma on Al_2O_3 target (left) and the space-time displacement of the two emission maxima describing the two plasma components (right) [*Ursu et al.*, 2010].

Under vacuum and ultra-vacuum conditions the laser-produced plasmas expand with a constant velocity, which can be extracted from the linear fit of the *d(t)* representation (right-hand-side of *Figure II.4*), while in the presence of a background gas the expansion can be described more accurately by a shockwave model [*Geohegan and Puretzky*, 1996] or by a drag model [*Harilal et al.*, 2003]. In literature we can find other successful usage of this technique especially considering the effect of the background pressure, laser wavelength or fluence on the plume expansion for both pure and complex targets [*Borowitz et al.*, 1987; *Puretzky et al.*, 1993; *Harilal et al.*, 2003]. These studies led to the observation of other peculiar effects, besides the plume splitting in two structures, under vacuum conditions [*Harilal., 2002; Gurlui and Focsa*, 2011] and in the presence of a background gas [*Puretzky et al.*, 1993; *Harilal et al.*, 2003], the presence of a third plasma component containing mainly nanoparticles and clusters (*Figure II.5*) [*Geohegan and*

Puretzky, 1996; *Harilal et al.*, 2003]. Of course the limitation of this technique is its inability to differentiate between the contribution of various species and their spatial distribution within a complex plasma, as we collect all the emitted light from the plasma (i.e. not spectrally dispersed). This can be overcome by using specific band pass optical filters which allow the observation of only one type of species. The advantage of this approach was used by [*Canulescu et al.*, 2009; *Schou*, 2009; *Bator et al.*, 2012], as they investigated the kinetic behavior of individual components and their spatial distribution during deposition of thin films and correlated their stoichiometry differences with the individual properties of the elements and the overall properties of the complex targets.
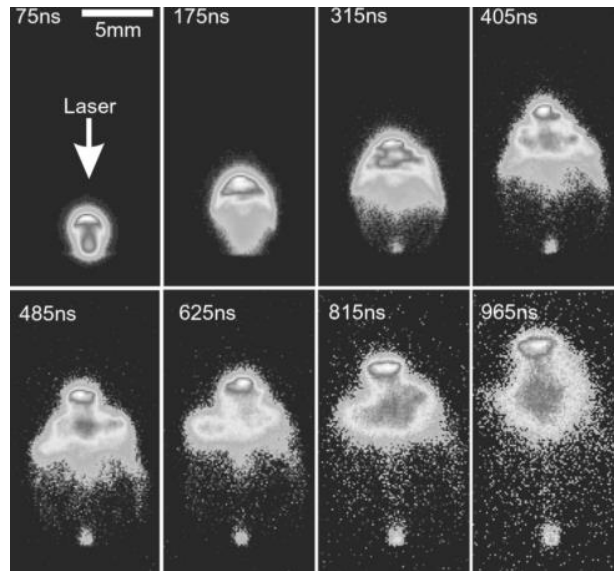
Figure II.5   ICCD images of laser-produced plasma on an Aluminum target in 1.3 Torr background air pressure [*Harilal et al.*, 2003].

The strength of a diagnosis process, with respect to this topic, consists in the ability to investigate as many aspects of the laser ablation plasma as possible in the same experimental conditions and set-up configurations. As a complementary technique to the ICCD fast camera imagining in literature, the most wide-spread is the Optical Emissions Spectroscopy. This technique will delve into the dynamics of individual particles and the internal energy of the plasma plume. It the next section we will present the general aspects of the technique and its relevance to the laser ablation topic.

II.2.2   Optical Emission Spectroscopy

Optical emission spectroscopy (OES) consists in collecting the light emitted by the plasma and transferring it to the detector through a dispersive system. This technique is well established for steady plasma discharges [*Bourg et al.*, 2002]. A more suitable version for the investigation of the LPP and its transient nature, is the space- and time-resolved OES, which translates as recording

the emitted light at various moments in time with respect to the laser pulse and at various distances with respect to the target surface. The spatial resolution is here defined by the optical system preceding the dispersing system, while the temporal resolution is given by the ICCD gate. The collected emission spectrum of the LPP can be (spectrally speaking) continuous (in the vicinity of the target and at short delays after the laser pulse [*Singh and Thakur*, 2006]) or discrete (at larger space-time coordinates [*Harilal et al*. 2013]). The discrete spectrum is composed of a series of emission lines that represent transitions between energetic discrete levels characteristic to every type of excited particles present in the plasma (see an example in *Figure II.6*). The spectral emission lines are characterized by three important parameters: wavelength, intensity and profile.

The Optical Emission Spectroscopy technique can help to determine the nature of the ejected particles through the energetic levels by identifying the wavelength and by using specialized databases [*Kramida et al.*, 2014]. The profile and intensity of the spectral lines can also provide information regarding the interactions between the ejected particles (e.g. Stark broadening [*Tankosić et al.*, 2001; *Cremers et al.*, 2006]) and the internal energy of the plasma (in form of electron temperature and electron density), respectively.

Before discussing some quantitative aspects of the technique and present the main plasma parameters that can be determined through OES, we must present some basic information about an important aspect connected to the measurement process – the thermodynamic equilibrium.
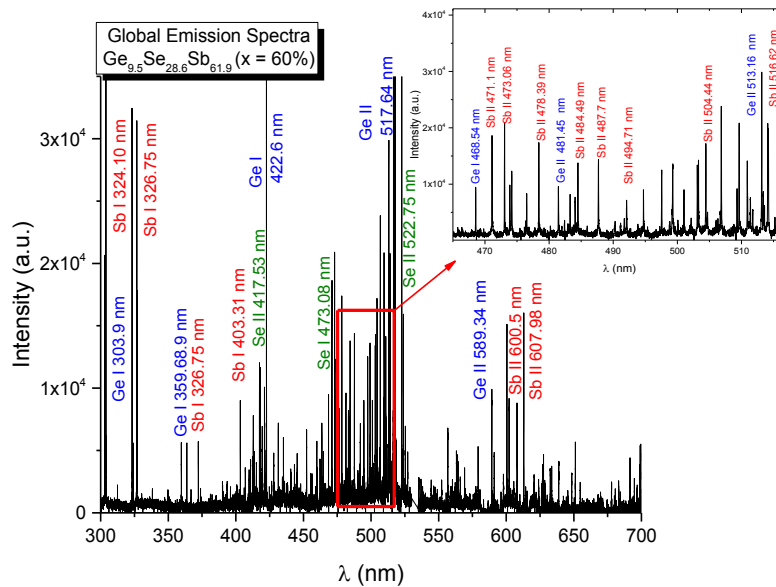
Figure II.6   An example of the discrete emission of a $(GeSe_2)_{40}(Sb_2Se_3)_{60}$ laser ablation plasma at 6 mm from the target (25 ns gate delay, 2 µs gate width) [*Irimiciuc et al.*, 2017a].

II.2.2.1   Thermodynamic equilibrium in laser-produced plasmas

In its most basic definition, a plasma is considered to be at thermodynamic equilibrium if all its temperatures are equal ($T_e = T_{ex} = T_i = T_{rot/vib}$). This is a strong restriction, because if such a relation is satisfied, it will mean that there is an equal distribution of energy in the plasma volume (the excitation processes are equal to the thermal/kinetic ones and the rotational/vibrational movement) which is rarely the case. Thus, the "global" thermodynamic equilibrium can in principle never be reached in the case of "laboratory plasmas", due to the radiative disequilibrium (the de-excitation rate is higher than the excitation one). Therefore, the existence of a local thermodynamic equilibrium (LTE) is investigated for the LPPs. The transient nature of the LPP implies a space-time dependence of all plasma parameters, this means the conditions for the LTE existence can be satisfied only for limited space-time ranges.

There are some general conditions used to estimate the local thermodynamic equilibrium. One of them relates to the electron density and states that LTE is reached if this plasma parameter is above a certain threshold. This is expressed by the McWhirter criterion [*Fujimoto et al.*, 1990; *Cristoforetti et al.*, 2013]:

$$N_e(cm^{-1}) \geq 1.6 \times 10^{12} \Delta E^3 (eV) T_e^{\frac{1}{2}}(K),$$ Eq. (II.1)

where N_e is the electron density, ΔE is the difference between the highest and the lowest atomic/ionic energy levels considered in the analysis, and T_e the electron temperature.

Although the McWhirter criterion is a widespread tool in estimating the LTE, it is not a sufficient condition [*Cristoforetti et al.,* 2010] to completely establish its existence (i.e. for a lower range of electron densities the corona equilibrium conditions can be applied [*Cristoforetti et al.*, 2013]). The criterion shows that LTE can be more easily achieved in cases of relatively dense plasmas, which is not always the case for LPP, where the density has a strong space-time dependence. Moreover, in the majority of plasma models used to describe the main plasma parameters, the plume is considered quasi-stationary. This means that within the investigated plasma volume the spatial gradients are sufficiently small so the effects induced by diffusion are neglected. For the case of partly ionized cold plasmas, as is the case of LPP, the diffusion process of atoms and ions represents again a strong restriction for the establishment of LTE. Therefore, as the LPP has a strong space-time evolution, the LTE is often verified in the proximity of the target (a few mm from the target and at short delays after the laser pulse).

The LTE model is used to determine a series of plasma parameters like excitation temperature or electron density. In the framework of this model the presence of LTE, assumes an equilibrium between all energies inside the plasma (i.e. the electronic temperature is equal to the excitation one). This statement is not particularly true, as it will be showed in the next chapter (*III*), due to the fact that not all the thermal energy of the plume is transferred to excitation processes.

Assuming an equilibrium (Boltzmann) distribution function for the excited states, the intensity characterizing an excitation line can be described as:

$$I_{ki} = N_0 \frac{hcA_{ki}g_k}{4\pi Z(T)\lambda} \exp\left(-\frac{E_k}{k_BT_e}\right),$$

Eq. (II.2)

where N_0 is the total number density of atoms (particles), λ is the transition wavelength, A_{ki} is the Einstein coefficient of the k - i transition, g_k the statistical weight of the upper level, E_k is the energy of the upper level, $Z(T)$ is the partition function [*Lochte-Holtgreven et al.*, 2000], h is the Planck constant, k_B the Boltzmann constant and c the light speed.

II.2.2.2 Electron density and plasma excitation temperature

Once established that the LTE model can be applied, the electron density can be estimated from the Saha-Eggert equation [*Griem*, 2005]. The relationship connects the plasma ionization equilibrium temperature to the proportion of population of two successive ionization states. The "simplest" case it is that of a neutral and a singly charged ion of the same species [*Irissou et al.*, 2002]:

$$n_e = 4.83 \cdot 10^{15} \frac{I^* g^+ A^+ \lambda^*}{I^+ g^* A^* \lambda^+} T_e^{1.5} e^{-\frac{V^+ + E^+ - E^*}{k_BT_e}},$$

Eq. (II.3)

where the (*, +) superscripts represent the neutral excited atom and the singly charged ion, respectively, I is the emission intensity of a spectral line of λ wavelength, T_e is the electron temperature (expressed in K), which is taken as the excitation temperature in LTE conditions, V^+ is the first ionization potential, and E is the energy of the upper level of the transition.

The electron temperature (which in the case of LTE is equal to the excitation temperature) can be simply calculated from *Eq. (II.4)* using the intensity ratio of two spectral lines emitted from the upper levels (E_1 and E_2) characterizing the same species (ion or atom):

$$T_e = \frac{E_2 - E_1}{k_b \ln\left(\frac{I_1 g_1 \lambda_1 f_1}{I_2 g_2 \lambda_2 f_2}\right)},$$

Eq. (II.4)

where f_1 and f_2 are the oscillator strengths of the two spectral lines.

The spectroscopic data (E, A, f) can be found in various databases (e.g. [*Kramida et al.*, 2014]). We note however that there are some reserves concerning these values (especially oscillator strengths), which can lead to significant uncertainties. In order to minimize the errors, it is suitable to use not two but a series of atomic lines with different upper excitation levels. The

Boltzmann plot method represents the logarithmic function of the line intensity versus the upper level energy:

$$\ln\left(\frac{I_{ki}\lambda}{g_k A_{ki}}\right) = \ln\left(N_0 \frac{hc}{4\pi Z(T)}\right) - \frac{E_k}{k_b T_e} \, . \qquad \text{Eq. (II.5)}$$

The slope of this representation will give the excitation temperature, and its linearity or the deviation from it is considered as an indication of LTE validity (an example can be seen in *Figure II.7*).
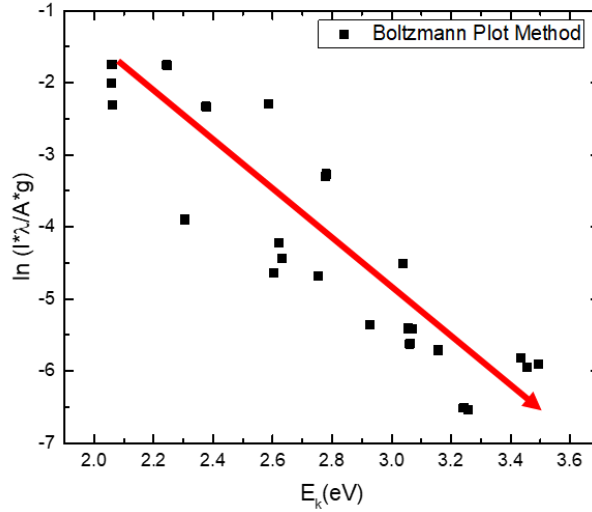
Figure II.7   Example of Boltzmann plot obtained for a ns laser produced plasma on a Mg target; spectrum collected from a 0.3 mm width plasma slice situated at d = 1 mm from the target with 2 µs ICCD gate width.

To conclude this brief presentation of the optical techniques used, we would like to mention that the space-and time-resolved OES can provide the spatial and temporal evolution of individual excited species (leading to the determination of the expansion velocities for atoms and ions) as well as their respective excitation temperature [*Geohegan et al.*, 1995; *Ursu et al.*, 2010; *Harilal et al., 1994*]. A major aspect that can be observed in literature is that the excitation temperature is not uniform amongst different species (e.g. ions present different excitation temperatures compared to the corresponding atoms [*Irimiciuc et al.*, 2017a]). This aspect will be discussed in the next chapter, where we will present the evolution of the excitation temperature for a wide range of plasmas. Other important results reported in the literature showed that the emitted ions expand with a higher velocity (10^4 m/s) than the corresponding atoms (10^3 m/s), with about one order of magnitude difference. Moreover, Geohegan's group performed some systematic OES and ICCD studies to understand the complex plasma chemistry that takes place during the expansion of a carbon plasma in various background gases [*Puretzky et al.*, 1993, 2000a, 2000b], which revealed

that complex molecules form during the expansion, with symmetrical distribution with respect to the plume axis.

II.2.3 Langmuir probe method for laser ablation plasmas

Historically the Langmuir probe (LP) method was first proposed by I. Langmuir [*Mott-Smith and Langmuir*, 1926] in order to facilitate the description of ionized gases. Both the theory and the technical aspects surrounding this experimental technique have evolved over time [*Lahm*, 1974; *Koopman*, 1971; *Merlino et al.*, 2007; *Doggett et al.*, 2009; *Donnelly et al.*, 2010a]. Nowadays the Langmuir probe presents great versatility, being used on various types of plasmas based on different technologies (laser-produced plasmas, discharge plasma, fusion plasmas or sputtering plasmas) and it presents itself in various configurations [*Ovsyannikov et al.*, 2000; *Chen*, 2003; *Tang et al.*, 2012] (single probe – plane, cylindrical, spherical (*Figure II.8*), double or triple probe), being accepted as one of the major techniques for plasma investigations. The dynamics of the plasma particles (ions and electrons) in the vicinity of the probe does not differ fundamentally from one probe configuration to another, consequently no major difference will appear in the LP theory variants corresponding to the different geometrical configurations. In the following we will briefly describe the dynamics of the electrons and ions in the vicinity of the probe and how this can lead to the determination of a series of basic plasma parameters (temperature, density, plasma potential and velocity).
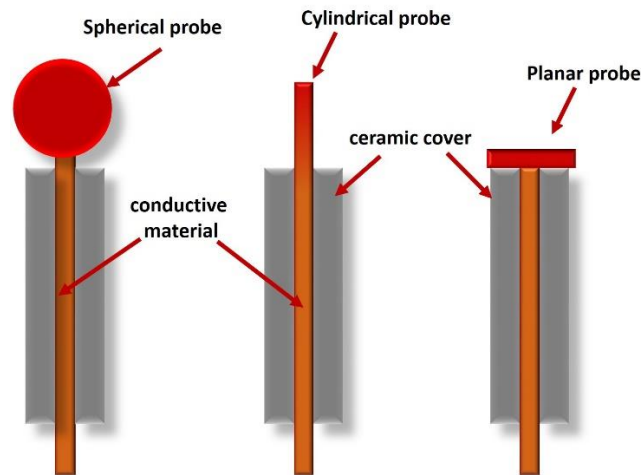
Figure II.8   An illustration of different types of Langmuir probes.

Let us consider, for now, the case of an ideal stationary plasma (i.e. neutral from an electric point of view, homogeneous and presenting local or global thermodynamic equilibrium). When the probe (a metallic electrode, for simplicity we will consider it plane) is immersed inside the plasma, the electrons, ions and atoms will arrive to the probe due to their thermal movement. Given the difference between the masses of the electrons and the ions, the amount of electrons per time unit that will arrive to the probe will be larger than that of ions per time unit, and thus will

negatively charge the probe surface. As a result, a surface is formed where the electrons will be rejected, while the ions will be accelerated towards the probe. Within this surface, the plasma neutrality is broken and there are no secondary ionizations. In this stationary regime, the overall number of electrons will be equal to that of the ions. This can be written as the equality between the two fluxes:

$$j_e = \frac{1}{4} e n_e v_e = j_i = \frac{1}{4} e n_i v_i,$$

Eq. (II.6)

with n_e, n_i being the charged particles number densities and v_e, and v_i the velocities with which the particles reach the probe.

When the probe is biased, either positively or negatively, an electrical field will be generated around the probe. As such, only one type of particle will pass towards the probe, while the other will be repelled. The "collecting" area from the plasma will be defined by the value of the applied voltage and the density of the plasma. Generally, this is called space charge surface, and it can spread on a few Debye lengths. The Debye length defines a minimum volume for which properties like plasma neutrality and local thermodynamic equilibrium are satisfied. The space charge is described by the Child relation $D = \lambda_{Debye} \frac{\sqrt{2}}{3} \left(\frac{2eV}{k_b T_e} \right)^{\frac{3}{4}}$, where D describes the thickness of the plasma sheet where the electron density is negligible, and $\lambda_{Debye} = \sqrt{\frac{k_b T_e \varepsilon_0}{n_e e^2}}$. The role of the applied voltage is not only to differentiate between different types of charges, but also to separate them based on their energy. Thus, by sweeping a wide enough rage of bias values, we will be able to collect all electrons and ions. If we take into account the simplest case, that of the planar configuration, the condition necessary to extract a particle from the plume is that the kinetic energy of the particle (the component oriented towards the probe surface) is higher than the space charge surface field $e(V_{Plasma} - V_{Probe})$, with V_{Plasma} the plasma potential and V_{Probe} the voltage applied on the probe. Therefore, the nature of the collected charge (and thus the probe current) will be dictated by the polarization of the target. For a positive potential, all the electrons will be collected, and due to their Maxwell-Boltzmann velocity distribution, the final relationship describing the electron current is:

$$I_{Probe} = I(V_{Probe}) = I_e - I_i = I_{e0} \exp\left[-e\left(V_{Plasma} - V_{Probe}\right) / k_B T_e \right] - I_{i0}, \quad V_{Probe} < V_{Plasma}, \quad \text{Eq. (II.7)}$$

while for a negative potential

$$I_{\mathrm{Pr}obe} = I_{e0} - I_{i0}\exp\left[-e(V_{\mathrm{Pr}obe} - V_{Plasma})/k_B T_i\right], \; V_{\mathrm{Pr}obe} > V_{Plasma} \;, \qquad\qquad \text{Eq. (II.8)}$$

where I_{Probe} is the current collected by the probe, I_e and I_i are the electronic and, respectively, the ionic currents, I_{e0} and I_{i0} are the respective saturation currents, e is the electronic charge, k_B is the Boltzmann constant, T_e and T_i are the electronic and ionic temperatures, respectively.

While the bias voltages are swept from high negative values to their corresponding positive ones, a characteristic similar to the ones presented in *Figure II.9* is recorded. This is called the *I-V* characteristic. Although the shape of the characteristic is slightly dependent on the geometry of the probe, we can typically identify three different regions:

➢ The saturation ionic region defined by a small current amplitude and a relatively fast saturation for the ionic current. The saturation current is defined as $I_{i0} = Aen_i\sqrt{\dfrac{T_e}{2m_i}}$

   (where A is the probe area, e is the electron charge, n_i is the ionic density, T_e the electron temperature and m_i is the ionic mass)

➢ A transition part, where we identify an important point on the characteristic: the floating potential (V_f) for which the current on the probe is null, followed by an exponential increase of the electronic current. The inflection point of the characteristic, where the current changes from and exponential dependence on the V_{Pprobe} to a squared root one, will define the plasma potential V_{Plasma}.

➢ The saturation electronic region defined by a maximum electronic current collected by the probe. The saturation current is defined as $I_{e0} = Aen_e\sqrt{\dfrac{T_e}{2\pi m_e}}$. This region is particularly characteristic to the planar probe, while for other configurations the electron saturation is not reached. This is due to the increase of the space charge surface around the LP.
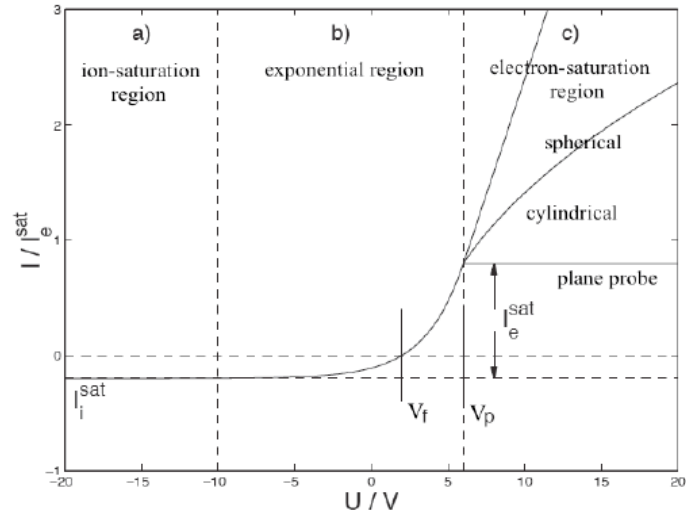
Figure II.9   Typical I-V characteristics for various probe configuration [*Chen*, 1995; *Bhattarai and Mishra*, 2017].

Once the *I-V* characteristic obtained, there are other parameters that can be identified. By reducing the ionic current and representing the evolution of the electron current as a function of the applied voltage in a logarithmic scale (*Figure II.10*), we can further determine the electron temperature, the plasma potential and subsequently we can estimate the particle densities, the thermal velocities and the Debye length.
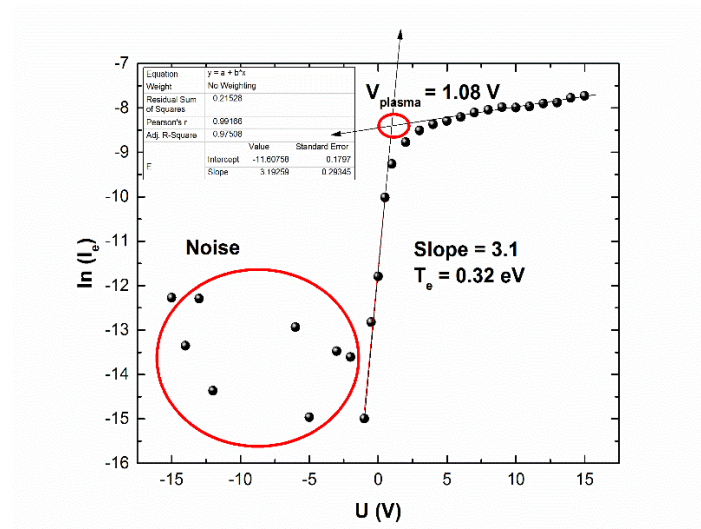
Figure II.10   Example of semi-logarithmic representation of the electronic current [*Irimiciuc et al.*, 2017b].

This technique can give good results for stationary plasmas, where by changing the position of the probe one can map the properties of the plasma. A special case is attributed to transient plasmas, as is the case of LPP for which all properties present spatial and temporal evolution. This variation of the Langmuir probe theory for transient plasmas was developed in the 1970's by

Koopman [*Koopman*, 1971]. For the case of laser-produced plasma, the current time-of-flight profiles $I = f(t)$ are representative of the velocity distribution of the ejected particles, through the relation $v = d/t$, where d is the target-probe distance and t is the arrival time of the particle at the probe. This is based on the assumption that the particle velocity is constant on the way from target to probe, which is supported (for LPP expansion under vacuum) by both experimental observations [*Gurlui et al.*, 2008; *Focsa et al.*, 2009; *Ursu et al.*, 2009] and theoretical considerations. According to Kelly's model [*Kelly and Dreyfus*, 1988], in the proximity of the target each particle will experience several collisions leading to the formation of a Knudsen layer, followed by a supersonic expansion [*Mihesan et al.*, 2004]. The Knudsen layer transforms the "half-range" ($v_z > 0$, with z axis along the normal to the target) velocity distribution present at the sample surface into a "full-range" ($-\infty < v_z < +\infty$) Maxwell distribution superimposed on a drift velocity v_{drift}. In this hypothesis, the time-dependence of the probe signal is given by [*Zimmermann and Ho*, 1995]:

$$I_i(t) \propto \frac{1}{t^4} \exp\left[-\frac{m_i}{2k_b T_i}\left(\frac{d}{t} - v_{drift} \right)^2 \right].$$

Eq. (II.9)

Equation II.9 describes well our experimental data, as it can be seen in *Figure II.11* where the current TOF profile of a Cu plasma for a probe bias of -10 V was fitted.
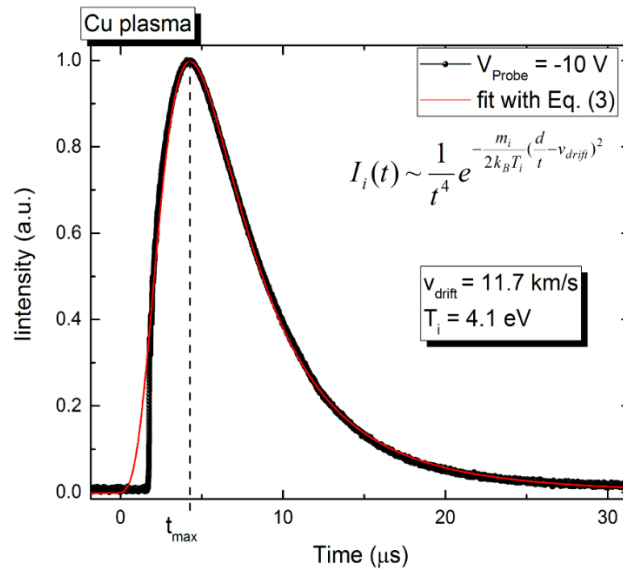
Figure II.11   Example of ion temporal trace current of a fs LPP on a Cu target (V_{Probe} = - 10 V) fitted with a shifted Maxwell-Boltzmann distribution [*Irimiciuc et al.*, 2017b].

This can be simplified even more, as it was showed in [*Doggett and Lunney*, 2009b; *Dogar et al.*, 2011; *Irimiciuc et al.*, 2014], where it was considered that the movement of the charged particle "cloud" is defined by its "center-of-mass" velocity v_{COM}, derived as d/t_{max}, where t_{max} (see

Figure II.11) is the moment at which the current reaches its maximum (this would correspond to the most probable velocity in a velocity distribution representation). The saturation ion current is then defined as

$$I_{i0} = eAn_i v_{COM}$$

These approaches, although they give important results, "ignore" the temporal evolution of the plasma parameters, in this case $T_{e,i}$, $n_{e,i}$, considering instead an overall temperature and a constant drift velocity and a negligible thermal movement of the ejected particle. The situation can be salvaged by sampling the electronic and ionic temporal traces and various moments in time (*Figure II.12a*). If the range of V_{Probe} covers both electronic and ionic saturation region, then we will be able to determine a series of plasma parameters ($T_{e,i}$ *(t)*, $n_{e,i}$ *(t)*, V_{Plasma} *(t)*, $V_{Floating}$ *(t)*, $v_{thermal}$ *(t)* and λ_{Debye} *(t)*). Finding the saturation regions for the LPP can be rather difficult as the properties of the plume depend strongly on the external parameters (laser fluence, background pressure, space-time coordinates). By assuming a v_{COM} of the order of 10^4 m/s for the ejected particles (confirmed through ICCD fast camera photography [*Ursu*, 2009, 2010; *Mihaila*, 2010; *Pompilian*, 2013]) this will mean that in order to reach saturation a minimum V_{Probe} of approximately ± 20 V is necessary.

In *Figure II.12* are represented a series of characteristic signals for an Al plasma and the reconstructed *I-V* characteristics for two time-delays. If the *I-V* characteristic can be reconstructed at each moment of time, this allows us to treat the laser ablation plasma at each specific moment as being a homogeneous, stationary plasma, having a local thermodynamic equilibrium. Given these assumptions, some clear limitations arise. At short evolution times and small distances, the active surface is too large in comparison to the plasma volume and theoretical results are no longer valid since the probe shouldn't influence the plasma around it. Consequently, most LP measurements [*Doggett and Lunney*, 2009a, 2009b; *Donnelly et al.*, 2010b], are performed at long distances (typically a few cm) and at long evolution times (after 1 μs). This is understandable as the plume does increase its volume as it evolves, while the collecting area remains constant. Another important aspect which will be exploited in the next chapters is the influence that the probe has on the plasma surrounding it and how one can choose the optimal parameters for the electrical investigations.
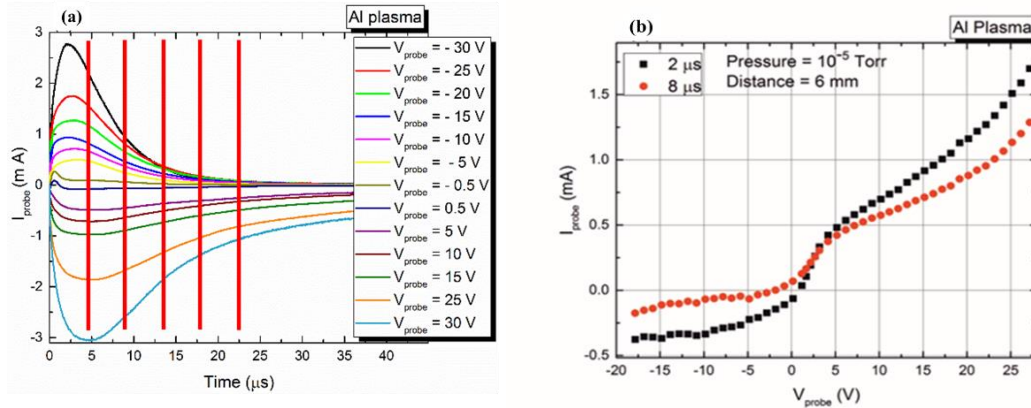
Figure II.12   Aluminum laser-produced plasma: ionic and electronic currents collected at 6 mm from the target for various probe biases (a) and the reconstructed I-V characteristics at two different delays [*Irimiciuc et al.*, 2017b] (b).

In the following we will present an overview of the experimental apparatus at the University of Lille, used for the investigations performed in this thesis. The working principles of the devices will be presented, along with some details about the practical performance and physical limitations of the instruments.

II.3   Experimental set-up at the University of Lille
II.3.1   Overview

The experiments were performed in a cylindrical stainless-steel vacuum chamber [*Ursu et al.*, 2010; *Pompilian et al.*, 2013] (~ 10 l volume, 30 cm height, 20 cm diameter) presented in *Figure II.13* and *Figure II.14*. The chamber is evacuated down to a residual background pressure of ~ 10^{-6} Torr using a 550 l/s Leybold Turbovac MAG W 600iP turbomolecular pump placed in vertical position at the bottom of the chamber, forepumped by a 6.6 m^3/h Agilent SH-110 Dry Scroll Vacuum Pump (ultimate pressure – 5 x 10^{-2} Torr). The turbomolecular pump was isolated from the chamber by a manual gate valve (VAT). The pressure was continuously monitored by a full-range gauge (Pfeiffer PRB 260).
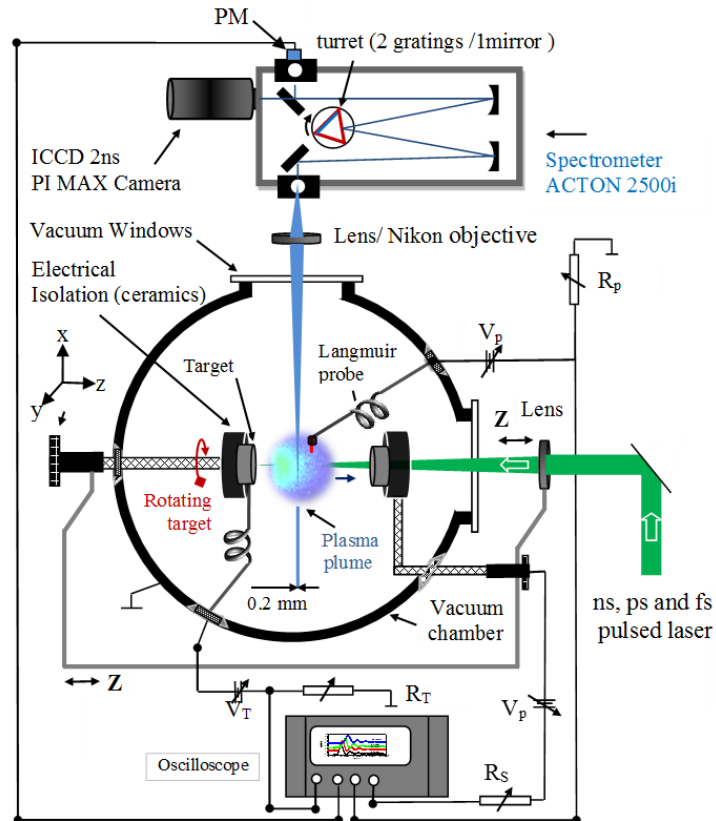
Figure II.13   Schematic representation of the experimental set-up at the University of Lille.
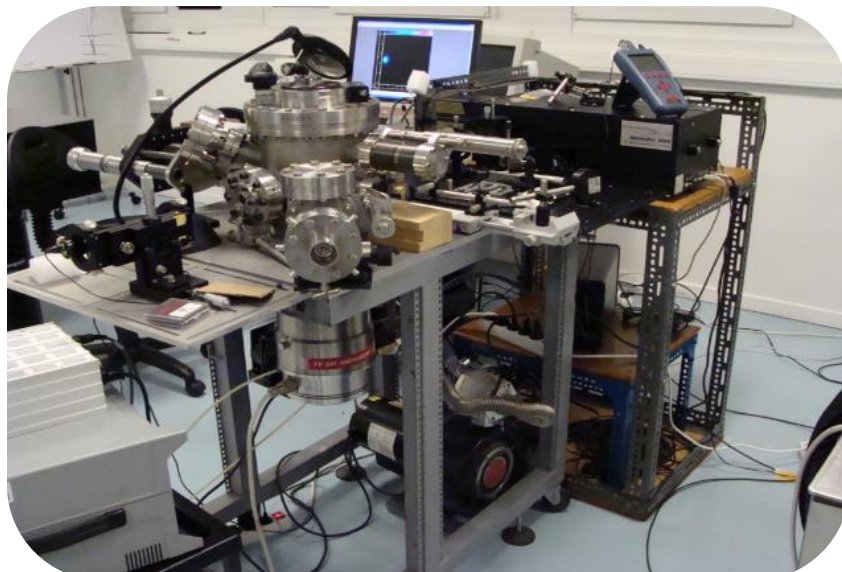
Figure II.14   Photography of the experimental set-up.

The targets are placed on a micrometric high precision XYZ stage that can also be rotated with variable velocities by a motorized vacuum feedthrough (MDC Vacuum). The targets are placed on a metallic target holder, which was isolated and electrically grounded during the experiments.

II.3.2   Targets used

For the fundamental investigations of LPP generated on pure metals, we used a series of 6 materials: Al, Mn, Ti, Ni, Cu, Zn (*Table II.1*). The targets were 1 cm diameter, 2 mm thick discs of high purity (99.9%). The materials were chosen so that all the physical properties of the materials would span a wide range of values [*Smithells et al.*, 2004]. From the low electrical/thermal conductivities of Mn and Ti to the higher values of Al and Cu, and from low melting points of Zn and Al to the higher values reached in the case of Ti or Ni. This aspect was particularly important when relating to one of the aims of the thesis, which was to investigate the link between the physical properties of the target and those of the laser produced plasmas.

Table II.1   Metallic investigated targets and some selected physical properties [*Smithells et al.*, 2004].

Target	Atomic weight (amu)	Melting point (K)	Heat of fusion (kJ/mol)	Boiling point (K)	Heat of vaporization (kJ/mol)	Ionization potential (eV)	Thermal conductivity (W/mK)	Electrical conductivity (MS/m)
Al	26.98	933	10.71	2792	294	7.64	235	38
Mn	54.93	1519	12.91	2334	221	7.43	7.8	0.62
Ni	58.69	1728	17.48	3186	377	7.63	91	14
Cu	63.54	1358	13.26	2835	300	7.72	400	59
Ti	47.86	1941	18.7	3560	425	6.82	22	2.5
Zn	65.38	692	7.35	1180	119	9.39	120	17

For the study of complex targets, we chose to investigate the dynamics of plasma plume generated by ablation of chalcogenide glasses, in continuity to previous studies performed by the group. Their individual chemical composition and concentration ratios are showed in *Table II.2*. The targets were synthesized by conventional melting and quenching technique (30 minutes at 850 ºC in a rocking furnace followed by 10 hours treatment at 800 ºC [*Olivier et al.*, 2014]) using high purity (5N) elements Ge, Sb, and Se bulk samples from the pseudo-binary $(GeSe_2)_{100-x}(Sb_2Se_3)_x$ (where x varies from 0 to 60%) system [*Němec et al.*, 2014; *Olivier et al.*, 2014]. The

resulting glass rods were then annealed at 20 °C below their glass transition temperature for 6 hours and then slowly cooled down to room temperature. For our experiments, the resulting glass was sliced and polished into 25 mm diameter, 2 mm thick discs.

Table II.2   Chemical composition of the chalcogenide targets.

Sb_2Se_3 concentration (x %)	Composition	Ge: Sb: Se ratio
0	$GeSe_2$	1:0:2
10	$Ge_{28.1}Sb_{6.3}Se_{65.6}$	1:0.22:2.33
20	$Ge_{23.5}Sb_{11.8}Se_{65.6}$	1:0.5:2.8
30	$Ge_{19.4}Sb_{16,7}Se_{63.9}$	1:0.86:3.3
40	$Ge_{15.8}Sb_{21.1}Se_{63.2}$	1:1.33:4
50	$Ge_{12.5}Sb_{25}Se_{62.5}$	1:2:5
60	$Ge_{9.5}Sb_{28.6}Se_{61.9}$	1:3:6.5

II.3.3   Pulsed lasers

The experiments involved the use of two different types of lasers: a nanosecond Q-switched Nd:YAG (Quantel Brilliant Eazy) and a femtosecond/picosecond mode-locked Ti:Sa (Spectra Physics). The nanosecond laser can be used in three configurations which lead to three distinct wavelengths 1064 nm, 532 nm and 266 nm, delivering a maximum energy per pulse of 330, 165, and 35 mJ respectively, at a repetition rate of 10 Hz. The temporal pulse width for each wavelength is in the range 4 - 5 ns (depending on the harmonics employed). The investigations in the nanosecond ablation regime were performed using the second harmonic of the laser (532 nm, 5 ns, 10 Hz).

For the shorter pulses (fs and ps) we used a Ti:Sa mode-locked amplified chain. The system contains two main parts: the femtosecond oscillator Ti: Sapphire, Spectra Physics model Tsunami with a repetition frequency of 76 MHz, a pulse width of 40 fs and a maximum energy/pulse of 4 nJ coupled with a regenerative amplifier, Spectra Physics model SPITFIRE. The fs/ps system is based on the CPA (Chirped Pulse Amplification, *Figure II.15*) technique developed in 1985 by [*Strickland and Mourou*, 1985]. The ultrashort pulses are generated at low pulse energy through

the use of an ultrashort-pulse mode-locked laser oscillator. This locked-mode laser typically can generate pulses at a high repetition rate (~80 MHz) with energies per pulse in the range of 10^{-9} J and with pulse durations in the range of 10^{-14} s. These pulses are then chirped using a dispersive delay line consisting in a diffraction-grating arrangement. The pulse is stretched from a duration under 100 fs to typically 100 ps, decreasing its peak power by three orders of magnitude. One or more stages of laser amplification are used to increase the energy of the pulse, by 6 - 9 orders of magnitude, to a fluence sufficient enough to efficiently extract energy from the laser amplifier. After the optical amplification, a second grating pair is used to recompress the pulse back to the initial duration. After amplification, the repetition rate is reduced typically to 1 kHz.
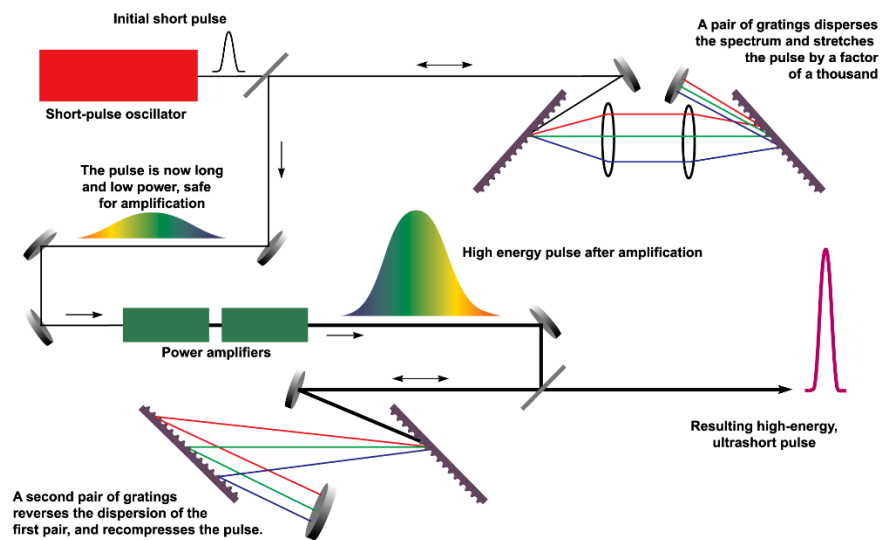
Figure II.15   Concept of Chirped Pulsed Amplification.

The Spectra Physics system available in our laboratory can work in three different temporal regimes, with pulse durations of 40 fs, 120 fs and 1-2 ps, and repetition rates ranging from 4 Hz up to 1 kHz. Among these, we used only two regimes (40 fs and 1 ps). The maximum energy per pulse available was ~ 1.7 mJ for the fs regime and 1.2 mJ for the ps one, for a beam diameter of ~ 8 mm. The spectral bandwidths are 52 nm for 40 fs regime, 10 nm for 120 fs regime and ~ 1 nm for the 1-2 ps one, around the central emission wavelength of 800 nm. The peak powers achieved using this system are 50 GW, 17 GW and 1 GW, respectively.

In all three regimes (ns, ps, fs) the beam energy was kept constant during the experiments and the value of the laser fluence was adjusted by changing the area irradiated (spot diameter: 0.5 mm for ns pulse, 0.16 mm for fs and ps pulses). The laser energy/pulse was monitored by pyroelectric joulemeters (Ophir).

II.3.4   Experimental configurations

II.3.4.1   Optical measurements

From an optical perspective, the dynamics of the plasma plume has been studied by means of a high-resolution monochromator (Acton SP2500i, 500 mm focal length) and an intensified charge-coupled device (ICCD) camera (Roper Scientific PI MAX2-1003-UNIGEN2, 1024×1024 pixels, minimum gating time 2 ns). The monochromator is fitted with one mirror and two diffraction gratings (low-resolution – 300 l/mm, blazed at 300 nm, and high-resolution – 2400 l/mm, blazed at 240 nm) mounted on the same three-position turret, which allows an exchange between imaging, low-resolution and high-resolution spectroscopy experiments. The monochromator presents and alternative exit port fitted with a photomultiplier (Hamamatsu PD 439, 0.5 ns rise time) used to record the temporal profiles of a given spectral line. The PM output is sent to a fast-digital oscilloscope (LeCroy Wave Runner 6200A).

In order to obtain preliminary insight on the dynamics of the laser ablation plasma plume, ICCD sequential pictures of the spectrally unresolved plasma optical emission were recorded at various delays (typically between 25 ns and 12-20 μs) with respect to the laser pulse. For these experiments, a Nikon objective was used to image the whole plasma plume on the ICCD array through the kinematic entrance slit (12 mm x 12 mm opening) of the spectrometer and with the turret fixed in the mirror position. The ICCD camera was triggered with a fast response photodiode placed outside the chamber and an internal routine was used to increment the delay between the laser pulse and the gate opening. For this configuration, gate widths of 20 - 50 ns were usually employed, in order to catch as much as possible sharp temporal snapshots in the space-time evolution of the plume. For the case of nanosecond LPP, the images were acquired in the 25 ns – 2 μs range with 10 events per accumulation and for a better quality of the image 5 accumulations were used leading to an average of 50 events per picture. For fs and ps LPP, the images were acquired in the 25 ns – 20 μs range due to the lengthier life time. In this case 25 accumulations of 25 events each were averaged, which led to an overall average of 625 events (pulses) per recorded image.

For spectrally resolved studies, the plasma plume emission was imaged on the monochromator entrance slit using a system of two lenses (one with 5 cm diameter and f = 22 cm placed in the proximity of the vacuum chamber window, and another one with 2.5 cm diameter and f = 10 cm) (see *Figure II.16*). Preliminary low resolution spectra were recorded using the 300 l/mm grating and a monochromator entrance slit width of 30 μm in order to identify the spectral regions of interest. In this configuration ~ 80 nm wide spectra were recorded for a given position of the grating, with a spectral resolution of ~ 0.5 nm. High-resolution spectra were recorded with the 2400 l/mm grating and a slit width of 30 μm, resulting in a spectral resolution of ~ 0.06 nm on ~ 8 nm broad spectrum for a given grating position. The complete spectrum was obtained by using the "step-and-glue" procedure of the monochromator/camera software, which automatically increments the grating position once a given (8 nm wide) spectrum was recorded.

The entrance slit of the spectrometer defines a 0.3 mm width plasma plume "slices" parallel to the target surface, which was imaged (~ 1:10 magnification) by the lens (f = 10 cm) on the monochromator entrance slit. The optical system was maintained fixed during the experiments and, for space-resolved measurements, we translated the focusing lens – target system as a whole (i.e. without modifying the distance between them and, thus, keeping the laser fluence constant), as they were both attached to the same XYZ micrometric translation stage. For all optical investigations experiments, the laser beam was focused by a f = 25 cm lens in normal incidence with respect to the target surface. This arrangement ensures the same ablation spot diameter on the target, i.e. the same fluence, for all the experiments performed. With this system, good spatial resolution (0.3 mm along the normal to the target, for a monochromator entrance slit of 30 μm) and S/N ratio (usually > 1000) have been achieved.
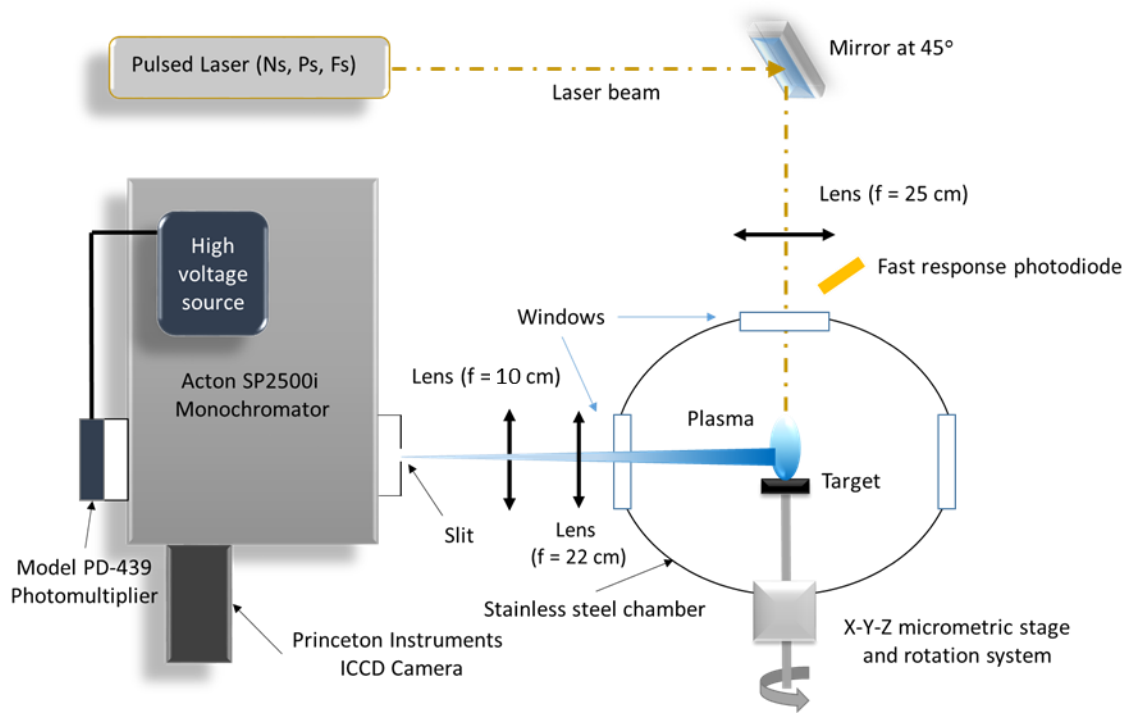
Figure II.16   Schematic representation of the experimental set-up used for the optical investigations.

II.3.4.2   Electrical measurements

The plasma evolution was also monitored by a cylindrical Langmuir probe made of stainless steel (0.8 mm diameter, 5 mm length), placed parallel to the target surface at various distances starting from 5 mm up to 40 mm (in 12 points), on the plasma expansion axis (*Figure III.17*). The probe was biased at 40 different voltages spanning between -35 V and +35 V using a stabilized DC power source, while the target and vacuum chamber were electrically grounded. The DC power source was built out of six 9 V batteries (in serial configuration) in order to avoid any

artefacts that might be introduced by the measuring system. The electronic and ionic currents were measured from the voltage drop on a 4.6 kΩ resistor (Rp) and the transitory signals were recorded with a digital 600 MHz, 2.5 GS/s Oscilloscope (LeCroy Wave Runner 6200A) at 1 MΩ or 50 Ω input impedance. A fast photodiode was used to trigger the oscilloscope on the laser pulse. Each experimental point was recorded by averaging the current signals over 50 laser pulses. The continuous rotation movement of the target offered fresh ablation surfaces per each pulse A schematic representation of the system used for the electrical investigations is present in *Figure II.17*.
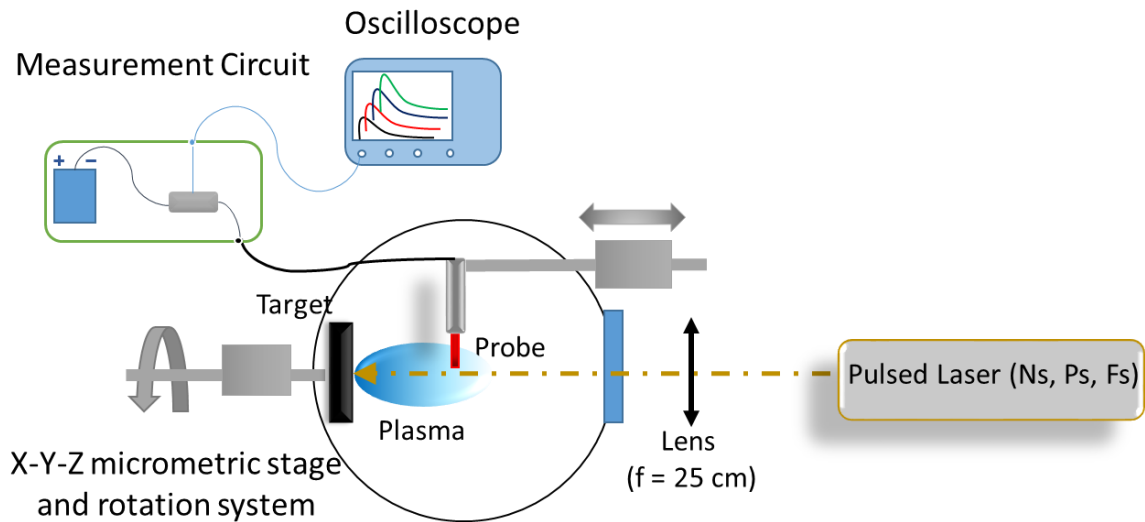
Figure II.17   Schematic representation of the experimental set-up used for the electrical investigations.

In conclusion, each experimental technique manages to create an image of the plasma from a different perspective. The optical methods are non-invasive and offer information over the excited atomic and ionic states from the plume, while the electrical ones are invasive and offer information about the thermal and kinetic energies of the plasma particles. The two methods are complementary. The Langmuir probe gives better results if it is placed at longed distanced and later moments of time, while the optical ones work well for short space-time coordinates where the optical emission is more intense. Between the two of them we can investigate the plasma at all possible time scales. Thus hybrid diagnosis systems (containing optical and electrical approaches) could prove to be helpful for fundamental an applicative research. In the next Chapter we will present the results obtained by implementing the investigation techniques presented here for the study of ns, ps and fs laser-produced plasmas on pure metallic targets and for the study of plasma produced on chalcogenide targets in PLD conditions.

References for Chapter II

Amoruso, S., J. Schou, J. G. Lunney, and C. Phipps (2010), Ablation Plume Dynamics in a Background Gas, *SPIE Proc. Ser., 5448*, 665–676.

Anoop, K. K., M. P. Polek, R. Bruzzese, S. Amoruso, and S. S. Harilal (2015), Multidiagnostic analysis of ion dynamics in ultrafast laser ablation of metals over a large fluence range, *J. Appl. Phys.*, *117(8)*, 083108.

Acquavivay, S., A. P. Caricatoy, M. L. De Giorgiy, G. Dinescuz, and A. Perroneyx (1997), Evidence for CN in spectroscopic studies of laser-induced plasma during pulsed irradiation of graphite targets in nitrogen and ammonia Evidence for CN in spectroscopic studies of laser-induced plasma during pulsed irradiation of graphite targets in nitrog, *J. Phys. B-At. Opt.*, *30*, 4405–4414.

Bator, M., Y. Hu, M. Esposito, C. W. Schneider, T. Lippert, and A. Wokaun (2012), Composition and species evolution in a laser-induced LuMnO3 plasma, *Appl. Surf. Sci.*, *258(23)*, 9355–9358.

Bhattarai, S., and L. N. Mishra (2017), Theoretical Study of Spherical Langmuir Probe in Maxwellian Plasma, *Int. J. Phys. Sci., Vol. 5, 2017, Pages 73-81*, *5(3)*, 73–81.

Boné, A., N. Lemos, G. Figueira, and J. M. Dias (2016), Quantitative shadowgraphy for laser–plasma interactions, *J. Phys. D. Appl. Phys.*, *49(15),* 155204.

Borowitz, J. L., S. Eliezer, Y. Gazit, M. Givon, S. Jackel, A. Ludmirsky, D. Salzmann, E. Yarkoni, A. Zigler, and B. Arad (1987), Temporally resolved target potential measurements in laser-target interactions, *J. Phys. D. Appl. Phys.*, *20(2)*, 210–214.

Canulescu, S., E. L. Papadopoulou, D. Anglos, T. Lippert, C. W. Schneider, and A. Wokaun (2009), Mechanisms of the laser plume expansion during the ablation of $LiMn_2O_4$, *J. Appl. Phys.*, *105(6)*, 631077.

Chen, F. F. (1995), *Introduction to Plasma Physics*, Springer US.

Chen, F. F. (2003), *Lecture Notes on Langmuir Probe Diagnostics*, Electrical Engineering Department University of California, Los Angeles.

Chen, J., T. Lippert, A. Ojeda-G-P, D. Stender, C. W. Schneider, and A. Wokaun (2014), Langmuir probe measurements and mass spectrometry of plasma plumes generated by laser ablation of La0.4Ca0.6MnO3, *J. Appl. Phys.*, *116*(7), 73303.

Cremers, D. A., and L. J. Radziemski (2006), *Handbook of Laser-Induced Breakdown Spectroscopy*, John Wiley & Sons Ltd, Oxford, UK.

Craciun, V., J. Elders, J.G.E. Gardeniers, and I. W. Boyd (1994), Characteristics of high quality ZnO thin films deposited by pulsed laser deposition, *Appl. Phys. Lett., 65(23)*, 2963-2965.

Cristoforetti, G., S. Legnaioli, L. Pardini, V. Palleschi, A. Salvetti, and E. Tognoni (2006), Spectroscopic and shadowgraphic analysis of laser induced plasmas in the orthogonal double pulse pre-ablation configuration, *Spectrochim. Acta. B*, *61*(3), 340–350.

Cristoforetti, G., E. Tognoni, and L. A. Gizzi (2013), Thermodynamic equilibrium states in laser-induced plasmas:

From the general case to laser-induced breakdown spectroscopy plasmas, *Spectrochim. Acta B*, *90*, 1–22.

Dogar, A. H., B. Ilyas, S. Ullah, A. Nadeem, and A. Qayyum (2011), Langmuir probe measurements of Nd-YAG laser-produced copper plasmas, *IEEE Trans. Plasma Sci.*, *39*, 897–900.

Doggett, B., and J. G. Lunney (2011), Expansion dynamics of laser produced plasma, *J. Appl. Phys.*, *109(9)*, 093304.

Donnelly, T., J. G. Lunney, S. Amoruso, R. Bruzzese, X. Wang, and X. Ni (2010a), Dynamics of the plumes produced by ultrafast laser ablation of metals, *J. Appl. Phys.*, *108(4)*, 043309.

Donnelly, T., J. G. Lunney, S. Amoruso, R. Bruzzese, X. Wang, and C. Phipps (2010b), Plume dynamics in femtosecond laser ablation of metals, *AIP Conf. Proc., 643*, 643–655.

Doria, D., A. Lorusso, F. Belloni, and V. Nassisi (2004), Characterization of a nonequilibrium XeCl laser-plasma by a movable Faraday cup, *Rev. Sci. Instrum.*, *75(2)*, 387-392.

Dzierga, K., W. Zawadzki, B. Pokrzywka, and S. Pellerin (2006), Experimental investigations of plasma perturbation in Thomson scattering applied to thermal plasma diagnostics, *Phys. Rev. E*, *74(2)*, 026404.

Focsa, C., P. Nemec, M. Ziskind, C. Ursu, S. Gurlui, and V. Nazabal (2009), Laser ablation of As_xSe_{100-x} chalcogenide glasses: Plume investigations, *Appl. Surf. Sci.*, *255(10)*, 5307–5311.

Focsa, C., S. Gurlui, P. Nica, M. Agop, and M. Ziskind (2017), Plume splitting and oscillatory behavior in transient plasmas generated by high-fluence laser ablation in vacuum, *Appl. Surf. Sci.*(in press).

Fujimoto, T. (1990), Validity criteria for local thermodynamic equilibrium in plasma spectroscopy, *Phys. Rev. A*, *42(11)*, 6588–6601.

Geohegan, D. B. (1992), Fast-Iccd Photography and Gated Photon Counting Measurements of Blackbody Emission from Particulates Generated in The KrF-Laser Ablation of BN and YBCO, *Mat. Res. Soc. Proc.*, *285*, 27-32.

Geohegan, D. B., and A. a. Puretzky (1996), Laser ablation plume thermalization dynamics in background gases: combined imaging, optical absorption and emission spectroscopy, and ion probe measurements, *Appl. Surf. Sci.*, *96–98*, 131–138.

Griem, H. R. (2005), *Principles of plasma spectroscopy*, Cambridge Univ. Press.

Gurlui, S., and C. Focsa (2011), Laser Ablation Transient Plasma Structures Expansion in Vacuum, *IEEE Trans. Plasma Sci.*, *39(11)*, 2820–2821.

Gurlui, S., M. Agop, P. Nica, M. Ziskind, and C. Focsa (2008), Experimental and theoretical investigations of a laser-produced aluminum plasma, *Phys. Rev. E*, *78(2)*, 26405.

Hansen, T. N., J. Schou, and J. G. Lunney (1999), Langmuir probe study of plasma expansion in pulsed laser ablation, *Appl. Phys. A.*, *69*, S601–S604.

Harilal, S. S., R. C. Issac, C. V Bindhu, V. P. N. Nampoori, and C. P. G. Vallabhan (1999), Optical emission studies of species in laser-produced plasma from carbon, *J. Phys. D. Appl. Phys.*, *30(12)*, 1703–1709.

Harilal, S. S., C. V. Bindhu, M. S. Tillack, F. Najmabadi, and A. C. Gaeris (2003), Internal structure and expansion

dynamics of laser ablation plumes into ambient gases, *J. Appl. Phys.*, *93(5)*, 2380.

Harilal, S. S., G. V. Miloshevsky, T. Sizyuk, and A. Hassanein (2013), Effects of excitation laser wavelength on Ly-α and He-α line emission from nitrogen plasmas, *Phys. Plasmas*, *20(1)*, 013105.

Harilal, S. S., N. Farid, J. R. Freeman, P. K. Diwakar, N. L. LaHaye, and A. Hassanein (2014), Background gas collisional effects on expanding fs and ns laser ablation plumes, *Appl. Phys. A-Mater.*, *117(1)*, 319–326.

Hussein, A. E., P. K. Diwakar, S. S. Harilal, and A. Hassanein (2013), The role of laser wavelength on plasma generation and expansion of ablation plumes in air, *J. Appl. Phys, 113(14)*, 143305.

Irimiciuc, S. A., I. Mihaila, and M. Agop, (2014), Experimental and theoretical aspects of a laser produced plasma, *Phys. Plasmas*, *21(9)*, 93509.

Irimiciuc, S., R. Boidin, G. Bulai, S. Gurlui, P. Nemec, V. Nazabal, and C. Focsa (2017a), Laser ablation of $(GeSe_2)_{100-x}(Sb_2Se_3)_x$ chalcogenide glasses: Influence of the target composition on the plasma plume dynamics, *Appl. Surf. Sci., 419,* 594-600.

Irimiciuc, S. A., S. Gurlui, G. Bulai, P. Nica, M. Agop, and C. Focsa (2017b), Langmuir probe investigation of transient plasmas generated by femtosecond laser ablation of several metals: Influence of the target physical properties on the plume dynamics, *Appl. Surf. Sci.*, *417*, 108–118.

Irissou, E., B. Le Drogoff, M. Chaker, and D. Guay (2002), Correlation between plasma expansion dynamics and gold-thin film structure during pulsed-laser deposition, Appl. Phys. Lett., *80(10),* 1716 - 1718.

Janesick, J. R. (2013), *Scientific Charge-Coupled Devices*, edited by J. R. Janesick, SPIE, Washington.

Kelly, R., and R. W. Dreyfus (1988), On the effect of Knudsen-layer formation on studies of vaporization, sputtering, and desorption, *Surf. Sci.*, *198(1–2)*, 263–276.

Kokai, F., K. Takahashi, K. Shimizu, M. Yudasaka, and S. Iijima (1999), Shadowgraphic and emission imaging spectroscopic studies of the laser ablation of graphite in an Ar gas atmosphere, *Appl. Phys. A-Mater.*, *69(7)*, 223–227

Koopman, D. W. (1971), Langmuir Probe and Microwave Measurements of the Properties of Streaming Plasmas Generated by Focused Laser Pulses, *Phys. Fluids*, *14(8)*, 1707 - 1716.

Kramida, A., Y. Ralchenko, J. Reader, and NIST ASD Team (2014), NIST Atomic Spectra Database Lines Form, *NIST At. Spectra Database (ver. 5.2) [Online]*, Available: http://physics.nist.gov/asd, doi:2015. Available from: http://physics.nist.gov/asd

Lahm, S. H. (1965), Unified theory of langmuir probe in a collisionless plasma, *Phys. Fluids, 8(1),* 73-87.

Liu, X., D. Du, and G. Mourou (1997), Laser ablation and micromachining with ultrashort laser pulses, *IEEE J. Quantum Elect.*, *33(10)*, 1706 - 1716.

Lochte-Holtgreven, W., E. North-Holland, A. A. Ovsyannikov, and M. F. Zhukov (2000), *Plasma Diagnostics*, Cambridge International Science Publishing.

Merlino, R. L. (2007), Understanding Langmuir probe current-voltage characteristics, *Am. J. Phys.*, *75(12)*, 1078-

1785.

Mihaila, I., C. Ursu, A. Gegiuc, and G. Popa (2010), Diagnostics of plasma plume produced by laser ablation using ICCD imaging and transient electrical probe technique, *J. Phys. Conf. Ser.*, *207*, 12005.

Mihesan, C., N. Lebrun, M. Ziskind, B. Chazallon, C. Focsa, and J. L. Destombes (2004), IR laser resonant desorption of formaldehyde-H2O ices: Hydrated cluster formation and velocity distribution, *Surf. Sci.*, *566–568*(1–3), 650–658.

Mott-Smith, H. M., and I. Langmuir (1926), The theory of collectors in gaseous discharges, *Phys. Rev.*, *28*(4), 727–763.

Němec, P., M. Olivier, E. Baudet, A. Kalendová, P. Benda, and V. Nazabal (2014), Optical properties of $(GeSe2)_{100-x}(Sb_2Se_3)_x$ glasses in near- and middle-infrared spectral regions, *Mater. Res. Bull.*, *51*, 176–179.

Olivier, M., J.C. Tchahame, P. Němec, M. Chauvet, V. Besse, C. Cassagne, G. Boudebs, G. Renversez, R. Boidin, E. Baudet, and V. Nazabal (2014), Structure, nonlinear properties and photosensitivity of $(GeSe_2)_{100-x}(Sb_2Se_3)_x$ glasses, *Opt. Mater. Express*, *4(3)*, 525–54025.

Ovsyannikov, A. A., and M. F. Zhukov (2000), *Plasma Diagnostics*, Cambridge International Science Publishing.

Pompilian, O. G. (2013), Pulsed Laser Deposition and Characterization of Chalcogenide Thin Films, Université Lille 1 – Sciences Et Technologies.

Pompilian, O. G., S. Gurlui, P. Nemec, V. Nazabal, M. Ziskind, and C. Focsa (2013), Plasma diagnostics in pulsed laser deposition of GaLaS chalcogenides, *Appl. Surf. Sci.*, *278*, 352–356

Puretzky, A. A., D. B. Geohegan, R. E. Haufler, R. L. Hettich, X. Y. Zheng, and R. N. Compton (1993), Laser ablation of graphite in different buffer gases, *AIP Conf. Proc.*, *288*(1993), 365–374.

Puretzky, A. A., D. B. Geohegan, X. Fan, and S. J. Pennycook (2000a), Dynamics of single-wall carbon nanotube synthesis by laser vaporization, *Appl. Phys. A.-Mater.*, *70(2)*, 153–160.

Puretzky, A. A., D. B. Geohegan, X. Fan, and S. J. Pennycook (2000b), In situ imaging and spectroscopy of single-wall carbon nanotube synthesis by laser vaporization, *Appl. Phys. Lett.*, *76(2)*, 182–184.

Schou, J. (2009), Physical aspects of the pulsed laser deposition technique: The stoichiometric transfer of material from target to film, *Appl. Surf. Sci.*, *255(10)*, 5191–5198.

Singh, J., and S. Thakur (2006), *Laser Induced Breakdown Spectroscopy*, Elsevier, Amsterdam.

Smithells, C. J., W. F.. Gale, and T. C.. Totemeier (2004), *Smithells metals reference book*, Elsevier Butterworth-Heinemann.

Strickland, D., and G. Mourou (1985), Compression of amplified chirped optical pulses, *Opt. Commun.*, *56(3)*, 219–221.

Sunil, S., A. Kumar, R. K. Singh, and K. P. Subramanian (2008), Measurements of electron temperature and density of multi-component plasma plume formed by laser-blow-off of LiF-C film, *J. Phys. D. Appl. Phys.*, *41(8)*, 85211.

Tang, E., S. Xiang, M. Yang, and L. Li (2012), Sweep Langmuir Probe and Triple Probe Diagnostics for Transient Plasma Produced by Hypervelocity Impact, *Plasma Sci. Technol.*, *14(8)*, 747–753.

Tankosić, D., L. Č. Popović, and M. S. Dimitrijević (2001), Electron-impact stark broadening parameters for ti ii and ti iii spectral lines, *At. Data Nucl. Data*, *77(2)*, 277–310.

Ursu, C. (2010), Caracterisation par methodes optiques et electriques du plasma produit par ablation laser, PhD Thesis; Université Lille 1 – Sciences Et Technologies.

Ursu, C., and P. Nica (2013), Diagnosis of carbon laser produced plasma by using an electrostatic energy analyzer, *Optoelectron. Adv. Mat., 15(1)*, 42–45.

Ursu, C., S. Gurlui, C. Focsa, and G. Popa (2009), Space- and time-resolved optical diagnosis for the study of laser ablation plasma dynamics, *Nucl. Instrum. Meth. B, 267(2)*, 446–450.

Ursu, C., O. G. Pompilian, S. Gurlui, P. Nica, M. Agop, M. Dudeck, and C. Focsa (2010), Al_2O_3 ceramics under high-fluence irradiation: plasma plume dynamics through space- and time-resolved optical emission spectroscopy, *Appl. Phys. A-Mater.*, *101(1)*, 153–159.

Weaver, I., G. W. Martin, W. G. Graham, T. Morrow, and C. L. S. Lewis (1999), The Langmuir probe as a diagnostic of the electron component within low temperature laser ablated plasma plumes, *Rev. Sci. Instrum.*, *70(3)*, 1801–1805.

Yao, Y. L., H. Chen, and W. Zhang (2005), Time scale effects in laser material removal: a review, *Int. J. Adv. Manuf. Tech.*, *26(5)*, 598–608.

Yeates, P., C. Fallon, E. T. Kennedy, and J. T. Costello (2013), Atomic mass dependent electrostatic diagnostics of colliding laser plasma plumes, *Phys. Plasmas*, *20(9)*, 093106.

Zimmermann, F. M., and W. Ho (1995), State resolved studies of photochemical dynamics at surfaces, *Surf. Sci. Rep.*, *22(4–6)*, 127–247.

Chapter III   Experimental investigations of laser-produced plasma plumes

III.1 Introduction

Among the applications of laser ablation discussed in Chapter I, probably one of the most significant is the Pulsed Laser Deposition (PLD). The technique has been validated over 30 years ago when <u>Dijkkamp</u> et al. [*Dijkkamp et al.*, 1987] reported for the first time "successful preparation of thin films of Y-Ba-Cu-O superconductors using pulsed excimer laser evaporation of a single bulk material target in vacuum". Over the years, the technique has been used to obtain high quality thin films for a wide range of technological applications [*Miotello and Ossi*, 2010]. The versatility of the PLD technique resides in its dependence on a series of external parameters (background gas [*Amoruso et al.*, 2004, 2008; *Chen et al.*, 2013], laser fluence [*Hermann et al.*, 2008], laser beam wavelength [*Burdt et al.*, 2010], target nature or target-substrate distance [*Johnson and Christy*, 1974; *Donnelly et al.*, 2010b]). Nowadays, a significant number of papers [*Puretzky et al.*, 1993; *Thestrup et al.*, 2002; *Amoruso et al.*, 2005b; *Donnelly et al.*, 2010, *Dascalu et al., 2013*, *Pompilian et al., 2013,2014, Bulai et al., 2015,*] dedicated to laser produced plasmas (LPP) investigations through various methods have been published with the aim to completely understand the deposition process and provide a better control of the quality and properties of the deposited films. The investigation techniques are also meant to further explore the fundamental processes involved in the laser - matter interaction and to investigate the plasma chemistry and dynamics so that specific technological applications are improved. The papers published until now focused on the effects caused by laser beam and target properties on the damage induced to the surface of the bulk material and/or the subsequent particle ejection, the effects of the background pressure on the kinetics of the ablated cloud [*Harilal et al.*, 2014a] and the formation of complex structures [*Borowitz et al.*, 1987; *Harilal et al.*, 1997; *Nica et al.*, 2010a; *Focsa et al.*, 2017], and (maybe one of the most important study from an applicative perspective) on the effect of the target and plasma properties on the quality of the grown thin film [*Phipps*, 1994]. Due to the multi-parametric dependence of laser ablation and PLD on the external factors, the experiments need to be performed under identical conditions (fluence, background pressure, target polarization) in order to extract reliable information regarding the connection between the physical properties of the target and the plasma parameters (defined for each distance and moment of time).

In this chapter, we undergo the task of experimentally investigating the connection between the properties of the target and those of the laser ablation plasma. As such, we started with fundamental space- and time-resolved optical and electrical investigations of laser-produced plasmas on a series of metals in order to understand how the properties of the metallic target influence those of the nanosecond-LPP. We extended the study to different ablation regimes (ps and fs) in order to understand if the relations between the properties of the plasma and those of the target depend on the laser type used for plasma generation. To correlate and apply these findings to the growth of thin films, we also investigate the dynamics of the LPP on Al targets in PLD configuration, focusing on the plume dynamics in the substrate area and on the oscillatory behavior of the ns-LPP. Finally the study was focused on the investigations through optical methods of LPP on complex chalcogenide targets, where the focus will be on how the structural changes in the targets can affect the dynamics of the plasmas.

III.2 Optical and electrical investigations of laser-produced plasmas on single-element targets in various temporal regimes

III.2.1 Nanosecond Laser Ablation

In this section, we will present the results of our experimental investigations on nanosecond laser-produced plasmas on various metallic targets in identical experimental conditions. The investigation techniques are the ones described in Chapter II. For both optical and electrical investigations a Nd:YAG laser beam (10 ns, 10 Hz, 532 nm) was focused on a 0.025 mm^2 area leading to constant laser fluence of 10 J/cm^2. The background pressure was 10^{-6} Torr and the targets were electrically grounded. The aim of the study was to investigate how the nature of the target affects the global evolution of the plasma, through ICCD fast camera imaging, and the individual dynamics of the ejected particles through space- and time-resolved OES and Langmuir probe measurements. Moreover, a study was performed regarding the influence of the laser fluence on the global dynamics of the plume and the results were compared with the ones available in the literature.

III.2.1.1 ICCD fast camera imaging

The ICCD measurements were performed in order to study the global dynamics of the laser-produced plasmas on each target and then to correlate the results with the properties of the target. An example can be seen in *Figure III.1* where we present six snapshots acquired with a gate width of 10 ns after 150 ns with respect to the laser pulse. We can observe that each plume has a characteristic spatial distribution, area and intensity, induced by the physical properties of the target. Moreover, *Figure III.1* shows that the Mn plasma has a diminished size and a clearer separation between the two structures, while the Al plasma has a larger volume and a more uniform distribution throughout the volume, thus making the separation between the two structures harder to be identified. This can be induced by the possible differences in plasma density and velocity. A higher velocity could lead to a faster expansion and, implicitly, to a more expanded plasma in a relatively short time (a few hundreds of nanoseconds).
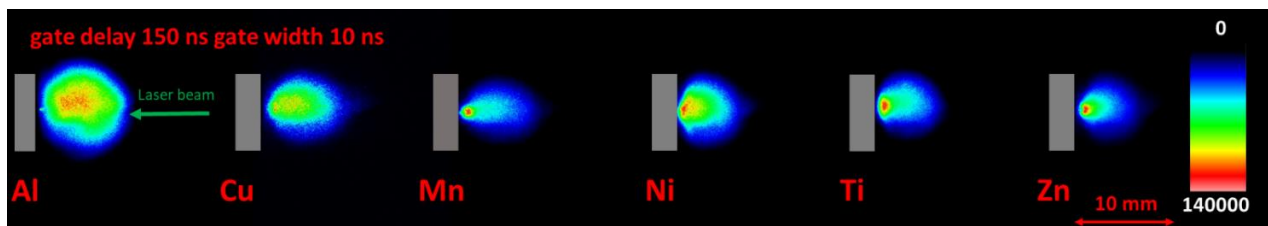
Figure III.1   ICCD images of laser-produced plasma plumes on various metallic targets in identical conditions of laser fluence and background pressure, acquired 150 ns after the laser pulse.

In order to estimate the expansion velocities, we recorded bi-dimensional images ("snapshots") of the laser-produced plasmas at constant laser fluence (10 J/cm^2) at various moments in time with respect to the laser beam. We were therefore able to reconstruct a movie from all the collected "snapshots" depicting the evolution of each individual plasma in time (*Figure III.2*). During the expansion, the LPP increases its volume and the center-of-mass, estimated as the maximum emission intensity zone, shifts towards higher distances as the recording time is changed. This leads to the conclusion that the expansion velocity is constant during the whole life-time of the plume.
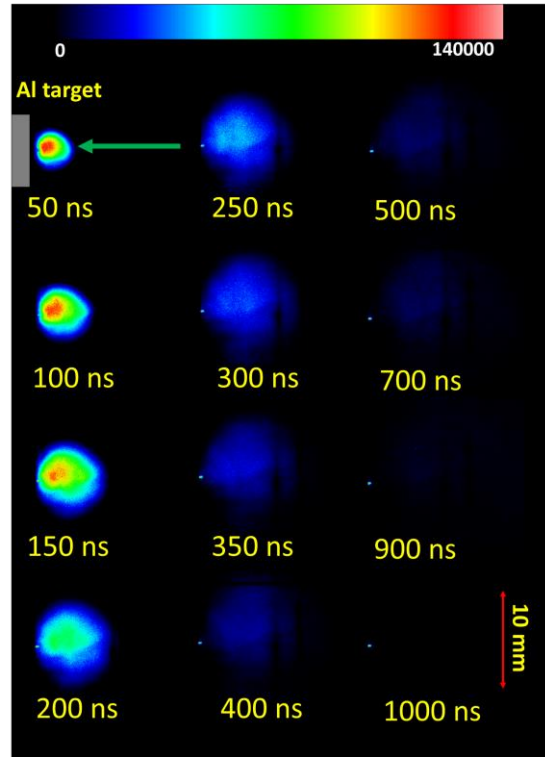
Figure III.2   ICCD images of laser-produced plasma plumes on Al, depicting the global evolution of the plasma during 1 μs after the laser shot.

The cross-section on the expansion direction of the recorded images (*Figure III.3a)* shows more clearly the presence of two maxima which were attributed to two plasma components. Due to the difference in their expansion velocities (*Figure III.3b*), in the following we will refer to the fast structure as the "first structure" and to the slow structure as the "second structure". For most of the investigated plasmas we obtained velocities of tens of km/s for the first structure, while for the second structure velocities of km/s. However, exceptions were found for the Al and Ti plasma probably due to their lower atomic mass in comparison to the other elements. This aspect of the laser-produced plasma is consistent with other reported results from literature. The situation changes when a background gas is introduced [*Bulgakova and Bulgakov*, 1998; *Amoruso et al.*, 2008; *Harilal et al.*, 2014a]. In this case the velocity is significantly reduced and could lead even

to the stopping (suppressing the plasma's expansion) of the plume [*Canulescu et al.*, 2009; *Ojeda-G-P et al.*, 2017].
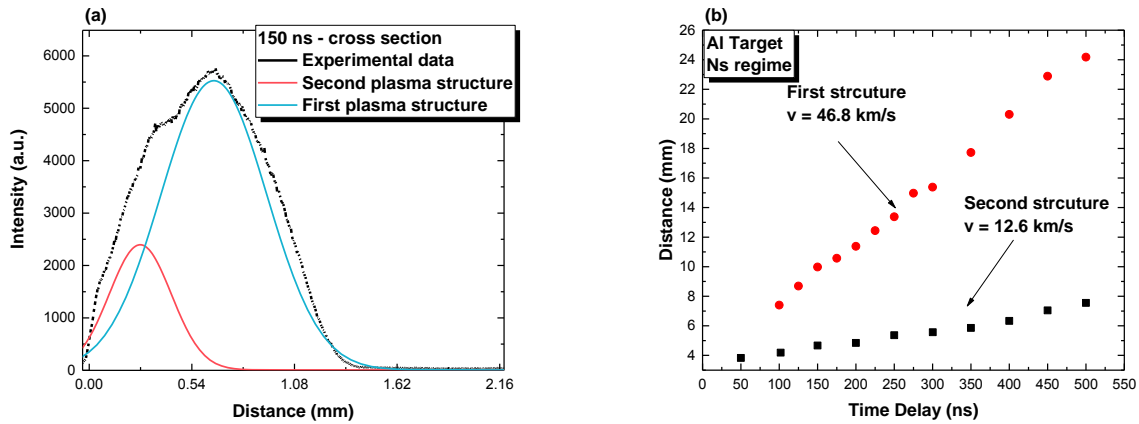
Figure III.3   Cross section on the expansion direction of an ICCD snapshot acquired at 150 ns delay (a) and the center-of-mass space-time evolution for both plasma structures (b)

The plume splitting behavior has been experimentally reported by several groups, being generally attributed to the interaction between the plasma plume and the background gas [*Harilal et al.*, 2003a]. However, in the past decade the splitting of the ns-LPP into two different structures was also observed in high-vacuum conditions [*Ursu et al.*, 2009; *Gurlui and Focsa*, 2011; *Irimiciuc et al.*, 2017a; *Focsa et al.*, 2017]. Thus, the plume splitting process may rather be considered as a result of the different ejection mechanisms involved in the ns-laser ablation process. Therefore, the first – fast structure of the plume is ascribed to the electrostatic ejection mechanism (Coulomb explosion [*Bulgakova et al.*, 2005]), while the second - slow structure corresponds to the thermal mechanisms (phase explosion [*Kelly and Miotello*, 1996], explosive boiling [*Kelly and Miotello*, 1998], evaporation [*Bulgakov and Bulgakova*, 2007]). Our results show the presence of a third plasma structure described by a small emission region in the proximity of the target. In literature this structure is attributed to the presence of clusters, nanoparticles or molecules and it has its origin in the Knudsen layer which is usually characterized by black body radiation [*Harilal et al., 2003; Amoruso et al., 2004; Canulescu et al., 2009*].

We also extended our study to other laser fluences in order to understand the effect of this parameter on the plume dynamics. We modified the laser fluence by changing the beam energy per pulse, while keeping constant the irradiated area. The fluence was changed from 1.5 J/cm^2 up to 15 J/cm^2. A primary noticeable effect was the change in the shape of the plume; the plasma became elongated across the expansion direction for higher fluences [*Cremers et al.*, 2006], while for lower fluences it had a quasi-spherical shape (*Figure III.4*).
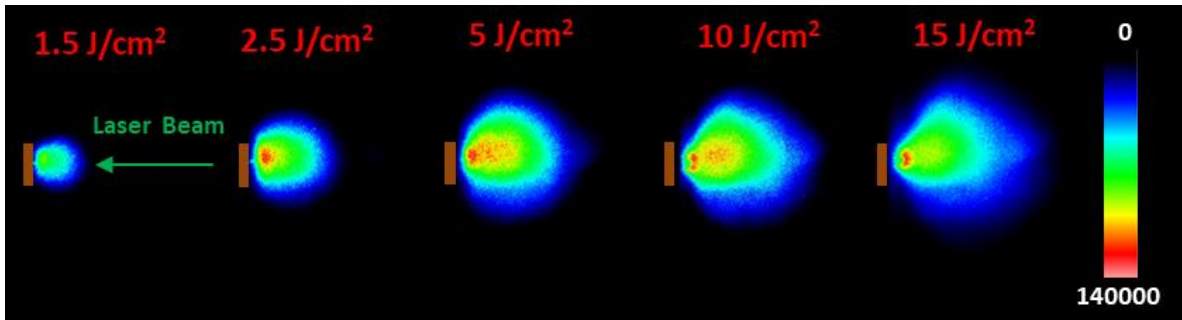
Figure III.4   ICCD snapshots of ns laser-produced plasma plumes on a copper target at 150 ns delay for various fluences.

Using the same approach as before, we estimated the expansion velocities of each plasma structure. The results are presented in *Figure III.5* and reveal that the velocity is augmented with the increase of the laser fluence. In literature, this increase is followed by a saturation region [*Amoruso et al.*, 1997]. In our study, this saturation region is more visible for Cu plasma, while for Zn or Mn we could observe a quasi-linear increase.
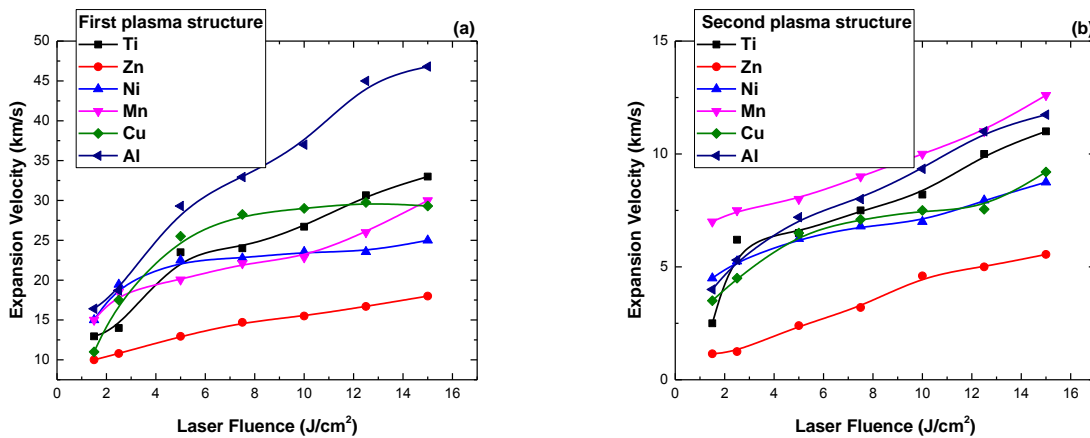
Figure III.5   Expansion velocities of the first (a) and second (b) plasma structures for all investigated plasmas *vs* laser fluence.

Although, the ICCD technique provides important information, it does not differentiate between the contributions of each species to the plume dynamics. That is why we used complementary methods based on optical emission spectroscopy to study the behavior of individual species and their dynamics. This short section gives just a preliminary view of the trends recorded for the overall dynamics of the plume and detailed comments on the relationships with the target materials will be given in the *Section III.3*.

III.2.1.2   Optical Emission Spectroscopy

Space- and time-resolved optical emission spectroscopy has proved to be a suitable technique that can differentiate between the individual dynamics of the plumes and their internal structure [*Cremers et al.*, 2006]. Therefore, we used it in our study to record the local emission spectra at different distances from the target surface in identical conditions for all investigated plasmas. In order to have an overview of the various species present in the plasma, we started with recording "global" emission spectra, i.e. using long integration times (gate width = 2 µs). In *Figure III.6* we observe that all recorded spectra, regardless of the nature of the target, exhibit spectral lines coming from both atoms (Cu – 514 nm, Al – 396.4 nm, Mn - 403.3 nm, Zn – 428.5 nm, Ti – 467.9 nm, Ni - 310.15 nm) and singly- (Cu II - 490.6 nm, Al II – 358.6 nm, Mn II – 424.42 nm, Zn II – 481.1 nm, Ti II – 491.11 nm, Ni II – 432.6 nm) or doubly-charged ions (Cu III - 435 nm, Al III – 477.99 nm, Zn III – 506.42 nm, Ti III – 472.12 nm). The abundance of the emission lines differs from one material to another. These differences are understandable given the differences in the kinetic and thermal energies of the plasmas and the energy levels that characterize the emission of each individual species [*Ralchenko*, 2005].

The measurements were performed systematically on a distance range from 1 mm to 40 mm in 20 different spatial points. The time-resolved measurements were performed at 1 mm from the target and by using a 50 ns gate width we investigated the evolution of the excitation temperature in the first 500 - 700 ns. This allowed us to use the Boltzmann method [*Cremers et al.*, 2006; *Pompilian et al.*, 2013] (described in *Chapter II*) to determine the excitation temperature of all the species that are present in the plasma (for atoms, singly- and doubly-charged ions). Besides the differences in excitation temperatures of different plasmas, we also observed that the excitation temperatures of the particles in the high ionization states are higher than those of the neutral atoms. As an example, for the Al plasma analyzes at a distance of 1 mm from the target surface we obtained an excitation temperatures of 1.6 eV, 2.2 eV and 6.2 eV for Al I, Al II and Al III, respectively (see *Figure III.7*). These important differences can be seen as a deviation from the LTE, but we have to take into account the density of the lines per specific species. Because the Boltzman plot method is a statistical one, for a better estimation of the temperature we need to consider a wide range of excited states per each species. This can be achieved for atoms, as the majority of the recorded lines correspond to excited states of the studied element, but only a few are attributed to ions. The difference between the excitation temperatures of different species can be based on the selective heating of the plasma constituents by the ns-pulse tail.
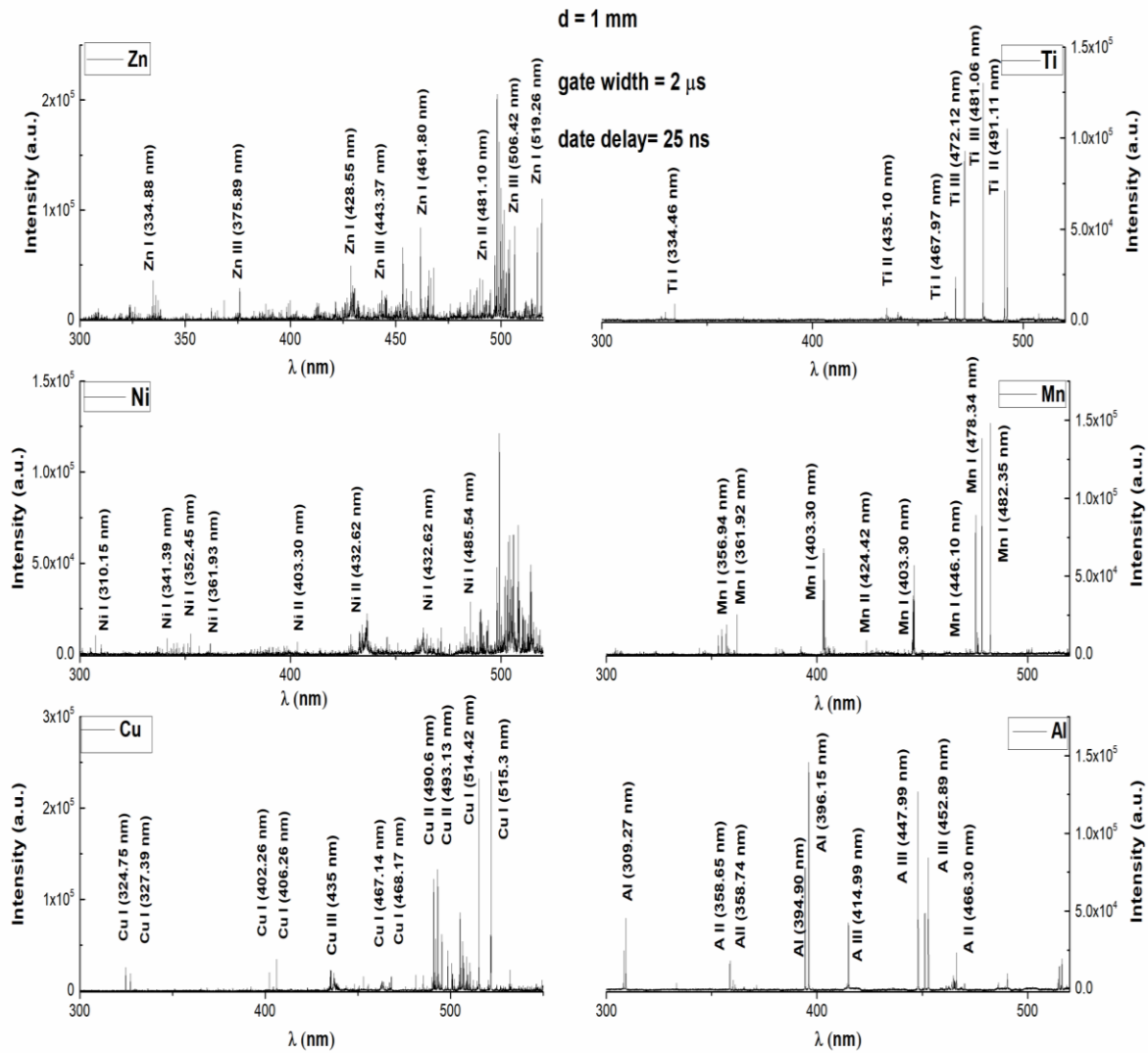
Figure III.6   Emission spectra of all investigated plasmas at 1 mm from the target using a gate width of 2 μs and a gate delay of 25 ns.
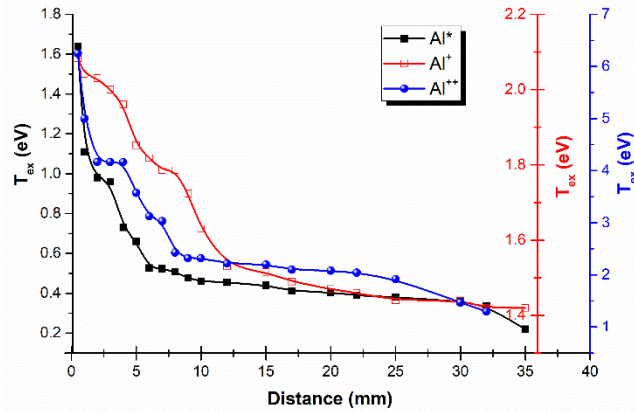
Figure III.7   Spatial evolution of the excitation temperatures found for Al I (396.15 nm), Al II (358.6 nm) and Al III (477.99 nm) determined from the optical emission spectra collected with a 50 ns gate width and 25 ns gate delay.

The results obtained for all the investigated targets are presented in *Figure III.8* where one could notice a decrease in excitation temperature for metallic atoms in both space and time. This result is in good agreement with other similar studies [*Delserieys*, 2001.; *Amoruso et al.*, 2002b; *Mazhukin et al.*, 2003; *Ursu et al.*, 2009; *Pompilian et al.*, 2013].
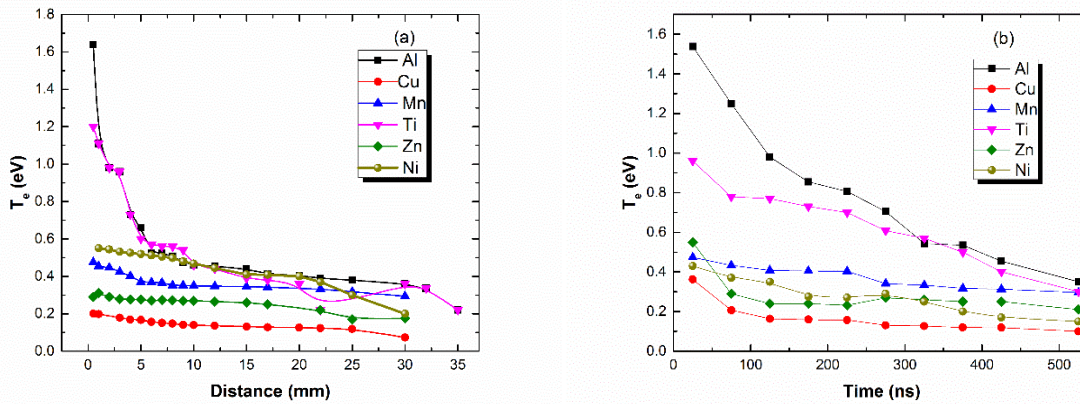
Figure III.8   Spatial (a) and temporal (b) evolution of the excitation temperature for metallic atoms of the laser-produced plasma plumes.

The time decrease in excitation temperature is generally considered a characteristic of laser-produced plasmas [*Barthelemy et al.*, 2005]. The particularities of each system are given by the range of excitation temperatures, particle density and their space – time evolution. The local values of the excitation temperatures can be influenced by the background gas mass and pressure [*Geohegan and Puretzky*, 1996; *Amoruso et al.*, 2008], laser fluence [*Claeyssens et al.*, 2002] and

target properties [*Ursu*, 2010]. Here we observe that the overall values are found to be higher for the Al and Ti plasmas, while lower values were obtained for Zn and Cu plasmas. The effect of the target atomic mass can be tentatively observed here, as targets with a higher atomic mass present a lower excitation temperature. The nature of the function connecting these two properties, alongside other relations between the target properties and those of the plasmas, will be discussed in detail in *Section III.3*.

In order to separate and investigate the contribution of each species to the plume kinetics, we performed time-resolved measurements using a fast response photomultiplier mounted on the high-resolution monochromator. A specific behavior is presented in *Figure III.9,* where we emphasized specific time-of-flight (TOF) traces for the Cu atom (Cu I - 521.83 nm) and ions (Cu II - 505.17 nm and Cu III - 435.19 nm) at 1 mm from the target.

The graphical representation (*Figure III.9*) highlights a difference between temporal traces of the signals corresponding to the atoms and those of the ions. The recorded signal describe the amount of time required for a particular species to "fly" by the optical detector. The signals acquired for atoms generally last almost twice as long as those of the ions [*Ursu et al., 2010*]. It can also be observed that doubly ionized species have a shorter life time than those of the singly ionized. This can be ascribed to the separation made during the Coulomb explosions [*Bulgakova et al.*, 2005] which leads to the formation of the first plasma structure, where, due to the charge separation, the positive charged particle will be accelerated in an electric field (ambipolar diffusion). This leads to a change in velocity and thus life-time of the respective ions and multiply-charged ions.
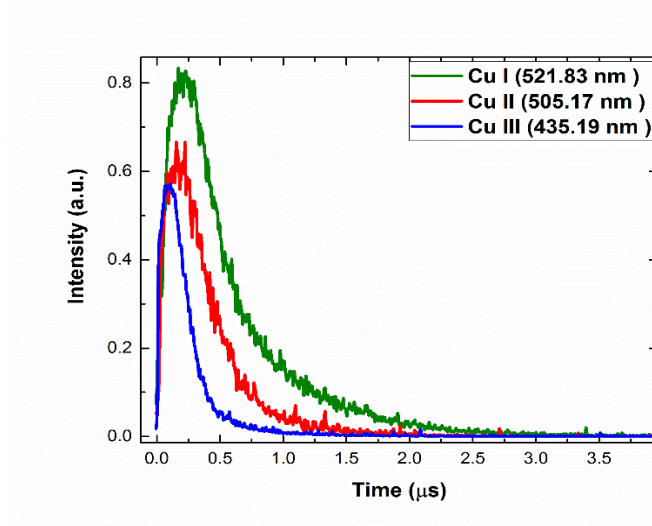
Figure III.9   Temporal evolution of the Cu I-521.83 nm, Cu II-505.17 nm and Cu III-435.19 nm emission lines at a distance of 1 mm from the target recorded with a sub-ns rise-time photomultiplier.

These measurements allowed us to determine the expansion velocity for each species by recording the TOF signals at different distances with respect to the target surface (*Figure III.10*). Plotting the distance *vs.* the moment when the maximum emission is recorded we were able to estimate the "most-probable" expansion velocities of each species (*Figure III.10* and *Table III.1*). For our study, we found that the highest values were reached for the targets with the lowest atomic mass (Al, Ti), while the "heaviest" materials are described by lower expansion velocities. The values are in good agreement with results from other studies [*Ursu et al.*, 2009; *Pompilian et al.*, 2013; *Irimiciuc et al.*, 2017a; Geohegan and Puretzky, 1995; Harilal et al., 2003b; Amoruso et al., 2005d] and could introduce the idea that the splitting of the plume can be influenced by the different ablation mechanisms involved in the ablation process [*Tsakiris et al.*, 2014; *Focsa et al.*, 2017]. We can conclude from here that the structuring of the plume and the separation (splitting) are both kinetic processes strongly related to the ejection mechanism and to the properties of the target.
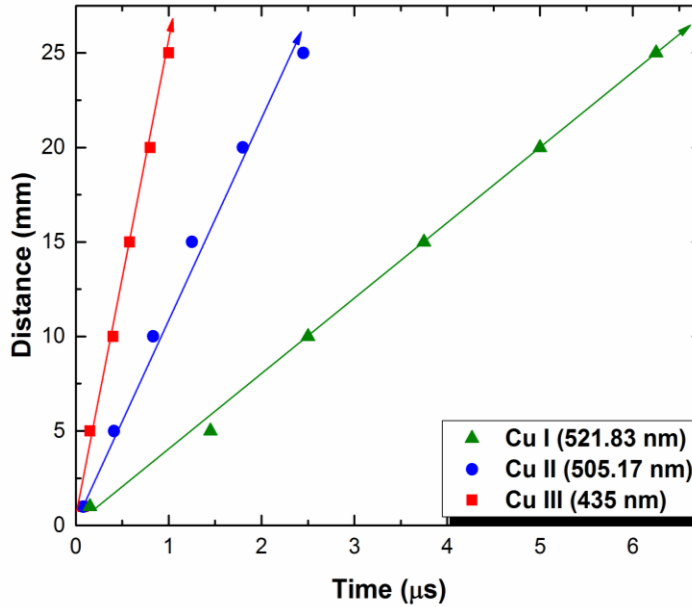
Figure III.10   The space-time displacement of the maximum emission for the Cu I - 521.83 nm, Cu II - 505.17 nm and Cu III - 435.19 nm spectral lines recorded with a sub-ns rise-time photomultiplier.

Table III.1   The expansion velocities for the atoms and the corresponding ions determined by means of PMT measurements for all investigated targets.

Target	Neutral atom velocity (km/s)	Singly-charged ion velocity (km/s)	Doubly-charged ion velocity (km/s)
Al	14.7	30	95.41
Cu	3.3	12	25.6
Mn	5.6	20.4	31.34
Ni	3.3	13.88	28.81
Ti	8.8	25	66
Zn	1.11	12	16.94

Focusing on the TOF signal of the atoms (Cu I in *Figure III.11*) we observed that at long distances (above 18 mm from the target surface) a second peak is noticeable. The two-peak distribution can be attributed to the two specific plasma structures which were evidenced through ICCD imaging in this study and was reported in other laser-produced plasmas, regardless of the ablation regime [*Geohegan and Puretzky, 1995; Amoruso et al., 2006; Harilal et al., 2003b*]. This separation is observed only for atoms, and given their higher intensity confirms the fact that the split does not segregated the atoms from ions. The plume splitting leads to the formation of two independent plasma components containing both atoms and ions.
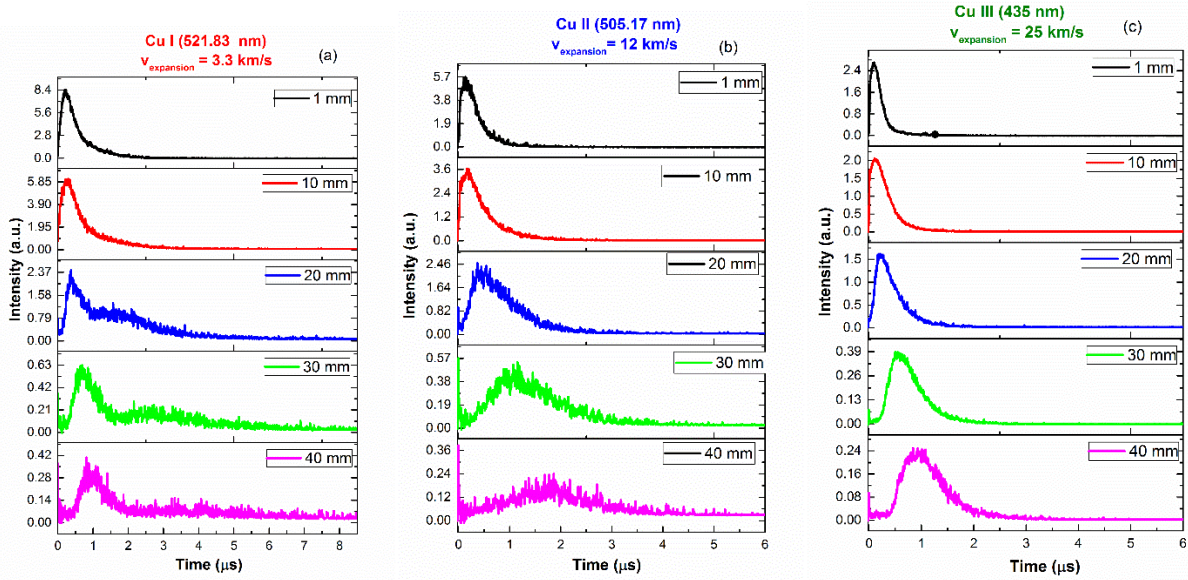
Figure III.11 TOF distribution of emission lines and their spatial evolutions for Cu atom (a) and ions (b-c).

III.2.1.3   Langmuir Probe Investigations

As it was presented in the previous chapter, the Langmuir Probe (LP) method is one of the simplest diagnostic tools for plasma investigations. It consists in immersing an electrode in the plasma in order to collect either the ionic or the electronic current, depending on the probe biasing. While the optical methods focus on the light emitted by the excited species, the LP method gives information regarding the kinetics of the charged plasma particles (electrons and ions). In other words, the LP method is a complementary method with respect to the optical ones presented earlier. In this section, we applied comparatively two methods for LPP investigation. The first one is based on the treatment of the current-voltage characteristics (*I-V* plots) derived from the time-of-flight current profiles recorded at various probe biases and sampled at specific delays after the laser pulse. In the second approach, the recorded ionic currents are fitted with a shifted-Maxwellian function. In principle, the first ("classical") approach regards mainly the thermal movement of the particles at specific moments of time, thus the plasma is considered stationary with Maxwellian distribution function. From this time-resolved approach, electronic temperature and density can be derived using the collected *I-V* characteristic by classical LP theory (*Chapter II*). Moreover, extending the technique to different probe - target distances, a spatial distribution of these parameters can be obtained. The second approach is a more global (general) one, and takes into account the flow of the plasma towards the target by means of TOF signals. The drift velocity is constant during the expansion, while the values of the overall ionic temperature (averaged over the whole expansion time) are extracted at various distances. These differences given by the local-global approaches are very important and will be recalled at various points in the following.

Figure III.12a displays the time-of-flight (TOF) profiles recorded by the LP biased at various voltages in the [-30 V, +30 V] range for ns-ablation of Al target. By sampling these TOF

signals at various delays (1 - 20 µs) after the laser pulse, one can reconstruct the *I-V* characteristics corresponding to these evolution times. *Figure III.12b* shows, as an example, the *I-V* plots for Al plasma at 11 µs - 15 µs delays. The time-dependence of plasma parameters (electron temperature, plasma potential, ion density, thermal velocity and Debye length) were obtained by analyzing all such *I-V* characteristics using the steps presented in *Chapter II*. At this particular short space-time scale, our previous data [*Gurlui et al.*, 2008; *Nica et al.*, 2009, 2010a] revealed the presence of complex oscillatory character of the probe current, the results also being confirmed by other authors [*Amoruso et al.*, 1999; *Sunil et al.*, 2008; *Kumar et al.*, 2009; *Singh et al.*, 2014]. The oscillating regime is not covered by the LP method as the temporal evolutions of the plasma parameters were studied here at delays greater than 1 µs. However, these phenomena are discussed on a different section (*Section III.4*).
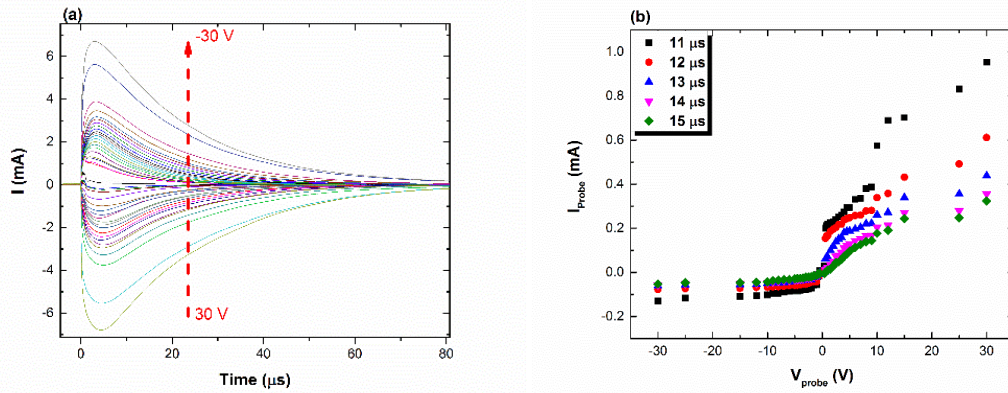
Figure III.12   Probe current traces for Al plasma at 5 mm from the target (a) and the reconstructed I-V characteristics (b).

The space- and time-resolved studies were employed for all six plasmas. An example is presented in *Figure III.13,* where we plotted the temporal evolution of T_e, N_i, V_{Plasma}, $v_{thermal,}$ that were determined from current traces extracted at 5 mm from the target and the spatial distribution at 1 µs after the laser beam interacts with the target. We observe that all mentioned plasma parameters are decreasing in both space and time. For the example given here, the electron temperature is in the range of 5.5 - 1 eV for the whole expansion time, the ion density decreases by about one order of magnitude from $1 \times 10^{20} \, m^{-3}$ at 1 µs to $4 \times 10^{19} \, m^{-3}$ at 20 µs. All traces depicting the evolution of the plasma parameters present a maximum for lower space-time coordinates and decrease as the plume expands. Considering the results obtained for all investigated plasmas, we can state that the highest values for the electron temperature were found for Cu and Al plasmas (6 - 7 eV), while the lowest values were found for the Mn and Ti plasma (~ 2-3 eV). The highest ionic density was found for the Zn produced plasma. This is most probably given by the Zn properties such as low melting and vaporization temperatures and relatively high thermal conductivity. On the other end, the Al plasma was found to have the lowest ion density. As seen in the previous section the velocities derived for the Zn plasma were the lowest, compared with the other targets. We can assume that in this case the main part of the beam energy is used to

extract a higher content of Zn from the target while in the case of Al some part of the absorbed energy is transferred to the kinetic energy of the ejected particles.
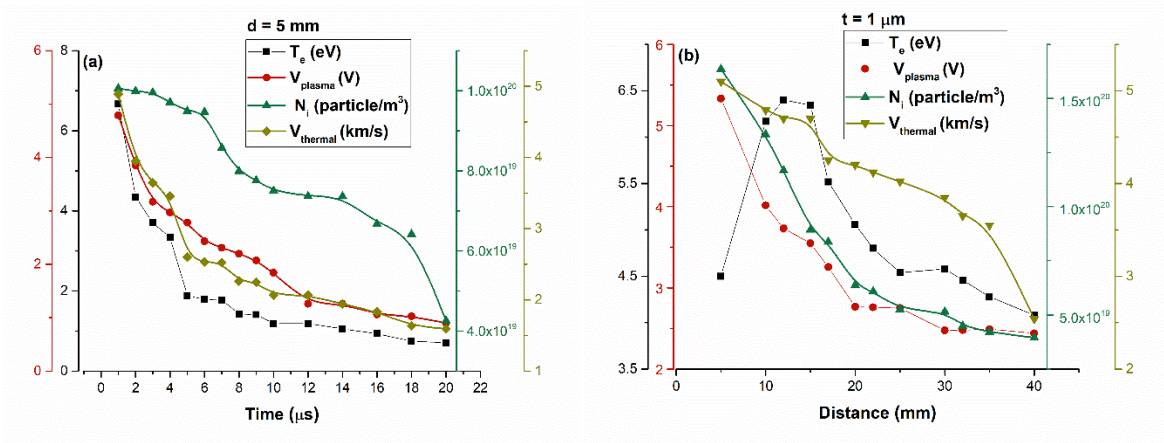
Figure III.13   Electron temperature, plasma potential, ion density and thermal velocity of an Al ns-laser produced plasma temporal dependence (a) at a fixed distance (d = 5 mm) and the spatial one (b) at a fixed moment in time (t = 1 μs).

As the technique was applied for various distances at different moments in time, for each plasma parameter we build maps V_{Plasma} (x, t), $v_{thermal}$ (x, t), T_e (x, t) and N_i (x, t). These are represented in *Figure III.14*. We found here that the values of the parameters describing the internal energy of the plume (such as electron temperature, thermal velocity and plasma potential) are decreasing. We also observed a rarefying of the plume through the decrease of the ionic density. Our results are in good agreement with the prediction of classical theoretical models like the ones proposed by Anisimov and Luk'yanchuk [*Anisimov and Luk'yanchuk*, 2002], which present an exponential decrease for plasma parameters (i.e., density or temperature) considering that all particles are produced through thermal ablation mechanisms. In our experiments, we observed two contributions in the temporal evolution, one having a maximum before 1 μs and another maximum after 10 μs. This result is in good agreement with the ICCD images and underlines that each plasma structure (component) that results after the plume split, is described by an individual plasma temperature, thermal velocity, particle density and plasma potential. From the position of the peaks/maxima we can estimate the expansion velocities of these structures. For the slow structure, a velocity of km/s was found and for the fast one values of tens of km/s, results consistent with the ones obtained through ICCD fast camera imaging.
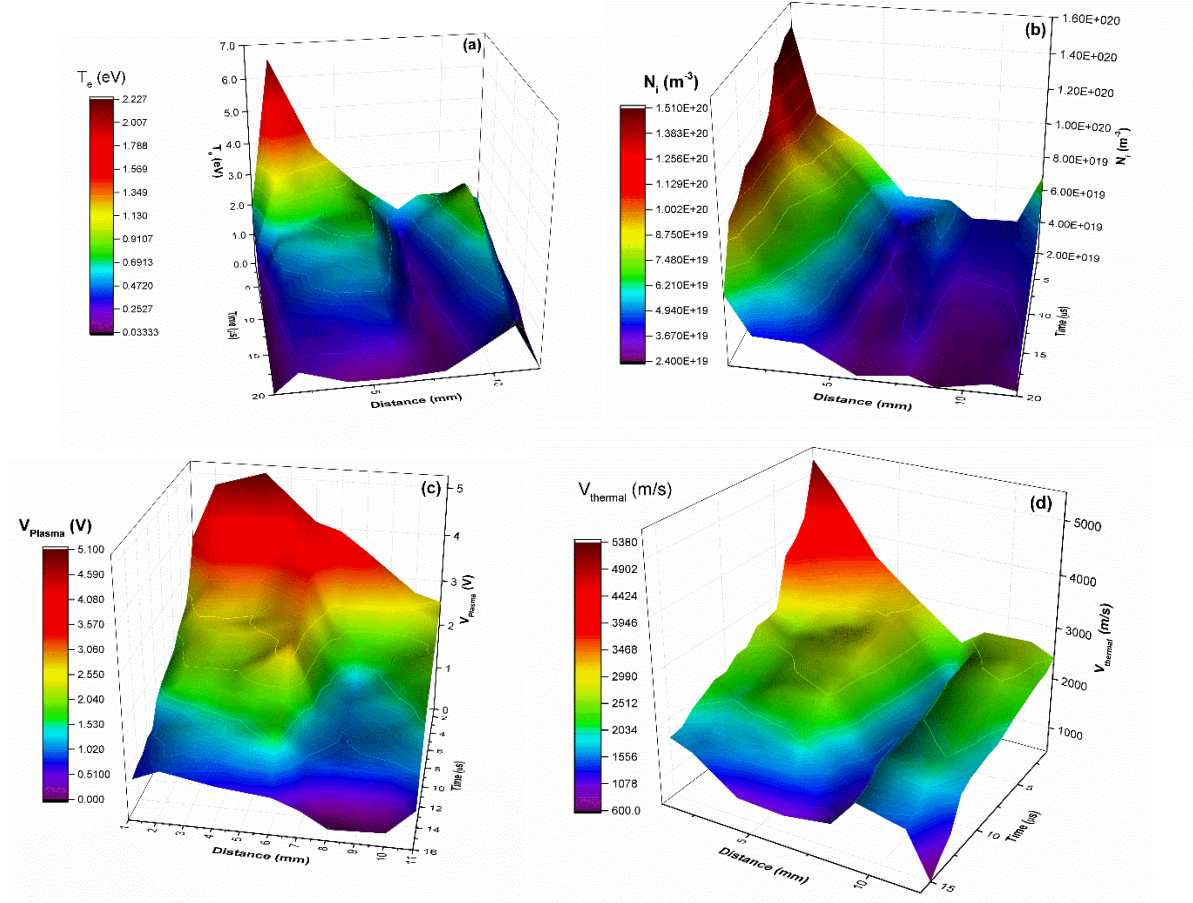
Figure III.14   Surface plots of T_e, N_i, V_{Plasma} and $v_{thermal}$ in space and time for ns-Al plasma.

The validation of our results does not come only from comparison with classical theoretical models or new, fractal ones (which are detailed in *Chapter IV*). The results can also be confirmed by understanding the confidence degree of the LP method. In *Chapter II*, the technique is presented as being an invasive one, thus the plasma will be perturbed by the presence of the probe. This especially becomes important for measurements performed at short distances. A way of estimating the perturbation induced in the plasma considers the Debye length. The Debye length is a characteristic length in plasma, defined as the minimum distance at which an external perturbation is confined (or as the minimum plasma volume for which we can consider the quasi-neutrality of the plasma) and determined as $\lambda_{Debye} = \left(\dfrac{\varepsilon_0 k_B T_e}{e^2 n_e} \right)^{1/2}$. Given the expression of the Debye length, one can expect an increase of this parameter during plume expansion. This translates as a decrease in the collision rate and particle thermal movement [*Popa and Sirghi*, 2000], while the average distance between the plasma particles is increasing. During our studies/experiments, for all investigated plasmas we found Debye length values between a few μm and up to tens of μm at

higher space-time coordinates. The result is in good agreement with other experimental studies [*Gamaly et al.*, 2002a].

Parameters such as electron temperature and plasma potential do not provide sufficient information to describe the whole dynamics of the plume. This determined us to evaluate a parameter with explicit information regarding the kinetic behavior of the plume. In laser-produced plasmas, the particles have two different contributions to the expansion velocity. One is given by the ablation mechanisms and acts as the driving force for the whole plume and another is given by the collision and the stochasticity of the particles during expansion. The electrical investigations through Langmuir probe theory mainly consider the thermal movement since the classical approach does not take into account additional contributions to the drift motion. The thermal velocity is strongly related to the electron temperature and its overall trend should be reflected in the one of the velocity. As observed from *Figure III.14d,* the values of the thermal velocity decrease exponentially starting from a few km/s towards values of hundreds of m/s, result consistent throughout all plasmas investigated in the ns ablation regime.

To obtain information on the kinetics of the plasmas (drift velocity), it is important to consider that not both the electrons and the ions are described by a Maxwellian distribution function. In the LP method framework, at each moment in time the plume is analyzed in a stationary regime and assuming a Maxwellian distribution we can obtain information on the expansion velocity component induced by the thermal movement of the plasma particles, neglecting the overall drift movement. Generally, laser-produced plasmas can be described more accurately by a non-Maxwellian distribution where a drift velocity is over-imposed on the Maxwellian distribution [*Gill et al.*, 1996; *Nica et al.*, 2010a; *Irimiciuc et al.*, 2017b]. The solution is to fit the temporal trace of the saturation ionic current with a shifted Maxwellian distribution and obtain information about the ionic drift velocity or the ion temperature (*Figure III.15a*). These particular parameters can be determined by plotting the ionic temporal traces using the following function:

$$I(t) \propto \frac{1}{t^4} \exp\left[-\frac{m}{k_B T_i} \left(\frac{d}{t} - v_{drift} \right)^2 \right], \qquad \text{Eq. (III.1)}$$

where m is the mass of the ions, T_i is the ions temperature, d is the fixed point inside the volume of the plume where the probe was placed and v_{drift} is the drift velocity of the ions. One important aspect of using such a theoretical approximation for the TOF signals is that this approximation disregards the temporal evolution of the ion temperature and the drift velocity. We only obtain values describing the overall evolution of the plume.

In *Figure III.15b* we observe that the ionic temperature decreases quasi-exponentially with the distance and presents similar values (same order of magnitude) with the ones obtained for the electron temperatures. The values obtained for the ionic temperature are mediated over the whole expansion time and thus some deviations with respect to the electron temperatures are expected. Still, the results are close to the ones from the time-resolved approach. The correlations between

the two approaches that describe the plasma plume dynamics at different time scales can support the assumption of a local thermodynamic equilibrium.
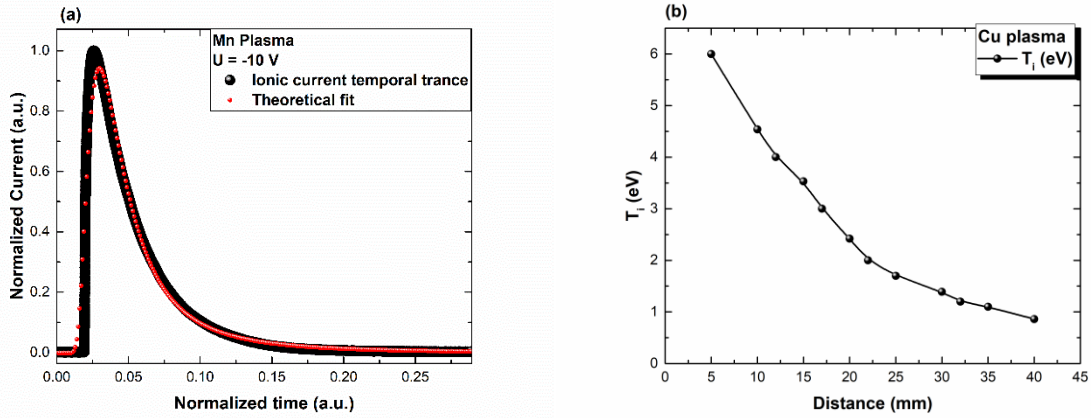
Figure III.15   Shifted Maxwell fit of TOF temporal evolution of the ionic current (a) and the spatial evolution of the ionic temperature (b).

For the global study (see *Figure III.16*), the highest ionic temperatures were found for Cu and Al (~ 6 eV) plasmas, while the lowest values were obtained for Mn and Ti (~ 0.5 eV). This result is similar with the one obtained through the LP sequential study. The similarities between the two approaches tell us that the link between the plasma plume and the target is not conditioned by the technique (we can look at the plasma either from a global perspective or a local one).
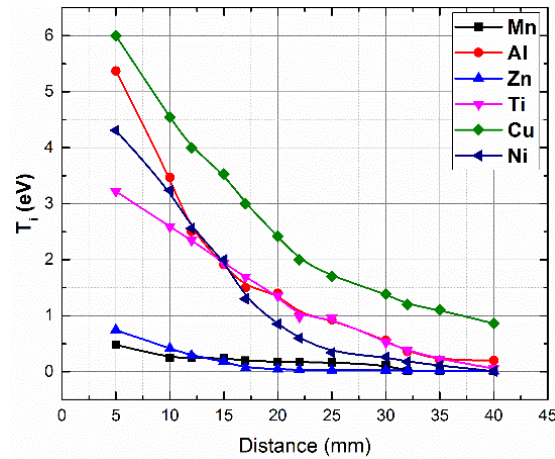
Figure III.16   The spatial evolution of the overall ionic temperatures (T_i) characteristic for all investigated plasmas in the ns ablation regime.

Using the shifted Maxwell-Boltzmann approach, we estimated a constant drift velocity with values of tens of km/s. The highest values were found for Cu (55 km/s), while the lower ones were obtained for Mn (10 km/s). An interesting observation is that the values found for the drift

velocity using the shifted Maxwell-Boltzmann fit are similar to the ones obtained through optical investigations for the fast structure and for the ions (produced by electrostatic interactions). Also, a similar statement can be made for the thermal velocity determined through LP method. The values obtained for the plasma thermal velocity are similar to the ones found for the slow structure (described by thermal interactions) and expansion velocities of the ejected atoms.

It could be said that the drift movement is dictated by the fast structure (fast ions and atoms escaping the target through electrostatic mechanism), while the thermal movement is more predominant in the second structure (particle ejected through thermal mechanisms). This statement will be confronted during this chapter with the results in other temporal regimes (ps, fs).

III.2.2 Picosecond Laser Ablation

Considering the results presented in the previous section, we further extended our study on the analysis of the ps laser-produced plasmas. The experiments were performed in identical conditions as for the nanosecond case. The plasmas were produced by focusing the beam from the picosecond Ti:Sa (1 ps, 100 Hz, 800 nm) laser energy on 0.0196 mm^2 area leading to a constant laser fluence of 8.7 J/cm^2. During the experiments, the background pressure was 10^{-6} Torr and the metallic targets were electrically grounded. By implementing the same investigations techniques (ICCD fast camera imaging, space- and time-resolved OES and Langmuir probe measurements) the aim of this study was to observe and understand the differences induced by the shorter ablation regime and to continue investigating the link between the properties of the plasmas and those of the target at this shorter ablation regime.

III.2.2.1 ICCD fast camera imaging

Bi-dimensional images of transient plasmas generated by ps laser ablation of metallic targets were recorded by implementing the ICCD fast camera photography technique. Sequential images were recorded on a 25 ns → 3 µs – 5 µs range, with respect to the laser pulse. In *Figure III.17* are presented examples of images recorded for each of the six investigated plasmas acquired with a gate width of 10 ns after 150 ns from the laser pulse. The gate width was increased as images were recorded at longer time-delays. As observed for ns-LPP, each plasma presents different dimensions (assuming that the "emitting volume" is representative of the "plasma volume") and a different emission intensity range induced by the physical properties of the target. The plasma produced on the Al target has a larger volume but a lower emissivity, while the Ni or Zn plasmas have smaller volumes but are relatively more intense. This means that the plasma produced on Zn or Ni targets are more directional and could present a lower expansion velocity and a relative higher particle density. The shorter ablation regime affects the shape of the plasma, here being more elongated and having a relatively smaller volume, but the ratios between the plasma volumes characteristics for each target are in line with the observation made for the nanosecond regime. For all investigated plasmas we observe a splitting of the (non-dispersed) emitted light. We identify one small area close to the target with a high emission intensity and a larger area defined by a lower overall emission positioned at higher distances. The differences between the global emitted

light by each plasma can be considered as a result of the modification of all the main plasma parameters (plasma temperature, density or expansion velocity) and this will be discussed in the following.
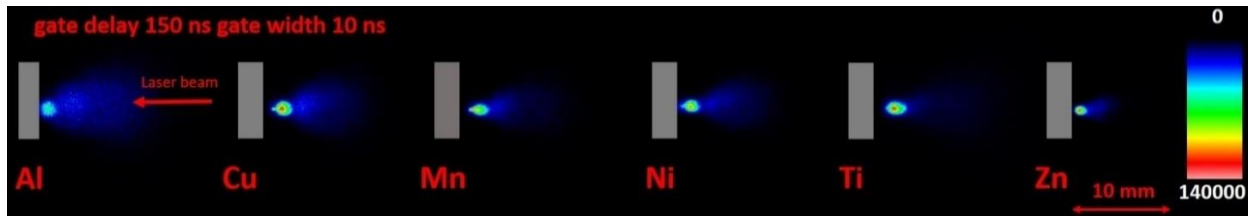
Figure III.17   ICCD images of plasma generated by ps laser ablation on various metalic targets in identical conditions of laser fluence and background pressure, aquired 150 ns after the laser pulse.

Furthermore, another relevant example of the recorded images is given in *Figure III.18*, where the evolution of ps-LPP on an Al target is presented at several time delays. For a more clear comparison and to underline the differences induced by a shorter pulse width on the plasmas evolution, we chose to represent the dynamics for the same material as in the case of ns laser ablation. During the expansion, the LPP increases its volume and the center-of-mass (attributed to the maximum of intensity) shifts towards larger distances as the recording time delay is changed. The ps-LPPs and their components are described by constant expansion velocities. The Al ps-LPP has a smaller volume compared with the one in ns-LPP and the splitting process occurs at shorter evolution times (~ 50-100 ns as opposed to 120-150 ns in ns-LLP). The lifetime of the Al plasma emission is about 900 ns, background noise becoming overwhelming past this threshold. At longer evolution times a third small structure, similar to the ns case, was observed, which is attributed to the small area filled with clusters and nanoparticles [*Chichkov et al.*, 1996; *Perdrix et al.*, 2001; *Amoruso et al.*, 2005b].
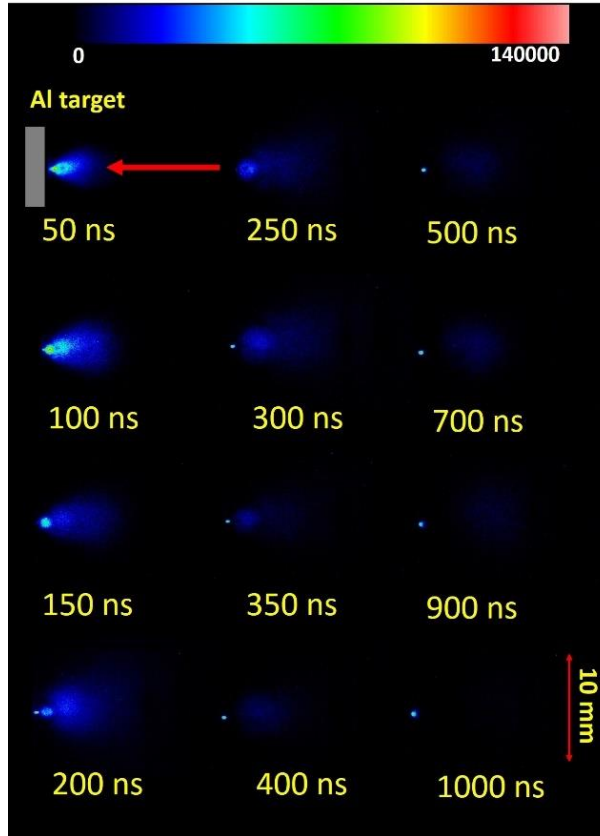
Figure III.18   ICCD images of ps laser produced Al plasma plumes showing the global temporal evolution up to 1 μs.

After analyzing the ICCD ps-LPP results from a qualitative point of view, further quantitative information related to global emission and plume structure was obtained by performing a cross-section of the recorded images across the expansion direction (*Figure III.19a*). We identified two distinct maxima, attributed to the two-component system described in the case of ns LPP structure. By plotting the displacement of these maxima, we determined the expansion velocities for each structure (*Figure III.19b*). For the first structure, we have obtained velocities of tens of km/s, while for the second structure we found velocities of few km/s. The plasmas with the highest expansion velocities are the Al plasma (26.8 km/s - 1st component and 10 km/s - 2nd component) and Ti plasma (25.4 km/s - 1st component and 8.6 km/s - 2nd component), while the lowest velocities were found for the Cu plasma (22.6 km/s - 1st component and 6.5 km/s - 2nd component) and Zn plasma (15.15 km/s - 1st component and 4.6 km/s 2nd - component). If for the ns laser ablation regime, the velocities were in the range 48 - 18 km/s for the fast component and 12 - 5.5 km/s for the slower one, here the velocity values are slightly smaller but have the same order of magnitude.
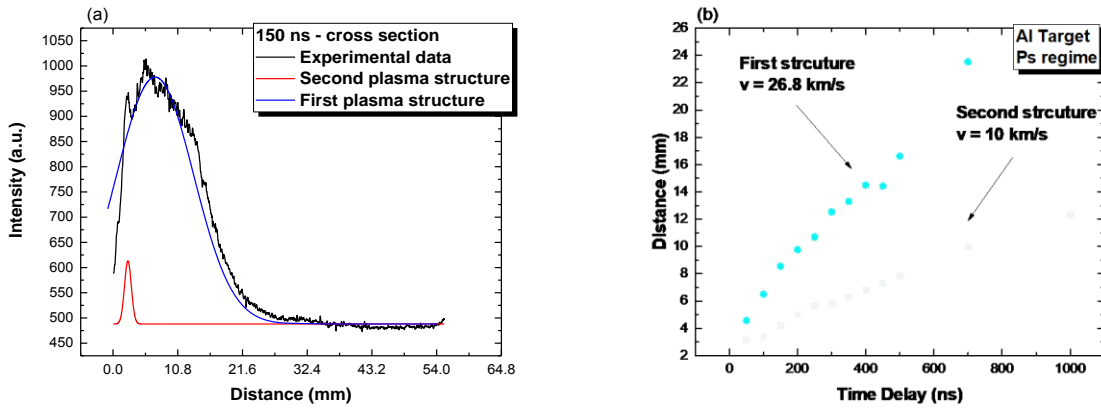
Figure III.19   Cross section of ps Al laser produced plasma ICCD image at 150 ns delay (a) and the center-of-mass evolution space-time displacement for both plasma structures (b).

In the previous section we attributed for each component one ejection mechanisms (1st component consists of particles ejected by the electrostatic mechanisms [*Gamaly et al.*, 2002b; *Bulgakova et al.*, 2005] and 2nd component contains particles ejected by thermal mechanisms [*Miotello and Kelly*, 1995; *Kelly and Miotello*, 1996]). Due to the shorter width of the pulse, the LPP in the ps regime does not interact with the laser pulse and the presence or/and the effect of thermal mechanisms is considerably reduced. This is due to the fact that the laser pulse duration is of the same order of magnitude as the hot carriers-lattice relaxation time: a few ps [*Kononenko et al.*, 1997]. For picosecond laser ablation, the scientific literature [*Yao et al.*, 2005; *Singh and Thakur*, 2006] states that the main ablation mechanism is Coulomb explosion and that the lattice could be melted through thermal processes when relatively high fluences are used, this leading to the presence of the second plasma structure. In our experimental conditions (fluence ~ 8 J/cm^2), the ICCD measurements showed the effects of both thermal and electrostatic ablation mechanism.

III.2.2.2   Optical emission spectroscopy

Optical emission spectroscopy has been successfully used in order to obtain information about the parameters of the LPP, such as temperature or particle density [*Harilal et al.*, 1997; *Aragón and Aguilera*, 2008; *Ursu et al.*, 2009; *Pompilian et al.*, 2013; *Sausa*, 2017]. The OES investigations on ps-LPP were performed in a similar manner to the ones on ns-LPP. To compare the results from the different ablation temporal regimes, we recorded the local emission spectra in the same distance range of 1 - 30 mm from the target. The other experimental conditions were identical for all investigated plasmas. *Figure III.20* presents the emission spectra recorded at 25 ns after the interaction the laser beam – target interaction (2 μs gate width). In this case, the spectra were collected by averaging over 500 events, due to the low emissivity of the ps generated plume.
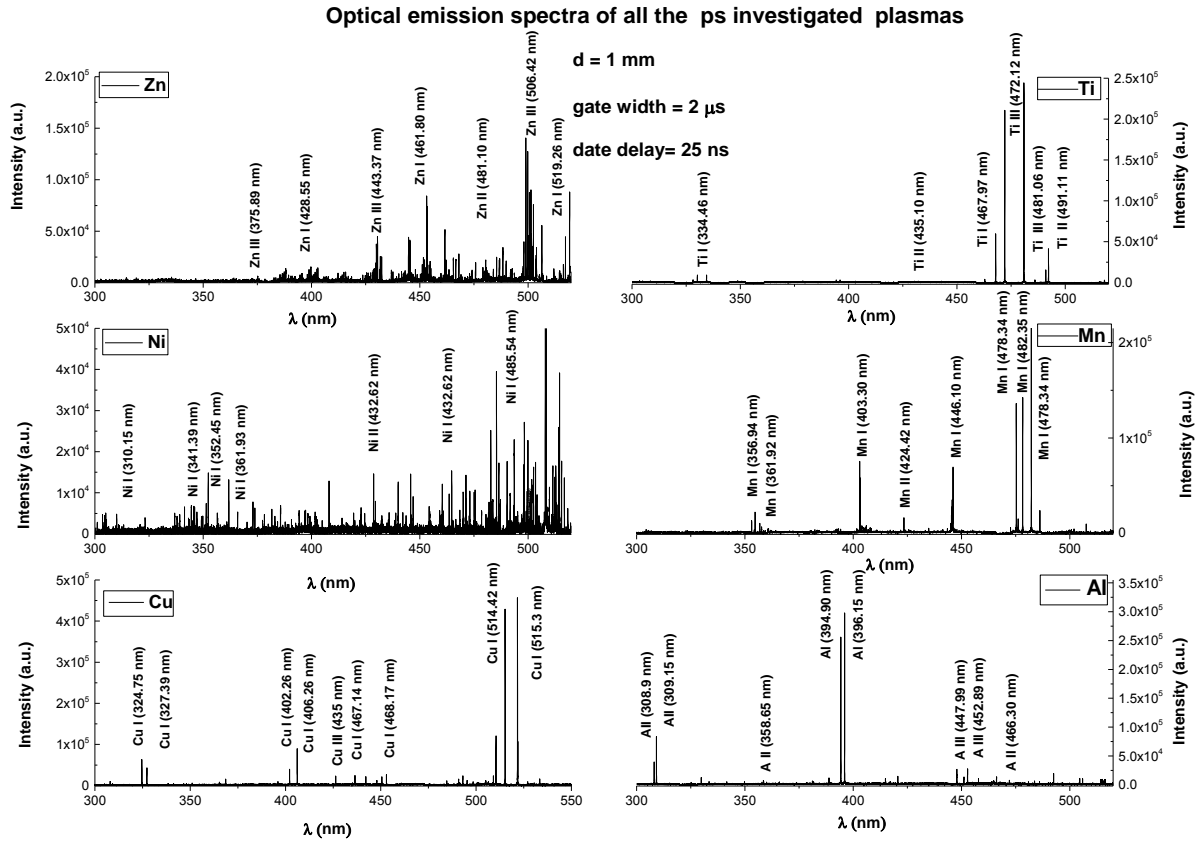
Figure III.20   Emission spectra of all the investigated plasmas in the ps regime, recorded at 25
ns gate delay and 1 mm from the target using a gate width of 2 µs (a - f).

As it was the case of ns LPP, for all the investigated plasmas we identified emission lines corresponding to specific atoms and singly- or multiply-charged ions. As it can be observed, the main difference here is given by the relative low intensity of the emission lines. This can be explained (compared to the ns ablation case) by the fact that the plasma is not heated by the ps ablation pulse due to the absence of absorption of the incoming laser beam. The lines attributed to the metallic ions suffered an abrupt decrease in intensity or cannot even be detected, while the most intense lines belong to neutral atoms. In order to estimate the electron temperature of the plume by using the Boltzmann plot method (*Figure III.21a*), we have to determine the excitation temperature of all the species present in the plasma (for atoms, ions and multiply charged ions). We observed that the Boltzmann plots for the atomic lines roughly follow a linear decrease, which is usually interpreted as an indicative of LTE. We applied the same treatment to the ionic lines, for the plasmas where it was possible (Ti, Zn, Ni), and we obtained higher values for the excitation temperature (with a difference of about one order of magnitude). This difference was interpreted in the previous section as a deviation from LTE. The evolution of the excitation temperature derived from the optical emission spectra at various distances is represented in *Figure III.21b*. For

all plasmas, the maximum temperature was found close to the target and the values decreased significantly as the distance was increased.
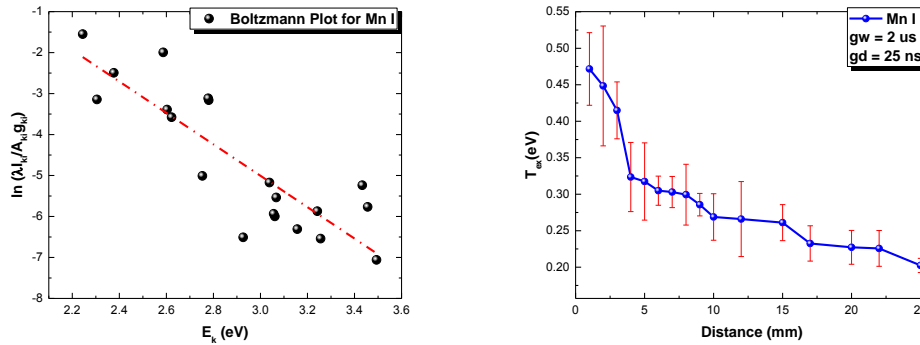
Figure III.21   Boltzmann Plot for the emission lines corresponding to Mn I (a) and spatial evolution of the Mn I excitation temperatures (b).

Because the LPP emissivity is at its maximum at 1 mm from the target, time-resolved measurements were performed at this distance using a 100-ns gate width to record optical emission spectra for all investigated targets. Overall, the excitation temperature values were below 1 eV with an exception for Al, where the decrease starts at about 1.15 eV (*Figure III.22 a*). These results are consistent with the findings from ns-LPP investigations, here the largest values were also obtained for the Al plasma, while the lowest ones for the ps-LPP produced on Zn target. The measurements were performed with gate delays starting from 25 ns up to 500 - 700 ns. Using the same data treatment as for the ns-LPP, we obtained the temporal evolution of the excitation temperature at 1 mm from the target (*Figure III.22b*). We also observed that all the temperature values are smaller than the ones determined for the ns-LPP. This difference between the two temporal regimes is given by the fact that, in this case, the laser beam doesn't heat the plasma anymore.
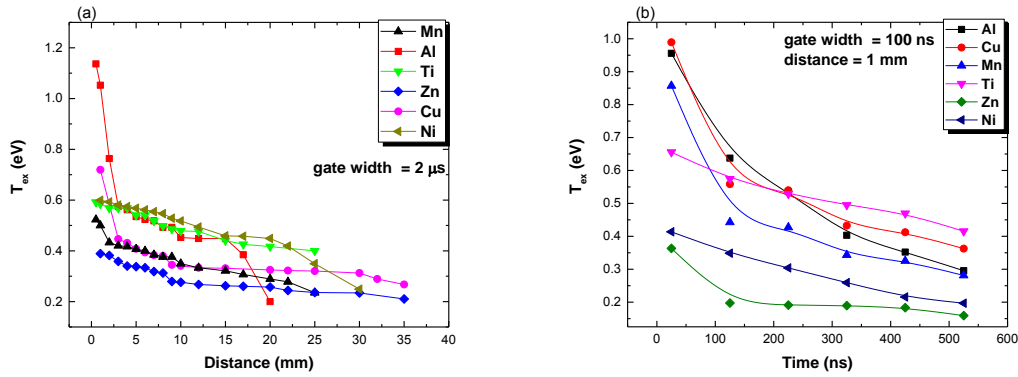
Figure III.22   Spatial (a) and temporal (b) evolution (at 1 mm from the surface) of the excitation temperature for metallic atoms of the ps LPPs.

The information extracted from the optical investigations only describes the plasma particles for a limited energetic range given by specific emission lines. Using optical techniques we are able to look at the plumes dynamics through the evolution of excited particles. In order to extend our view on the ps-LPP we analyzed the charged particles through electrical methods. The complementary study is even more relevant here where the observed ionic emission lines are rare or are not even recorded.

III.2.1.3   Langmuir Probe measurements

In this section, we applied the two complementary approaches based on the LP methods, used for the study of ns-LPP. The first one is based on the treatment of current-voltage characteristics (*I-V* plots) derived from the time-of-flight current profiles recorded between ± 30V at various distances 5 mm – 40 mm. The signals were then sampled following the steps presented in Chapter II. In principle, the first method allows us to mainly describe the thermal movement of the particles at specific moments of time, with the Maxwellian distribution function being accepted for all plasma particles. The second one considers the recorded currents as velocity distributions of flying ions and fits them with a shifted-Maxwellian function.

The ionic and electronic traces collected for the Al ps-LPP are presented in *Figure III.23a* and the corresponding *I-V* characteristics reconstructed at various time delays (1 - 20 μs) are plotted in *Figure III.23b*. We have represented here the signals obtained in the same conditions as in the previous section *(III.2.1.3)*. The ionic currents have a much more reduced amplitude while the electronic currents have a higher intensity and present a complex evolution. From *Figure III.23a* we can see that there are two maxima in the electronic current, one at about 2 μs and a second at 8-9 μs. This temporal distribution observed for the electronic current is in line with the ICCD measurement where we observed two clear components in the ps-LPP.
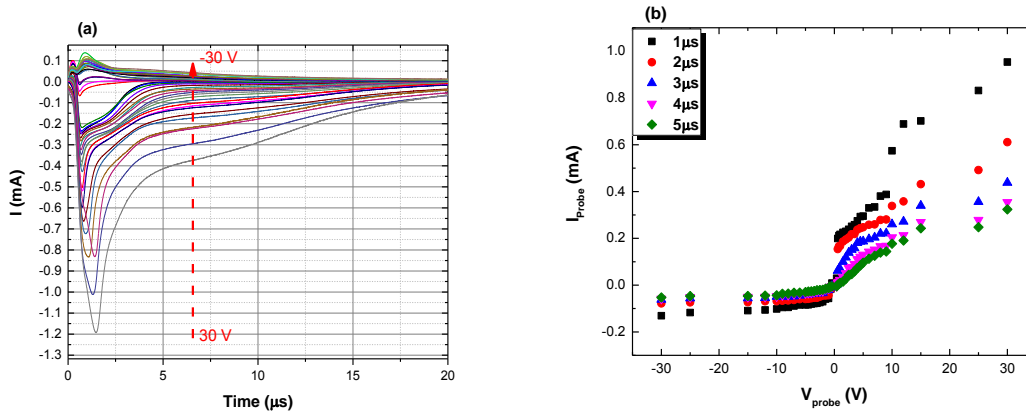
Figure III.23   Probe current traces for Al plasma at 5 mm (a) and the reconstructed I-V characteristics (b).

By following the same steps presented in *Chapter II* and analyzing all the *I-V* characteristics (~ 140 characteristics per target) reconstructed for all the corresponding distances, the space - time dependence of electron temperature, plasma potential, ion density, thermal velocity and Debye length was obtained. *Figure III.24* presents, as an example, the spatial and temporal evolution of the main plasma parameters for an Al plasma generated by laser ablation in the ps regime. The temporal evolution of T_e, N_i, V_{Plasma}, $v_{thermal}$ are extracted from the ionic and electronic traces collected at 10 mm from the target and the spatial distribution at 1 μs time delay. All the parameters follow similar traces as the ones obtained in the nanosecond regime. Slight differences between the values obtained in the two regimes (ns - ps) were observed. The electron temperature varied in the rage of 5.7 – 0.6 eV during the whole expansion time and the ion density decreased from $5x10^{19}$ m^{-3} at 1 μs to $2x10^{19}$ m^{-3} at 20 μs. All plasma parameters presented a maximum at small space time coordinates and decreased as the plume expanded. By analyzing all the data extracted from all the investigated targets and having an overview of the ps-LPP, we can state that the highest electron temperatures were found for Cu and Al plasma (5 - 6 eV) while the lowest values were observed for the Mn and Ti plasmas (~ 1-2 eV). The Zn and Al produced plasma presented the highest ionic densities (~ 10^{20} m^{-3}), most probably due to their low melting and vaporization temperatures. The Ti plasma is on the other end of this distribution with the lowest ion density induced by the higher vaporization heat [*Thestrup et al.*, 2002]. The results are in line with the ones obtained in the ns regime. The main difference comes from the estimation of the Debye length. While in ns regime we obtained values of tens of μm, in ps regime the highest values were up to hundreds of μm. This particular result is in good agreement with the qualitative observation made about the ICCD images of the ps-LPP where we saw that the plasmas are smaller and have a lower global emission.
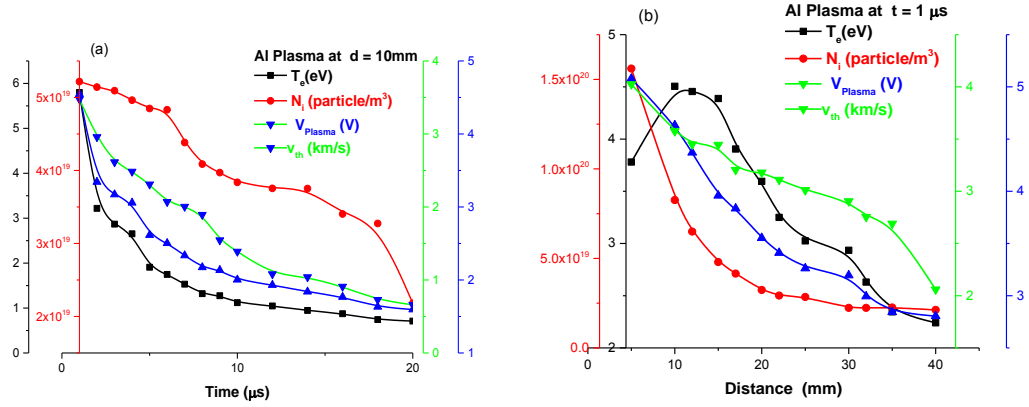
Figure III.24   Temporal (a) distribution (at 10 mm from the target) and spatial (b) distribution (at 1 µs delay) of electron temperature, plasma potential, ionic density and thermal velocity for the Al ps LPP.

Analyzing the space-time maps of T_e (x, t), N_i (x, t), V_{Plasma} (x, t) and $v_{thermal}$ (x, t), - *Figure III.25(a-d)* - we observed that although the thermal mechanisms are not predominant in the ps regime, the electron temperature, thermal velocity and plasma potential present a two-maxima evolution. This was attributed to the contributions induced by the second plasma structure. This means that the internal energy of the plume characterized by the previously named parameters is divided between the two components (fast one and slow one). Moreover, the ionic density decreases exponentially for about one order of magnitude during expansion. Our results corroborate the simulation performed by the group of Xinwei Wang [*Gacek and Wang*, 2009], which predicts the presence of two plasma structures based on two different ablation mechanisms. The overall decrease of all plasma parameters is in line with other theoretical models usually used to describe the dynamics of the LPP [*Anisimov et al.*, 1995; *Amoruso*, 1999; *Agop et al.*, 2009; *Irimiciuc et al.*, 2017c].
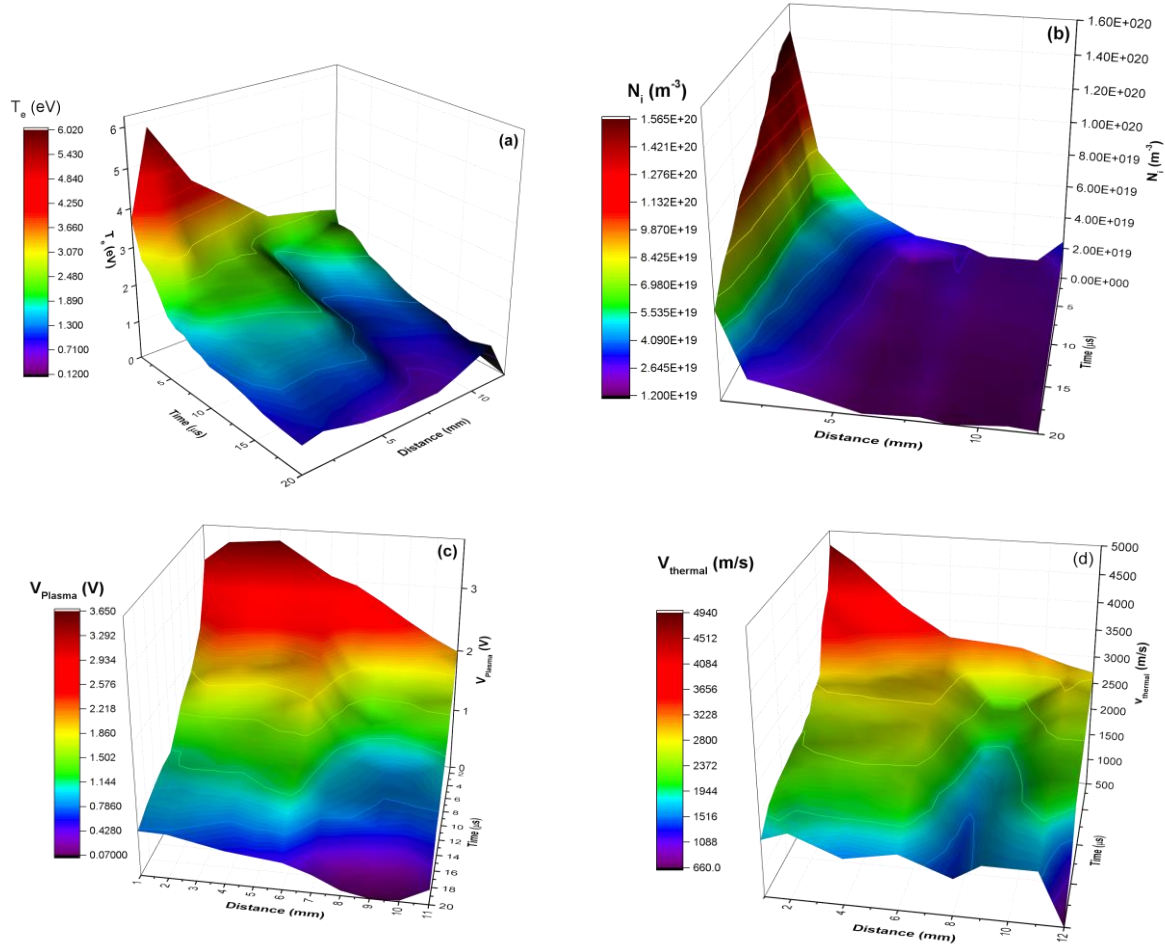
Figure III.25   Surface plots of T_e (a), N_i (b), V_{Plasma} (c) and $v_{thermal}$ (d) in space and time for the ps - Al plasma.

The second part of our LP investigations was focused on the global dynamics of the ejected ions. This was necessary to estimate some plasma parameters that explicitly describe the kinetics of the ejected particles. We used the same technique as in the case on ns-LPP where a shifted Maxwellian distribution was considered to fit the temporal evolution of the ionic current. Generally, laser-produced plasmas, regardless of their ablation regime, can be described more accurately by non-Maxwellian distributions [*Irimiciuc et al.*, 2017b]. By fitting the ionic current (*Figure III.26a*) we were able to determine the drift velocity and the time-averaged ionic temperature. Although no temporal evolution can by studied by this approach, we are able to find the velocities of the expanding ions and then compare them with the ICCD fast camera imaging results and to discuss the coherence between the ionic and electronic temperatures.

The values obtained for the overall ionic temperature (*Figure III.26b*) are similar to the ones obtained for the local electron plasma temperature (*Figure III.25*). This leads us to assume that the charged particles could be in LTE during expansion even farther from the target (a few

cm). The values for the drift velocities were on the order of tens of km/s, similar to the ones determined for the fast plasma structure from the ICCD imaging.

The main conclusion from these optical and electrical investigations is that the overall dependences and trends are similar to the ones presented in the section dedicated to the study of ns-LPP. The differences come in the shape of the plume, lower expansion velocities, excitation, electronic and ionic temperatures and particle density. These discrepancies are based on the absence of interaction between the ps laser beam and the expanding plume. The shorter pulse width could suppress to some extent the thermal ablation mechanism, as at this time-scale the thermal damage inflicted to the lattice is reduced.
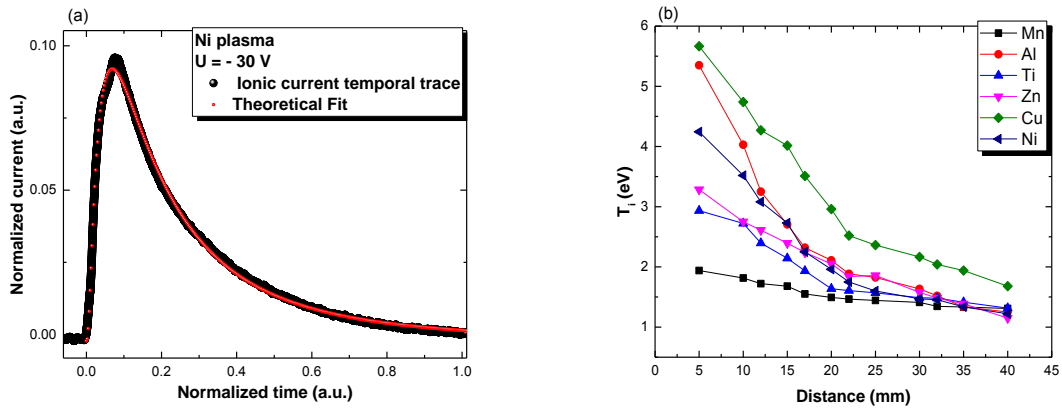
Figure III.26   Shifted Maxwell fit of TOF temporal evolution of the ionic current at -30 V for the Ni plasma (a) and the spatial evolution of the ionic temperature for all investigated plasmas (b).

III.2.3   Femtosecond laser ablation

In this section, we will present the result of our experimental investigations on femtosecond laser-produced plasmas on various metallic targets in similar conditions with the ones used for nanosecond and picosecond regimes. For both the optical and electrical investigations, a Ti:Sa laser beam (40 fs, 100 Hz, 800 nm), focused to a 130 μm diameter circular spot on the target (leading to constant laser fluence of 12.5 J/cm^2) and a background pressure of 10^{-6} Torr were used. The targets were electrically grounded. The aim of the study was to investigate through ICCD fast camera imaging the global evolution of the plasma, while the local evolution of the ejected particles was investigated through space- and time-resolved OES and Langmuir probe measurements. The results are discussed with respect to the previous ablation regimes and the particular mechanisms involved in fs-laser ablation.

III.2.3.1   ICCD fast camera imaging

Analogous to the other ablation regimes, we used ICCD fast camera imaging to record bi-dimensional images of the femtosecond laser-produced plasmas of the same metallic targets (Al, Cu, Mn, Ni, Ti, Zn) in order to investigate the general structural characteristics and their global dynamics. Examples of the recorded snapshots of all investigated types of plasmas (10 ns gate width, 150 ns gate delay, 50 accumulations) are presented in *Figure III.27*. From a qualitative point of view, the ICCD images provided a glimpse of information regarding the shape and intensity of the plasmas. The fs LPPs present a "weak" light emission in comparison to those produced by ns or ps laser ablation. These preliminary results are in good agreement with the theoretical description of the fs ablation regime, discussed in *Chapter I*. From our ICCD investigations, we can conclude that the investigated fs LPP follow, roughly, the same pattern, having a thin, elongated shape with slight variations given by the material properties. Relevant examples for this are the plasma plumes produced on Mn and Al targets that have a more prominent lateral expansion and spatial distribution. A deeper analysis of the differences regarding the shape of the ejected cloud and the influencing properties of each material will be presented in *Section III.3*.
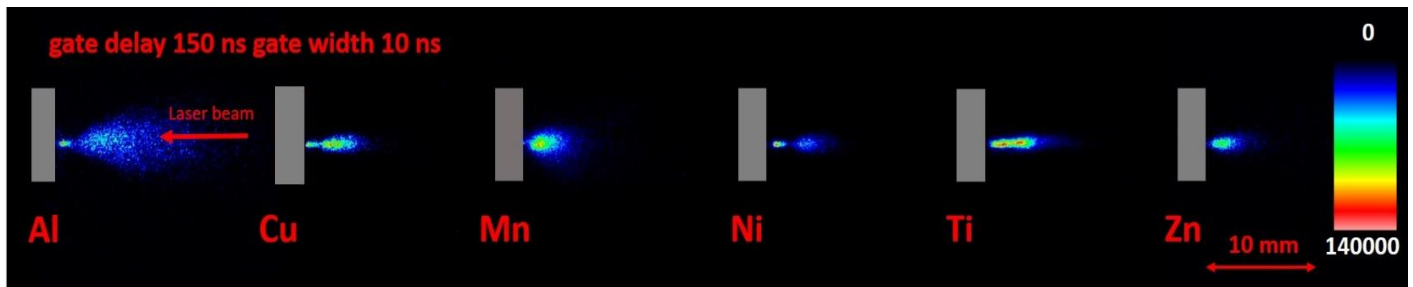
Figure III.27   ICCD images of femtosecond laser produced plasma plumes on various mettalic targets in identical conditions of laser fluence and background pressure, aquired at 150 ns after the laser pulse.

All investigated plasmas feature two components, which expand with different velocities. Since for the fs ablation regime the thermal effects are reduced [*Rode and Tikhonchuk*, 2001], it is important to describe the dynamics of each plasma component in order to understand more about their origin. In *Figure III.28* we highlighted the evolution of the aluminum fs laser produced plasma up to 1 μs. We observed that a clear split into two components occurs even at short evolution times (below 50 ns), similar to the ps case. The first structure can be identified in *Figure III.28* as more prominent, being more dispersed while the second one is observed in the proximity of the target, expanding at a much slower pace.
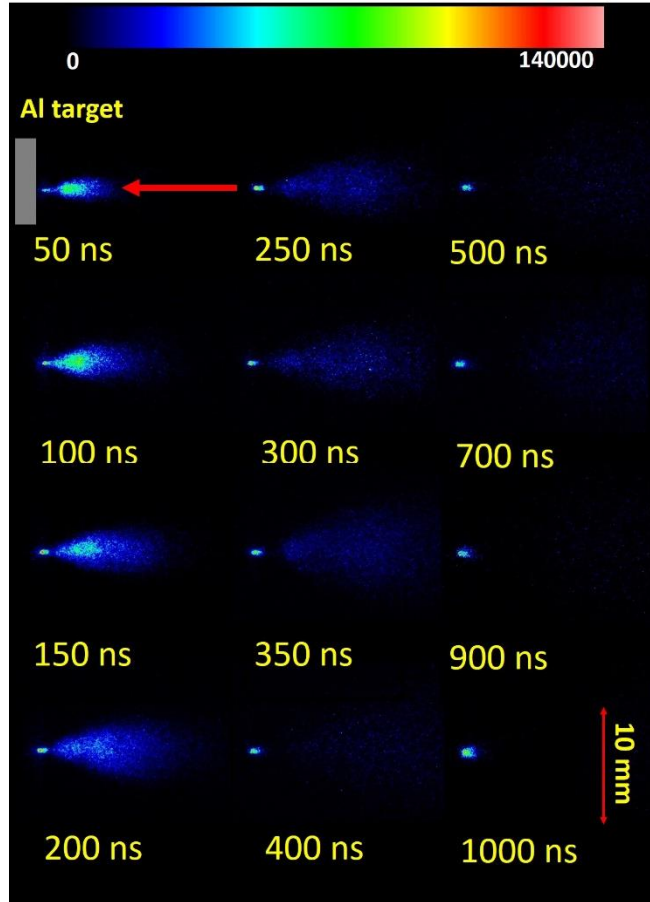
Figure III.28   ICCD images of laser-produced plasma plumes on Al revealing the global evolution of the plasma during 1 μs temporal range.

During the expansion, the center-of-mass identified in the ICCD image as having the highest intensity, shifts towards larger distances as the recording time is changed, following a linear dependence. This confirms the constant expansion velocity found for the other ablation regimes. As it was already mentioned, a dual structured plasma plume is generated by fs regime, similar to the case of ns and ps LPP. These observation is consistent with other findings from the literature [*Amoruso et al.*, 2000; *Claeyssens et al.*, 2002; *Vitiello et al.*, 2005]. During some investigations on the dynamics of a fs Si plasma, Amoroso et al. [*Amoruso et al.*, 2006] observed a fast structure expanding with a velocity having values of tens of km/s and a slower one defined by a much lower velocity with values of a few hundreds of m/s; Yang et al. [*Yang et al.*, 2015] provided evidence for a two-component Ti fs LPP with a fast component having an expansion velocity of 23 km/s and a slower one expanding with 8 km/s; we also considered the work of Donnely et al. [*Donnelly et al.*, 2010b], where they investigated the nanoparticles component of LPP generated by laser ablation of an Au target. By means of LP measurements and absorption, they obtained the same two-component plasma (1st component – 14 km/s and 2nd component – 140 m/s) and they proved that the major part of the plume was contained in the second structure.

The first plasma structure is produced by the electrostatic ablation mechanisms, while the second one contains nanoparticles and its formation is determined by a different ablation mechanism (phase explosion or thermal vaporization). To emphasize this, we performed a cross-section of the recorded images across the expansion direction of the plasma plume (*Figure III.29a*) and we observed the two maxima expanding with different velocities (*Figure III.29b*). For the first structure, we have obtained velocities of tens of km/s, while for the second structure velocities of a few km/s. Another important aspect that was evidenced through ICCD imaging was the significant differences between the two plasma components. The fast structure has an emission lifetime of hundreds of ns (depending on the target), while the slow component lasts significantly longer, being observed, for most plasmas, even after 15 - 20 μs. The lengthiest lifetime was found for Ni target (~ 50 μs), whereas we noticed only 5 μs for the Ti plasma. These results are in good agreement with the findings of Amoruso et al. [*Amoruso et al.*, 2005a], as they demonstrated that fs laser ablation is a viable method for nanoparticle production. They determined for the second component of a Si LPP a lifetime of approximately 20 μs and an expansion velocity of 600 m/s, while the first component expanding with a velocity of 10 km/s lasted approximately 5 μs.
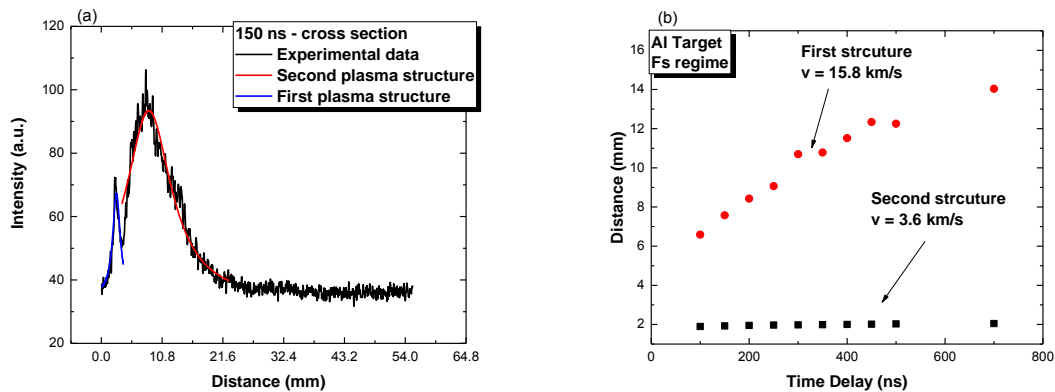
Figure III.29   Cross section on the expansion direction of an ICCD snapshot aquired at 150 ns delay (a) and the space-time evolution of the "center-of-mass" (maximum emitting point) of both plasma structures (b).

The velocities found for the fast component are consistent with our previous results obtained for the same structure in the ns and ps regime. The slow component presents relatively high expansion velocities, similar to the structure generated by thermal mechanism in the case of ns laser ablation [*Bulgakova et al.*, 2005; *Ursu et al.*, 2009; *Focsa et al.*, 2017] and higher than the ones observed by other groups [*Gamaly et al.*, 2002a; *Toftmann et al.*, 2013; *Anoop et al.*, 2014b] which performed time-resolved investigations of fs-LPP. This could be explained by the differences in the laser fluence, target properties and overall differences in the experimental conditions used in each particular study.

III.2.3.2   Optical Emission Spectroscopy

In a similar manner to the studies previously presented for ns and ps temporal regimes, we discuss in this section results achieved by implementing the optical emission spectroscopy technique. Until now we advocated the use of this technique for LPP investigations because, as it was mentioned before, it provides information regarding the individual dynamics of the plasma constituents (atoms and multiple charged ions). We employed the technique to record spatially and temporally resolved emission spectra of the plasma plume. The time-resolved studies were performed at 1 mm from the target surface. Space-resolved measurements, involving the recording of emission spectra at various distances from the target (in the range 1 – 30 mm), were performed in 16 different points in order to obtain a relatively good spatial resolution. In *Figure III.30* we presented some examples of time-averaged emitted spectra (for all the investigated targets) recorded with 2 µs gate width and 25 ns delay with respect to the laser pulse. As it can be seen from the images, we identified lines corresponding to atoms, ions and multiply charged ions. From a qualitative perspective, we observed some similarities between "global" spectra of fs LPP and the ones of other employed temporal regimes LPP in the fact that previously identified emission lines are present in this case as well. The significant difference between the global spectra of the plasmas generated in the three temporal regimes is the diminution in number of identified lines corresponding to the singly and multiply charged ions as the laser pulse duration shortens. Also, for the ion emission lines we observed that the intensity decreases considerably with respect to the intensity of the atomic lines. This statement is supported by similar information derived from the ICCD images.
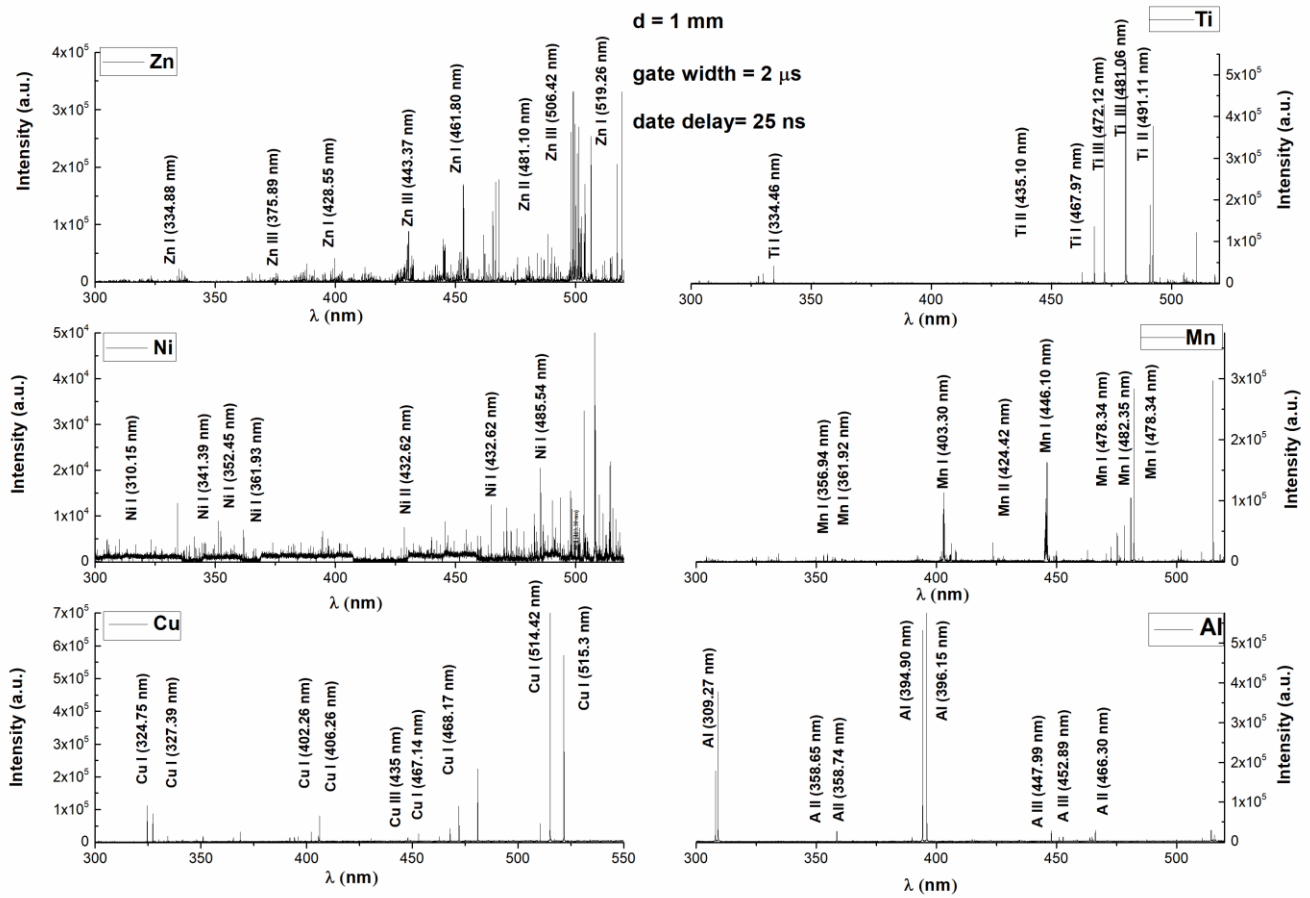
Figure III.30   Emission spectra of all investigated fs LPPs at 1 mm from the target using a gate width of 2 μs.

Focusing on the time-resolved measurements, we will discuss in this paragraph, in a general manner, some quantitative results obtained by means of optical emission spectroscopy. One of the most important plasma parameters, excitation temperature, can be determined for all plasma species using the Boltzmann method described in *Chapter II*. Detailed aspects regarding excitation temperature of different plasmas will be discussed in *Section III.3*. Similar to the case of ns and ps regimes, the computed values of the excitation temperature for ions are higher than those of the atoms. Referring, as an example, to the Cu plasma we obtained excitation temperatures ranging from 0.66 eV to 0.26 eV for Cu atoms, while for Cu singly charged ions we obtained values from 1.8 eV to 0.8 eV. As explained before, ideally, at LTE [*Fujimoto and McWhirter*, 1990] the excitation temperature must be the same for every individual species, therefore the variation in the obtained values can be attributed to deviation from local thermodynamic equilibrium. In the same time, we have to take into account the lack of emission lines for the ions in comparison to the atoms. This is important because the Boltzmann method is susceptible to

errors based on the emission line density of a species in a spectrum. In other words, for our case, the Boltzmann plot for the atomic temperature incorporated more lines than the plot for the ionic excitation temperature, because the energy required to excite atoms is considerably lower. A suitable example in this case would be for an Al plasma, where a singly charged ion, characterized by an emission line with $\lambda = 358.6$ nm, is described by high energy levels ($E_k = 15.3$ eV and $E_i = 11.8$ eV) in comparison to an Al atom characterized by an emission line at 396.15 nm, which is described by low energy levels ($E_k = 3.14$ eV and $E_i = 0.13$ eV). We would like to mention that the values for the excitation temperature obtained for the fs regime are clearly smaller in comparison to those of ns or ps LPP. The result is due to the lack of "heating" of the plume by the incoming laser pulse. The ratio between the atomic excitation temperature and the ionic one is similar to the previous two cases, with the excitation temperature of the ions being about one order of magnitude higher than the ones obtained for the atoms.

The overall evolution, in both space and time, of the excitation temperature, regardless of the target, is described by a quasi-exponential decrease. The obtained values are smaller than 1 eV, with an exception for Al plasma which presents the highest excitation temperature of 1.2 eV. The lowest excitation temperature was found for the Mn plasma (~ 0.3 eV). The temporal evolution of the temperature (*Figure III.31b*) reveals a smaller range of values. This is affected by the 50 ns gate width which was used to obtain a good temporal resolution.
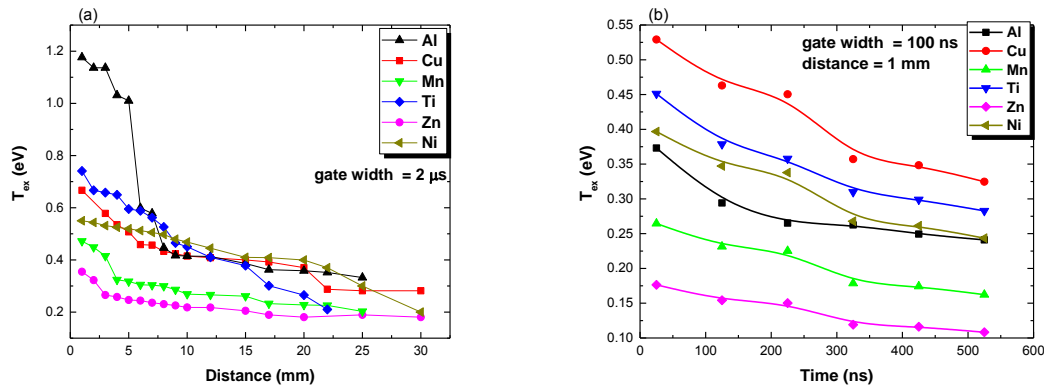
Figure III.31   Spatial (a) and temporal (b) evolution of the excitation temperature for metallic atoms.

The highest temperature was found for Cu (0.55 eV) and Ti (0.45 eV), while the lowest for Zn (0.17 eV) and Mn (0.26 eV). Our results seem to be consistent with the findings of other groups that have reported studies on fs laser ablation and where similar optical techniques were employed. Harilal's group [*Harilal et al.*, 2003b, 2014b] performed laser ablation of brass and reported an exponential decrease of the electron temperature with time (from 1.03 eV to 0.5 eV). Similar values were reported by the same group in a recent paper for fs ablation of Copper [*Anoop et al.*, 2014a]. Le Drogoff et al. [*Le Drogoff et al.*, 2001] reported excitation temperatures between 0.6 eV and 0.34 eV for fs-laser ablation of an Al-based metallic alloy.

Although by comparison the results are similar to the ones found in the literature, it is objectively difficult to compare the obtained values due to the differences in the experimental conditions, experimental set-ups and techniques used by different groups. We would like to remind the fact that although the particular values are different, the general order of magnitude of our computed values is similar to the one reported in literature.

III.2.3.3   Langmuir Probe measurements

Figure III.32a displays the time-of-flight (TOF) profiles recorded by the LP biased at various voltages in the [-30 V, +30 V] range for fs-ablation of Al target. TOF signals were sampled at different delays in a 20 µs range, after the laser pulse, and the I-*V* characteristics were then reconstructed at each evolution times. As an example, *Figure III.32b* shows the *I-V* plots for Al plasma at 1 µs - 4 µs delays. The time-dependence of plasma parameters (electron temperature, plasma potential, ion density, thermal velocity and Debye length) was obtained by following the procedure presented in *Chapter II* and applied for the previous temporal regimes.
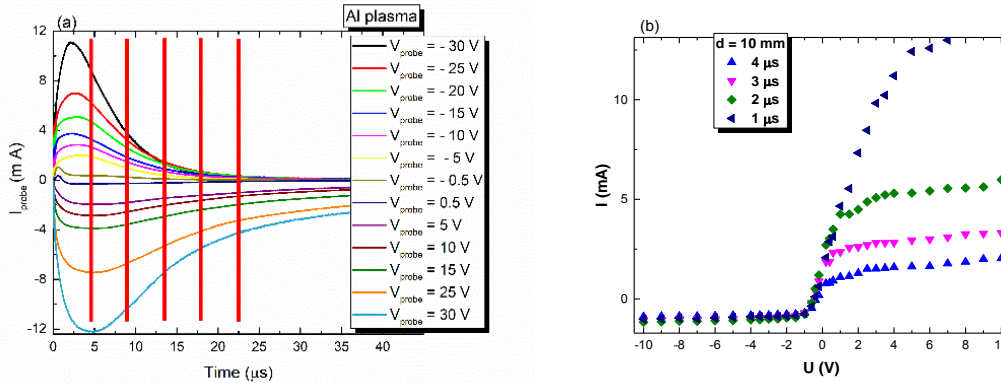
Figure III.32   Probe current traces for Al plasma at 10 mm (a) and the reconstructed I-V characteristics (b).

For all investigated plasmas, the ionic and electronic currents where collected at the same distances, and the I-V characteristics were reconstructed at the same moments of time. An example is presented in *Figure III.33a,* where the temporal evolutions of T_e, N_i, V_{Plasma}, $v_{thermal}$ are plotted. These were determined from current traces recorded at 10 mm from the target. The spatial distribution at 1 µs after the laser beam interacts with the target is presented in *Figure III.33b*. We observe that all mentioned plasma parameters are decreasing in both space and time. For the example given here, the electron temperature is in the range of 5 – 0.7 eV during the whole expansion time, the ion density decreases from $6x10^{19}$ m^{-3} at 1 µs to $1.2x10^{19}$ m^{-3} at 20 µs. All plasma parameters present a maximum in the vicinity of the target (5 mm and 1 µs) and are decreasing as the plume expands. When considering all targets, we observe that the results from fs regime are somehow similar to the ones from the ns and ps regime. The highest values for the electron temperature were found for Cu and Al plasma (~ 9 eV at 5 mm from the target) while the lowest ones were found for the Mn and Ti plasma (~ 5 - 6 eV). Values determined for the plasma

potential and the thermal velocity are in line with our previously reported results [*Irimiciuc et al.*, 2017b] and with the results presented in the previous sections. The plasma potential is in the range of a few V, while the thermal velocity is of the order of km/s.
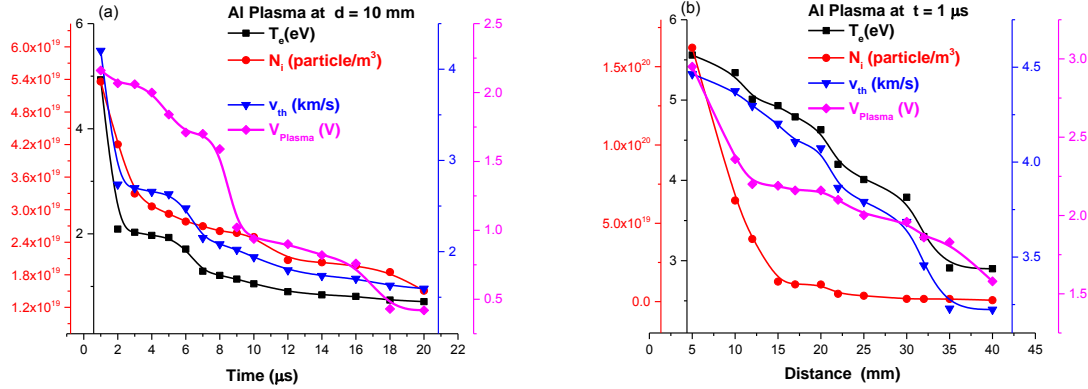
Figure III.33   Electronic temperature, plasma potential, ion density and thermal velocity dependence in time (a) at a fixed distance (d = 5 mm), and in space (b) for a fixed moment of time (t = 1 μs) for fs - Al plasma.

Space-time maps were built for each plasma parameter: V_{Plasma} (x, t), $v_{thermal}$ (x, t), T_e (x, t) and N_i (x, t) and are represented in *Figure III.34*. We found here that the internal energy of the plume characterized by electron temperature, thermal velocity and plasma potential is decreasing in time, simultaneously with the rarefying of the plume indicated by the decrease of the ionic density. We observe a quasi-exponential decrease with the maximum values being obtained at 5 mm from the target and after 1 μs. Because our measurements are performed at longer time-delays (starting from 1 μs), the fast component already disappears, according to our ICCD measurements, thus we manage to describe only the second plasma component.
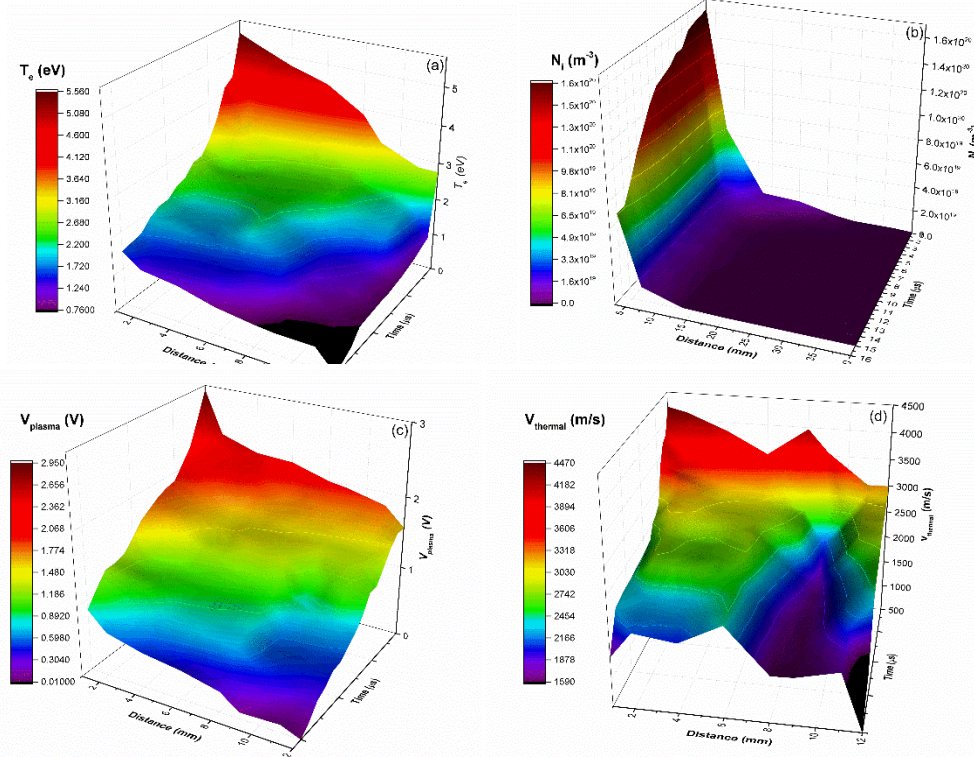
Figure III.34   Surface plots of T_e (a), N_i (b), V_{Plasma} (c) *and* $v_{thermal}$ (d) in space and time for a fs -
Al plasma.

In the previous section we used the Debye length in order to estimate how much the probe affects the plasma. This is more significant here, as we observed the fs-LPP are more directional and have a smaller volume. As for the previous ablation regime, we observe an increase from tens of μm up to hundreds of μm. This result is consistent with the decrease observed in the particle density and in the thermal velocity.

Some other single-element targets (W, In, Te) were investigated only in the fs-regime. Details on these can be found in [*Irimiciuc et al., 2017b*]. However for the sake of the uniformity with the ns and ps regimes, we made a choice to present in this manuscript only the metals that were investigated in all three regimes.

The drift movement of the fs-LPP was investigated by considering a non-Maxwellian distribution [*Nica et al.*, 2009; *Focsa et al.*, 2017; *Irimiciuc et al.*, 2017b] for the ejected ions. The recorded temporal traces were fitted with a shifted Maxwell distribution (*Figure III.35*). Time - integrated values of the drift velocity and ionic temperature were determined in different points along the expansion direction (5 - 40 mm).
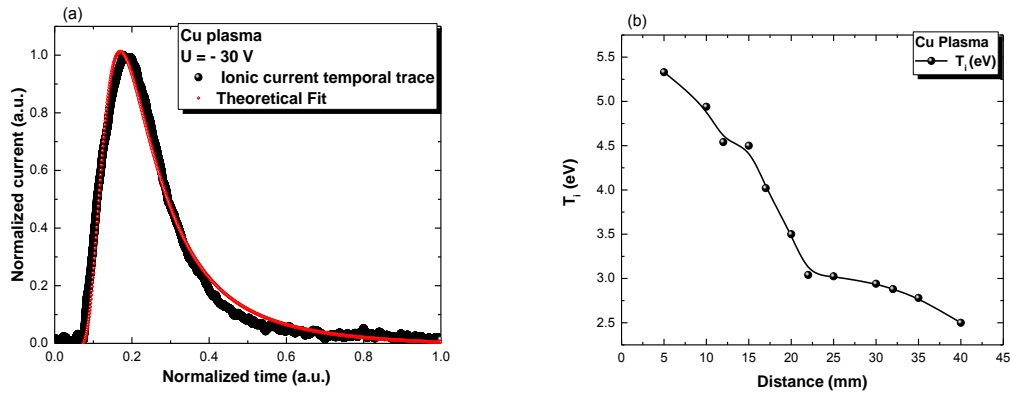
Figure III.35   Shifted Maxwellian fit of the ionic current TOF profile (a) and the spatial evolution of the ionic temperature (b).

In *Figure III.36* we observe that the ionic temperatures of all targets decrease quasi-exponentially with the distance and presents similar values with the ones obtained for the electronic temperatures. The values obtained for the ionic temperature are integrated over the whole expansion time. We observe however that the values obtained from the shifted Maxwell fit are similar to the ones from the time-resolved approach. For the time-averaged study, the highest ionic temperatures were found for Cu and Al (5 - 5.5 eV) plasmas, while the lowest values were obtained for Mn and Ti (~ 2.3 eV).
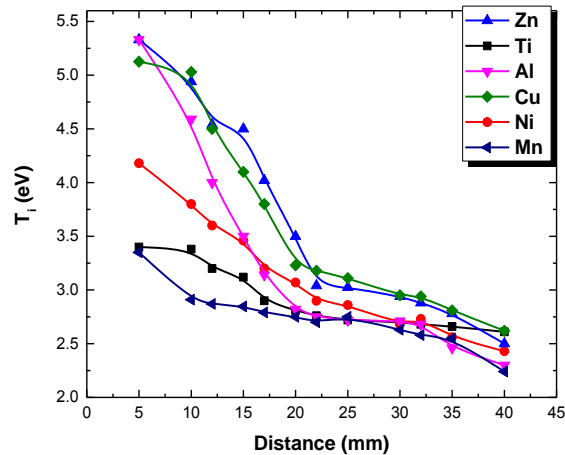
Figure III.36   Spatial evolution of T_i for all investigated plasmas in the fs regime.

Using the shifted Maxwell-Boltzmann approach, we also estimated the drift velocities, which were of tens of km/s and were constant during the expansion. The highest values were found for Cu (55 km/s), while the lowest was obtained for Mn (9.8 km/s), consistent with the results

presented in the previous sections. The values found for the drift velocity using the shifted Maxwell Boltzmann fit and the sequential LP method are similar to the ones estimated from ICCD fast camera imaging for the fast and slow component of the plume. Although here the thermal contributions to the second plasma structure are not as dominant as in the ns case, the results are still in good agreement with the ones observed in the previous two sections. However, it was reported [*Donnelly et al.*, 2010b] that the majority of the ejected particles in fs laser ablation are present in the second structure (containing nanoparticles). It can be expected that the main contribution to the electron thermal movement is contained by the second structure due to the low electron mass and high mobility.

The sequential LP method was successfully implemented by other groups for femtosecond laser-produced plasma, with similar results. Hendron et al. [*Hendron et al.*, 1997] obtained electron temperatures below 1 eV at 2 μs time delay and plasma potentials of ~ 1.3 V (5 μs) for Cu plasma generated by fs-laser ablation. For the same ablation regime, Dogar et al. [*Dogar et al.*, 2011] found electronic temperatures in the same range as in this study (up to 3.28 eV at 2 μs), while the ion densities were of the order of $1 – 3x10^{18} m^{-3}$, about one order of magnitude lower than the ones found here. Weaver et al. [*Weaver et al.*, 1999] obtained ~ $10^{19} m^{-3}$ electron densities for Cu plasma generated by ns-laser ablation with T_e values below 0.3 eV. In contrast, a shifted Maxwellian fit of a Faraday cup signal recorded for copper plasma by Doria et al. [*Doria et al.*, 2004] revealed values of ~ 8 km/s for the v_{drift} and tens of eV for the ion temperature. The same global approach applied for LP measurements on Aluminum plasma [*Singh et al.*, 2014] yielded drift velocities of ~ 19 km/s and ionic temperatures as high as 130 eV. One should consider that part of the differences between these reported results are induced by the differences in experimental parameters such as laser fluence, target-probe distance and probe geometry.

Both time-resolved and time-averaged ("global") methods present advantages and disadvantages, and one must carefully manipulate the physical significance of "global" parameters that "describe" the overall evolution of the plasma (e.g. ionic temperature and drift velocity derived from shifted-Maxwellian fits), when compared to "local" values of temperature and thermal velocity derived from the I-V characteristic approach, which characterize a specific plasma volume at a specific evolution time.

Because Langmuir probe is an intrusive method most of the time optical emission spectroscopy and ICCD imaging as complementary methods are used to build the full "image" of the laser-produced plasmas. The complementarity between these two approaches allows to investigate the charged particles and their thermal and kinetic energy from both local and global perspectives and the excited energetic levels of the atoms and ions seen at global scale (ICCD imaging) and local scales (OES). The local - global scale differences and their effect on the way we understand the dynamics through each perspective will be explored in the framework of our fractal model presented in *Chapter IV*.

III.3   Target influence on the plume dynamics

In the previous section we presented the results from the space- and time-resolved optical and electrical investigations of laser-produced plasmas on various single-element metallic targets (Al, Ti, Mn, Ni, Cu, Zn) in three different ablation regimes (nanosecond, picosecond and femtosecond). We observed some differences between the data extracted for each ablation regime which are attributed to the fundamental mechanisms involved in the laser ablation process, mechanisms which are briefly presented in *Chapter I*. These aspects on the laser-produced plasmas formation and dynamics in different ablation regimes were also discussed in other papers [*Perdrix et al.*, 2001; *Cremers et al.*, 2006; *Zorba et al.*, 2008; *Molian et al.*, 2009], where the focus was on parameters like ablation threshold, ablation crater and usefulness of each ablation regime as a tool for the LIBS technique. In the previous sections, in each individual ablation regime we observed that the plasma parameters presented similar space-time evolution. Because, in the same ablation regime, the experiments were performed in identical experimental conditions, the differences between the properties of the LPP should only be influenced by the properties of the target. In this section, we will attempt to correlate the dynamic properties of the plasma plume to the physical properties of the target. We will also compare the results with other reports from literature and we will discuss the generality of the results in terms of range of materials and laser beam properties.

In *Figure III.37* we present a characteristic snapshot of a Ti plasmas produced in nanosecond, picosecond and femtosecond regimes. We observe that there are important differences between the three ablation regimes. The ns-LPP has a stronger global emission and it is described by a larger volume, while the picosecond and femtosecond laser produced plasmas are more directional and the emission is concentrated around the expansion axis with reduced lateral extension. These results were discussed also in the previous section, and are seen as general characteristic of all LPPs regardless of the nature of the target. Similar results were previously reported in other papers [*Noll*, 2012; *Verhoff et al.*, 2012; *Freeman et al.*, 2013], where the authors present differences in the width of the ionic distribution of about 30º between the plasma plumes produced by nanosecond and femtosecond ablation. All these are qualitative estimations of the overall visible emission of the plume. Here, the used investigation technique allowed us to obtain quantitative results on the expansion velocities of the two plasma components. We will further discuss the relationship between the properties of the target and the values of the expansion velocities for the plasma plume generated in each ablation regime.
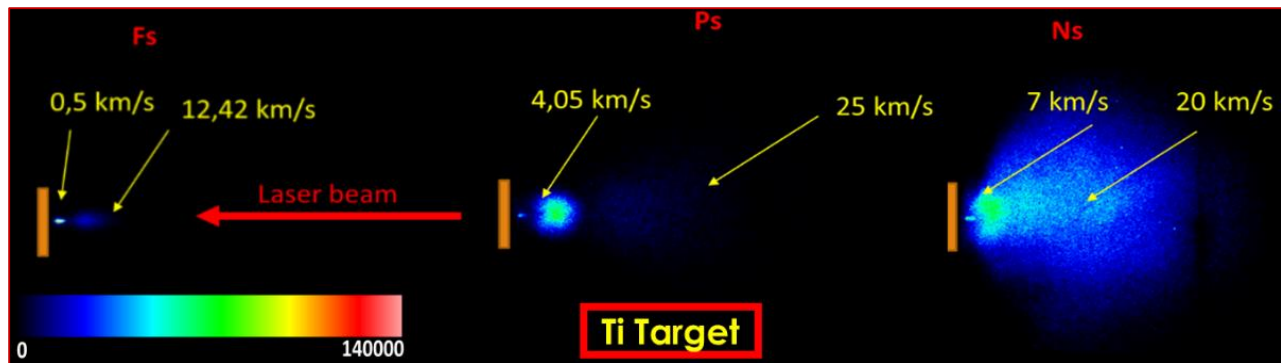
Figure III.37   ICCD snapshots recorded after 150 ns of a Ti LPP in fs, ps and ns ablation regimes.

The evolution of the expansion velocity of the two plasma components (generated in the three ablation regimes) with the atomic mass of the target is presented in *Figure III.38a*. The plotted velocities were derived from the ICCD fast camera imaging measurements. We observed that the ns-LPPs have the highest velocities followed by the ones generated in ps and fs regimes. The evolution with the atomic mass is respected in all three ablation regimes. As the mass of the particle increases, the values for the center-of-mass [*Ursu et al.*, 2009; *Irimiciuc et al.*, 2017a] expansion velocities are decreasing. This result is in good agreement with the results reported by Canulescu et al. [*Canulescu et al.*, 2009], where, by using a similar investigating technique on ns-LPP on a $LiMn_2O_4$ target, they found that elements with a lower atomic mass are expanding with a higher velocity. In our studies, this dependence can be found for both plasma structures and for all investigated ablation regimes.

Because each of the two components are generated though different ablation mechanisms, it is difficult to impose/assume a direct relationship between the expansion velocity and the atomic mass. The usual approach reported in the literature [*Anisimov*, 1968; *Kelly and Dreyfus*, 1988; *Amoruso et al.*, 2000] is to consider the classical relation for the kinetic energy and assume a $v \sim m^{-1/2}$ relationship between the atomic mass and the expansion velocity. However, this method is based only on the thermal ejection of the particles as being the main driving mechanism. In the case of fs or ps regime it is also worth taking into account the contribution of the electrostatic mechanisms to the overall values of the plasma plume components.

When representing the expansion velocity as a function of the vaporization heat (*Figure III.38b-c)* we observe that the values for the 1st and 2nd structures are proportional with the increase of the vaporization heat. With the increase of the vaporization heat the particle ejection through the thermal evaporation will be inhibited, thus allowing us to assume that the beam energy will be converted to kinetic energy. Also, we observed that the evolution presents two areas (< 300 kJ/mol and > 300 kJ/mol) described by a linear trace but different slopes. The first area is defined by the Zn, Mn and Al plasmas while the second area covers the other investigated targets Cu, Ni and Ti. Both sets of targets are described by the same linear trace but with a different slope.

The evolution of the expansion velocity as measured from ICCD imaging does characterize the overall dynamics of the LPP. Our assumption was that the expansion velocity, and thus the kinetic energy of the plume is affected by parameters like atomic mass or heat of vaporization. The study was extended to other parameters expressing the energy of the plume such as the excitation temperature.
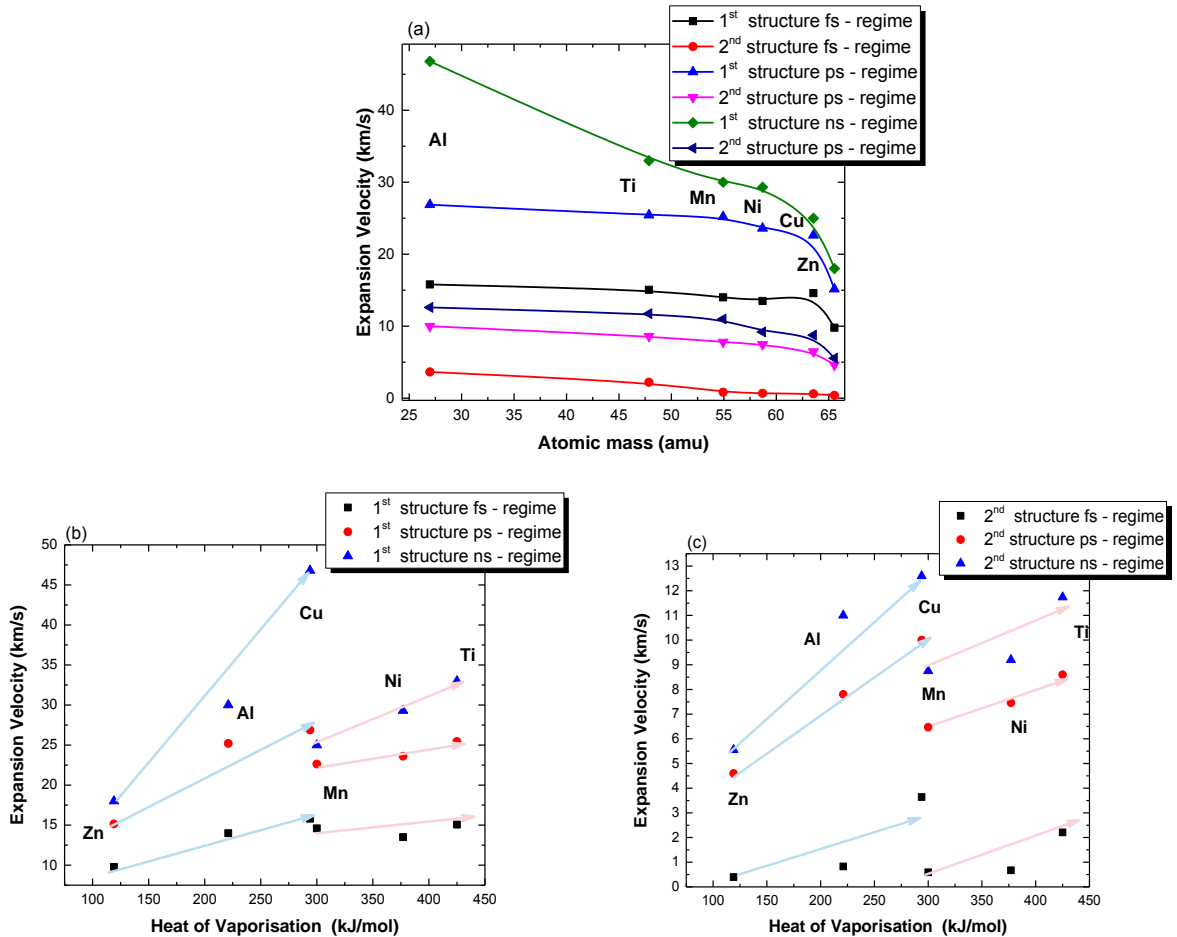
Figure III.38   The evolution of the expansion velocities with atomic mass (a) and vaporization heat (b, c) for each plasma component in all three ablation regimes (ns, ps, fs).

In *Figure III.39a* we represented the excitation temperature evolution with the atomic mass of the target. The evolution is similar to the one found for the expansion velocities. We observe that, for a specific distance, the plasmas produced on the "lighter" targets have higher excitation temperatures which decrease as the atomic mass of the target increases. Also, we notice that the temperatures for the ns ablation regime are higher than the ones obtained in the ps or fs regime, differences which were discussed in the previous section. This result is in good agreement with other studies that focused on the differences observed in the excitation temperature [*Leitz et al.*, 2011; *Flanigan and Levis*, 2014] between the LPPs produced in different ablation regimes. We

note that the evolution of the excitation temperature with the atomic mass (presented in Figure *III.39b*) does not depend on the measuring distance, as the same dependence was observed at 1 mm and 20 mm from the target.
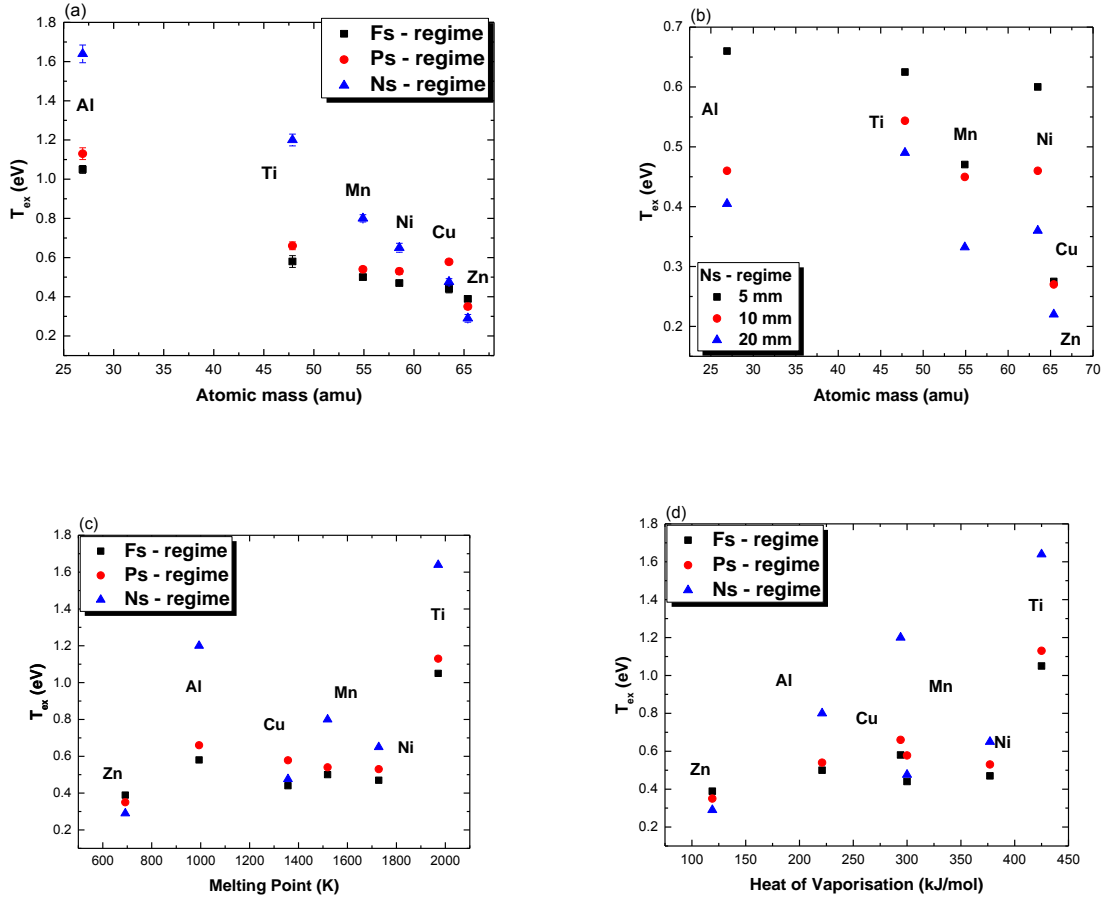
Figure III.39   Excitation temperatures extracted from the spectra collected at 1 mm from the target as function of the atomic mass (a), $T_{ex}(m)$ at different distances for the ns-LPP (b) and the dependence on the melting point (c) and vaporization heat (d).

When investigating the impact of the heat of vaporization or of the melting point of the metallic targets on the excitation temperature of the ejected atoms, we observe a similar dependence as in the case of expanding velocity. The excitation temperature increases as the heat of vaporization and the melting point increase. For the materials with a higher melting point or vaporization heat, based on our results, we assume the beam energy is converted into the internal energy of the plume (through excitations) and into the kinetic energy (through expansion velocity). Even though in fs and ps ablation regime the thermal effects are reduced and the electron-ion energy transfer (in the bulk material) and electron heat conduction times are significantly higher than the pulse width, the influences of these thermal physical parameters can still be observed.

We also looked at other parameters (electrical or thermal conductivity, boiling point, ionization potential) but no clear dependence was obtained. An example is presented in *Figure III.40* where we plotted the excitation temperatures derived from the emission spectra recorded at 1 mm from the target. While a general trend of decrease can be seen, it is not defined by a clear function. For instance, we found for the Mn and Cu plasmas similar excitation temperatures, in spite of Mn target having the lowest electrical and thermal conductivity and Cu being a highly conductive material. The plasma with the highest value of the excitation temperature was the one generated on a Ti target, the material with the highest heat of vaporization, boiling point and ionization energy, while the lowest value was found for the plasma generated on the material having the lowest heat of vaporization, melting point and ionization energy (Mn). It does seem like all these parameters are contributing to the value of the excitation temperature. Thus, we cannot determine a direct relation between the thermal/electrical conductivities and the excitation processes. We will further look at other plasma parameters, derived from complementary techniques.
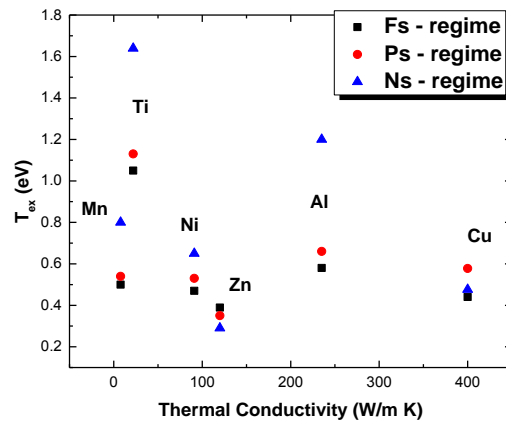
Figure III.40   Excitation temperatures extracted from the spectra collected at 1 mm from the target as function of the thermal conductivity.

If we take an ensemble look at all the ablation mechanisms involved in the three investigated regimes, the electrostatic mechanisms are the only ones that transcend all the ablation regimes. In the case of nanosecond laser irradiation, the ablation process is dominated by thermal processes which lead to melting and vaporization, material removal and the absorption of incident energy taking place during the pulse duration. By contrast, for shorter ablation regimes (fs and ps laser ablation) the laser pulse is shorter than the characteristic relaxation times [*Harilal et al.*, 2014b]. The heat load to the surrounding material is reduced, allowing a well-defined heat-affected area in contrast to ns regime where the re-solidification of melted layers leads to irregularities on the material surface [*Bulgakova et al.*, 1998]. As it was presented in the first chapter, for low fluence fs-laser irradiation, the Coulomb explosion is the dominant ejection mechanism, while at

sufficiently high laser intensities the phase explosion is followed by non-thermal vaporization of the bulk material and becomes the main mechanism for material removal [*Harilal et al.*, 2014b].

In the framework of the LP technique all plasma parameters that are extracted are related to the charged particles (electron temperature, density, ionic temperature, thermal velocity, plasma potential). Although the thermal velocity describes mainly the movement of the electrons, it can be correlated to the local thermal energy of the plume. In a similar manner, the drift velocity determined using the method presented in *Chapter II* can be related to the overall kinetic energy of the ions. Because the energy of the ejected particles is strongly connected to the cohesive energy, we will first look at the dependences on the material properties related to the electrostatic ablation mechanism [*Bulgakova et al.*, 2005; *Lin et al.*, 2012].

Increased thermal and drift velocities were observed as the electrical conductivity (*Figure III.41a-b*) of the target was augmented. As the conductivity of the target increases, a higher concentration of electrons will be ejected through electrostatic mechanisms leading to the formation of an intense positive charge region on the target surface in the very first moments of the ablation inception. The charge separation leads to a strong ambipolar electric field in which the ions are accelerated.

The thermal velocities present a quasi-linear increase from values of 2 km/s for the material with the lowest electrical conductivity to ~ 5 km/s for Cu which has the highest electrical and thermal conductivities. The drift velocities presented a steep rise for low conductivity elements reaching a quasi-saturation regime after $20 - 40 \times 10^6$ Sm^{-1}. This evolution is in line with the dynamics proposed in the theoretical study of Bulgakova et al. [*Bulgakova et al.*, 2005], where a Coulomb Explosion (CE) mechanism (*Chapter I*) is considered for particle ejection.
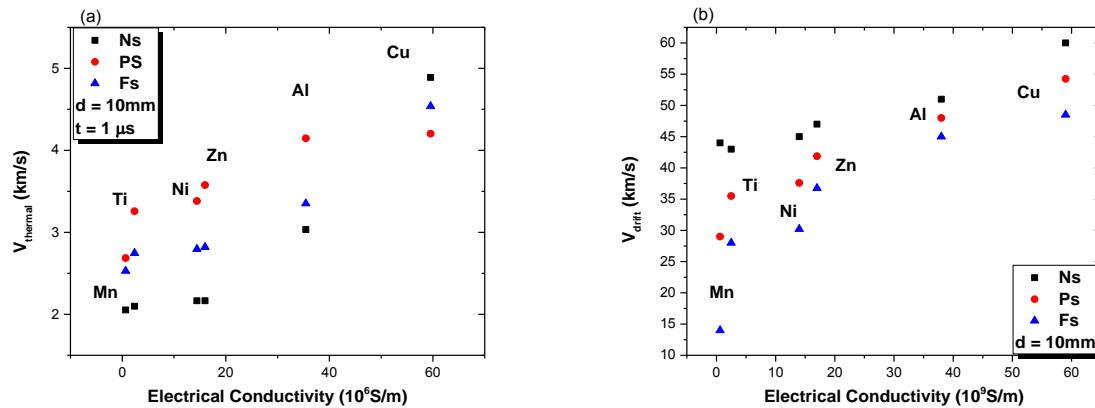
Figure III.41   Dependence of the electron thermal velocity (d = 10 mm and t = 1µs) (a) and ionic drift velocity (d = 10 mm) (b) on the electrical conductivity of the materials.

These results are also in good agreement with our findings [*Irimiciuc et al.*, 2017a] presented in *Section III.4*, where the expansion velocities of LPP from chalcogenide targets

increased as the electrical conductivity of the target was altered by the addition of Se_2Sb_3. We implemented the same treatment only for fs-LPP on a wider range of metallic targets (Al, Ni, Mn, Cu, In, Te, W) and we have found the same quasi-linear increase [*Irimiciuc et al.*, 2017b]. There we reported an exception to this rule for the Te plasma explained by the low boiling point (~ 1261 K) compared to all the other investigated materials which led us to believe that there might be some contributions of thermal mechanisms to plasma generation by laser ablation. However, in the following we will discuss only the metals investigated in all three ablation regimes: Al, Mn, Cu, Ni, Ti, Zn.

In *Figure III.42* we have represented the evolution of the plasma temperatures (electronic and ionic) with the electrical conductivity of the metals. The plasma potential and the electronic temperature presented a steep increase for low conductivity elements reaching a quasi-saturation regime after 20 x 10^6 Sm^{-1}. The same dependence was reported by our group [*Irimiciuc et al.*, 2017b] for a different set of materials (Al, Ni, Mn, Cu, In, Te, W). We would like to emphasize that although the materials differ, the range of conductivities is the same as both studies contain Cu which has the highest conductivity and Mn with the lowest value. The relationship between the electronic temperature and the electrical conductivity of the materials can be explained by considering a Coulomb Explosion (CE) mechanism for particle ejection in all ablation regimes. In the theoretical study of Bulgakova et al. [*Bulgakova et al.*, 2005], where a Coulomb Explosion (CE) mechanism is considered as the main ablation mechanism for the fs-LPP, the electric current density generated after laser ablation is proportional to the charge carrier mobility. Within the "classical" LP method, parameters like T_e are extracted by fitting the linear increase of the electronic region in a logarithmic representation of the *I-V* characteristic (*Chapter II*). Since the electrical conductivity is proportional to the charge mobility and subsequently to the collected probe signal, we proposed in [*Irimiciuc et al.*, 2017b] a *1/σ* dependence for T_e. The dependence proposed there for the fs ablation regime was found also for the ps and ns regimes, meaning that the electrostatic ablation mechanisms although are not the main ablation mechanisms as the thermal ones become more prominent are still influencing the energy of the ejected plume.
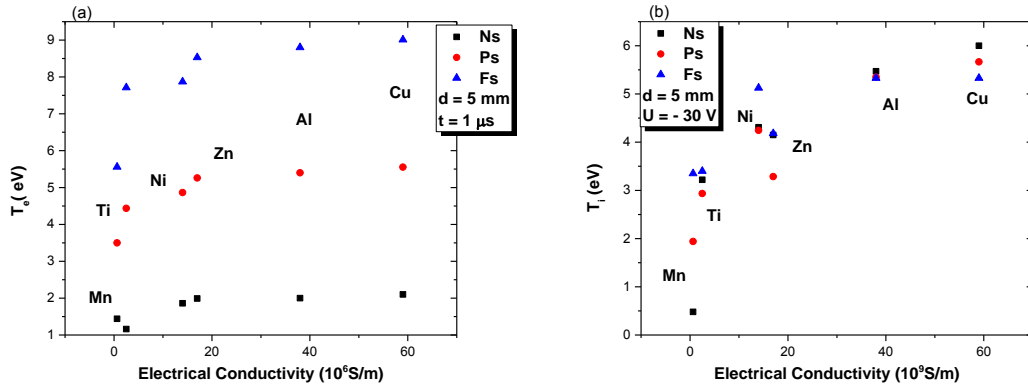
Figure III.42   Electronic (a) and ionic (b) temperatures dependence on the electrical conductivity of the investigated metals.

We also extended the formalism to the plasma potential (*Figure II.43b*) which is determined from the same logarithmic representation of the electronic current, being defined as the inflection point. The data was treated according to the empirical approach used in [*Irimiciuc et al.*, 2017b] and the experimental plasma potential values were fitted using a logarithm-type function:

$$V_{Plasma}(\sigma) = a_V + b_V \ln(c_V + \sigma), \qquad \text{Eq. (III.2)}$$

where σ is the electrical conductivity, $a_V(V)$, $b_V(V)$ and $c_V(S\ m^{-1})$ are positive constants. The electronic temperature was fitted using:

$$T(\sigma) = c_T - \frac{b_T}{\sigma + a_T}, \qquad \text{Eq. (III.3)}$$

where $a_T(S\ m^{-1})$, $b_T(eV\ S\ m^{-1})$ and $c_T(eV)$ are positive constants.

The resulted values for the respective constants are presented in *Table III.3*. We observe that for each ablation regime we can attribute a series of empirical constants. The values of the empirical constants are higher for the data extracted from the fs-LPP, which is consistent with the values of the excitation temperatures and plasma potentials determined in that particular ablation regime.

Table III.3. The values of the empirical constants for each ablation regime derived after fitting the excitation temperature and plasma potential evolution with the electrical conductivities of the metallic targets.

Constant	Femtosecond regime	Picosecond regime	Nanosecond regime
a_T ($S\ m^{-1}$)	$0.0091 \pm 1 \cdot 10^{-5}$	$0.0049 \pm 3 \cdot 10^{-5}$	$0.0034 \pm 2 \cdot 10^{-5}$
b_T ($eV.S\ m^{-1}$)	$0.35 \pm 2 \cdot 10^{-3}$	$0.0115 \pm 6 \cdot 10^{-4}$	$0.0038 \pm 4 \cdot 10^{-4}$
c_T (eV)	$9.12 \pm 3 \cdot 10^{-2}$	$3.22 \pm 5 \cdot 10^{-3}$	$2.1 \pm 8 \cdot 10^{-2}$
a_V (V)	$14.7 \pm 6 \cdot 10^{-2}$	$13.1 \pm 1 \cdot 10^{-1}$	$10 \pm 5 \cdot 10^{-1}$
b_V (V)	$4.7 \pm 2 \cdot 10^{-1}$	$3.7 \pm 5 \cdot 10^{-2}$	$3.16 \pm 4 \cdot 10^{-2}$
c_V ($S\ m^{-1}$)	$0.06 \pm 2 \cdot 10^{-3}$	$0.03 \pm 1 \cdot 10^{-2}$	$0.01 \pm 7 \cdot 10^{-4}$

We choose to fit the electronic temperatures (*Figure III.42*) instead of the ionic ones, as T_e represents a well-defined "local" (in space and time) measurement at 1 µs delay and 5 mm from the target, while T_i represents a "global" parameter, averaged on the entire time-of-flight. We note however that T_i is following roughly the same evolution as the excitation temperature, with the mention that between the three ablation regimes there is not a clear distinction. The functions that we used to fit the experimental data are of empiric nature and manage to successfully follow the dependences between the energetic plasma parameters (T_e, V_{Plasma}) and the electrical conductivity of the materials (*Figure III.43*). To our knowledge this is the first report of a mathematical correlation between the plasma plume parameters and the target material properties. A further study regarding the variation of these plasma parameters with other metal characteristics (such as atomic weight or ionization potential) did not reveal any direct dependency, thus a clear physical description of the fitting constants was not possible. These could be influenced by a number of target properties and their respective contributions could not be delimited.
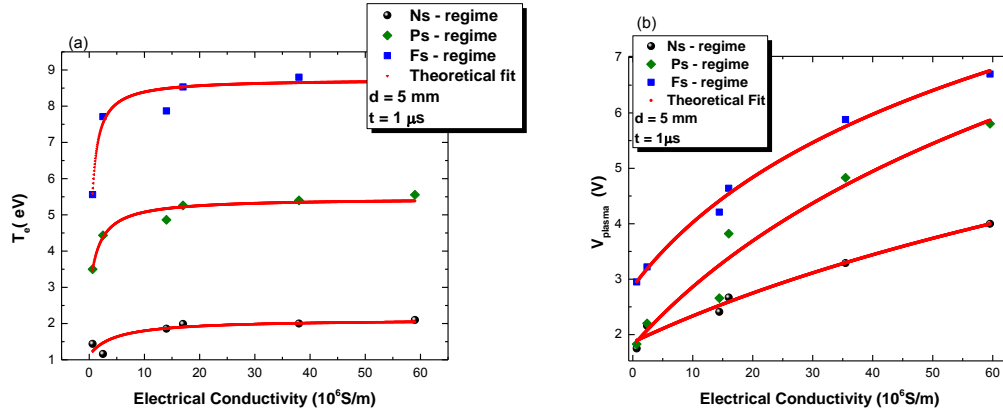
Figure III.43   Electron temperature (a) and plasma potential (b) dependence on the electrical conductivity of the investigated metals fitted with the empirical functions.

Given the diversity of the materials that were used and the fact that they cover a wide range of conductivity values (approximately two orders of magnitude), the problem of generalization can be raised. The concept can be appealing as the proposed function cover a wide range of excitation temperatures (0.2 eV - 9 eV) and plasma potentials (1 V – 7 V). We would like however to stress that these values characterize only a particular plasma volume investigated at a specific moment of time. So, we represented in *Figure III.44* the ns-LPP electronic temperature dependence on the electrical conductivity at different distances. The result revealed that the same dependence can be seen throughout the plasma volume. There is however a limit to it (~ 20 mm) from where the data become more scattered. It appears as a "loss of memory" for the plasma where the LPP becomes more thermalized due to the losses in energy and particle density.

We can state however that these functions describe well the considered set of materials in the considered range of laser fluence and background pressure. Further investigations are required to establish if these functions describe other type of materials (semiconductors and/or dielectrics) in different experimental conditions (different pressures, laser fluence and wavelength).
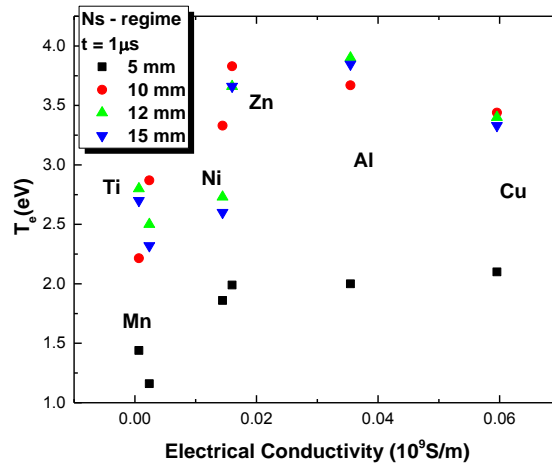
Figure III.44   Electron temperature dependence on the electrical conductivity at 1 μs at different target-probe distances.

A similar variation of the plasma potential and electronic temperature was obtained when considering the thermal conductivity as well. The similitude between the two representations (electrical and thermal conductivities) might suggest the presence of thermal effects. Although these results indicate the contribution from a second ejection mechanism influenced by other target properties (e.g. melting point) one should consider that the electrical (σ) and thermal conductivity (k) are connected through the Weidman–Franz law ($k = LT\sigma$, where L is the Lorenz number, and T is the system temperature).

In *Figure III.45* we represented the electronic temperature dependence on the melting point. The data for the electronic temperature is characteristic for a probe-target distance of 5 mm and a time-delay of 1 μs. For the data extracted in the ns regime the electronic temperature decreases as the melting point of the material increases, which could mean that the contribution to the electronic temperature induced by the thermal effects is reduced. For ns-laser ablation, thermal mechanisms are predominant and usually lead to the vaporization and cluster formation or re-deposition of the ejected material. Since thermal effects are more predominant in nanosecond ablation regime we will first investigate how the physical properties, like melting point or heat of vaporization point, can influence the properties of the ns-LPP. Then we will extend the same formalism to the ps and fs regimes, where the thermal damages are usually reduced. We observed for the shorter ablation regimes a similar dependence as in the ns ablation regimes. This could lead us to the conclusion that the thermal properties of the target can also influence the values of the plasma parameters.
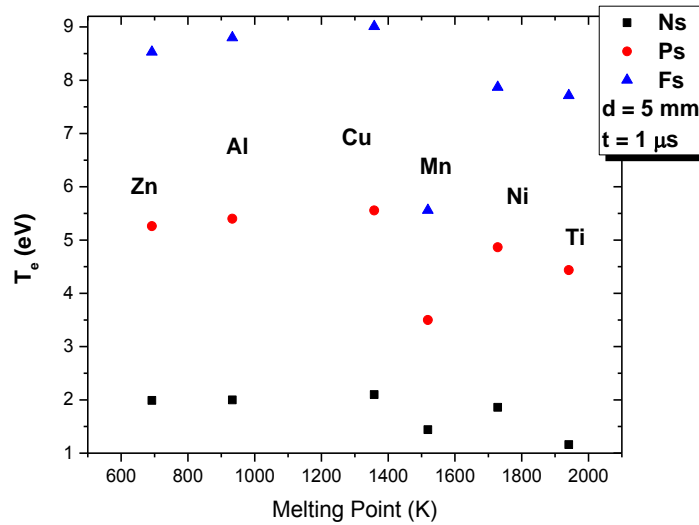
Figure III.45   Electron temperature (determined at 1 µs and 5 mm from the target) dependence on the melting point.

All the discussion regarding the energetic plasma parameters like electronic/excitation temperatures, plasma potential, thermal/drift velocities and how the ablation mechanisms are influencing the dynamics of the ejected particles was made on the basis that our empirical relationship transcends all three ablation regimes. One confirmation of our data could come from comparison with data already published by other groups. The main parameters considered in literature are the total ionic densities and are usually compared with the bonding energy of the ions in the crystalline lattice [*Cabalin and Laserna*, 1998; *Salle et al.*, 1999; *Schmidt et al.*, 2000; *Thestrup et al.*, 2002; *Zavestovskaya et al.*, 2008]. The bonding energy describes the volatility of the materials, which can be also defined using the heat of vaporization or the melting point.

For example, *Figure III.46* shows the decrease of the saturation ion density (taken at 10 µs) with the melting point of the target material. A similar observation was found in [*Salle et al.*, 1999] where the ns ablation plasmas of different targets (Mo, Fe, Mn, Cu, Al, Zn, Pb and Sn) were investigated. A significant decrease in the ablation efficiency (estimated as a function of the ablated crater depth) with the increase of the melting point was observed. The same type of influence of the melting point on the ablation yield was found by Thestrup et al. [*Thestrup et al.*, 2002] when investigating the ns-laser produced plasmas of metallic targets (Al, Cu, Zn, Bi and Ag). A decrease of about two orders of magnitude in ablation yield with the increase of cohesive energy was observed by Schou et al. [*Schou et al.*, 2005]. In [*Thestrup et al.*, 2002] and [*Schou et al.*, 2005], both melting point and cohesive energy are considered as a measure of the degree of volatility. In this study, the data follow the same dependence proposed by previously mentioned authors.
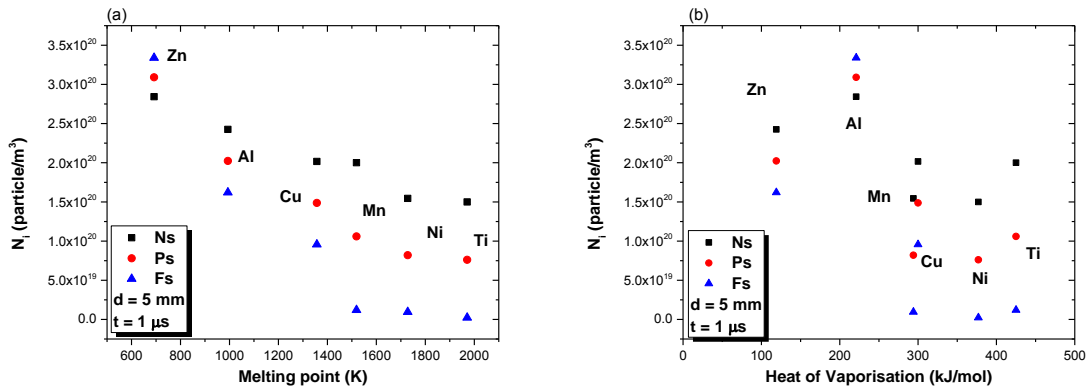
Figure III.46   Ionic density dependence on the melting point (a) and the heat of vaporization (b).

Although we have found some dependences between the physical properties of the target and the kinetic and energetic parameters of the laser-produced plasma plumes, we do not have a clear grip on the real reasoning behind it. Some of them have been correlated with the formation mechanisms of the two-plasma structure, but it is difficult so say that there is no other contribution to these evolutions.

III.4   Peculiar effects in nanosecond laser produced plasmas: plume reflection and ionic current oscillations

Although the fundamental studies presented earlier on pure metallic targets offered a great amount of information on the structure and dynamics of the laser-produced plasma plumes, they cover just one side of the PLD problem. The investigations for ns, ps, fs ablation regimes were made in the so called "free flow" regime. During expansion, the plume does not interact with any object (substrates [*Canulescu et al.*, 2009; *Chen et al.*, 2014; *González-posada*, 2016; *Focsa et al.*, 2017], planar Langmuir probes [*Donnelly et al.*, 2010b, 2010c; *Doggett and Lunney*, 2011]) and the background pressure is low enough so that there are no supplementary collisions between the ejected particles and the residual gas particles [*Geohegan and Puretzky*, 1996; *Wen et al.*, 2007; *Schou*, 2009; *Amoruso et al.*, 2010; *Harilal et al.*, 2014a; *Glavin et al.*, 2015]. But, when we try to apply the obtained results to the deposition process we need to take into account that in a typical PLD configuration the plume expansion is limited by the substrate, and usually these experiments require higher background pressures. In this section, we will present the result from a preliminary study based on ICCD fast camera imaging and LP techniques, focused on the global plume dynamics of an Aluminum plasma in PLD conditions. Also we will discuss some peculiar effects related to the LPP interaction with the substrate and the ion dynamics as measured by the Langmuir probe method.

In order to mimic the PLD conditions, a metallic substrate was placed at various distances (13 mm, 16 mm, 23 mm, 33 mm and 43 mm) parallel to the target. The metallic substrate is a stainless-steel disc (6 cm in diameter) with a 4 mm diameter hole made on its axis to keep the

normal incidence irradiation conditions used in the previous studies. The target and substrate were mechanically connected and electrically isolated from each other, both substrate and laser focusing lens were attached to the XYZ micrometric stage (see *Chapter II*), the whole system was moved as a whole to ensure constant laser fluence (5 J/cm^2). The target was rotated to present fresh ablation surfaces during data accumulation. The experiments were performed at various background pressures (10^{-6}, 10^{-4} and 10^{-3} Torr).

In *Figure III.47* we present the sequential snapshot of the laser-produced plasma plume on an Aluminum target, acquired with a gate width of 20 ns in the delay range 25 ns -1000 ns. The experiments were performed in low vacuum conditions ($\sim 10^{-6}$ Torr) with the aim of investigating the effect of the substrate and the plume behavior in its vicinity. We observe that if we place the substrate at a relatively long distance (43 mm) the plume dynamics at short evolution times (< 400 ns) is not significantly affected. There, we observe again the plume splitting into two components, result consistent with the time frame observed in the free flow case. At longer evolution time, we observe some additional excitations in the region of the substrate but the overall dynamics is not affected as the plume expands and the emission "dies" after approximately 1 µs. As we move the substrate at shorter distances (23 mm) we observe that the visible emission of the plume is reduced as well as the life time of the plume. We can also observe an increase in the intensity of the excitation in the substrate area due to the increase of the interactions between the ejected particles and the substrate surface. For a distance of 13 mm we observe a significant change in the shape of the plume and its emission. For this configuration, we observed also a third emission area close to the target. Due to the small distance between the substrate and the target, the plume will be confined and this will affect the thermal and kinetic energy of the particles reaching the substrate and also the overall lateral plume expansion.
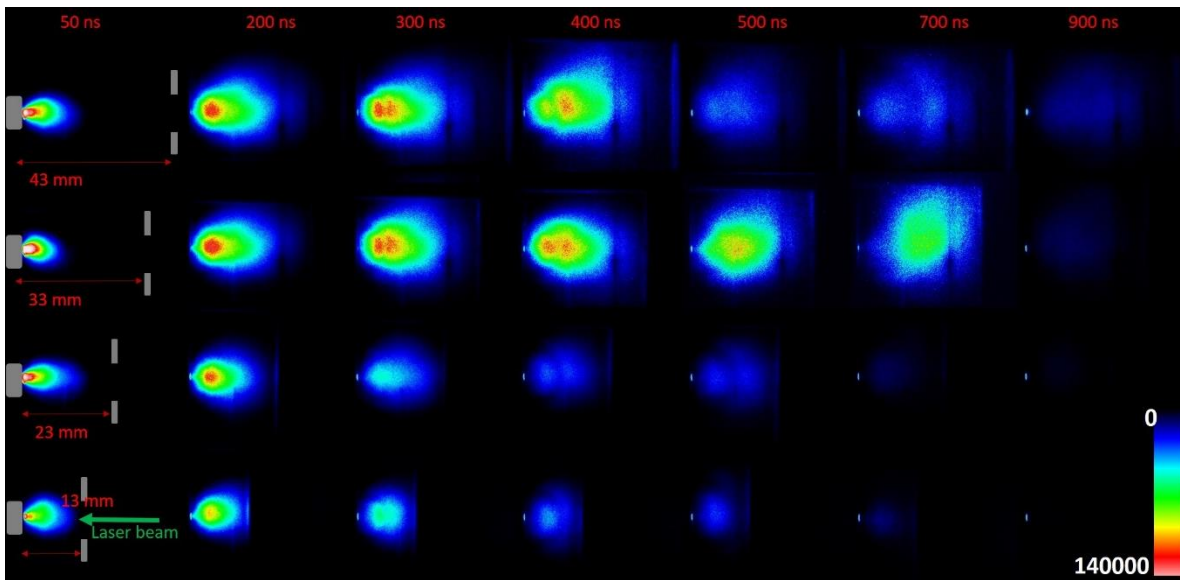
Figure III.47   ICCD images (gate width = 20 ns) of an Aluminum plasma, acquired for a delay range of 25 – 900 ns at different target-substrate distances.

In order to see more clearly the effect of the substrate we plotted in *Figure III.48* cross sections of the 400 ns snapshots recorded for all four configurations. There we observe clearly that the emission at the substrate becomes more significant for small target-substrate distances relative to the overall emission of the plume which decreases. For short distances (23 mm and 13 mm), the third component of the plume, which is considered to contain mainly nanoparticles and clusters, becomes more visible, probably due to the confinement of the plume in the axial direction. In this case, given the presence of the substrate and subsequently of an important concentration of reflected particles, this luminous area can also be induced by the re-excitation of the returning particles.
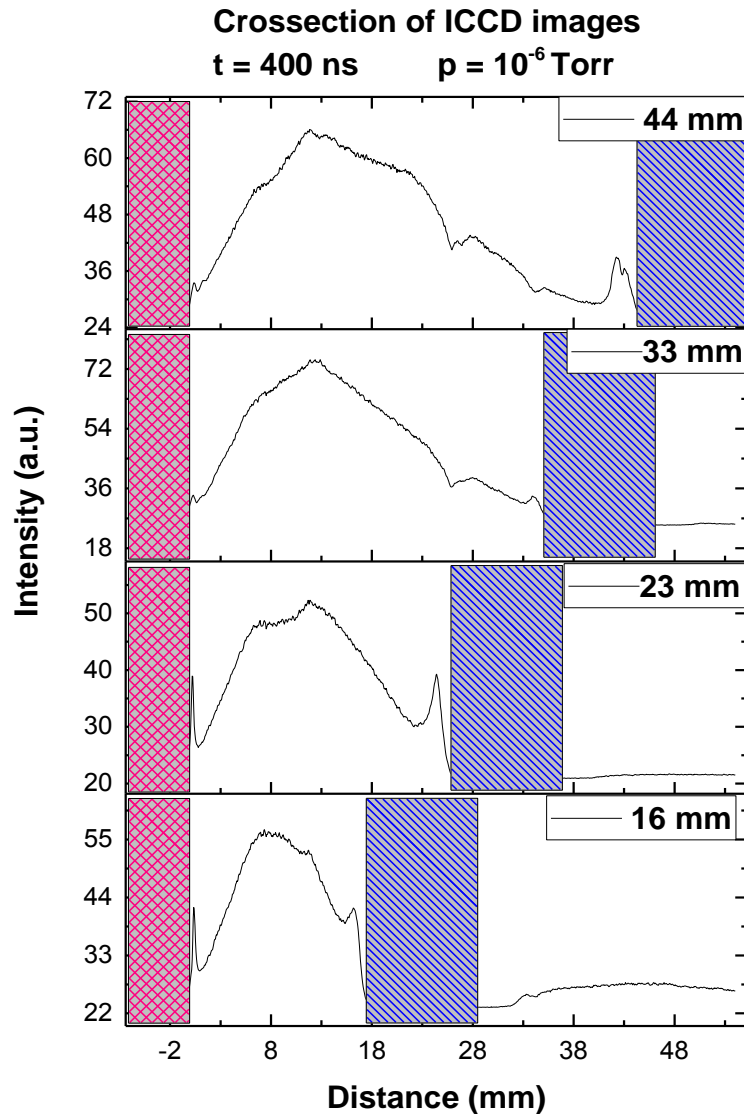
Figure III.48   Cross-sections of the 400 ns delay snapshots (gate width = 20 ns) of an Al plasma in all four configurations.

To explain the plume dynamics, we need to consider the behavior of the particles in the vicinity of the substrate. If the energy of the incoming particles is low they will arrive at the target and their kinetic energy will transform in thermal momentum at the substrate surface, which will startup one of the three growth mechanisms. If the energy of the incoming particles is high, a re-sputtering of deposited particle back into the chamber can take place or even a removal of substrate particles. Another type of particles that can be identified are the backscattered particles. These particles are a result of interaction of the incoming plume particles with the substrate, being reflected back towards the target. Supplementary excitations are induced due to their collisions with the incoming plume [Alfonso et al, 1996]. From the fast camera imaging, it is hard to differentiate between the possible phenomena (plume reflection and sputtering of the substrate), as we record only the non-dispersed emission of the plasma plume. But with certainty we can say that there is an increase in the global emission due to the plume interaction with the substrate. The dynamic of the LPP in the region of the substrate has been extensively investigated by Ojeda et al [*Ojeda et al.*, 2016]. In a recent paper where they performed ICCD imaging of laser-produced plasma on complex targets and observed that in high pressure conditions, re-deposition on the target and the area around the target is significant while the deposition rate decreases. The ICCD images allowed them to observe that for specific target-distance and background pressure conditions, the plume is reflected by the substrate and the supplementary excitations in the substrate area are given by the reflected particles colliding with the incoming ablated cloud. Moreover, the stopping of the plume in front of the substrate can occur if the background pressure exceeds a certain limit.

In order to have a better understanding of the involved phenomena we increased the background pressure up to 10^{-3} Torr of residual gas and reduced the target-substrate distance (13 mm). In *Figure III.49* we plotted the axial cross-section of two snapshots recorded at 100 ns and 1200 ns. At short evolution times, we can see the splitting of the plume into two components and a reduced emission at the substrate. As the plume evolves, similarly to what we observed in vacuum conditions, a third component appears in the vicinity of the target and the visible emission in the substrate area increases. With the increase in pressure the structuring of the plume in three components is more enhanced as well as the reflection of the Al particles, which leads to a strong emission in the vicinity of the substrate.
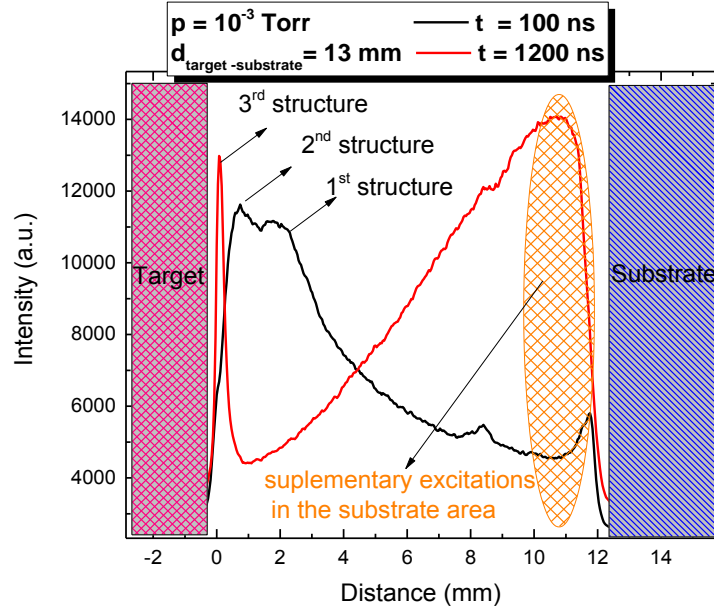
Figure III.49   Comparison between axial cross-sections of ICCD snapshots (gate width = 20 ns) of an Aluminum plasma, recoded at 100 ns and 1200 ns from the laser pulse.

To differentiate between plume reflection and possible sputtering of the substrate we recorded the emission spectra of the plume at 1 mm from the target and at 1 mm from the substrate. If a sputtering of the substrate takes place, one should observe other emission lines (beside the ones of Al) in the vicinity of the substrate as this is made of stainless steel. However, the spectrum collected near the substrate contained only emission lines characteristic to Al, thus confirming the plumes reflection scenario rather than the sputtering of the substrate. The main difference is that the intensity of the emitted lines in the substrate area were 2-3 orders of magnitude lower than the one collected at 1 mm from the target.

To study if the reflection of the plume is related to the background pressure, we performed ICCD fast camera imaging at different background pressures. The results are presented in *Figure III.50.* There we can see that the effects at the substrate are enhanced at higher background pressures [*Harilal et al.*, 2014a]. The overall dynamics of the plume is affected by the presence of the background gas. We can see that the global emission of the Al LPP is higher in the presence of the background gas and the expansion velocity seems to be affected.
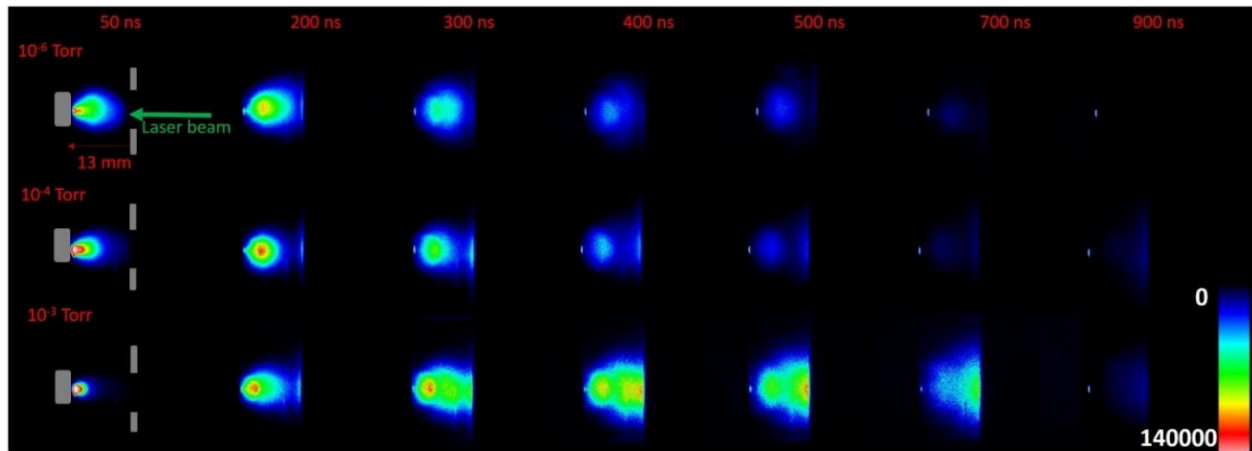
Figure III.50   ICCD imaging of an Aluminum plasma produced at various background pressures.

Quantitative information regarding the effect of the background pressure and the presence of the substrate, on the expansion velocity of the plume and its components, was obtained by plotting the displacement of the maximum emission attributed to each structure as a function of time. The results are shown in *Figure III.51* where we represented the velocity evolution of the two plasma components with the target-substrate distance (at two different pressures) and with the background pressure. We observe that as the target-substrate distance is increased the expansion velocity increases and it reaches a saturation value (free flow value) [*Wen et al.*, 2007; *Farid et al.*, 2014]. This dependence was found for all background pressures. Due to the confinement of the plume and subsequent reflection at the substrate, the overall velocity decreases as the distance was changed from 43 mm to 16 mm. Decreased velocity values along with increased global plume emission were also observed when the background pressure augmented. This is expected as the number of collisions increases leading to subsequent excitation (*Figure III.51)* and thus converting part of the kinetic energy into thermal energy [*Geohegan and Puretzky*, 1996; *Amoruso et al.*, 2008].
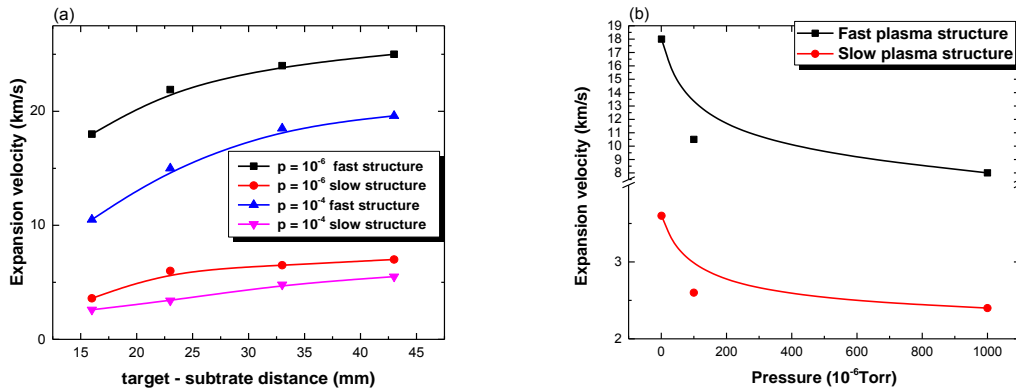
Figure III.51   Expansion velocity evolution with target-substrate distance for 10^{-4} Torr and 10^{-6} Torr (a) and with the background pressure for 13 mm substrate - target distance (b).

By investigating the global emission dynamics in different PLD configurations and for different background gas pressures, we were able to see that the evolution of the plume is affected by the configuration of the deposition system. To further explore the influence of these conditions on the evolution of individual plasma particles (atoms and ions) we used two complementary techniques based on space- and time-resolved optical and electrical investigations by means of LP and PMT measurements.

III.4.1   Space- and time-resolved optical and electrical investigations of LPP in PLD conditions

For these complementary measurements, the substrate was placed at 43 mm from the target and the background pressure was kept at 10^{-6} Torr. The electrical investigations were performed by collecting the ionic current from the plasma plume with the stainless steel cylindrical Langmuir probe biased at – 30 V and placed at various distances (2 – 40 mm) from the target (on its axis). For the optical measurements (see *Chapter II*), the PMT (990 V amplifier voltage) was used to investigate the spatial and temporal evolution of atomic (396.15 nm) and ionic (358.75 nm) Al lines at distances from target varying in the 0.5 – 30 mm range. Both signals were recorded using the LeCroy Wave Runner 6200A oscilloscope (2 GS/s) with 50 Ω input impedance.

The results from the Langmuir probe measurements are presented in *Figure III.52*. Using this experimental configuration, we were able to correlate the life-time of the ionic current with the one of the plasma plume determined through ICCD images. We notice however the "strange" shape of the ionic current, which has a multi-peak structure [*Laska et al.,* 2000; *Gurlui et al.,* 2008; *Sunil et al.,* 2008; *Kumar et al*; 2009; *Singh et al*., 2014]. We also observe another expected phenomenon: the maxima of the ionic current presents a shift towards higher arrival times as the target - probe distance is increased. For the determination of the ionic expansion velocity we

plotted the distance as a function of the temporal displacement of the first maxima and fitted with a linear function. The estimated velocity of 18.8 km/s is in good agreement with the results obtained through optical measurements and the ones reported in other papers *[Focsa et al.,* 2009*; Ursu,* 2010*; Irimiciuc et al.,* 2014a*,* 2017a*; Pompilian et al.,* 2014*; Geohegan and Puretky,* 1995*;Harilal et al.,* 2014a*; Amoruso et al.,* 2006]*.
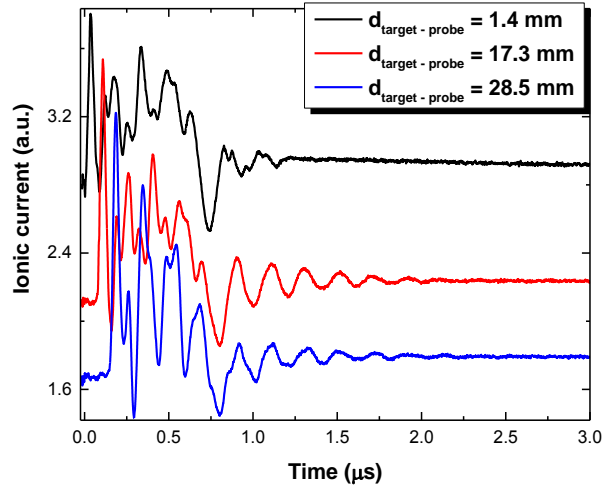
Figure III.52   Ionic traces collected by a Langmuir probe biased at V_{Probe} = -30 V, using an input impedance of 50 Ω, at various probe-target distances.

As we briefly mentioned in the previous sections, there is an oscillatory regime (< 1μs) overlapping the shifted Maxwellian distribution of the ions which is observed for all three ablation regimes that were investigated (ns, ps, fs). In PLD configuration, we observe a strong oscillatory behavior mainly present for short delay times (< 700 ns) which can be seen through the whole volume of the plume, even up to a few cm from the target. This peculiar effect was reported by our group in [*Gurlui et al.*, 2008; *Nica et al.*, 2009, 2010a, 2010b, 2012; *Focsa et al.*, 2017]. This oscillatory structure of the ionic current was observed in plasmas generated by ns or fs laser ablation of various metallic targets in high vacuum conditions.

The presence of multiple structures in laser-produced plasmas is generally accepted as being based on the formation of an ambipolar electrical field (single or multiple double layers) during expansion. This corresponds to the Coulomb scenario presented in *Chapter I*. According to the work published by Bulgakova et al. [Bulgakova et al., 2005], during the first moments of expansion the electrons will diffuse faster than the heavier particle like atoms or ions. This leads to the formation of an electrical field that will accelerate the ions and decelerate the electrons. This early dynamics of the charged particles might induce an oscillating behavior after which, due to losses through collisions, an asymptotic expansion velocity is obtained.

This scenario is particularly appealing for relatively high laser ablation irradiances (10^{12} - 10^{15} W/cm^2), where the presence of 10 GHz oscillations was reported in the vicinity of the target. Early works [Eliezer and Hora; 1989] on LPP oscillations reported the formation of double (or multiple) layers with widths of 100 μm and electrical fields up to10^6 V/cm. The same approach was used to explain the current oscillations even at lower irradiances ($10^5 - 10^8$ W/cm^2) [Gilton et al., 1990; Amoruso et al., 1999]. Other groups have attempted to explain this multi-peak structure of the ionic current with the presence of multiply-charged ions [Laska et al., 2000] in the case of pure targets. For the case of multi-component targets the structure was interpreted in terms of mass dependence of the expansion velocities of different plume components [Sunil et al., 2008]. However, a follow-up study of the same group [Kumar et al., 2009] proved by triple-probe technique (which allowed the real-time measurement of the electron temperature) that the observed oscillations are a "genuine" feature of the fluctuations propagation within the plasma plume.

In spite of all this, a complete (i.e. valid for all ablation laser pulse durations) understanding of LPP oscillations remains challenging. From an experimental perspective, the group of Bulgakova [Bulgakova et al., 2000] demonstrated for the case of ns laser ablation of graphite the presence of fast and ultrafast ion peaks (with the ultrafast species attributed to the doubly-charged ions) and analyzed their dependence on the laser fluence. On the other hand, from a theoretical perspective, the same group reported that the presence of multiple double-layers is strongly related to the existence of two species of electrons ("hot" and "cold") that correlates to the two-temperature plasma model. The image changes in the case of a single-electron-temperature plasma where only one double-layer can be expected. Increasing the ratio of "hot" to "cold" electrons (either by density or temperature) will aid the occurrence of multiple double layers. All these results seem to point out to a strong relationship which would exist between all these peculiar effects: two-electron-temperature plasmas, fast electrons, double-layer formation, and plume splitting in multiple structures and occurrence of oscillations.

Our space-time resolved approach allowed us to observe that as the distance increases there is a significant change in the shape of the oscillatory structure of the ionic currents. *Figure III.53* displays the ionic traces collected at two distances, one in the proximity of the target (1.4 mm) and another one in the substrate region (38.3 mm). From the FFT of the ionic current extracted in the vicinity of the target we observed two oscillation frequencies, one having a value of 6.1 MHz, in the range of the values reported by our group in other previous papers, and a higher frequency of 13.7 MHz. The structure of the LP signal changes as the probe is closer to the substrate (*Figure III.53b*). Here, we observed only one oscillation frequency (~ 5.8 MHz) and a shift of the first maximum towards longer time-delays.
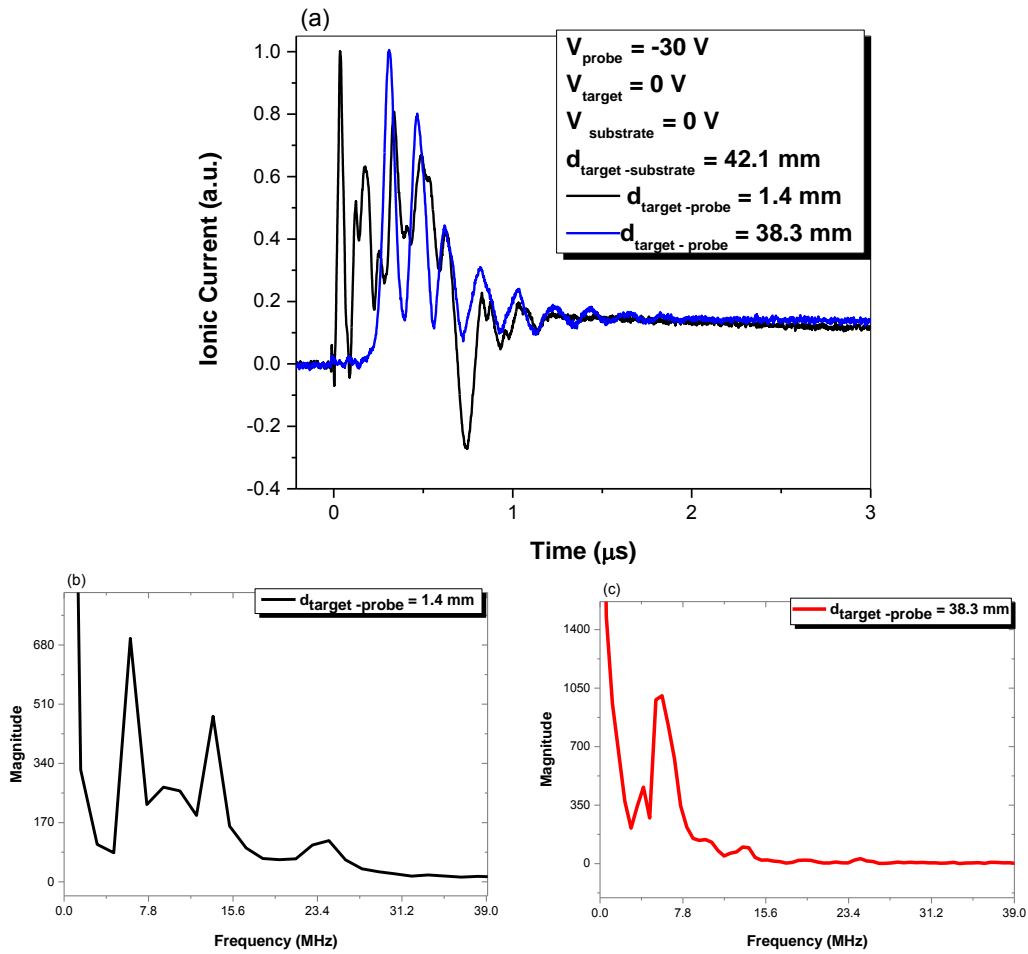
Figure III.53   Ionic temporal traces collected for a probe bias of V_{Probe} = -30 V at two distances with respect to the target surface: 1.4 mm and 38.3 mm (a) and the corresponding Fast Fourier Transform (FFT) for each of the two ionic currents (b) - (c).

The ionic oscillations have a complex space-dependent structure, and for a better understanding of these peculiar effects we performed complementary space- and time-resolved optical measurements. We recorded the temporal evolution of two Al emission lines: Al I (396.15 nm), Al II (358.75), at the same distances at which the LP collected the ionic currents. The recorded signals, presented in *Figure III.54*, show that the lifetime of the ions is about 600 ns while the one of the atoms is ~ 1500 ns, results consisted with other similar studies from literature [*Geohegan and Puretzky*, 1995; *Harilal et al.*, 2003b; *Amoruso et al.*, 2005d; *Ursu et al.*, 2009; *Ursu*, 2010; *Pompilian et al.*, 2013; *Irimiciuc et al.*, 2017a;]. Also, we notice that the maximum of these traces shifts towards longer time-delays as the distance increases, following a linear function. This allowed us to estimate the expansion velocity of both species. For the atoms, we found a velocity of 4.0 km/s while for the ions we obtained a value of ~ 10 km/s. These results are in good

agreement with the LP measurements where we determined a velocity of 18.8 km/s and with the ICCD fast camera imaging where we found velocities of 18 km/s and 4 km/s for the fast and slow components, respectively.
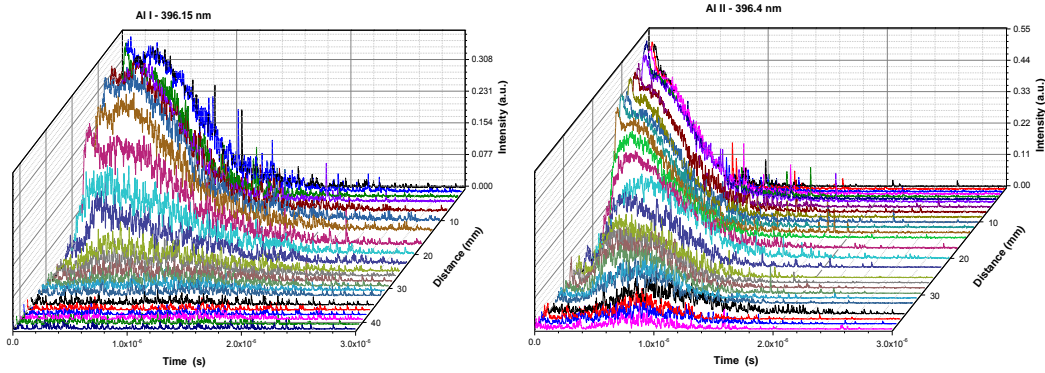
Figure III.54   Temporal evolution of the Al atom (396.15 nm) (a) and ion (356.6 nm) (b) spectral lines emission, recorded by a sub-ns rise-time photomultiplier, at various distances from the target surface.

In order to compare the results obtained through optical and electrical methods, in *Figure III.55* we plotted the temporal trace of the ionic current (V_{probe} = -30 V) and the PMT signal recorded for the Al I (396.15 nm) and Al II (358.6nm) at a distance of 18 mm from the target. The optical signals seem to be strongly affected by fluctuations. If we look closely, the "drops" of the Al I and Al II optical signals are quasi-periodic. Thus, the optical measurements confirm the oscillation behavior observed through LP measurements.
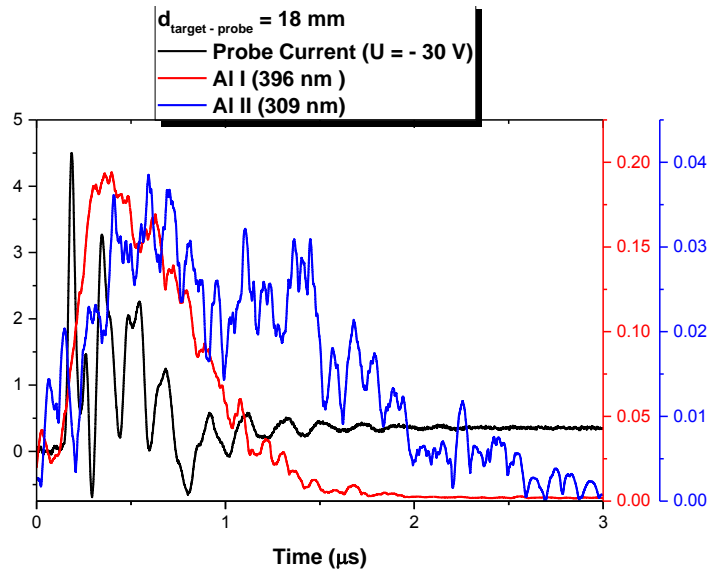
Figure III.55   Presence of an oscillatory regime on both optical and electrical signals.

Finally, in order to correlate the results from the optical and electrical investigations, we represented the spatial evolution of the oscillation frequencies as determined from the ionic current (LP) and the optical signals (PMT) of ions and atoms (*Figure III.56*). We observe that the oscillation frequency of the neutral atoms is of MHz order (5-7 MHz) and is approximately constant with respect to the measurement distance, result consistent with the values of the "low" frequency recorded with the LP, which remains constant during expansion. The oscillation frequency of the ions (in the optical signal) decreases starting from 11 MHz at 1 mm towards ~ 7 MHz at 30 mm. We can see however that there is an important point (~ 12.5 mm) which separates the plume into two zones. A first zone (between 1 - 12.5 mm) where we can see the two frequencies in the LP signal and where the ions and the atoms oscillate with different frequencies. A second zone, at longer distances (between 12.5 mm and 43 mm), where the frequencies of the atoms and the ions determined through PMT measurements converge to the values of the "low" frequency determined though LP, while the "high" frequency disappears.
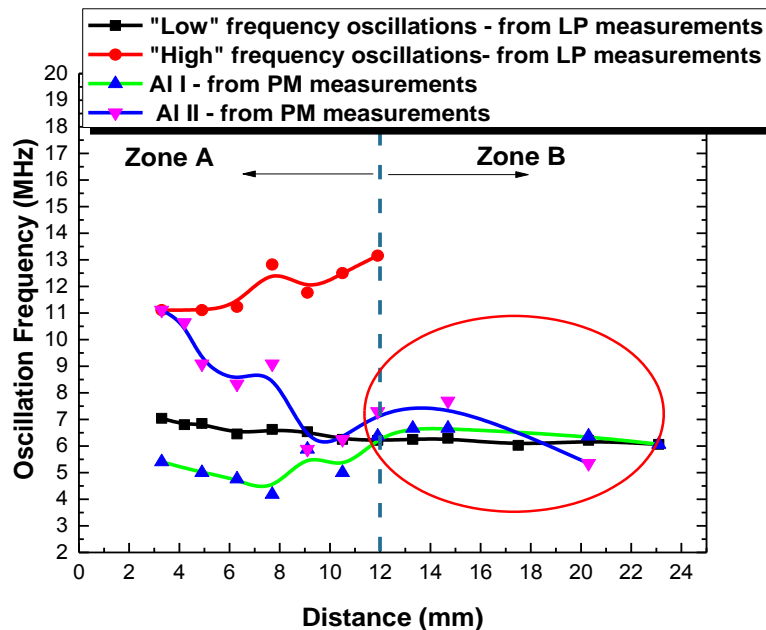
Figure III.56   Oscillation frequencies evolution inside the plasma volume.

To summarize, the space- and time-resolved optical and electrical investigations in PLD configuration reveal a strong oscillation behavior on the LP ionic current as well as on the Al I and Al II optical signals recorded with the fast response PMT. The confinement of the plume in axial direction and the plume reflection induced by the presence of the substrate can lead to the increase of this complex dynamics. The effect of the substrate was studied by collecting the ionic current at 5 mm from the target while the substrate was positioned at 13, 23, 33 and 43 mm. The ionic signal presented two oscillation frequencies with the high frequency decreasing from 13.2 MHz to 11.5 MHz and the low frequency from 6 MHz towards 4 MHz. The changes in the oscillation

frequency are small, but seem to be in line with our hypothesis that the confinement induced by the substrate leads to an enhancement of the oscillatory regime [*Singh et al.*, 2014].

Regarding the presence of two oscillation modes (low and high frequency) and the difference observed in the oscillation frequency of Al atoms and ions, we would attempt to explain the results in the framework of the double layer induced oscillation scenario [*Eliezer and Hora*, 1989]. The charge separation occurring in the proximity of the target and the subsequent charge separation will lead to oscillation of the charged particles. This will define the edge of the plume as it expands. Thus, the oscillations are contained in the fast component of the plume [*Focsa et al.*, 2017]. If we now take into account our results presented in *Section III.2.1.3*, where we showed a two-temperature spatial distribution, with different expansion velocities of the two main plasma structures and the clear separation between them observed through ICCD imaging, we can state that the two components should be considered as two different entities. As a result each plasma component should be described by a specific plasma temperature, plasma potential and expansion velocities. These differences will lead to the occurrence of an "interface" [*Popa and Sirghi*, 2000; *Bulgakov and Bulgakova*, 2002] separating the two components. The strong fluctuations present in the fast structure could induce, through the "interface" separating the two components, an oscillatory behavior in the second structure. This is in line with our qualitative explanations given in the framework on the fractal model, where we considered that the oscillatory regime is induced by a double layer connecting the two plasma components. The high frequency mode is observable only when there is a strong interaction between the two structures. As the plume expands the system oscillates on the "fundamental" frequency (low frequency mode) where both atoms and ions are oscillating simultaneously.

At this point the link between the data obtained from optical and electrical methods is not completely understood. In order to clarify some of these results and the dependences obtained here, supplementary investigations are required. Most probably time-resolved LP measurement in the oscillation part of the ionic current would allow us to correlate the ionic oscillations with the behavior of all plasma parameters provided by the LP technique.

III.5 Optical investigations of nanosecond laser-produced plasmas on chalcogenide targets

III.5.1 Introduction

Although the study of pure metallic targets in free expansion and PLD configuration led to some interesting results that confirm the viability of such diagnostics techniques and their importance to some laser based technologies, we needed to expand our array of targets. Because one of the main advantages of PLD is the congruent transfer of stoichiometry between the target and the thin film, we extended our study towards more complex targets. This was realized in the framework of a strong collaboration between University of Lille 1 (France), University of Pardubice (Czech Republic) and University of Rennes 1 (France), which led over the years to systematic studies of several families of chalcogenides (Ge-Sb-Te; Ga-La-S; Ge-Se-Sb) in bulk and thin film form, coupled with optical and electrical investigations of laser produced plasmas [*Focsa et al.,* 2009*; Pompilian,* 2013*; Pompilian et al.,* 2013,2014*, Olivier et al.,* 2015] on such targets for the improvement of the deposition process. One of the main purposes for this thesis was to investigate and understand the influence of the target properties on the characteristics of the laser-produced plasmas. Thus, we investigated the dynamics of laser-produced plasmas in PLD configuration on 7 chalcogenide (($GeSe_2)_{100-x}(Sb_2Se_3)_x$, x = 0-60) targets (see *Chapter II*, *Table II.2* for details). The base compound was $GeSe_2$ on which a mixture of Sb_2Se_3 was added in various concentrations (0 – 60%). With the addition of Sb_2Se_3 the physical properties of the glass targets were changed and the aim of the study was to understand how the addition of Sb_2Se_3 affects the overall plume dynamics, by using some of the techniques used in the previous sections.

III.5.2 ICCD imaging

The global dynamics of the plasma originating from the interaction of the laser pulse with Ge-Sb-Se glasses was studied by recording ICCD images (20 ns gate width) at different delays after the laser pulse. As an example, sequential snapshots of the expanding $GeSe_2$ and $(GeSe_2)_{40}(Sb_2Se_3)_{60}$ plume are presented in *Figure III.57*. The ICCD images recorded for all samples revealed a splitting process of the plasma plume into three components. The splitting of the LPP generated by laser ablation is a common phenomenon being observed in different ablation regimes as it was shown in the *Sections III.2 - 4*. For laser ablation of complex targets like chalcogenide systems [*Němec et al.*, 2014; *Olivier et al.*, 2014b; *Pompilian et al.*, 2014], generally two-structure plasmas were observed, result consistent with other findings from literature [*Geohegan and Puretkzy,* 1995*;Focsa et al.*, 2009; *Pompilian*, 2013; *Harilal et al.* 2014*; Amoruso et al.* 2005a]. For this chalcogenide system, a third plume component, close to the target, with well-defined interface and large contact area with the surface was found. The presence of a supplementary structure in the vicinity of the target was also reported by Canulescu et al [*Canulescu et al., 2009*]. Their study focused on optical investigation of LPP of $LiMn_2O_4$ in low vacuum. The third plasma structure was here associated to multiple scattering interactions, which

determined a differential decrease of the ejected particle velocity. Another report by Amoruso et al. [*Amoruso et al.*, 2010] mentioned a third structure with a low expansion velocity ~ 10^2 m/s containing nanoparticles and being characterized by a blackbody-like emission.
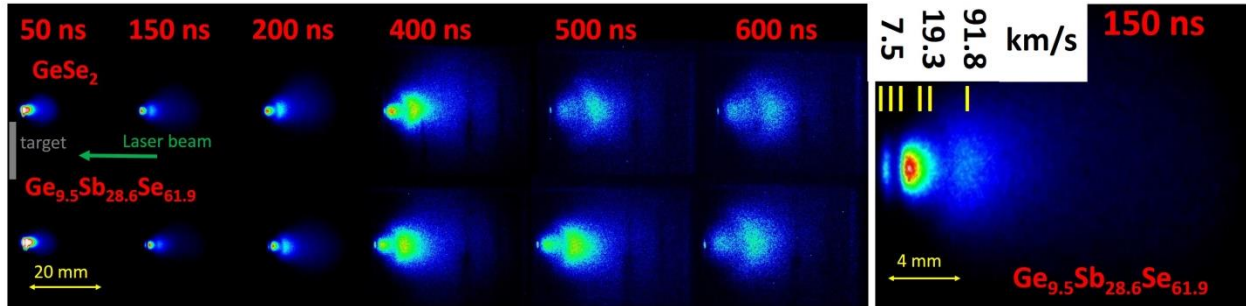
Figure III.57   ICCD images of laser-produced plasmas on GeSe$_2$ and Ge$_{9.5}$Sb$_{28.6}$Se$_{61.9}$ using a gate width of 20 ns [*Irimiciuc et al.*, 2017a].

For more information on the plume expansion dynamics and its evolution with the Sb$_2$Se$_3$ concentration, we recorded different snapshots of the plasma at different moments in time with respect to the laser pulse. The velocities of the three plasma components were derived from the linear fit of the displacement of the maximum emission point at different delays (*Figure III.58a*). We observed that all plasma structures are expanding with a constant velocity. *Figures III.58b* and *III.58c* presents the dependence of the calculated expansion velocities on the Sb$_2$Se$_3$ concentration and on the Sb:Ge ratio, respectively.

The velocities of all three plasma components increase with the addition of Sb$_2$Se$_3$ content reaching maximum values of 92 km/s for the first structure, 19 km/s for the second structure and 8 km/s for the third component for the (GeSe$_2$)$_{40}$(Sb$_2$Se$_3$)$_{60}$ target. Considering that the experiments were performed under identical conditions (background pressure and laser fluence), the evolution of the expansion velocities is considered to be correlated to the changes in structural and electrical/thermal properties of the targets. Considering the complex structure and dynamics of the laser-produced plasma on the chalcogenide glasses, complementary space- and time-resolved optical diagnostics of the individual plasma plume components were performed.
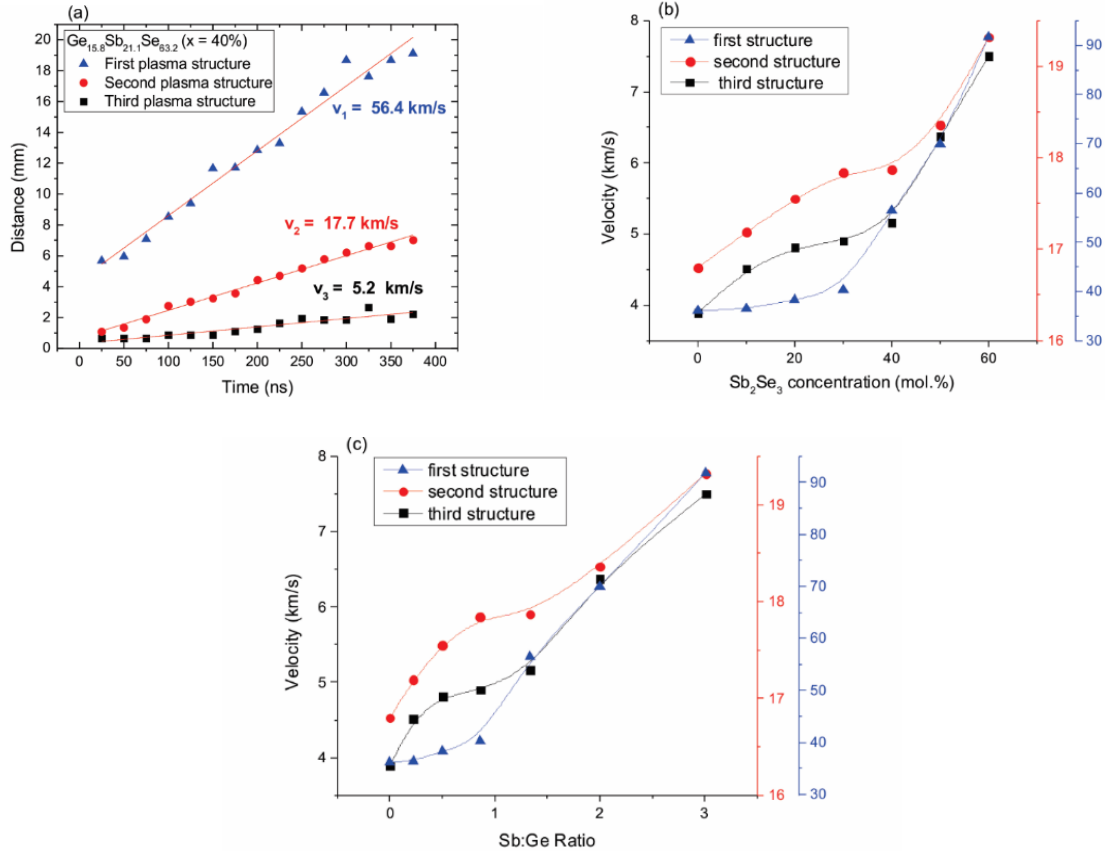
Figure III.58   The maximum emission point displacement in time (a), the dependence of the expansion velocities on the Sb_2Se_3 concentration (b) and on the Sb:Ge ratio (c).

III.5.3   Space- and time-resolved optical emission spectroscopy

To analyze the contributions of different species found in the plasma plume, a space-time resolved spectroscopic study was performed. First, global (i.e. 2 μs integrated) emission spectra of a 200 μm wide plasma slice situated at 6 mm from the target surface was recorded in the 300-700 nm spectral region. *Figure III.59* presents an example of the emission spectra recorded for the $(GeSe_2)_{40}(Sb_2Se_3)_{60}$ target. All the observed emission lines were identified using the available database [*Kramida et al.*, 2014] as corresponding to both excited and ionized states of the three elements. Higher density of lines was observed for Ge and Sb, while only a few lines were attributed to Se atoms or ions.
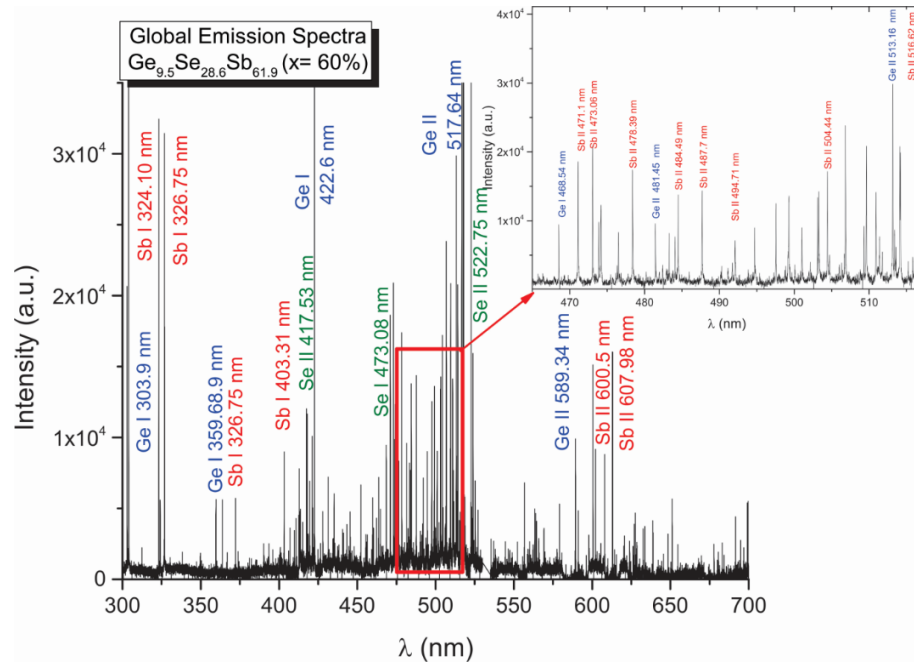
Figure III.59   Global emission spectrum of the $(GeSe_2)_{40}(Sb_2Se_3)_{60}$ laser ablation plasma recorded at 6 mm from the target (25 ns gate delay, 2 µs gate width).

The emission intensity can be assumed as proportional to the number density of the corresponding element in the plume [*Noll*, 2012]. Some qualitative information regarding the influence of the Sb_2Se_3 addition on the plasma structure can be obtained by studying the changes in spectral line intensities (*Figure III.60*). As the content of Sb_2Se_3 increases, we observed an overall decrease in Ge emission line intensity (Ge I-303.9 nm: E_k 4.96 eV– E_i 0.88 eV and Ge II-517.86 nm: E_k 12.43 eV – E_i 10.08 eV) and an increase of Sb lines (Sb I 326.75nm: E_k 5.82 eV– E_i 2.03 eV and Sb II 600.5 nm: E_k 10.68 eV – E_i 8.62 eV). For Se lines (Se I 473.08 nm and Se II 522.75 nm) although the intensity decreases following a similar pattern as for Ge, the range is much smaller, so it can be considered as being constant (with intensities ranging between 4.25 a.u. and 4.6 a.u.). These dependences are in good correspondence with the compositional changes of the bulk materials where only a 4.8% decrease in Se content was found, while Ge and Sb concentrations presented a variation of 23.8% and 28.6%, respectively. For Se II we observed a deviation from the compositional changes in the target for which a slight increase of the emission intensity (2 a.u. – 3 a.u.) with the Sb_2Se_3 content was observed. The increase of the expansion velocity for all three components in the Sb-rich targets can lead to a higher ionization efficiency of all plasma components through collision processes, thus an increase in ionic species. The intensity evolutions of Sb II emission lines are consistent with the increase of the Sb concentration in the target. On the other hand for Ge ions the composition variation overcomes the enhanced ionization efficiency.
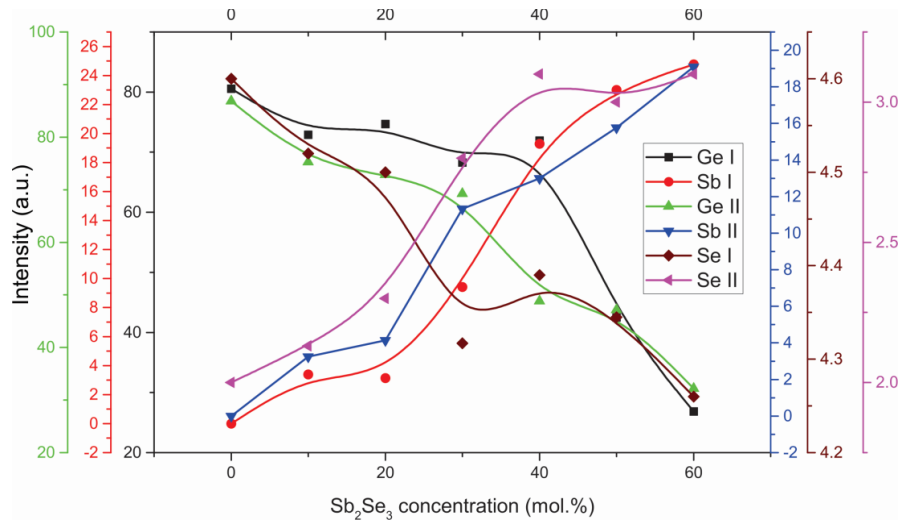
Figure III.60   The evolution of the maximum intensity of the spectral lines of Ge I, Ge II, Sb I, Sb II, Se I and Se II with the Sb_2Se_3 content at 6 mm distance from the target (25 ns gate delay, 2 µs gate width).

With the purpose of obtaining information on the excitation mechanisms and to study the plasma structure, the temporal dynamics of both atoms and ions were analyzed by means of the excited states populations. The temporal evolution of the emission spectrum lines recorded at different distances from the target surface have been investigated using the fast response photomultiplier (950 V amplifying voltage was used for a good signal to noise ratio). An example of emission intensity temporal profiles obtained for germanium and antimony neutrals and ions (recorded at 1 mm from the $Ge_{19.4}Sb_{16.7}Se_{63.9}$ (x=30%) target) is presented in *Figure III.61a*. As the variations of Se concentration in the target (and thus in the spectra) are limited, we focused our attention towards the study of the most intense Ge and Sb emission lines.
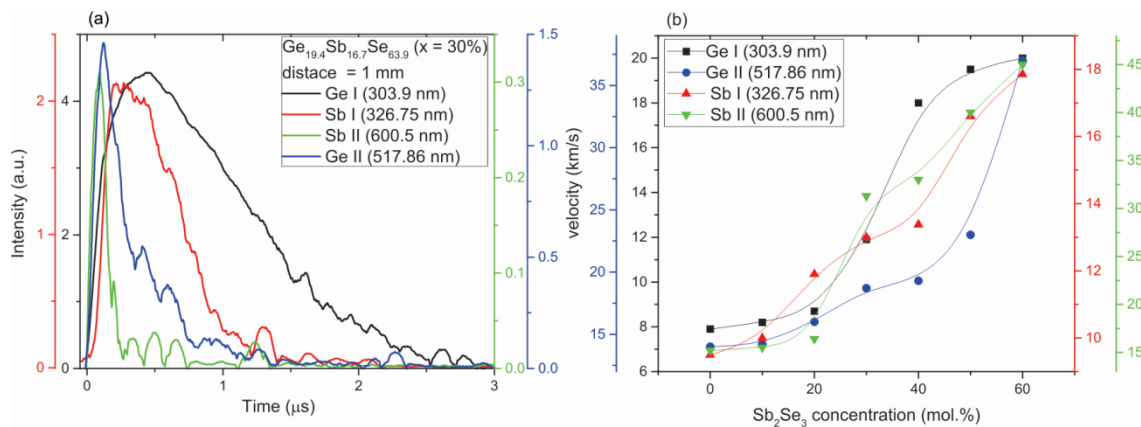
Figure III.61   Temporal evolution of the Ge and Sb excited atoms and ions optical emission at 1 mm from the target (a) and the evolution of the corresponding expansion velocities with the Sb_2Se_3 content (b).

We observe that both Ge and Sb neutrals exhibit a longer emission time than the corresponding ions, result in good agreement with other works [*Geohegan and Puretzky*, 1995; *Harilal et al.*, 2003b; *Amoruso et al.*, 2005d; *Ursu et al.*, 2009; *Ursu and Nica*, 2013; *Focsa et al.*, 2017], which could be explained by the differential acceleration of ions during the first stages of expansion [*Bulgakova et al.*, 2005]. The expansion velocity of each species was determined by analyzing the shift of the maximum emission time of the corresponding spectral line at different distances. This allowed us to investigate their evolution with the increase of Sb_2Se_3 concentration (*Figure III.61b*). The results reveal the presence of energetic Ge and Sb ions in the plume with expansion velocities ranging between 15 – 45 km/s and neutral species presenting lower velocity values varying from 8 km/s to 20 km/s for the high antimony concentration targets. Correlating these results with the ones obtained by ICCD fast camera imaging we can conclude that while the first structure ("fast" component) consists mainly in ionic species, the second one ("slow" component) is formed predominantly by neutrals with velocities below 20 km/s. Both techniques present an increase of the global and individual expansion velocities with the increase of Sb_2Se_3 content in the bulk sample.

For information on the internal energies of the plasmas, the average excitation temperatures were derived from the optical emission spectra using the Boltzmann equation (*Chapter II*). An example of the obtained Boltzmann plots for Ge and Sb atoms is given in *Figure III.62a*. There is a discrepancy between the abundance of atomic lines observed in the emission spectra and the number of lines used to determine the excitation temperature. This is due to the fact that only a few lines had a complete description of the energy level characteristics in the available databases.
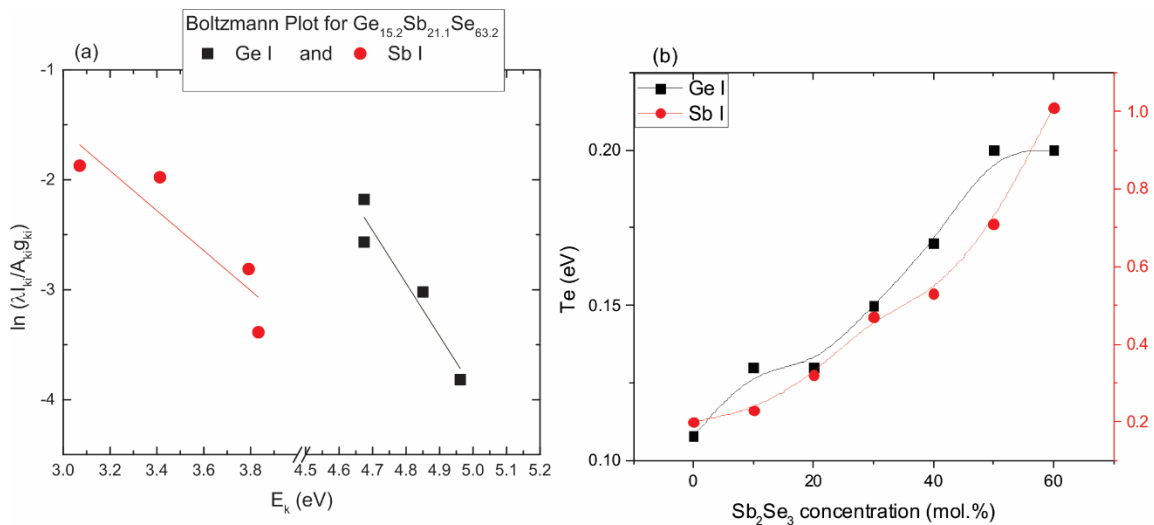
Figure III.62   Boltzmann plot for the emission lines corresponding to Ge I and Sb I (a) and the excitation temperature dependence on the Sb_2Se_3 concentration (b) at 6 mm from the target surface.

Figure III.62b presents the evolution of the average excitation temperature for Ge and Sb atoms with the increase of Sb_2Se_3 concentration. The excitation plasma temperature presented a quasi-linear increase with the Sb_2Se_3 content, varying from 0.1eV to 0.2eV for Ge species and from 0.2 eV to 1 eV for Sb species. We would like to mention that a similar treatment was applied to the Ge ions, where a similar evolution with the Sb_2Se_3 content was evidenced. The main difference observed there was that the excitation temperatures were about one order of magnitude higher than the ones of the atoms. Similar discrepancies were pointed out in the previous sections on single-element metallic targets ablation. The differences in excitation temperatures of different atomic and ionic species raise the question of the existence of a local thermodynamic equilibrium in our plasma. The ejected species seem not to be equilibrated in thermal energy (temperature) by the insufficient collisions subsequent to the initial ejection from the target. There is however a thermodynamic equilibrium in Boltzmann sense for each species, at least on the limited energy ranges considered (3 – 3.8 eV for Sb and 4.6 – 5 eV for Ge).

Based on the results extracted from ICCD fast camera imaging and space- and time-resolved optical emission spectroscopy results, the fast plasma structure is considered to be mainly formed by ionic species while the second one is represented by neutrals. This splitting of the plasma plume was observed for other types of materials [*Harilal et al.*, 2003a; *Focsa et al.*, 2017], as shown in the previous sections, and the formation and expansion of each structure is based on distinct ejection mechanisms. The first structure is due to electrostatic interactions [*Bulgakova et al.*, 2005] as, at very short time scale, the positive charge left on the target surface by electron laser excitation and detachment would accelerate the positive ions outwards the surface. The neutrals found in the second plasma structure are generated through thermal processes that require more time to establish. The low velocity values (< 10 km/s) of the third plasma structure is consistent with the presence of nanoparticles [*Amoruso et al.*, 2002a], clusters or molecules which have a higher mass and thus a lower mobility compared to the species present in the first two plume components.

III.5.4   Discussion

In this section, the main results are related to the important changes in expansion velocity of the plume components as well as in the emission lines intensity and average excitation temperature with the addition of Sb_2Se_3. These results can be considered as effects induced by the structural and electrical/thermal changes in the target. In a previous study on the same Ge-Sb-Se based bulk chalcogenides [*Olivier et al.*, 2015], a reduction of the band gap energy from 2.16 to 1.62 eV was reported together with a monotonous decrease of the glass transition temperature with the increase of the Sb_2Se_3 content from 10% to 60 %. The paper of Afifi et al. [*Afifi et al.*, 1992] shows an increase in electrical and thermal conductivity coefficients, coupled with a decrease in activation energy with the increase in Sb concentration in $Se_{75}Ge_{25-x}Sb_x$ glass systems. They correlate these compositional evolutions with the growth of the density of "weak" bonds in the studied system. The electrical properties of the glasses are given by the presence of weak bonds and their density decrease leads to a higher conductivity of the Sb rich compounds [*Afifi et al.*,

1992]. These results are in good agreement with the ones reported in [*Olivier et al.*, 2014a] on the bulk $(GeSe_2)_{100-x}(Sb_2Se_3)_x$ system. Raman spectroscopy measurements revealed a decrease in peak intensity of Ge-Ge bond vibrations (170 and 270 cm^{-1}) and an increase of 190 cm^{-1} peak contribution corresponding to Sb-Se bond vibration in [SbSe$_{3/2}$] pyramids as Sb_2Se_3 amount increased.

Considering that the first plasma structure is mainly formed by electrostatic interactions, the compositional evolution of conductivity can explain the increase of the velocity of the fast plume component with the antimony concentration. As the conductivity of the samples increases, the formation of a more intense positive charge region on the target surface will occur in the very first moments of the ablation due to higher concentration of electrons ejected through electrostatic mechanisms. The charge separation leads to a strong ambipolar electric field in which the positive charges are accelerated. The latter structures (second and third plasma structures) containing mostly Ge, Sb and Se neutrals, are produced by thermal processes and the velocity evolution can be explained by the decrease in the glass transition temperature (and thus rigidity of the network [*Pietroy et al.*, 2012]) and the increase in "weak" bonds density with increasing the Sb_2Se_3 content. This means that less energy will be used to melt and vaporize the material and consequently more particles with higher thermal and kinetic energy are ejected from the target using the same fluence conditions. The increase in particle velocity will subsequently lead to an increase in collision rate and possibly in excitation processes which can justify the evolution of the excitation temperatures of Ge and Sb found by the Boltzmann plot method.

III.6   Conclusions

Systematic space-and time-resolved optical and electrical investigations were performed on transient plasmas generated by ns, ps, and fs laser ablation of 6 metallic targets: Cu, Mn, Ti, Al, Zn, Ni. The ICCD imaging revealed a plume splitting for all investigated plasmas into two structures with different expansion velocities. The space- and time-resolved OES measurements revealed the presence of atoms and singly- and multiply-charged ions for each of the investigated plasmas. Using the Boltzmann plot method the excitation temperature was estimated for each individual species. The data revealed a space-time decrease of the excitation temperatures. Each species was described by a specific excitation temperature where ions presented a higher temperature than the corresponding atoms. The electrical investigations showed a "classical" behavior of all plasma parameters, namely a decrease in particle density, plasma potential, ion and electron temperature and an increase of the Debye length with the distance from the target and time delay. The drift velocities determined by fitting the LP-TOF signals with a shifted Maxwellian function were correlated with the velocity of the fast plasma structure, while the thermal velocity with the one of the slow structure.

The plasma parameters derived from optical investigations were found to be correlated with the atomic mass and thermal properties of the targets. Although strong correlations were found between the excitation temperature and the heat of vaporization, at this moment it is difficult to derive a unique empirical function that would explain the experimental data.

The plasma parameters extracted from Langmuir probe measurements were linked to the electrical conductivities of the investigated elements. Considering a Coulomb explosion mechanism for particle ejection and a direct relation between the recorded signal and the electron mobility in the target, we proposed for the first time a mathematical correlation between the plasma parameters (plasma potential and electron temperature) and the electrical conductivity of the material. The observed increase for $V_{Plasma}(\sigma)$ was fitted using a logarithmic function, while for the evolution of $T_e(\sigma)$, a derivative of this function was used. Also, increased drift and thermal velocities were observed for the highly conductive targets.

The optical and electrical investigations of Al LPP in PLD conditions showed peculiar behaviors of the global dynamics of the plume and of the individual charged particles. ICCD fast camera imaging evidenced the plume reflection phenomena in the vicinity the substrate. Also, overall kinetic energy of the ejected particles was proven to be strongly affected by the PLD configuration, depending on the target-substrate distance and background pressure. The LP measurement revealed an oscillatory behavior of the plasma ions, result confirmed by OES measurements. By performing space-resolved measurements, the mapping of oscillating frequency was obtained. We found here that in the vicinity of the target the ions are oscillating on two frequencies (with one order of magnitude difference between them) and at longer distances only the "low" frequency is noticeable

ICCD imaging and time- and space-resolved optical emission spectroscopy were used to study the influence of Sb_2Se_3 content on the formation and expansion of plasma formed from $(GeSe_2)_{100-x}(Sb_2Se_3)_x$ chalcogenide glasses, together with the compositional dependence of the excitation temperature. For all glass targets, ICCD images recorded at different delays revealed the presence of three structures with distinct dynamics, which increased their velocities as the Sb_2Se_3 content was augmented. Further results obtained from time-of-flight profiles of the species present in the plume revealed the nature of each plasma structure: the first (fast) plasma structure consists mainly in ionic species, ejected through electrostatic interactions, the second structure, represented by neutral species, is due to thermal mechanisms and the third structure presenting much lower velocities is formed by nanoparticles and clusters generated by collisions between the backscattered and the ejected particles.

The plume characteristics were correlated to the structural and electrical/thermal changes induced by the addition of Sb_2Se_3 in the bulk material. The increased conductivity of antimony-rich samples was associated to the first plasma plume dynamics. The acceleration of the ions found in this plasma structure is considered to be a result of the more intense ambipolar electric field induced by the larger positive region formed by electron ejection. The velocities of the second and third plasma structures and also the excitation temperatures obtained by Boltzmann plots increased as Sb_2Se_3 was added. This behavior was explained by the decrease of the glass transition temperature in Sb-rich samples. As less of the incident energy is used to melt and vaporize the glass, more of it is transferred to kinetic and internal energy of the ejected particles. The higher kinetic energy is confirmed by the increase in velocity while the higher internal energy is correlated with the increase of the plume species excitation temperatures.

References for Chapter III

Afifi, M. A, H. H. Labib, and M. Fadel (1992), Electrical and Thermal Properties of Chalcogenide Glass System $Se_{75}Ge_{25-x}Sb_x$, *Appl. Phys.*, *A55*, 167–169.

Agop, M., P. E. Nica, S. Gurlui, C. Focsa, V. P. Paun, and M. Colotin (2009), Implications of an extended fractal hydrodynamic model, *Eur. Phys. J. D*, *56(3)*, 405–419.

Amoruso, S. (1999), Modeling of UV pulsed-laser ablation of metallic targets, *Appl. Phys. A-Mater.*, *69(3)*, 323–332.

Amoruso, S., M. Armenante, V. Berardi, R. Bruzzese, and N. Spinelli (1997), Absorption and saturation mechanisms in aluminium laser ablated plasmas, *Appl. Phys. A-Mater.*, *65*, 265–271.

Amoruso, S., R. Bruzzese, N. Spinelli, and R. Velotta (1999), Characterization of laser-ablation plasmas, *J. Phys. B At. Mol. Opt.*, *32(3299)*, 131–172.

Amoruso, S., X. Wang, C. Altucci, C. De Lisio, M. Armenante, and R. Bruzzese (2000), Thermal and nonthermal ion emission during high-fluence femtosecond laser ablation of metallic targets, *Appl. Phys. Lett*, *77(23)*, 3728–3730.

Amoruso, S., X. Wang, C. Altucci, C. De Lisio, and M. Armenante (2002a), Double-peak distribution of electron and ion emission during femtosecond laser ablation of metals, *Appl. Surf. Sci.*, *186*, 358–363.

Amoruso, S., R. Bruzzese, N. Spinelli, R. Velotta, X. Wang, and C. Ferdeghini (2002b), Optical emission investigation of laser-produced MgB_2 plume expanding in an Ar buffer gas, *Appl. Phys. Lett.*, *80(23)*, 4315.

Amoruso, S., I. Unitá, S. Fisiche, N. Federico, M. S. Angelo, V. Cintia, I. Napoli, B. Toftmann, and J. Schou (2004), Thermalization of a UV laser ablation plume in a background gas: From a directed to a diffusionlike flow, *Phys. Rev. E*, *69(5)*, 56403.

Amoruso, S., R. Bruzzese, M. Vitiello, N. N. Nedialkov, and P. A. Atanasov (2005a), Experimental and theoretical investigations of femtosecond laser ablation of aluminum in vacuum, *J. Appl. Phys.*, *98(4)*, 44907.

Amoruso, S., G. Ausanio, A. C. Barone, R. Bruzzese, L. Gragnaniello, M. Vitiello, and X. Wang (2005b), Ultrashort laser ablation of solid matter in vacuum: a comparison between the picosecond and femtosecond regimes, *J. Phys. B At. Mol. Opt.*, *38(20)*, L329–L338.

Amoruso, S., G. Ausanio, R. Bruzzese, L. Gragnaniello, L. Lanotte, M. Vitiello, and X. Wang (2006), Characterization of laser ablation of solid targets with near-infrared laser pulses of 100 fs and 1 ps duration, *Appl. Surf. Sci.*, *252(13)*, 4863–4870.

Amoruso, S., J. Schou, and J. G. Lunney (2008), Influence of the atomic mass of the background gas on laser ablation plume propagation, *Appl. Phys. A-Mater.*, *92(4)*, 907–911.

Amoruso, S., J. Schou, J. G. Lunney, and C. Phipps (2010), Ablation Plume Dynamics in a Background Gas, *AIP Conf. Proc.*, *1278*, 665–676.

Anisimov, S. I. (1968), Vaporization of metal absorbing laser radiation, *Soviet Phys. JETP*, *27(1)*, 2–3.

Anisimov, S. I., and B. S. Luk'yanchuk (2002), Selected problems of laser ablation theory, *Physics-Usp.*, *45(3)*, 293–324.

Anisimov, S. I., S. Luk'yanchuk, and A. Luches (1995), Dynamics of the three-dimensional expansion in a vapor produced by a laser pulse, *Soviet Phys. JETP*, *108(2)*, 240–257.

Anoop, K. K., R. Fittipaldi, A. Rubano, X. Wang, D. Paparo, A. Vecchione, L. Marrucci, R. Bruzzese, and S. Amoruso (2014a), Direct femtosecond laser ablation of copper with an optical vortex beam, *J. Appl. Phys.*, *116(11)*, 113102.

Anoop, K. K., A. Rubano, R. Fittipaldi, X. Wang, D. Paparo, A. Vecchione, L. Marrucci, R. Bruzzese, and S. Amoruso (2014b), Femtosecond laser surface structuring of silicon using optical vortex beams generated by a q-plate, *Appl. Phys. Lett.*, *104(24)*, 241604.

Aragón, C., and J. A. Aguilera (2008), Characterization of laser induced plasmas by optical emission spectroscopy: A review of experiments and methods, *Spectrochim. Acta - Part B*, *63(9)*, 893–916.

Barthelemy, O., J. Margot, S. La Ville, F. Vidal, M. Chaker, B. Le Drogoff, T. W. Johnston, and M. Sabsabi (2005), Investigation of the state of local thermodynamic equilibrium of a laser-produced aluminum plasma, *Appl. Spectrosc.*, *59(4)*, 529–536.

Borowitz, J. L., S. Eliezer, Y. Gazit, M. Givon, S. Jackel, A. Ludmirsky, D. Salzmann, E. Yarkoni, A. Zigler, and B. Arad (1987), Temporally resolved target potential measurements in laser-target interactions, *J. Phys. D. Appl. Phys.*, *20(2)*, 210–214.

Bulgakov, A. V., and N. M. Bulgakova (2007), Thermal model of pulsed laser ablation under the conditions of formation and heating of a radiation-absorbing plasma, *Quantum Electron*, *29*, 433–437.

Bulgakova, N. M., and A. V. Bulgakov (1998), Gas-dynamic effects of the interaction between a pulsed laser-ablation plume and the ambient gas : analogy with an underexpanded jet, *J. Phys. D. Appl. Phys.*, *31*, 693–703.

Bulgakova, N. M., R. Stoian, and A. Rosenfeld (1998a), Fast electronic transport and coulomb explosion in materials irradiated with ultrashort laser pulses, in *Laser ablation and its application., Ed. C. Pipps*, pp. 17–36, Springer, Berlin.

Bulgakova, N. M., R. Stoian, A. Rosenfeld, I. V. Hertel, W. Marine, and E. E. B. Campbell (2005), A general continuum approach to describe fast electronic transport in pulsed laser irradiated materials: The problem of Coulomb explosion, *Appl. Phys. A-Mater.*, *81(2)*, 345–356.

Burdt, R. A., Y. Tao, M. S. Tillack, S. Yuspeh, N. M. Shaikh, E. Flaxer, and F. Najmabadi (2010), Laser wavelength effects on the charge state resolved ion energy distributions from laser-produced Sn plasma, *J. Appl. Phys.*, *107(4)*, 43303.

Cabalin, L. M., and J. J. Laserna (1998), Experimental determination of laser induced breakdown thresholds of metals under nanosecond Q-switched laser operation, *Spectrochim. Acta - Part B*, *8547(98)*, 723-730.

Canulescu, S., E. L. Papadopoulou, D. Anglos, T. Lippert, C. W. Schneider, and A. Wokaun (2009), Mechanisms of the laser plume expansion during the ablation of $LiMn_2O_4$, *J. Appl. Phys.*, *105(6)*, 63107.

Chen, J., D. Stender, M. Bator, C. W. Schneider, T. Lippert, and A. Wokaun (2013), Influence of an O2 background gas on the composition and kinetic energies of species in laser induced La0.4Ca0.6MnO3 plasmas, *Appl. Surf. Sci.*, *278*, 317–320.

Chen, J., T. Lippert, A. Ojeda-G-P, D. Stender, C. W. Schneider, and A. Wokaun (2014), Langmuir probe measurements and mass spectrometry of plasma plumes generated by laser ablation of $La_{0.4}Ca_{0.6}MnO_3$, *J. Appl. Phys.*, *116(7)*, 73303.

Chichkov, B. N., C. Momma, S. Nolte, F. Alvensleben, and A. Tünnermann (1996), Femtosecond, picosecond and nanosecond laser ablation of solids, *Appl. Phys. A-Mater.*, *63(2)*, 109–115.

Claeyssens, F., M. N. R. Ashfold, E. Sofoulakis, C. G. Ristoscu, D. Anglos, and C. Fotakis (2002), Plume emissions

accompanying 248 nm laser ablation of graphite in vacuum: Effects of pulse duration, *J. Appl. Phys.*, *91(9)*, 6162–6172.

Cremers, D. A., and L. J. Radziemski (2006), *Handbook of laser-induced breakdown spectroscopy*, John Wiley & Sons, New York.

Delserieys, A. (2008), Optical diagnostics of laser plasmas, Phd thesis, School of Mathematics and Physics The Queen's University of Belfast Northern Ireland.

Dijkkamp, D., T. Venkatesan, X. D. Wu, S. A. Shaheen, N. Jisrawi, Y. H. Min-Lee, W. L. McLean, and M. Croft (1987), Preparation of Y-Ba-Cu oxide superconductor thin films using pulsed laser evaporation from high T_c bulk material, *Appl. Phys. Lett.*, *51(8)*, 619–621.

Dogar, A. H., B. Ilyas, S. Ullah, A. Nadeem, and A. Qayyum (2011), Langmuir probe measurements of Nd-YAG laser-produced copper plasmas, *IEEE Trans. Plasma Sci.*, *39*, 897–900.

Doggett, B., and J. G. Lunney (2011), Expansion dynamics of laser produced plasma, *J. Appl. Phys.*, *109(9)*, 093304.

Donnelly, T., J. G. Lunney, S. Amoruso, R. Bruzzese, X. Wang, and X. Ni (2010a), Dynamics of the plumes produced by ultrafast laser ablation of metals, *J. Appl. Phys.*, *108*(4), 043309.

Donnelly, T., J. G. Lunney, S. Amoruso, R. Bruzzese, X. Wang, and C. Phipps (2010c), Plume dynamics in femtosecond laser ablation of metals, *AIP Conf. Proc., 643*, 643–655.

Doria, D., A. Lorusso, F. Belloni, and V. Nassisi (2004), Characterization of a nonequilibrium XeCl laser-plasma by a movable Faraday cup, *Rev. Sci. Instrum.*, *75(2)*, 387-392.

Eliezer, S., and H. Hora (1989), Surface Waves in Laser-Produced Plasma Double Layers, *IEEE Trans. Plasma Sci. *, *17*, 0–4.

Farid, N., S. S. Harilal, H. Ding, and A. Hassanein (2014), Emission features and expansion dynamics of nanosecond laser ablation plumes at different ambient pressures, *J. Appl. Phys.*, *115(3)*, 033107.

Flanigan, P., and R. Levis (2014), Ambient Femtosecond Laser Vaporization and Nanosecond Laser Desorption Electrospray Ionization Mass Spectrometry, *Annu. Rev. Anal. Chem.*, *7(1)*, 229–256.

Focsa, C., P. Nemec, M. Ziskind, C. Ursu, S. Gurlui, and V. Nazabal (2009), Laser ablation of As_xSe_{100-x} chalcogenide glasses: Plume investigations, *Appl. Surf. Sci.*, *255(10)*, 5307–5311.

Focsa, C., S. Gurlui, P. Nica, M. Agop, and M. Ziskind (2017), Plume splitting and oscillatory behavior in transient plasmas generated by high-fluence laser ablation in vacuum, *Appl. Surf. Sci.*(in press).

Freeman, J. R., S. S. Harilal, P. K. Diwakar, B. Verhoff, and A. Hassanein (2013), Comparison of optical emission from nanosecond and femtosecond laser produced plasma in atmosphere and vacuum conditions, *Spectrochim. Acta Part B*, *87*, 43–50.

Fujimoto, T., and R. W. P. McWhirter (1990), Validity criteria for local thermodynamic equilibrium in plasma spectroscopy, *Phys. Rev. A*, *42(11)*, 6588–6601.

Gacek, S., and X. Wang (2009), Plume splitting in pico-second laser–material interaction under the influence of shock wave, *Phys. Lett. A*, *373(37)*, 3342–3349.

Gamaly, E. G., A. V. Rode, B. Luther-Davies, and V. T. Tikhonchuk, (2002b), Ablation of solids by femtosecond lasers: Ablation mechanism and ablation thresholds for metals and dielectrics, *Phys. Plasmas*, *9(3)*, 949-957.

Geohegan, D. B. (1992), Fast-Iccd Photography and Gated Photon Counting Measurements of Blackbody Emission from Particulates Generated in The KrF-Laser Ablation of BN and YBCO, *Mat. Res. S. P.*, *285*, 27-32.

Geohegan, D. B., and A. a. Puretzky (1996), Laser ablation plume thermalization dynamics in background gases: combined imaging, optical absorption and emission spectroscopy, and ion probe measurements, *Appl. Surf. Sci.*, *96–98*, 131–138.

Gill, C. G., T. M. Allen, J. E. Anderson, T. N. Taylor, P. B. Kelly, and N. S. Nogar (1996), Low-power resonant laser ablation of copper., *Appl. Opt.*, *35(12)*, 2069–2082.

Glavin, N. R., C. Muratore, M. L. Jespersen, J. Hu, T. S. Fisher, and A. A. Voevodin (2015), Temporally and spatially resolved plasma spectroscopy in pulsed laser deposition of ultra-thin boron nitride films, *J. Appl. Phys.*, *117(16)*, 165305.

González-Posada, A. O. (2016), Physical processes in pulsed laser deposition, Phd Thesis, ETH Zurich.

Gurlui, S., and C. Focsa (2011), Laser Ablation Transient Plasma Structures Expansion in Vacuum, *IEEE Trans. Plasma Sci.*, *39(11)*, 2820–2821.

Gurlui, S., M. Agop, P. Nica, M. Ziskind, and C. Focsa (2008), Experimental and theoretical investigations of a laser-produced aluminum plasma, *Phys. Rev. E*, *78(2)*, 26405.

Gurlui, S., M. Sanduloviciu, C. Mihesan, M. Ziskind, and C. Focsa (2009), Periodic Phenomena In Laser-Ablation Plasma Plumes : A Self-Organization Scenario, *AIP Conf. Proc.*, *821(1)*, 279–282.

Harilal, S. S., R. C. Issac, C. V. Bindhu, V. P. N. Nampoori, and C. P. G. Vallabhan (1997), Emission characteristics and dynamics of C2 from laser produced graphite plasma, *J. Appl. Phys.*, *81(1)*, 3637–3643.

Harilal, S. S., C. V. Bindhu, V. P. N. Nampoori, and C. P. G. Vallabhan (1998), Influence of ambient gas on the temperature and density of laser produced carbon plasma, *Appl. Phys. Lett.*, *72(2)*, 167–169.

Harilal, S. S., C. V. Bindhu, M. S. Tillack, F. Najmabadi, and A. C. Gaeris (2003a), Internal structure and expansion dynamics of laser ablation plumes into ambient gases, *J. Appl. Phys.*, *93(5)*, 2380–2388.

Harilal, S. S., N. Farid, J. R. Freeman, P. K. Diwakar, N. L. LaHaye, and A. Hassanein (2014a), Background gas collisional effects on expanding fs and ns laser ablation plumes, *Appl. Phys. A*, *117(1)*, 319–326.

Harilal, S. S., J. R. Freeman, P. K. Diwakar, and A. Hassanein (2014b), Femtosecond Laser Ablation: Fundamentals and Applications, in *Laser-Induced Breakdown Spectroscopy Theory and Applications*, Eds. S. Musazzi and U. Perini, 143–166, Springer, Berlin.

Hendron, J. M., C. M. O. Mahony, T. Morrow, and W. G. Graham (1997), Langmuir probe measurements of plasma parameters in the late stages of a laser ablated plume, *J. Appl. Phys.*, *81(5)*, 2131-2134.

Hermann, J., S. Noël, T. E. Itina, E. Axente, and M. E. Povarnitsyn (2008), Correlation between ablation efficiency and nanoparticle generation during the short-pulse laser ablation of metals, *Laser Phys.*, *18(4)*, 374–379.

Irimiciuc, S. A., M. Agop, P. Nica, S. Gurlui, D. Mihaileanu, S. Toma, and C. Focsa (2014a), Dispersive effects in laser ablation plasmas, *J. Appl. Phys.*, *53*, 116202.

Irimiciuc, S. A., I. Mihaila, and M. Agop, (2014b), Experimental and theoretical aspects of a laser produced plasma, *Phys. Plasmas*, *21(9)*, 93509.

Irimiciuc, S., R. Boidin, G. Bulai, S. Gurlui, P. Nemec, V. Nazabal, and C. Focsa (2017a), Laser ablation of $(GeSe_2)_{100-x}(Sb_2Se_3)_x$ chalcogenide glasses: Influence of the target composition on the plasma plume dynamics, *Appl. Surf.*

Sci., *419*, 594-600.

Irimiciuc, S. A., S. Gurlui, G. Bulai, P. Nica, M. Agop, and C. Focsa (2017b), Langmuir probe investigation of transient plasmas generated by femtosecond laser ablation of several metals: Influence of the target physical properties on the plume dynamics, *Appl. Surf. Sci.*, *417*, 108–118.

Irimiciuc, S. A., S. Gurlui, P. Nica, C. Focsa, and M. Agop (2017c), A compact non-differential approach for modeling laser ablation plasma dynamics, *J. Appl. Phys.*, *121(8)*, 083301.

Johnson, P., and R. Christy (1974), Optical constants of transition metals: Ti, V, Cr, Mn, Fe, Co, Ni, and Pd, *Phys. Rev. B*, *9(12)*, 5056–5070.

Kelly, R., and R. W. Dreyfus (1988), On the effect of Knudsen-layer formation on studies of vaporization, sputtering, and desorption, *Surf. Sci.*, *198(1–2)*, 263–276.

Kelly, R., and A. Miotello (1996), Comments on explosive mechanisms of laser sputtering, *Appl. Surf. Sci.*, *96–98*, 205–215.

Kelly, R., and A. Miotello (1998), On the role of thermal processes in sputtering and composition changes due to ions or laser pulses, *Nucl. Instrum. Meth. B*, *141(1–4)*, 49–60.

Kononenko, T., S. Garnov, S. Klimentov, V. Konov, E. Loubnin, F. Dausinger, A. Raiber, and C. Taut (1997), Laser ablation of metals and ceramics in picosecond–nanosecond pulsewidth in the presence of different ambient atmospheres, *Appl. Surf. Sci.*, *109–110*, 48–51.

Kramida, A., Y. Ralchenko, J. Reader, and NIST ASD Team (2014), NIST Atomic Spectra Database Lines Form, *NIST At. Spectra Database (ver. 5.2) [Online]*, Available at: http://physics.nist.gov/asd

Kumar, A., R. K. Singh, J. Thomas, and S. Sunil (2009), Parametric study of expanding plasma plume formed by laser-blow-off of thin film using triple Langmuir probe, *J. Appl. Phys.*, *106(4)*, 043306.

Leitz, K. H., B. Redlingsher, Y. Reg, A. Otto, and M. Schmidt (2011), Metal ablation with short and ultrashort laser pulses, *Phys. Proc. 12(2)*, 230–238.

Lieberman, M. A. (1989), Model of plasma immersion ion implantation, *J. Appl. Phys.*, *66(7)*, 2926-2929.

Lin, X., H. Chen, S. Jiang, and C. Zhang (2012), A Coulomb explosion theoretical model of femtosecond laser ablation materials, *Sci. China Technol. Sci.*, *55(3)*, 694–701.

Mazhukin, V. I., V. V. Nossov, M. G. Nickiforov, and I. Smurov (2003), Optical breakdown in aluminum vapor induced by ultraviolet laser radiation, *J. Appl. Phys.*, *93(1)*, 56-66.

Mihaila, I., C. Ursu, A. Gegiuc, and G. Popa (2010), Diagnostics of plasma plume produced by laser ablation using ICCD imaging and transient electrical probe technique, *J. Phys. Conf. Ser.*, *207*, 12005.

Miller, C. J. (1994), *Laser Ablation*, Springer Heidelberg.

Miotello, A., and R. Kelly (1995), Critical assessment of thermal models for laser sputtering at high fluences, *Appl. Phys. Lett.*, *67*, 3535.

Miotello, A., and P. M. Ossi (2010), *Laser-surface interactions for new materials production : tailoring structure and properties*, Springer, Berlin.

Molian, P., B. Pecholt, and S. Gupta (2009), Picosecond pulsed laser ablation and micromachining of 4H-SiC wafers, *Appl. Surf. Sci.*, *255(8)*, 4515–4520.

Němec, P., M. Olivier, E. Baudet, A. Kalendová, P. Benda, and V. Nazabal (2014), Optical properties of (GeSe2)100-x(Sb 2Se3)x glasses in near- and middle-infrared spectral regions, *Mater. Res. Bull.*, *51*, 176–179.

Nica, P., P. Vizureanu, M. Agop, S. Gurlui, C. Focsa, N. Forna, P. D. Ioannou, and Z. Borsos (2009), Experimental and theoretical aspects of aluminum expanding laser plasma, *Jpn. J. Appl. Phys.*, *48*, 1–7.

Nica, P., M. Agop, S. Gurlui, and C. Focsa (2010a), Oscillatory Langmuir probe ion current in laser-produced plasma expansion, *EPL - Europhysics Lett.*, *89(6)*, 65001.

Nica, P., M. Agop, S. Gurlui, C. Bejinariu, and C. Focsa (2012), Characterization of Aluminum Laser Produced Plasma by Target Current Measurements, *Jpn. J. Appl. Phys.*, *51(10R)*, 106102.

Niculescu, O., D. G. Dimitriu, V. P. Paun, P. D. Matasaru, D. Scurtu, and M. Agop (2010), Experimental and theoretical investigations of a plasma fireball dynamics, *Phys. Plasmas*, *17(4)*, 42305.

Noll, R. (2012), Laser-Induced Breakdown Spectroscopy: Fundamentals and Applications, Springer-Verlag Berlin.

Ojeda-G-P, A., C. W. Schneider, M. Döbeli, T. Lippert, and A. Wokaun (2017), Plasma plume dynamics, rebound, and recoating of the ablation target in pulsed laser deposition, *J. Appl. Phys.*, *121(13)*, 135306.

Olivier, M., J.C. Tchahame, P. Nemec, M. Chauvet, V. Besse, C. Cassagne, G. Boudebs, G. Renversez, R. Boidin, E. Baudet, and V. Nazabal (2014b), Structure, nonlinear properties, and photosensitivity of $(GeSe_2)_{100-x}(Sb_2Se_3)_x$ glasses, *Opt. Mater. Express*, *4(3)*, 525–540.

Olivier, M., P. Němec, G. Boudebs, R. Boidin, C. Focsa, and V. Nazabal (2015), Photosensitivity of pulsed laser deposited Ge-Sb-Se thin films, *Opt. Mater. Express*, *5(4)*, 781-793.

Perdrix, M., C. E. A. Saclay, D. P. E. S. Lsla, and G. Yvette (2001), Femtosecond, Picosecond and Nanosecond Laser Microablation: Laser Plasma and Crater Investigation, *Laser Part. Beams*, *4424(1),* 574–579.

Pietroy, D., Y. Di Maio, B. Moine, E. Baubeau, and E. Audouard (2012), Femtosecond laser volume ablation rate and threshold measurements by differential weighing., *Opt. Express*, *20(28)*, 29900–8.

Pompilian, O. G. (2013), Pulsed Laser Deposition and Characterization of Chalcogenide Thin Films, PhD. Thesis, Université Lille 1 – Sciences Et Technologies.

Pompilian, O. G., S. Gurlui, P. Nemec, V. Nazabal, M. Ziskind, and C. Focsa (2013), Plasma diagnostics in pulsed laser deposition of GaLaS chalcogenides, *Appl. Surf. Sci.*, *278*, 352–356.

Pompilian, O. G., G. Dascalu, I. Mihaila, S. Gurlui, M. Olivier, P. Nemec, V. Nazabal, N. Cimpoesu, and C. Focsa (2014), Pulsed laser deposition of rare-earth-doped gallium lanthanum sulphide chalcogenide glass thin films, *Appl. Phys. A-Mater.*, *117(1)*, 197–205.

Popa, G., and L. Sirghi (2000), *Bazele fizicii plasmei*, Ed. Universităţii , Iasi.

Puretzky, A. A., D. B. Geohegan, R. E. Haufler, R. L. Hettich, X. Y. Zheng, and R. N. Compton (1993), Laser ablation of graphite in different buffer gases, *AIP Conf. Proc.*, *288,* 366-374.

Ralchenko, Y. (2005), NIST atomic spectra database, *Mem. S. A. It. Suppl.*, *8*, 96–102.

Salle, B., C. Chaleard, V. Detalle, J.-L. Lacour, P. Mauchien, C. Nouvellon, and A. Semerok (1999), Laser ablation efficiency of metal samples with UV laser nanosecond pulses, *Appl. Surf. Sci.*, *138–139*, 302–305.

Sausa, R. C. (2017), Time-resolved imaging and optical spectroscopy of plasma plumes during pulsed laser material deposition, *Appl. Opt.*, *56(3)*, B123-B133.

Schmidt, V., W. Husinsky, and G. Betz (2000), Dynamics of laser desorption and ablation of metals at the threshold on the femtosecond time scale, *Phys. Rev. Lett.*, *85(16)*, 3516–3519.

Schou, J. (2009), Physical aspects of the pulsed laser deposition technique: The stoichiometric transfer of material from target to film, *Appl. Surf. Sci.*, *255(10)*, 5191–5198.

Schou, J., B. Toftmann, and S. Amoruso (2005), Pulsed laser deposition: from basic processes to film deposition, Proc. SPIE, *5830*, 1–10.

Singh, S. C., C. Fallon, P. Hayden, M. Mujawar, P. Yeates, and J. T. Costello (2014), Ion flux enhancements and oscillations in spatially confined laser produced aluminum plasmas, *Phys. Plasmas*, *21(9)*, 93113.

Sunil, S., A. Kumar, R. K. Singh, and K. P. Subramanian (2008), Measurements of electron temperature and density of multi-component plasma plume formed by laser-blow-off of LiF-C film, *J. Phys. D. Appl. Phys.*, *41(8)*, 85211.

Thestrup, B., B. Toftmann, J. Schou, B. Doggett, and J. G. Lunney (2002), Ion dynamics in laser ablation plumes from selected metals at 355 nm, *Appl. Surf. Sci.*, *197–198*, 175–180.

Toftmann, B., B. Doggett, C. Budtz-Jørgensen, J. Schou, and J. G. Lunney (2013), Femtosecond ultraviolet laser ablation of silver and comparison with nanosecond ablation, *J. Appl. Phys.*, *113(8)*, 083304.

Tsakiris, N., K. K. Anoop, G. Ausanio, M. Gill-Comeau, R. Bruzzese, S. Amoruso, and L. J. Lewis (2014), Ultrashort laser ablation of bulk copper targets: Dynamics and size distribution of the generated nanoparticles, *J. Appl. Phys.*, *115(24)*, 243301.

Ursu, C. (2010), Caracterisation par methodes optiques et electriques du plasma produit par ablation laser, PhD. Thesis, Université Lille 1 – Sciences Et Technologies.

Ursu, C., and P. Nica (2013), Diagnosis of carbon laser produced plasma by using an electrostatic energy analyzer, *J. Optoelectron. Adv. Mater., 15(1)*, 42–45.

Ursu, C., S. Gurlui, C. Focsa, and G. Popa (2009), Space- and time-resolved optical diagnosis for the study of laser ablation plasma dynamics, *Nucl. Instrum. Meth. B*, *267(2)*, 446–450.

Verhoff, B., S. S. Harilal, J. R. Freeman, P. K. Diwakar, and A. Hassanein (2012), Dynamics of femto- and nanosecond laser ablation plumes investigated using optical emission spectroscopy, *J. Appl. Phys.*, *112(9)*, 093303.

Vitiello, M., S. Amoruso, C. Altucci, C. de Lisio, and X. Wang (2005), The emission of atoms and nanoparticles during femtosecond laser ablation of gold, *Appl. Surf. Sci.*, *248(1–4)*, 163–166.

Weaver, I., G. W. Martin, W. G. Graham, T. Morrow, and C. L. S. Lewis (1999), The Langmuir probe as a diagnostic of the electron component within low temperature laser ablated plasma plumes, *Rev. Sci. Instrum.*, *70(3)*,1801-1805.

Wen, S.-B., X. Mao, R. Greif, and R. E. Russo (2007), Laser ablation induced vapor plume expansion into a background gas. II. Experimental analysis, *J. Appl. Phys.*, *101(2)*, 23115.

Yang, C., Y. Tian, L. Cui, and D. Zhang (2015), Laser-induced changes in titanium by femtosecond, picosecond and millisecond laser ablation, *Radiat. Eff. Defect. S.*, *170(6)*, 528–540.

Yao, Y. L., H. Chen, and W. Zhang (2005), Time scale effects in laser material removal: a review, *Int. J. Adv. Manuf. Technol.*, *26(5)*, 598–608.

Zavestovskaya, I. N., O. A. Glazov, and N. N. Demchenko (2008), Threshold Characteristics of Ultrashort Laser Pulse

Ablation of Metals., *Proc. 3rd Int. Conf. Front. Plasma Phys. Technol., 3*, 10–18.

Zorba, V., N. Boukos, I. Zergioti, and C. Fotakis (2008), Ultraviolet femtosecond, picosecond and nanosecond laser microstructuring of silicon: structural and optical properties, *Appl. Opt.*, *47(11)*, 1846-1850.

Chapter IV Theoretical studies of laser–produced plasmas

IV.1   The general basis of a non-differential theoretical model

The overall advancement of the laser ablation topic involved intensive theoretical and experimental studies with the aim to obtain more insight about all physical phenomena involved in this process. Historically, the development of the theoretical models was consistent with the laser-based technology improvements. As a result, the majority of the first theoretical attempts was focused on explaining the main physical processes such as heating, melting and vaporization of the target. Several groups have reported detailed analysis regarding the laser – solid interaction in the nanosecond regime [*Wood et al.,* 1981; *Singh et al.*, 1989; *Peterlongo et al.*, 1994; *Boardman et al.*, 1996; *Amoruso et al.*, 1999]. Early theoretical models [*Singh et al.*, 1978] were focused on the prediction of the amount of material ablated per pulse using a simple energy balance equation. Another theoretical model developed by Dabby et al. [*Dabby et al.*, 1972] used a 1-D heat conduction equation and focused on the evaporation of the top surface and the estimation of the ablation rate. Other thermal models were developed by Conde et al. [*Conde et al.*, 2004] and Jeong et al. [*Jeong et al.*, 1998]. The first approach was built for laser ablation of Si and used to study the morphological changes (i.e. surface roughening) that take place on the surface due to laser irradiation. The latter model is based on a one-dimensional thermal approach for laser ablation of Al and was used to simulate the dynamics of the vapor flow and the effects of target surface reflectivity on the laser fluence threshold during the ablation process. For shorter laser pulses the non-equilibrium between the electrons and phonons [*Rethfeld et al.*, 2002] is better described by the two – temperature model [*Anisimov et al.*, 1974]. This model assumes that electrons and phonons distributions can be characterized by the electron temperature and lattice temperature, while the energy transport is described by a one-dimensional diffusion model.

The overall laser ablation process is very complex and many aspects remain still to be fully explained since it contains, besides laser-solid interactions, the process of plasma formation and expansion and the laser-plasma interaction. Thus, more and more complex theoretical models were developed in order to consider the formation and expansion of the plasma plume and the laser-plasma interaction. The aim of all this advancements was to estimate the spatial-temporal distribution of the plasma parameters such as electron temperature, particle density and pressure. The theoretical model developed by Wu and Shin [*Wu and Shin*, 2006] was used to study the dynamics of the evaporation, the plasma formation and the laser-plasma interaction. Another approach used by Bulgakova et al. [*Bulgakova et al.*, 2005] took into account laser absorption processes by the plasma volume during ablation of a solid graphite target. Other theoretical models were based on the plasma shielding effects. Vasantgadkar et al. [*Vasantgadkar et al.*, 2010] used a finite element approach to predict the target temperature and the ablation depth, while Fang et al. [*Fang et al.*, 2008] developed a thermal model for iron targets that takes into account the vaporization and plasma shielding effects. Bogaerts et al. [*Bogaerts et al.*, 2003] developed a time-dependent model of plasma shielding and expansion. Amongst the models describing the dynamics

of the expanding ablation plasma plume, Monte Carlo simulations and hydrodynamic equations approaches have been commonly used.

In the analysis of the laser ablation process with very intense nanosecond or shorter laser pulses, it is useful to consider the adiabatic approximation [*Anisimov et al.*, 1995]. In the framework of the adiabatic model the laser-ablation process can be divided into three main stages: the evaporation of the target, the plasma formation and the expansion of the ablated plume in vacuum. The adiabatic approximation assumes that the entire laser energy converts fully into internal energy of the target and is subsequently transferred to the plasma plume. The laser energy can be further absorbed by the ejected cloud and partially transformed into kinetic energy of the ablation plume.

Therefore, when performing theoretical simulations, one must choose an adequate model as all the existent ones are dedicated for a particular range of "a priori" conditions (pulse width, laser fluence, material properties, etc.). In order to simplify the approach, it would be desirable to find a generalized approach that will allow us, in the framework of the same model, to go through different perspectives of the same physical object (from a global view to a localized one).

An unified approach can be attempted by using the scale relativity theory (SRT) [*Nottale*, 1993, 2010]. The SRT is built by adding to the physical laws of the traditional theoretical models new ones relating to the scale resolution. The space-time coordinates used here are intrinsic variables which, during the scale transformation, will have a similar role as the one played by the velocities in the case of motion transformation [*Nottale*, 1993, 2010]. Such a model is founded on the fractal space-time concept [*El Naschie*, 1995; *Weibel*, 2005] and on a generalization of Einstein's principle of relativity to scale transformations. Here, the space-time resolution describes the state of scale for the reference system reflecting the way the particle velocity characterizes the state of motion. Thus, by building such a framework, the models now require that the laws of physics can be applied for any frame, for any type of motion (known as principle of motion relativity) and for any scales (scale relativity principle). Mathematically, the principle of SRT can be achieved through the principle of scale-covariance, requiring that the equations are to be kept in their simplest form under transformations of resolution.

Under these assumptions, a new model can be developed. Let us consider the case of a complex fluid with "components" named "structural units" [*Badii et al.*, 1999; *Hou et al.*, 2009; *Mitchell et al.*, 2009; *Gatski et al.*, 2012], which manifests a chaotic behavior and which can reach self-similarities in association with strong fluctuations at all possible time-scales. This means that the dynamics of the complex fluid will be induced or affected by the fluctuations at even the smallest scales [*Hou et al*., 2009; *Mitchell et al,* 2009]. For temporal scales, which are large with respect to the inverse of the highest Lyapunov exponent [*Mandelbrot*, 1982; *Cristescu*, 2008], the deterministic trajectories can be further replaced by a collection of potential trajectories and the concept of definite positions can be replaced by that of probability density. The evolution of the

newly defined complex fluid cannot be foreseen simply by investigating the behavior of individual elements (i.e. in the case of a plasma these elements can be ions, electrons and/or atoms) or by superposing their behavior. Instead, it is determined by the manner in which individual elements can influence the global behavior of the system. In such conjecture, assuming that the complexity of the interaction processes is substituted by non-differentiability, it becomes no longer necessary to use the complete classical "arsenal" of quantities from the differentiable physical models (as mean free path, cross section, collision integral etc.). In the framework of the approach presented above (SRT) we assume that the fluid particles dynamics takes place on continuous, but non-differentiable curves (fractal curves). This means that the movement of the particles is reduced to a straight line between collisions and the functions, describing the dynamics, become non-differential in the collision points. Thus, all the physical phenomena involved in the dynamics are now dependent not only on the space-time coordinates, but also on the space-time scale resolution. From such a perspective, the physical quantities that describe the dynamics of complex fluids may be considered fractal functions [*Federer et al.*, 1990; *Gouyet et al.*, 1992; *Nottale*, 1993, 2010; *Stauffer et al.*, 2017]. Taking the generalization a step forward, the complex fluid structural units may be reduced *to* and identified *with* their own trajectories (geodesics), so that the complex fluid will behave as a special "fluid" lacking interactions by means of its geodesics in a non-differentiable (fractal) space which we will refer as a fractal fluid.

In this chapter, we will investigate from a non-differential approach (called Non-Standard Scale Resolution Theory (NSRT [*Merches and Agop*, 2015]), i.e. a SRT model in an arbitrary constant fractal dimension) the dynamics of a complex fluid with applicability in the study of laser-produced plasma dynamics.

IV.2 Implications of non-differentiability in the complex fluid dynamics

Assuming that the motions of the particles take place on continuous but non-differentiable curves (fractal curves), we can express some consequences on the fluid dynamics due to the fractality [*Nottale,* 1993, 2010]:

- The space in which we analyze the dynamics of the complex fluid is fractal. From a mathematical perspective, a curve can be non-differentiable if its length becomes infinite as the scale resolution tends to zero (Lebesque Theorem [*Mandelbrot*, 1982]). At this point, the curve becomes fractal, which means that it exhibits the property of self-similarity in every point. This could be further expanded towards the property of holography, by which we express that every part will reflect the whole system [*Federer et al.,* 1990; *Gouyet et al.*, 1992; *Mandelbrot,* 1982; *Stauffer et al.,* 2017]. Particularly in the case of a complex fluid, any continuous but non-differentiable curve attributed to each particle (complex fluid fractal curve) is explicitly a scale resolution δt dependent (i.e. the length of the curve asymptotically tends to infinity when δt decreases to zero);

- The physical laws defining our complex fluid and the related phenomena are linked to the actions of a set of functions during the zoom in/out operations of the resolution scale δt. Then, by applying the substitution principle, δt will become dt ($\delta t \equiv dt$) and, consequently, it will be considered an independent variable. We would like to note that we will keep the notation dt for the regular time as in the standard differential physical systems. Under this conditions, the "real" time associated to the complex fluid dynamics cannot not be a fractal, thus the time becomes also an affine parameter of the movement curves;

- The evolution of the complex fluid is defined through fractal variables, i.e., functions depending on the space-time variables and the resolution scale. In any point across the fractal curve, two derivatives of the variable field $Q(t, dt)$ can be defined as it follows:

$$\begin{aligned}\frac{d_+ Q(t,dt)}{dt} &= \lim_{\Delta t \to 0_+} \frac{Q(t+\Delta t, \Delta t) - Q(t, \Delta t)}{\Delta t} \\ \frac{d_- Q(t,dt)}{dt} &= \lim_{\Delta t \to 0_-} \frac{Q(t, \Delta t) - Q(t-\Delta t, \Delta t)}{\Delta t}\end{aligned} \quad , \qquad \text{Eq. (IV.1)}$$

The "+" sign corresponds to the complex fluid forward processes, while the "–" sign corresponds to the backwards ones.

- The variation on the spatial coordinate field $dX^i(t, dt)$ will be the basis on which we can describe the complex fluid dynamics and will be expressed according to the previous equations as the sum of the two contributions. One of them describing the independence on the scale resolution (differential part $d_\pm x^i(t)$), and the other one the scale resolution dependence (fractal part $d_\pm \xi^i(t)$):

$$d_\pm X^i\left(t,dt\right) = d_\pm x^i\left(t\right) + d_\pm \xi^i\left(t,dt\right). \qquad \text{Eq. (IV.2)}$$

- The fractal contribution of the spatial coordinate field, used for the treatment of the fluid complex dynamics, satisfies the following equation (named fractal equation) [*Mandelbrot*, 1982; *Nottale*, 1993, 2010]:

$$d_\pm \xi^i(t,dt) = \lambda_\pm^i (dt)^{1/D_F} , \qquad \text{Eq. (IV.3)}$$

where $\lambda_\pm^i$ are constant coefficients describing the fractalization type characteristic of our fluid and D_F defines the fractal dimension of the complex fluid non-differentiable curve.

The fractal dimension is not uniquely defined for one system. For instance, in the case of a complex fluid, the processes could generate geodesics with different fractal dimensions. The variation in the geodesics fractal dimensions presents itself as a consequence of the complex fluid structure:

i) $D_F = 2$ is characteristic to fluids where quantum type processes are generated;

ii) $D_F < 2$ describes fluids where are induced correlative type processes;

iii) $D_F > 2$ defines fluids where non-correlative processes can be found (an exhaustive discussion about the role of the fractal dimension is presented in [*Mandelbrot*, 1982; *Nottale*, 1993, 2010]).

- The standard time-reflection invariances for all variables are regained by combining the two derivatives d_+/dt and d_-/dt in the newly defined non-differentiable operator:

$$\frac{\hat{d}}{dt} = \frac{1}{2}\left(\frac{d_+ + d_-}{dt}\right) - \frac{i}{2}\left(\frac{d_+ - d_-}{dt}\right).$$

Eq. (IV.4)

This comes as an expected result from the complex prolongation procedure [*Merches and Agop*, 2015] applied to our physical system (complex fluid). Further, in order to obtain the complex fluid velocity fields, we apply the non-differentiable operator to the spatial coordinate field.

$$\hat{V}^i = \frac{\hat{d}X^i}{dt} = V_D^i - V_F^i,$$

Eq. (IV.5)

where

$$V_D^i = \frac{1}{2}\left(v_+^i + v_-^i\right), \quad V_F^i = \frac{1}{2}\left(v_+^i - v_-^i\right)$$

$$v_+^i = \frac{d_+ x^i + d_+ \xi^i}{dt}, \quad v_-^i = \frac{d_- x^i + d_- \xi^i}{dt}.$$

Eq. (IV.6)

In *Eq. (IV.6)*, V_D^i represents the real part of the velocity field, which is differentiable and scale resolution independent (also referred to as differentiable velocity field), while V_F^i represents the imaginary part of the velocity (non-differentiable and scale resolution dependent - fractal velocity field).

- Between a pair of points, in the absence of any external fields (constrains), there are an infinity of geodesics describing the transition from one point to another. This is a general characteristic for every scale that can be found in our system. That being said, in the fractal space defining the fluid, all particles are then substituted and identified with their own geodesics, in such a way that the presence of an external constraint is interpreted as a selection of the specific geodesics. All these properties: the infinity of the geodesics, their fractality and the two values of the derivative in the "collision" points, could imply a generalized fluid-like statistical description of our system. As a result, for a fractal fluid, all the average values are taken in the previously mentioned sense, thus the average of $d_\pm X^i$ becomes:

$$\left\langle d_\pm X^i \right\rangle \equiv d_\pm x^i, \qquad\qquad \text{Eq. (IV.7)}$$

with

$$\left\langle d_\pm \xi^i \right\rangle = 0. \qquad\qquad \text{Eq. (IV.8)}$$

The *Eq.* (*IV.8*) defines a fluid where the averages of the fractal fluctuations are null.

The evolution of the fractal fluid can be described through a covariant derivative. Let us further consider that the fractal fluid is "immersed" in a 3-D space, where the X^i are the spatial coordinates of the points present on the fractal curves. We also consider a variable field Q and the following Taylor expansion up to the second order

$$d_\pm Q\left(X^i, t\right) = \partial_t Q dt + \partial_i Q d_\pm X^i + \frac{1}{2}\partial_l \partial_k Q d_\pm X^l d_\pm X^k. \qquad \text{Eq. (IV.9)}$$

These relations are respected in every point described by the coordinates X^i, which can be selected through *Eq.* (*IV.9*). We can now define forward and backward average values for all fractal fluid variables from *Eq.* (*IV.9*) as:

$$\left\langle d_\pm Q \right\rangle = \left\langle \partial_t Q dt \right\rangle + \left\langle \partial_i Q d_\pm X^i \right\rangle + \frac{1}{2}\left\langle \partial_l \partial_k Q d_\pm X^l d_\pm X^k \right\rangle. \qquad \text{Eq. (IV.10)}$$

Let us further assume that the average values of the fractal field Q and its derivatives coincide with themselves, while the differentials $d_\pm X^i$ and dt are independent. As a result, the average of their products is identical with the product of their averages. Accordingly, (*Eq.IV.10*) becomes

$$d_\pm Q = \partial_t Q dt + \partial_i Q \left\langle d_\pm X^i \right\rangle + \frac{1}{2}\partial_l \partial_k Q \left\langle d_\pm X^l d_\pm X^k \right\rangle. \qquad \text{Eq. (IV.11)}$$

Even if the average value of $d_\pm \xi^i$ is null, for the higher order of $d_\pm \xi^i$ the situation can still be different. Let us further focus on the averages $\left\langle d_\pm \xi^l d_\pm \xi^k \right\rangle$. Using *Eq.* (*IV.3*) we can write

$$\left\langle d_\pm \xi^l d_\pm \xi^k \right\rangle = \pm \lambda_\pm^l \lambda_\pm^k \left(dt\right)^{(2/D_F)-1} dt, \qquad \text{Eq. (IV.12)}$$

with the mention that the "+" sign corresponds to $dt > 0$ while the "–" sign corresponds to $dt < 0$. In these conditions *Eq. (IV.11)* takes the following form:

$$d_\pm Q = \partial_t Q dt + \partial_i Q \left\langle d_\pm X^i \right\rangle + \frac{1}{2}\partial_l \partial_k Q d_\pm x^l d_\pm x^k \pm \frac{1}{2}\partial_l \partial_k Q \left[\lambda_\pm^l \lambda_\pm^k \left(dt\right)^{(2/D_F)-1} dt \right]. \text{ Eq. (IV.13)}$$

By neglecting the term containing the differentiable factor (a detailed description of the method used is presented in *[Merches and Agop*, 2015; *Nottale*, 1993, 2010] and dividing by dt we get:

$$\frac{d_\pm Q}{dt} = \partial_t Q + v_\pm^i \partial_i Q \pm \frac{1}{2}\lambda_\pm^l \lambda_\pm^k \left(dt\right)^{(2/D_F)-1}\partial_l \partial_k Q. \qquad \text{Eq. (IV.14)}$$

We can now define the following operator:

$$\frac{d_\pm}{dt} = \partial_t + v_\pm^i \partial_i \pm \frac{1}{2}\lambda_\pm^l \lambda_\pm^k \left(dt\right)^{(2/D_F)-1}\partial_l \partial_k. \qquad \text{Eq. (IV.15)}$$

In these conditions, considering *Eq. (IV.4)*, *Eq. (IV.5)* and *Eq. (IV.15)*, we can further determine $\hat{d}/dt$:

$$\frac{\hat{d}Q}{dt} = \partial_t Q + \hat{V}^i \partial_i Q + \frac{1}{4}\left(dt\right)^{(2/D_F)-1} D^{lk} \partial_l \partial_k Q \,, \qquad \text{Eq. (IV.16)}$$

where

$$D^{lk} = d^{lk} - i\overline{d}^{lk}$$
$$d^{lk} = \lambda_+^l \lambda_+^k - \lambda_-^l \lambda_-^k \,, \quad \overline{d}^{lk} = \lambda_+^l \lambda_+^k + \lambda_-^l \lambda_-^k \qquad \text{Eq. (IV.17)}$$

The *Eq. (IV.16)* also allows us to define the scale covariant derivative in the fractal fluid dynamics

$$\frac{\hat{d}}{dt} = \partial_t + \hat{V}^i \partial_i + \frac{1}{4}\left(dt\right)^{(2/D_F)-1} D^{lk} \partial_l \partial_k \,. \qquad \text{Eq. (IV.18)}$$

IV.3   Plasma dynamics though the fractal fluid approach

Once defined the base of equations for our model, the next natural step will be to apply it for the analysis of various physical systems. In our particular case, we want to analyze the dynamics of laser-produced plasmas. But, before we apply the mathematical approach presented above, certain questions arise: is this model suitable for laser-produced plasmas? What are the new features of the model with respect to other established theoretical approaches? Given the generality of the non-differential approach, is this dedicated only for LPP or it can be extended to other types of plasmas?

The particularities of laser ablation plasma formation and expansion have been presented in *Chapter I* and *Chapter III*, where we concluded that the laser-matter interaction is a multiscale problem. The evolution of the plume can be divided into two important stages: the initial stage is one dimensional and the second one consists in a three-dimensional expansion. The difference is not only geometrical but also in the physics involved. The initial one-dimensional stage covers the absorption of the laser light and the initial material expansion. At this point the longitudinal size of the heated material is still much smaller than the transverse size determined by the laser beam spot. During this period, characterized by laser-material interaction, ionization, energy and material transport are the most significant effects. After some time, the ejected cloud (plasma plume) becomes three dimensional. At this stage, the plume evolution is described by conventional hydrodynamics and it should be sensitive only to the integral parameters of the laser pulse.

As can be seen, developing a complete theoretical model using "classical" differential approaches under these circumstances becomes rather complicated [*Bulgakova et al.*, 2005; *Inogamov et al.*, 2009]. Actual theoretical models usually focus on various "parts" of the

phenomenon, either the heating of the target or the heat transfer inside the target [*Ho et al.*, 1996], the ejection mechanisms present in different types of materials, or the expansion [*Inogamov et al.*, 2009] and formation of the plume under different experimental conditions [*Harilal et al.*,2003]. The use of a fractal/non-differential theoretical model would allow us to investigate each type of interaction as a part of a unified model. Within the framework of the fractal model, we would be able to investigate the first part of the plume formation and the one-dimensional expansion, which takes place for short evolution times and small distances, or the final stages of expansion (long after the laser pulse, at distances of few millimeters from the target), where the plasma plume has a three-dimensional evolution. This can be achieved mainly because the whole idea behind building a theoretical model based on fractal functions is to have the liberty to "zoom in" or "zoom out" through different spatial and resolution scales. Ideally, the model would be able to predict the 1D - 3D transition through all the intermediate states (fractional dimensions). All these are compelling arguments for the necessity of a fractal mathematical approach, especially because it will allow us to describe both the global and the local interactions within the context of the same model.

So, the approach developed in the framework of the NSRT [*Merches and Agop*, 2015] implies that the complete set of equations necessary to describe a physical process needs to include, besides the movement, the equations related to the scales described by non-differentiable processes. The non-differentiability translates, for the plasma physics, as the movement of the ejected particles on fractal curves. We make use here of a collisional model for low temperature plasmas, which is definitely suitable for laser-produced plasmas. These approximations allow us to further investigate the plasma dynamics as being a fractal fluid without interactions, with the mention that all interactions are intrinsic, and thus included in the fractal parameters.

IV.3.1   Plasma geodesics

Let us apply the principle of scale covariance, which states that the laws of physics are invariant with respect to the scale transformations, in particular for the dynamics of plasma particles. Thus, the non-differential operator $\hat{d}/dt$ which substitutes the classical one d/dt, will play the role of scale covariant derivative, meaning that it will be used to write the fundamental dynamics equations. In these circumstances, applying the operator described described by *Eq. (IV.18)* to the complex velocity field (*Eq. (IV.5)*), in the absence of any external field or constraint, the plasma geodesics take the following form:

$$\frac{\hat{d}\hat{V}^i}{dt} = \partial_t \hat{V}^i + \hat{V}^l \partial_l \hat{V}^i + \frac{1}{4}\left(dt\right)^{(2/D_F)-1} D^{lk}\partial_l\partial_k\hat{V}^i = 0 \, , \qquad \text{Eq. (IV.19)}$$

where $\partial_t\hat{V}^i$ represents the local acceleration, $\hat{V}^l\partial_l\hat{V}^i$ is the convection and $D^{lk}\partial_l\partial_k\hat{V}^i$ describes the dissipation terms. Thus, the local acceleration, the convection and the dissipation are in balance in

every point of the non-differentiable curve. Here, the presence of the complex coefficient of viscosity-type $\frac{1}{4}(dt)^{(2/D_F)-1}D^{lk}$ specifies that within our model, the plasma behaves like a rheological fluid (i.e. the hysteretic properties of the double layers or of the multiple charged layers that can be found in discharge plasmas [*Dimitriu et al.*, 2015]).

Fractalization can be achieved through various procedures [*Mandelbrot*, 1982; *Nottale*, 1993, 2010; *Merches and Agop*, 2015]. Thus, if we admit that it is done by Markov-type stochastic processes [*Mandelbrot*, 1982], which involve Lévy-type movements [*Falconer*, 1985] of the plasma particles [*Gurlui et al.*, 2008; *Nica et al.*, 2009, 2012, *Irimiciuc et al.*, 2014a, 2014b], the $\lambda_{\pm}^{i}$ coefficients respect the following relationship:

$$\lambda_{+}^{i}\lambda_{+}^{l} = \lambda_{-}^{i}\lambda_{-}^{l} = 2\lambda\delta^{il} \ , \qquad \text{Eq. (IV.20)}$$

where δ^{il} is the Kronecker symbol, with the property

$$\delta^{il} = \begin{cases} 1, & i = l \\ 0, & i \neq l \end{cases} .$$

The equation of plasma geodesics (trajectories) takes, in these conditions, the simple form

$$\frac{\hat{d}\hat{V}^{i}}{dt} = \partial_{t}\hat{V}^{i} + \hat{V}^{l}\partial_{l}\hat{V}^{i} - i\lambda\left(dt\right)^{(2/D_F)-1}\partial^{l}\partial_{l}\hat{V}^{i} = 0 \qquad \text{Eq. (IV.21)}$$

Furthermore, we can separate the plasma dynamics on resolution scales (plasma geodesics equations on specific – differentiable and non-differentiable - resolution scales) in the form

$$\frac{\hat{d}\hat{V}_{F}^{i}}{dt} = \partial_{t}V_{F}^{i} + V_{D}^{l}\partial_{l}V_{F}^{i} - \left[V_{F}^{l} - \lambda\left(dt\right)^{(2/D_F)-1}\partial^{l}\right]\partial_{l}V_{D}^{i} = 0 \qquad \text{Eq. (IV.22)}$$

for the non-differentiable scale resolution and

$$\frac{\hat{d}\hat{V}_{D}^{i}}{dt} = \partial_{t}V_{D}^{i} + V_{D}^{l}\partial_{l}V_{D}^{i} - \left[V_{F}^{l} - \lambda\left(dt\right)^{(2/D_F)-1}\partial^{l}\right]\partial_{l}V_{F}^{i} = 0 \qquad \text{Eq. (IV.23)}$$

for the differential scale resolution.

A special case is that of the plasma dynamics associated to the fractal - non-fractal transition. These types of dynamics are extremely important since what is shown through experimental investigations are usually observed at a differentiable scale. The "intrinsic" plasma dynamics (for example the interactions between the plasma particles) are not directly seen through

experimental techniques, as they are described by means of scale resolution [*Notalle, 2011*]. In this condition, the velocity field associated to the fractal – non-fractal transition is introduced:

$$V^i = V_D^i - V_F^i$$

<div align="right">Eq. (IV.24)</div>

where V_D^i and V_F^i are given by *Eq.(IV.6).*

By subtracting the relations *Eq. (IV.22)* and *Eq. (IV.23)* we obtain the plasma geodesics equation associated to the fractal – non-fractal transition:

$$\partial_t V^i + V^l \partial_l V^i = 2\left[V_F^l + \lambda\left(dt\right)^{(2/D_F)-1}\partial^l\right]\partial_l V_F^i + \lambda\left(dt\right)^{(2/D_F)-1}\partial^l\partial_l V^i$$

<div align="right">. Eq. (IV.25)</div>

This equation can be put in correspondence with the standard Navier-Stokes type equation [*Landau and Lifshitz*, 1959; *Batchelor*, 1999]:

$$\partial_t v^i + v^i \partial_l v^i = \sum f^i + \zeta \partial^l \partial_l v^i \ ,$$

<div align="right">Eq. (IV.26)</div>

where $\sum f^i$ defines the overall external forces and ζ is the kinematic viscosity coefficient, if we admit the following correlations:

$$\sum f^i \rightarrow 2\left[V_F^l + \lambda\left(dt\right)^{(2/D_F)-1}\partial^l\right]\partial_l V_F^i$$

<div align="right">Eq. (IV.27)</div>

$$\zeta \rightarrow \lambda\left(dt\right)^{(2/D_F)-1} \ .$$

<div align="right">Eq. (IV.28)</div>

This means that the specific fractal force

$$f_F^i = 2\left[V_F^l + \lambda\left(dt\right)^{(2/D_F)-1}\partial^l\right]\partial_l V_F^i$$

<div align="right">Eq. (IV.29)</div>

is a measure of all "external constrains", while the "fractalization degree" $\lambda\left(dt\right)^{(2/D_F)-1}$ is a measure of the "internal constrictions", which manifests between the structural units of the complex fluid.

IV.3.2 Plasma geodesics in the Schrödinger-type representation

For irotational motions of the complex fluid structural units, the complex velocity field $\hat{v}^l$ satisfies the relationship

$$\varepsilon_{ikl}\partial^k\hat{v}^l = 0 \ ,$$

<div align="right">Eq. (IV.30)</div>

where ε_{ikl} represents the Levi-Civita pseudo-tensor. Then, for $\hat{V}^i$ we can choose the following form [*Gurlui et al.*, 2008; *Nica et al.*, 2009, 2012, *Irimiciuc et al.*, 2014a, 2014b; *Merches and Agop*, 2015]

$$\hat{V}^i = -2i\lambda \left(dt\right)^{(2/D_F)-1} \partial^i \ln\psi , \qquad \text{Eq. (IV.31)}$$

where the scalar potential of the complex velocity field is defined by means of $\ln\psi$. Furthermore, substituting *Eq. (IV.31)* in *Eq. (IV.21)*, we obtain:

$$\frac{d\hat{V}^i}{dt} = -2i\lambda \left(dt\right)^{(2/D_F)-1} \left\{ \partial_t \partial^i \ln\psi - i \left[2\lambda \left(dt\right)^{(2/D_F)-1} \left(\partial^l \ln\psi \partial_l \right) \partial^i \ln\psi + \lambda \left(dt\right)^{(2/D_F)-1} \partial^l \partial_l \partial^i \ln\psi \right] \right\} = 0$$

$$\text{Eq. (IV.32)}$$

Eq. (IV.32) can take yet another different form based on the following relations:

$$\partial^l \partial_l \ln\psi + \partial_i \ln\psi \partial^i \ln\psi = \frac{\partial_l \partial^l \psi}{\psi}$$

$$\partial^i \left(\frac{\partial^l \partial_l \psi}{\psi} \right) = 2 \left(\partial^l \ln\psi \partial_l \right) \partial^i \ln\psi + \partial^l \partial_l \partial^i \ln\psi \qquad \text{Eq. (IV.33)}$$

Therefore, *Eq. (IV.32)* becomes:

$$\frac{d\hat{V}^i}{dt} = -2i\lambda \left(dt\right)^{(2/D_F)-1} \partial^i \left[\partial_t \ln\psi - 2i\lambda \left(dt\right)^{(2/D_F)-1} \frac{\partial^l \partial_l \ln\psi}{\psi} \right] = 0 . \qquad \text{Eq. (IV.34)}$$

From here, by integrating up to an arbitrary phase factor of ψ, which for simplicity can be chosen as zero, we obtain the fractal equation of Schrödinger type (plasma geodesics in the Schrödinger-type representation), in the case without any external constraints:

$$\lambda^2 \left(dt\right)^{(4/D_F)-2} \partial^l \partial_l \psi + i\lambda \left(dt\right)^{(2/D_F)-1} \partial_t \psi = 0 . \qquad \text{Eq. (IV.35)}$$

If the external constraints are given through a scalar potential U, *Eq. (IV.35)* takes the following form:

$$\lambda^2 \left(dt\right)^{(4/D_F)-2} \partial^l \partial_l \psi + i\lambda \left(dt\right)^{(2/D_F)-1} \partial_t \psi - \frac{U}{2} \psi = 0 . \qquad \text{Eq. (IV.36)}$$

Let us investigate the case when the movement of the complex fluid structural units takes place on Peano-type curves (meaning $D_F = 2$) [*Mandelbrot*, 1982; *Falconer*, 1985], at Compton scale ($\lambda = \hbar/2m_0$, with $\hbar$ - Planck's reduced constant and m_0 - the rest mass of the structural unit).

Eq. (IV.35) and *Eq. (IV.36)* are reduced to the "classical" Schrödinger *Eq. IV. (35)* without external constrains:

$$\frac{\hbar^2}{2m_0}\Delta\psi + i\hbar\partial_t\psi = 0 \qquad \text{Eq. (IV.37)}$$

and to the Schrödinger *Eq. (IV.36)* with external constraints:

$$\frac{\hbar^2}{2m_0}\Delta\psi + i\hbar\partial_t\psi - U\psi = 0 , \qquad \text{Eq. (IV.38)}$$

respectively.

Such a formalism can be applied only in the case of quantum plasmas, degenerate plasmas (in which the Maxwellian-type distribution is replaced by a Fermi-Dirac distribution [*Shukla*, 2009; *Haas*, 2011]). As in the case of quantum physics, ψ does not have a physical significance in our fractal model. The physical relevance is gained either through *Eq. (IV.31)*, as a scalar potential of a complex velocity field,

$$\Phi = -2i\lambda(dt)^{(2/D_F)-1}\ln\psi , \qquad \text{Eq. (IV.39)}$$

or through the conservation law

$$\partial_t\rho + \partial_l j^l = 0 , \qquad \text{Eq. (IV.40)}$$

with

$$\rho = \psi\bar{\psi}, \; j^l = -i\lambda(dt)^{(4/D_F)-2}\left(\psi\partial^l\bar{\psi} - \bar{\psi}\partial^l\psi\right) \qquad \text{Eq. (IV.41)}$$

as a probability density.

IV.3.3 Plasma geodesics in the fractal hydrodynamic representation

Let us now write the plasma geodesics in the fractal hydrodynamic representation. By considering $\psi = \sqrt{\rho}\exp(iS)$ with $\sqrt{\rho}$ the amplitude and S the phase of Ψ, the complex velocity field *Eq. (IV.5)* takes the explicit form

$$\hat{V}^i = V_D^i - iV_F^i$$

$$V_D^i = 2i\lambda (dt)^{(2/D_F)-1} \partial^i S \quad .$$

Eq. (IV.42)

$$V_F^i = i\lambda (dt)^{(2/D_F)-1} \partial^i \ln \rho$$

Substituting *Eq. (IV.42)* in *Eq. (IV.21)* and separating the real and imaginary parts up to an arbitrary phase factor zero, we obtain:

$$\partial_t V_D^i + \left(V_D^l \partial_l\right) V_D^i = -\partial^i Q$$

Eq. (IV.43)

$$\partial_t \rho + \partial_i \left(\rho V_D^i\right) = 0 ,$$

Eq. (IV.44)

with *Q* being the specific non-differentiable (fractal) potential given by

$$Q = -2\lambda^2 (dt)^{(4/D_F)-2} \frac{\partial^l \partial_l \sqrt{\rho}}{\sqrt{\rho}} = -\frac{V_F^l V_{Fl}}{2} - \lambda (dt)^{(2/D_F)-1} \partial_i V_F^i .$$

Eq. (IV.45)

Again, if we take into account the presence of an external scalar potential *U, Eq. (IV.43)* becomes

$$\partial_t V_D^i + \left(V_D^l \partial_l\right) V_D^i = -\partial^i \left(Q + U\right).$$

Eq. (IV.46)

In these conditions, the previous equations can be structured either as *Eqs. (IV.43 - IV.45)*, which would correspond to the fractal hydrodynamic model without any external constraints, or as *Eqs. (IV.44 - IV.46)*, which corresponds to the fractal hydrodynamic model in the presence of external constraints. Regardless of the approach, they will define the plasma geodesics in the fractal hydrodynamic representation.

Eq. (IV.43) and *Eq. (IV.46)* correspond to the momentum conservation law with or without external conditions, while *Eq. (IV.44)* corresponds to the state density conservation laws. This leads to a few immediate consequences:

i)   all plasma particles are in permanent interaction with the "fractal medium" through the specific fractal potential (*Eq. (IV.45)*);

ii)   the fractal velocity field does not describe the real motion, proof of this is its absence from the state density conservation law. This is not an impediment to contribute to the momentum transfer by means of the specific fractal potential (*Eq. (IV.45)*);

iii)   the specific fractal potential introduces the fractal stress tensor:

$$\hat{\omega}_{il} = -2\lambda^2 \left(dt\right)^{(4/D_F)-2} \partial_i \partial_l \ln \rho \qquad\qquad \text{Eq. (IV.47)}$$

having the divergence

$$\partial^i \hat{\omega}_{il} = -\rho \partial_l Q \qquad\qquad \text{Eq. (IV.48)}$$

and generating a fractal force density which can be written as:

$$f_l = -\rho \partial_l Q \qquad\qquad \text{Eq. (IV.49)}$$

iv) if the fractal stress tensor is diagonal:

$$\hat{\omega}_{il} = -p \delta_{il} , \qquad\qquad \text{Eq. (IV.50)}$$

where p can be attributed to a "fractal pressure", then the equations (*Eq. (IV.43 – IV.45)*) become:

$$\partial_t V_D^i + V_D^l \partial_l V_D^i = -\rho^{-1} \partial_i p$$
$$\partial_t \rho + \partial_l \left(\rho V_D^l\right) = 0 \qquad\qquad \text{Eq. IV. (51)}$$

and

$$\partial_t V_D^i + V_D^l \partial_l V_D^i = -\rho^{-1} \partial_i p + \partial_i U$$
$$\partial_t \rho + \partial_l \left(\rho V_D^l\right) = 0 \qquad , \qquad\qquad \text{Eq. (IV.52)}$$

respectively.

The equation systems *Eq. (IV.51)* and *Eq. (IV.52)* can be reduced to the standard one used in plasma physics (the case of the bi-fluid model [*Chen*, 2003]) if the movement of the structural units is maintained on Peano-type curves, $D_F = 2$, and $\lambda = \zeta$, where ζ would correspond to the plasma kinetic viscosity.

IV.4   The role of the fractality in the stationary dynamics of a complex fluid. Laminar and turbulent flows

Let us analyze now the way in which the fractality affects the stationary dynamics of a complex fluid. To this end we will have at our disposal the following system of equations:

$$f^i = 2\left[V_F^l + \lambda\left(dt\right)^{(2/D_F)-1} \partial^l \right]\partial_l V^i = 0 \qquad\qquad \text{Eq. (IV.53)}$$

$$\partial_l V_F^l = 0.$$

<div align="right">Eq. (IV.54)</div>

The first equation describes the disappearance of the specific fractal force *(Eq. (IV.29))*, while the second one incorporates the incompressibility of the fractal fluid at a fractal scale (the state density at a fractal scale is constant).

In general it is difficult to obtain an analytic solution for our system of equations, taking into account its non-linear nature (through $V_F^l \partial_l V_F^i$). However, by considering only the dynamics of the particles in a plane (x, y) that contains the expansion direction (x), the fractal velocity field can be written as:

$$V_F^1 = V_x(\text{x,y})$$
$$V_F^2 = V_y(\text{x,y})$$

<div align="right">Eq. (IV.55)</div>

the system of equations *Eq. (IV.53)* and *Eq. (IV.54)* can be written as:

$$V_x \frac{\partial V_x}{\partial x} + V_y \frac{\partial V_x}{\partial x} = \lambda (dt)^{(2/D_F)-1} \frac{\partial^2 V_x}{\partial y^2},$$

<div align="right">Eq. (IV.56)</div>

$$\frac{\partial V_x}{\partial x} + \frac{\partial V_y}{\partial y} = 0,$$

<div align="right">Eq. (IV.57)</div>

which now admits analytical solutions. Indeed, with the boundary conditions:

$$\lim_{y \to 0} V_y(x, y) = 0, \quad \lim_{y \to 0} \frac{\partial V_x}{\partial y} = 0, \quad \lim_{y \to \infty} V_x(x, y) = 0$$

<div align="right">Eq. (IV.58)</div>

and the constant flux momentum per length unit:

$$\Theta = \rho \int_{-\infty}^{+\infty} V_x^2 dy = \text{const.}$$

<div align="right">Eq. (IV.59)</div>

using the procedure from [*Landau and Lifshitz*, 1959; *Batchelor*, 1999], the system of *Eq. (IV.56)* and *Eq. (IV.57)* has the following solution:

$$V_x = \frac{\left[1.5\left(\dfrac{\Theta}{6\rho}\right)^{2/3}\right]}{\left[\lambda(dt)^{(2/D_F)-1} x\right]^{1/3}} \cdot \operatorname{sech}^2 \frac{\left[(0.5y)\left(\dfrac{\Theta}{6\rho}\right)^{1/3}\right]}{\left[\lambda(dt)^{(2/D_F)-1} x\right]^{2/3}}$$

Eq. (IV.60)

$$V_y = \frac{\left[4.5\left(\dfrac{\Theta}{6\rho}\right)^{2/3}\right]}{\left[3\lambda(dt)^{(2/D_F)-1} x\right]^{1/3}} \cdot$$

$$\left[\frac{y\left(\dfrac{\Theta}{6\rho}\right)^{1/3}}{\left[\lambda(dt)^{(2/D_F)-1} x\right]^{2/3}} \cdot \operatorname{sech}^2 \frac{\left[(0.5y)\left(\dfrac{\Theta}{6\rho}\right)^{1/3}\right]}{\left[\lambda(dt)^{(2/D_F)-1} x\right]^{2/3}} - \tanh \frac{\left[(0.5y)\left(\dfrac{\Theta}{6\rho}\right)^{1/3}\right]}{\left[\lambda(dt)^{(2/D_F)-1} x\right]^{2/3}}\right]$$

Eq. (IV.61)

These solutions specify the fact that the fractal velocity field is strongly non-linear both through the soliton type component V_x (*Eq. (IV.60)*) as well as through the soliton-kink type component V_y (*Eq. IV.(61)*). On the properties and general characteristics of these types of solutions, one can consult [*Jackson*, 1978; *Cristescu*, 2008].

For $y = 0$, we obtain in *Eq. IV. (60)* the flow "critical" velocity (velocity component on the expansion axis) in the form

$$V_x(x, y = 0) = V_c = \frac{\left[1.5\left(\dfrac{\Theta}{6\rho}\right)^{2/3}\right]}{\left[\lambda(dt)^{(2/D_F)-1} x\right]^{1/3}} ,$$

Eq. (IV.62)

while *Eq.(IV.59)*, taking into account *Eq. (IV.62)*, becomes

$$\Theta = \rho \int_{-\infty}^{+\infty} V_x^2(x, y)\, dy = \int_{-d_c}^{+d_c} V_c^2(x,0)\, dy ,$$

Eq. (IV.63)

where $+/-d_c$ defines spatial limitation for the flow of the fractal fluid.

Eq. (IV.60) and *Eq. (IV.61)* can be simplified if we use the following notations:

$$\xi = \frac{x}{x_0}, \eta = \frac{y}{y_0}, V_\xi = \frac{V_x}{w_o}, V_\eta = \frac{V_y}{w_0},$$

$$\Omega = \frac{\left(\dfrac{\Theta}{6\rho}\right)^{2/3}}{w_0\left[\lambda(dt)^{(2/D_F)-1}x_o\right]^{1/3}}, \sigma = \frac{\left(\dfrac{\Theta}{6\rho}\right)^{1/3}y_0}{\left[\lambda(dt)^{(2/D_F)-1}x_o\right]^{2/3}}$$

<div align="right">Eq. (IV.64)</div>

where x_0, y_0, w_0 are "specific" lengths and the "specific" velocity, respectively, of the laminar flow of the complex fluid (i.e. in the case of laser-produced plasma these specific parameters could correspond to the Debye length and the thermal velocity, respectively). We would like to stress that the new parameter σ is inversely proportional with the scale resolution and thus it results the following system:

$$V_\xi(\xi,\eta) = \frac{1.5\Omega}{\xi^{1/3}}\operatorname{sech}^2\left(\frac{0.5\Omega\sigma\eta}{\xi^{2/3}}\right)$$

<div align="right">Eq. (IV.65)</div>

$$V_\eta(\xi,\eta) = \frac{4.5^{2/3}}{3^{1/3}}\frac{\Omega}{\xi^{1/3}}\left[\frac{\sigma\eta}{\xi^{2/3}}\operatorname{sech}^2\left(\frac{0.5\Omega\sigma\eta}{\xi^{2/3}}\right) - \tanh\left(\frac{0.5\Omega\sigma\eta}{\xi^{2/3}}\right)\right]$$

<div align="right">Eq. (IV.66)</div>

Since we have assumed above that the dynamics of laser-produced plasmas can be approximated with the one of a fractal fluid, let us investigate the evolution of the velocity field components on the expansion direction (ξ) and the corresponding orthogonal direction (η). In the following graphical representations the starting point of the flow, which is the equivalent of the interaction point between the laser beam and the target, is at ($\eta = 25$, $\xi = 0$). We present in *Figure IV.1* the dependence of the normalized velocity field V_ξ on the normalized spatial coordinates ξ, η for $\sigma = 0.3$; 1; 3. The effects of the nonlinearity degree (σ) can be perceived as a "footprint" of the scale resolution ($(dt)^{(2/D_F)-1}$) since the two parameters are related through Eq. (IV.64). We observe that for a higher fractalization degree the shape of the plume is bigger and it presents a larger spatial distribution, this changes as the fractalization degree decreases the plume becomes more directional and loses the lateral expansion previously observed. These results are similar to the ones obtained through ICCD imaging of laser-produced plasma in ns, ps and fs regime. For each pulse width, we attribute a specific scale resolution ($(dt)^{(2/D_F)-1}$) and a fractal dimension (D_F).
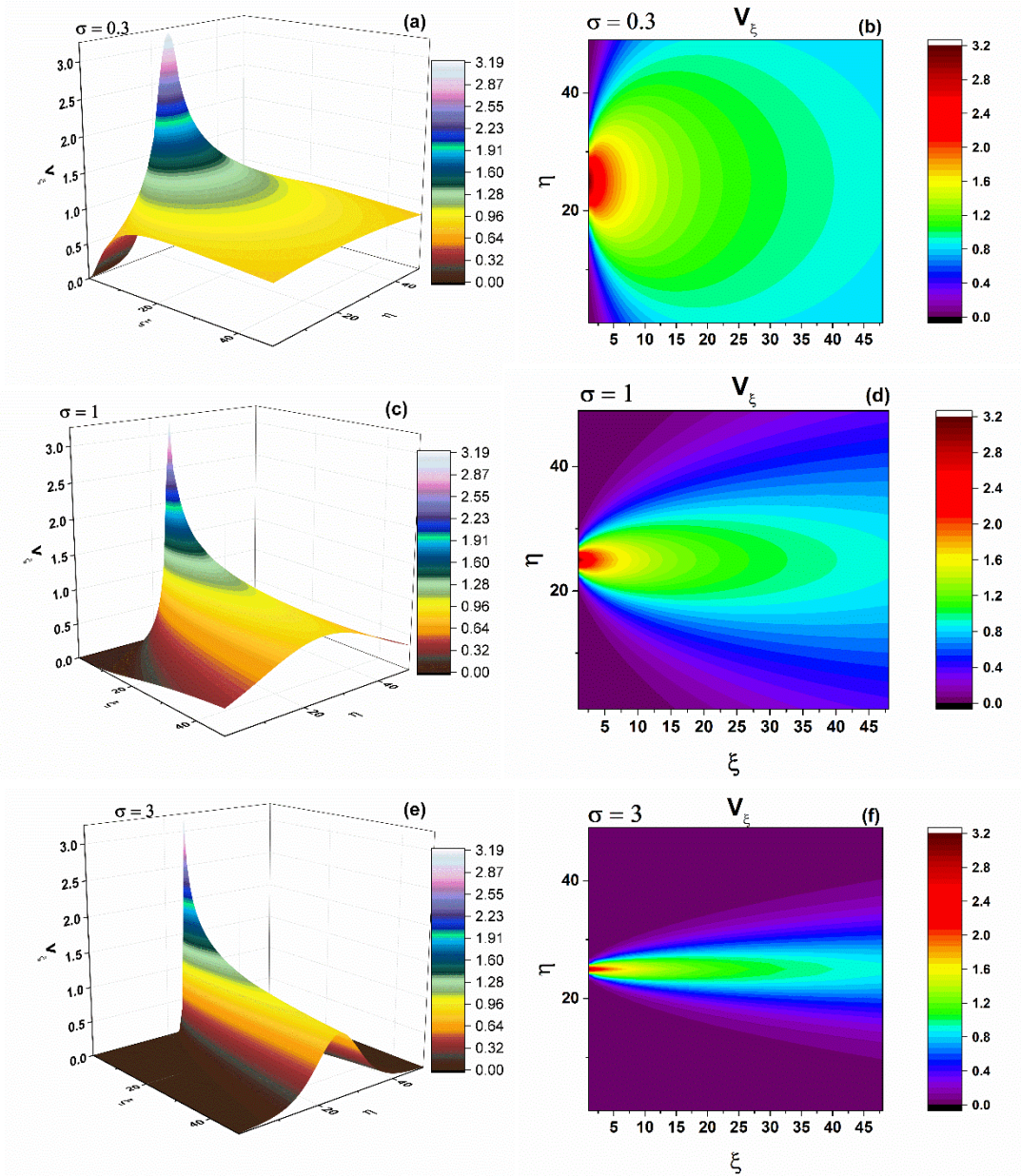
Figure IV.1   The dependence of the normalized velocity field V_ξ on the normalized spatial coordinates (ξ, η) for the nonlinearity degree $\sigma = 0.3$, 1 and 3, respectively: (a, c, e) 3D representation and (b, d, f) contour plots.

Regarding the second component of the normalized velocity (see *Figure IV.2*) we observe that the values are almost constant in the volume. As the scale resolution increases (i.e. σ decreases) we observe that the spatial spreading of V_η increases as well, while its module keeps about the same values. We can thus speculate that the changes in the plume dynamics will be given only (mainly) by the velocity component on the expansion direction.
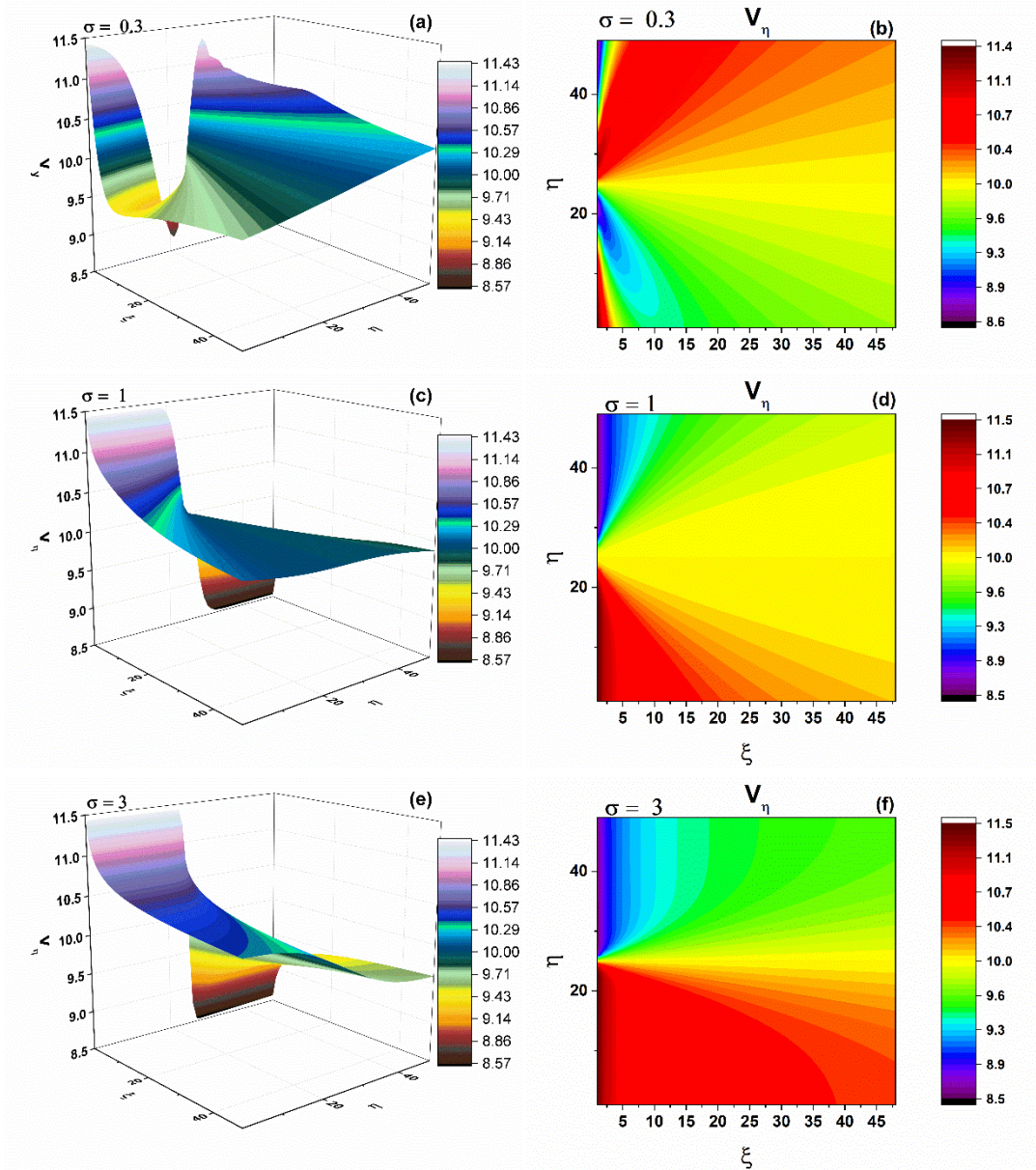
Figure IV.2   The dependence of the normalized velocity field V_η on the normalized spatial coordinates ξ, η for the nonlinearity degree $\sigma = 0.3$, 1 and 3, respectively: (a, c, e) 3D representation and (b, d, f) contour plots.

In order to understand if there are any internal constrains during expansion we need to evaluate the fractal force, which will probably allow us to understand the characteristic shapes of the velocity fields with respect to the changes induced by the scale resolution. The fractal force, in the stationary case is defined as:

$$F \sim \partial_\eta V_\xi - \partial_\xi V_\eta$$

$$F(\xi,\eta) = -\frac{1.5\Omega\,\mathrm{sech}^2\left(\dfrac{0.5\sigma\eta}{\xi^{2/3}}\right)\tanh\left(\dfrac{0.5\sigma\eta}{\xi^{2/3}}\right)\omega}{\xi} -$$

$$-\frac{1}{\xi^{1/3}}\left(0.9\Omega\left(-\frac{2}{3}\frac{\sigma\eta\,\mathrm{sech}^2\left(\dfrac{0.5\sigma\eta}{\xi^{2/3}}\right)}{\xi^{5/3}}+\frac{0.66\sigma^2\eta^2\,\mathrm{sech}^2\left(\dfrac{0.5\sigma\eta}{\xi^{2/3}}\right)\tanh\left(\dfrac{0.5\sigma\eta}{\xi^{2/3}}\right)}{\xi^{7/3}}+\frac{0.33\left[\left(1-\tanh^2\left(\dfrac{0.5\Omega\eta}{\xi^{2/3}}\right)\right)\sigma\eta\right]}{\xi^{5/3}}\right]3^{\frac{3}{2}}\right)+$$

$$+\frac{0.3\Omega\left(\dfrac{\sigma\eta\,\mathrm{sech}^2\left(\dfrac{0.5\sigma\eta}{\xi^{2/3}}\right)}{\xi^{2/3}}-\tanh\left(\dfrac{0.5\sigma\eta}{\xi^{2/3}}\right)\right)3^{\frac{3}{2}}}{\xi^{4/3}}$$

Eq. (IV.67)

In *Figure IV.3* we represented the normalized force field evolution on the two flow directions (ξ, η) for various nonlinear degrees. From the graphical representations, we observe that there are two regions: one defined by a positive value of the fractal force and another having the same amplitude but the opposite sign. For relatively small values of the scale resolution we observe a small angle between the two areas which is the reason for the elongated shape of the plume, while for higher values the angle increases which leads to the increase in the plasma volume and its angular distribution. These results are in good agreement with our experimental data and reveal that the expansion of the plasma is mainly given by the distribution of the fractal force, which affects primarily the velocity component on the expansion direction.

The stationary solution for the laminar flow case is the simplest approximation of the plume dynamics, and in order to extend our approach towards the physical reality we also need to consider the turbulent flow case. From this perspective in literature we can find some experimental proof of plasma turbulences during expansion. In general, the ablated plasma plume can be considered as a multi-phase flow having in its composition nanoparticles, clusters or molecules. Vortex and turbulence formation are relatively familiar fluid dynamics phenomena which can be explained based on various viscosity effects. An example from laser ablation of vortex formation is the specific mushroom-like shape of the ablated particles clouds which are usually found in laser ablation at high pressure. Some examples can be found in literature, notable is the use of planar LIF for the investigations of the turbulent movement of the ejected particles on Al [*Gilgenbach et*

157

al., 1990] or copper [*Sappey et al.*, 1991]. Other results might consist in the presence of vortices or turbulence favored by the inter-mix between target species and the background gas.
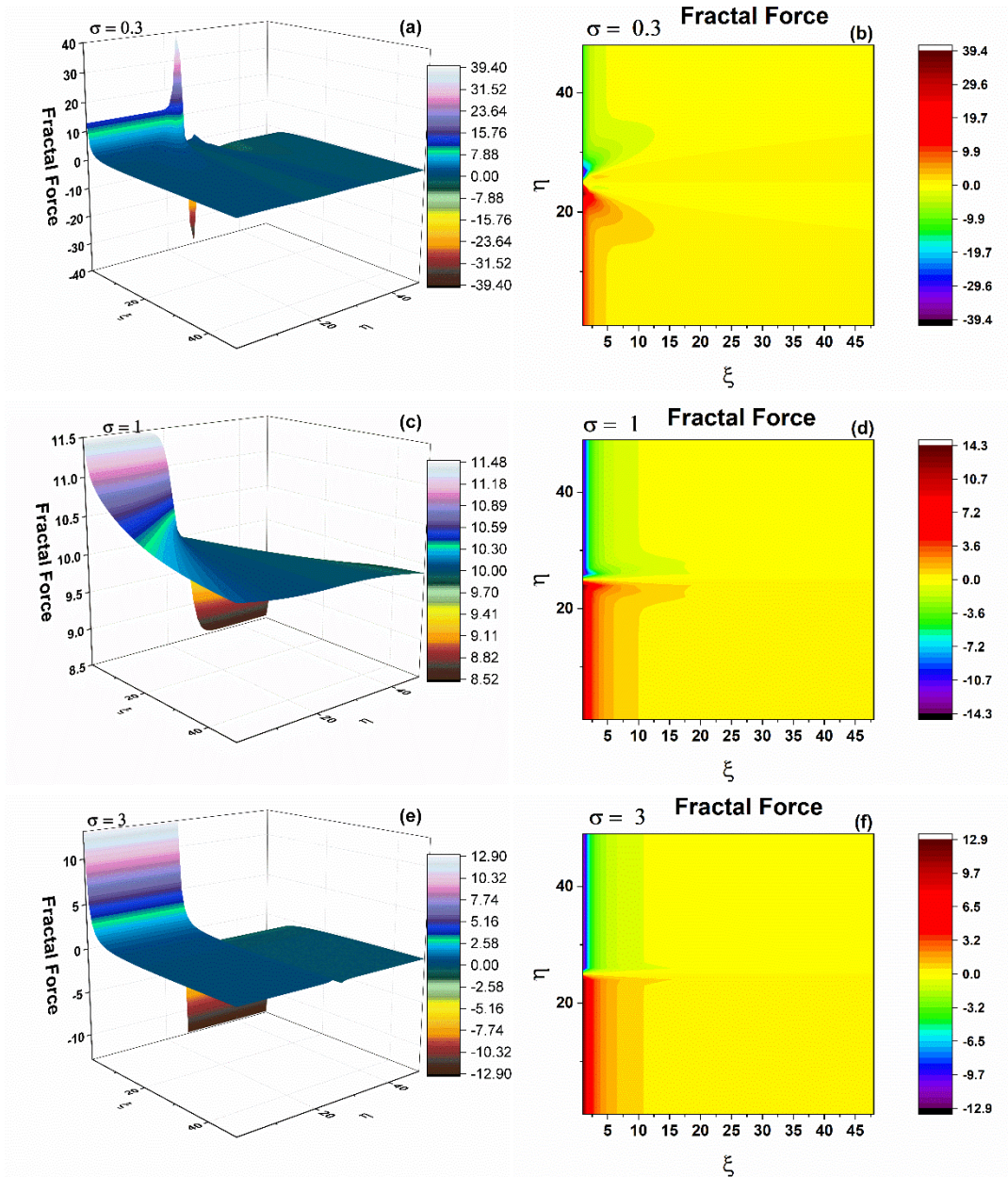
Figure IV.3   The dependence of the fractal force F on the normalized spatial coordinates ξ, η for the nonlinearity degree $\sigma = 0.3$, 1 and 3, respectively: (a, c, e) 3D representation and (b, d, f) contour plots.

In the case of a turbulent flow the calculations regarding the velocity field distribution are close to the ones presented for the laminar case. The main difference is that in this case the "viscosity" of the fluid is considered to be variable. In such a context following the procedure

presented in [*Landau and Lifshitz*, 1959; *Merches and Agop*, 2015], the velocity field takes the form:

$$V_x(x,y) = 0.5 \left(\frac{3J\sigma}{x}\right)^{1/2} \text{sech}^2 \left(\frac{\sigma_t y}{x}\right), \qquad \text{Eq. (IV.68)}$$

$$V_y(x,y) = 0.25 \left(\frac{3J\sigma_t}{x}\right)^{1/2} \left[2\left(\frac{\sigma_t y}{x}\right) \text{sech}^2 \left(\frac{\sigma_t y}{x}\right) - \tanh\left(\frac{\sigma_t y}{x}\right)\right], \quad \text{Eq. (IV.69)}$$

where σ_t is a measure of the nonlinearity degree, while J is the turbulent flux momentum per length unit which is constant.

As in the case of the laminar flow, *Eq. (IV.68)* and *Eq. (IV.69)* can be simplified by means of normalized variables:

$$\xi = \frac{x}{x_{0t}}, \eta = \frac{y}{y_{0t}}, \overline{V}_\xi = \frac{u}{w_{0t}}, \overline{V}_\eta = \frac{v}{w_{0t}}, \qquad \text{Eq. (IV.70)}$$

as well as the normalized parameters:

$$\overline{\Omega} = \left(\frac{3J}{y_{0t}}\right)^{1/2} \frac{1}{w_{0t}}, \tilde{\Omega} = \left(\frac{3J}{x_{0t}}\right)^{1/2} \frac{1}{w_{0t}}, \overline{\sigma} = \sigma_t \frac{y_{0t}}{x_{0t}}, \qquad \text{Eq. (IV.71)}$$

where x_{0t}, y_{0t} and w_{0t} are lengths and velocity, respectively, characterizing the turbulent flow of a fractal fluid. It results that:

$$\overline{V}_\xi(\xi,\eta) = 0.5 \overline{\Omega} \left(\frac{\sigma}{\xi}\right)^{1/2} \text{sech}^2 \left(\frac{\overline{\sigma}\eta}{\xi}\right), \qquad \text{Eq. (IV.72)}$$

$$\overline{V}_\eta(\xi,\eta) = 0.25 \tilde{\Omega} \left(\frac{1}{\sigma\xi}\right)^{1/2} \left[2\left(\frac{\overline{\sigma}\eta}{\xi}\right) \text{sech}^2 \left(\frac{\overline{\sigma}\eta}{\xi}\right) - \tanh\left(\frac{\overline{\sigma}\eta}{\xi}\right)\right]. \qquad \text{Eq. (IV.73)}$$

In our case the normalized force is given by the relation:

$$\bar{F}(\xi,\eta) = \partial_\eta \bar{V}_\eta - \partial_\xi \bar{V}_\xi = -\frac{\bar{\Omega}\sqrt{\frac{\bar{\sigma}}{\xi}}\operatorname{sech}^2\left(\frac{\bar{\sigma}\eta}{\xi}\right)\tanh\left(\frac{\bar{\sigma}\eta}{\xi}\right)\bar{\sigma}}{\xi} -$$

$$-\frac{0.125\hat{\tilde{\Omega}}\left[\frac{2\eta\bar{\sigma}\operatorname{sech}^2\left(\frac{\bar{\sigma}\eta}{\xi}\right)}{\xi} - \tanh\left(\frac{\bar{\sigma}\eta}{\xi}\right)\right]}{\sqrt{\frac{1}{\bar{\sigma}\xi}\bar{\sigma}\xi^2}} -$$

$$0.25\tilde{\Omega}\sqrt{\frac{1}{\bar{\sigma}\xi}}\left[-\frac{2\eta\bar{\sigma}\operatorname{sech}^2\left(\frac{\bar{\sigma}\eta}{\xi}\right)}{\xi^2} + \frac{4\eta^2\bar{\sigma}^2\operatorname{sech}^2\left(\frac{\bar{\sigma}\eta}{\xi}\right)\tanh\left(\frac{\bar{\sigma}\eta}{\xi}\right)}{\xi^3}\right]$$

$$+\frac{\left(1 - \frac{\tanh^2\left(\frac{\bar{\sigma}^2\eta}{\xi}\right)}{\xi^2}\right)\bar{\sigma}\eta}{\xi^2}$$

When representing the velocity component on the expansion direction (ξ), for a turbulent flow, we observe that there are no differences in the shapes or their dependence with the fractalization degree (*Figure IV.4*). However there are some small differences in the values of the expansion velocity achieved for various fractalization degrees. For a low value of the fractalization degree the velocities are higher with about one order of magnitude than the ones obtained for higher values of this parameter, results in very good agreement with our experimental findings where we obtained the same difference in center-of-mass velocities obtained through ICCD
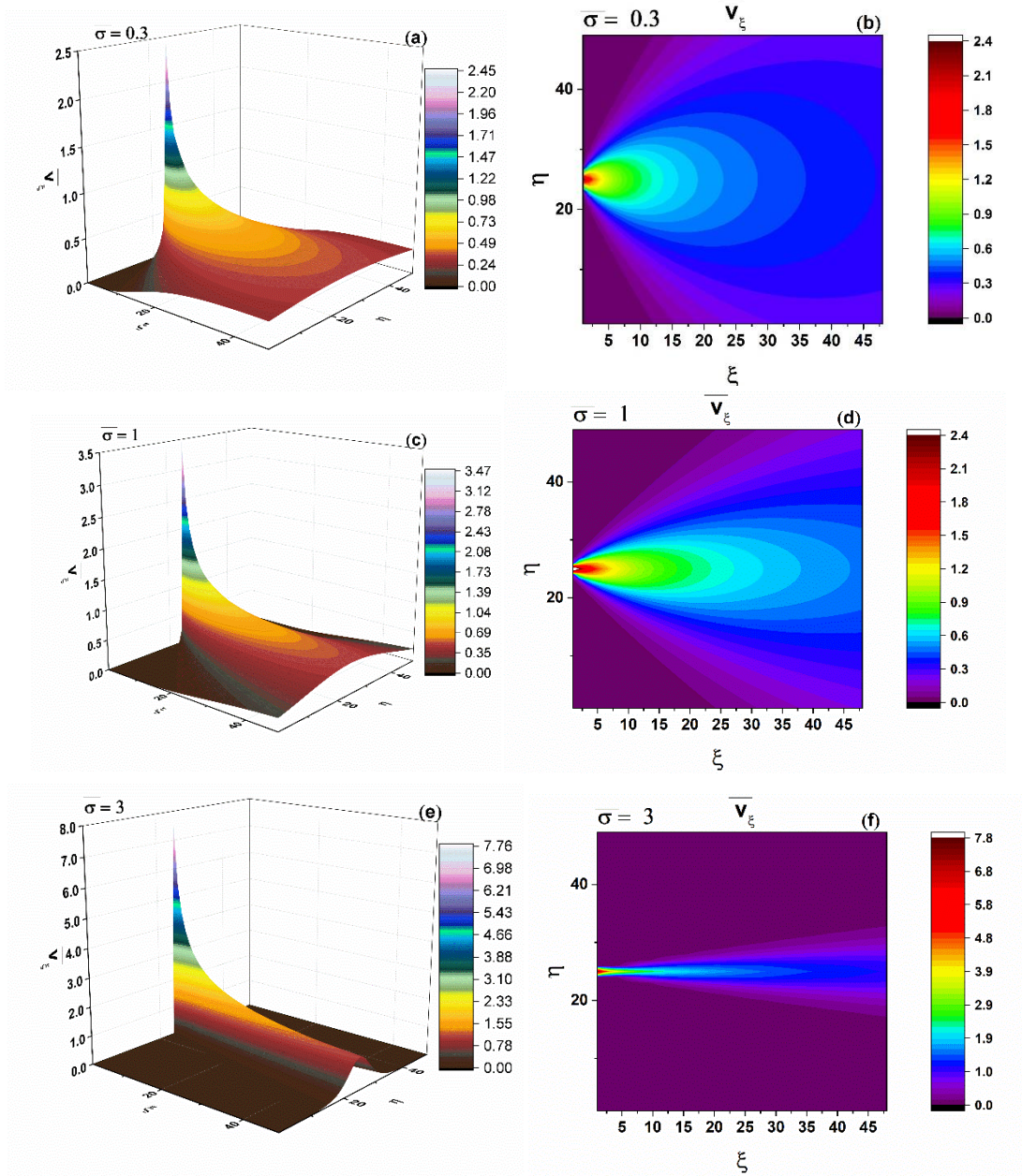
Figures IV.4   The dependence of the normalized velocity field $\overline{V_\xi}$ on the normalized spatial coordinates ξ, η for the nonlinearity degree $\bar\sigma$ = 0.3, 1, 3, respectively: (a, c, e) 3D representation and (b, d, f) contour plots.

When we represent the velocity component on the transverse direction η (*Figure IV.5*) we observe that the velocities follow an opposite evolution. As the nonlinearity degree increases the velocity increases as well. This result is understandable as this component is responsible with the losses of energy during expansion. In the case of ns laser-produced plasma, a higher velocity on η

direction is expected as the volume of the plume is higher and the expansion velocity is relatively smaller, as most of the energy is lost through collisions leading to a higher fractalization degree.
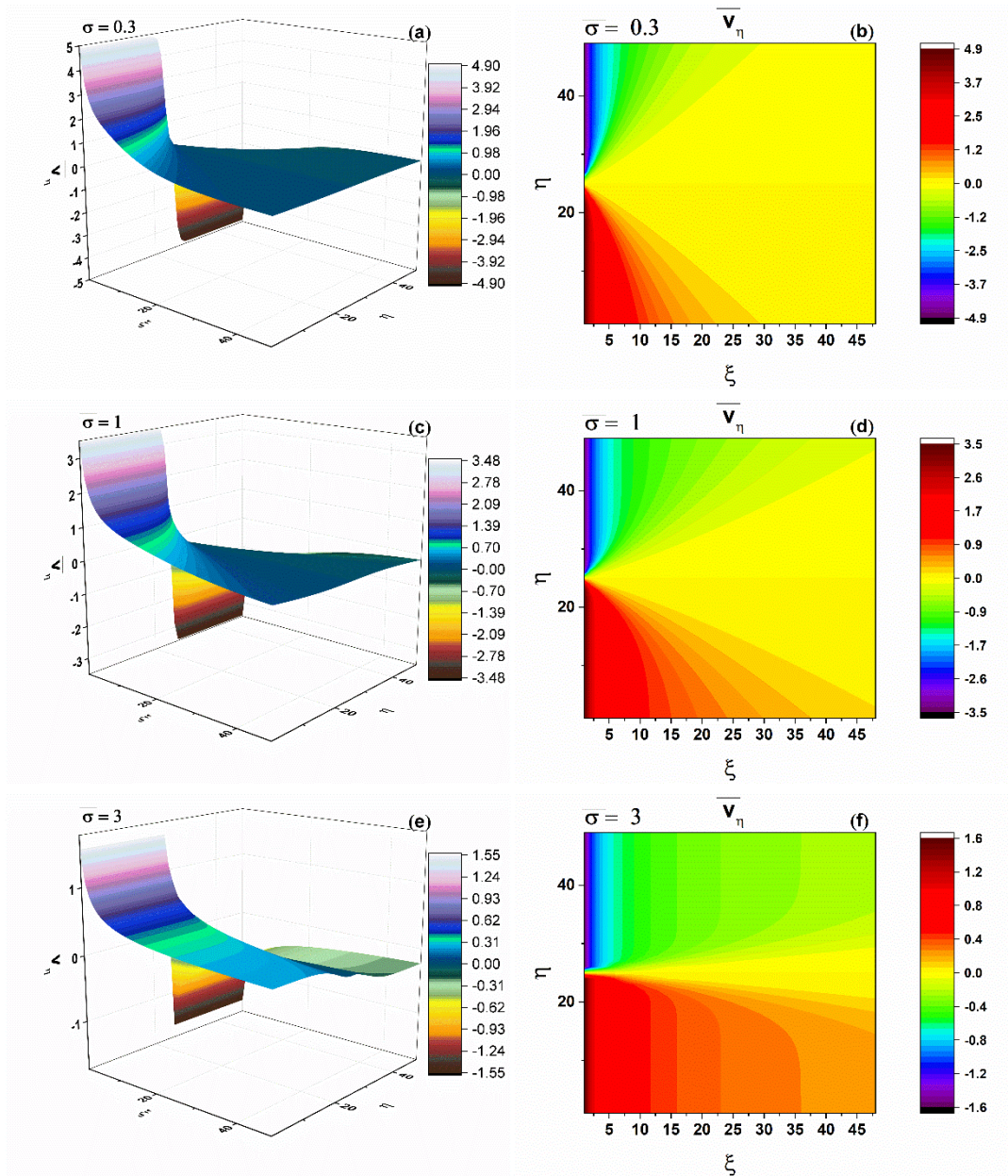
Figures IV.5   The dependence of the normalized velocity field $\overline{V}_\eta$ on the normalized spatial coordinates ξ, η for the nonlinearity degree $\bar{\sigma} = 0.3$, 1, 3, respectively: (a, c, e) 3D representation and (b, d, f) contour plots.

As we did in the laminar flow case we attempted to estimate the fractal force field spatial distribution for the latter case, that of the turbulent flow. We observe here (*Figure IV.6*) a different distribution of the fractal force. For small values of the nonlinearity degree we observe a relatively

uniform distribution and smaller values of the fractal force. This result is coherent with our previous results and showcases once again the fact that the velocity/energy distribution within the plasma volume is more uniform. We observe in *Figure IV.6* that the amplitude of the fractal force increases by about one order of magnitude with respect to the previous non-turbulent case and the distribution becomes "focused" around the expansion axis being null in the rest of the volume. For a low value of the fractalization degree (equivalent to a higher value of σ), the representation depicts the spatial distribution of the fractal force, revealing that the force increases its amplitude and is concentrated in two areas, which is similar to the laminar flow case.
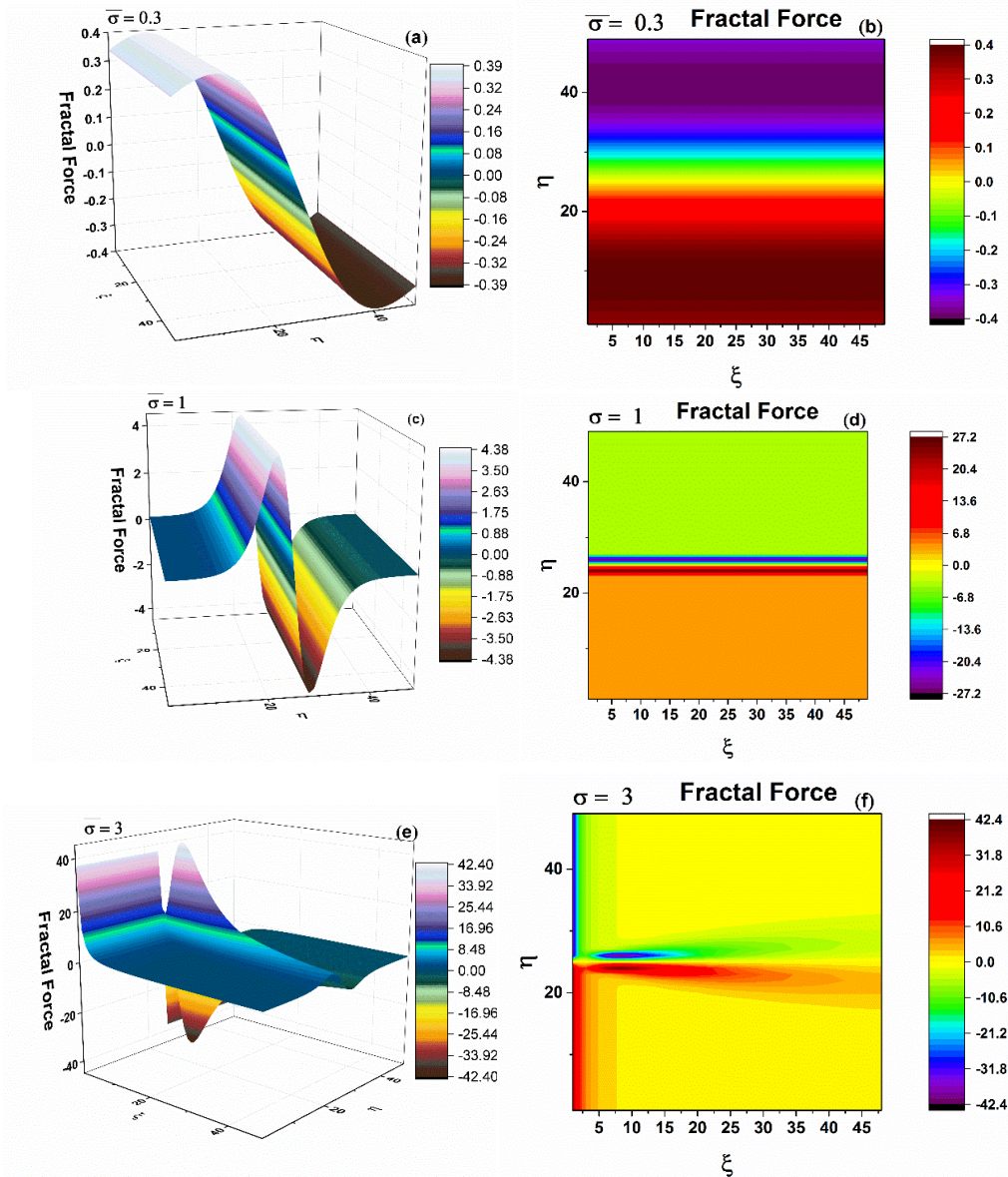
Figure IV.6   The dependence of the fractal force *F* on the normalized spatial coordinates ξ, η for the nonlinearity degree $\bar{\sigma}$ = 0.3, 1, and 3, respectively: (a, c, e) 3D representation and (b, d, f) contour plots.

The graphical simulation presented above, both in the case of laminar and turbulent flow showcased a possible strong connection between σ (which is inversely proportional with the fractalization degree) and the laser pulse width. Although results obtained here are important for the validation of the fractal hydrodynamic model, the information extracted is independent of time and thus our assessment of the LPP dynamics remains incomplete since the experimental data presented a synchronized space and time evolution. The obvious next step will be to perform the analysis for the time dependent solution and see what we can learn from this new type of analysis.

IV.5 A compact non-differential approach for modeling laser ablation plasma dynamics by means of a time-dependent solution

In our previous investigations, we only took into account the spatial evolution of the fractal fluid, which gave some important results. Let us now attempt to extend the model in order to analyze both the space and time evolution of the fluid, and thus to establish some correlations between the properties of the plasma and the theoretical parameters that describe the fractal fluid in the framework of our fractal hydrodynamic model. We would like to stress out that in the current presentation the theoretical model takes into account a relatively high number of parameters like the fractal-non-fractal transition coefficient, resolution scale or fractal dimension of the movement curves. Also, when the model is applied for the study of LPP dynamics other experimental factors need to be introduced, such as laser pulse Gaussian spatial and temporal distribution, probe and target bias, etc. As a result, the level of difficulty in performing the complete analysis of the LPP dynamics increases significantly. In order to use this approach, we will attempt to simplify through a viable choice of normalized dynamic variables with respect to the previously mentioned factors, both, from mathematical and physical perspectives, the interpretation of the plasma plume dynamics.

Let us now revisit the fractal hydrodynamic equations with an arbitrary constant fractal dimension. *Eq. (IV.43)* and *Eq. (IV.45)* will be further used to study the transient plasmas produced by nanosecond laser ablation. Again, given the non-linear nature of these equations, it still remains difficult to find an analytical solution for the outmost general case, as such the solution can be obtained for some particular circumstances: the one-dimensional case in the absence of any external potential ($U = 0$). In this approximation, the hydrodynamic equations become:

$$\partial_t v + v\partial_x v = -2\lambda^2 (dt)^{\left(\frac{4}{D_F}\right)-2} \partial_x (\rho^{-\frac{1}{2}} \partial_{xx} \rho^{-\frac{1}{2}}) , \qquad \text{Eq. (IV.75)}$$

$$\partial_t v + \partial_x \rho v = 0 . \qquad \text{Eq. (IV.76)}$$

We consider the initial conditions:

$$v(\text{x}, \text{t} = 0) = c , \qquad \text{Eq. (IV.77)}$$

$$\rho(\text{x}, \text{t} = 0) = \rho_0 e^{-\left(\frac{x}{\alpha}\right)^2} , \qquad \text{Eq. (IV.78)}$$

and the boundary ones:

$$v(\mathrm{x}=\mathrm{ct},\mathrm{t})=c\,,$$

<div align="right">Eq. (IV.79)</div>

$$\rho(\mathrm{x}=-\infty,\mathrm{t})=\rho(\mathrm{x}=\infty,\mathrm{t})=0\,.$$

<div align="right">Eq. (IV.80)</div>

where α is the half-width of the Gaussian distribution and c is the expansion velocity.

If the laser pulse intensity temporal distribution is of Gaussian type, we can consider a similar distribution for the plasma plume along the expansion direction and we can further assume that at $t = 0$ the center of the Gaussian distribution ρ expands with the velocity $<v(t=0)>=c$ and is spatially placed at $<x(t=0)>=0$. Since all the experimental investigations on the laser-produced plasmas were performed at time scales significantly longer than the laser pulse width, one can use the assumption from the previous chapter where we considered the drift velocity as being constant.

In the approximation that most of the laser energy is absorbed by the plume, as is the case of ns laser ablation, a relationship can be defined between the ejected particle density distribution and the energy temporal distribution of the laser beam. Using the boundary conditions *Eq. (IV.79)* and *Eq. (IV.80)* for any $t \neq 0$ or $<x>=ct$, one finds $<\partial_x Q>=0$ (for details see [*Agop et al.*, 2009, 2010; *Nica et al.*, 2009; *Irimiciuc et al.*, 2014a, 2014b]). This means that the particle density decreases significantly during expansion and it becomes null at large distances from the target.

The analytical solution for the *Eq. (IV.75)* and *Eq. (IV.76)*, with the initial conditions *Eq. (IV.77), Eq. (IV.78)* and the boundary ones *Eq. (IV.79)* and *Eq. (IV.80)*, in accord with the method presented in [*Agop et al.*, 2009; *Nica et al.*, 2009; *Irimiciuc et al.*, 2014a, 2014b] gives us the velocity field:

$$v(\mathrm{x},\mathrm{t})=\frac{c\alpha^2+\left[\dfrac{2\lambda(\mathrm{dt})^{(2/D_F)-1}}{\alpha}\right]^2 xt}{\alpha^2+\left[\dfrac{2\lambda(\mathrm{dt})^{(2/D_F)-1}}{\alpha}\right]^2 t^2}$$

<div align="right">Eq. (IV.81)</div>

and the density field:

$$\rho(\mathrm{x},\mathrm{t})=\frac{\pi^{-1/2}}{\left\{\alpha^2+\left[\dfrac{2\lambda(\mathrm{dt})^{(2/D_F)-1}}{\alpha}\right]^2 t^2\right\}^{1/2}}\exp\left\{-\frac{(x-ct)^2}{\alpha^2+\left[\dfrac{2\lambda(\mathrm{dt})^{(2/D_F)-1}}{\alpha}\right]^2 t^2}\right\}.$$

<div align="right">Eq. (IV.82)</div>

Using these results, we can reconstruct parameters such as current density, fractal potential and fractal force:

i) Current density

$$j(x,t) = v(x,y)\rho(x,t) =$$

$$\pi^{-1/2} \frac{c\alpha^2 + \left[\dfrac{2\lambda(dt)^{(2/D_F)-1}}{\alpha}\right]^2 xt}{\left\{\alpha^2 + \left[\dfrac{2\lambda(dt)^{(2/D_F)-1}}{\alpha}\right]^2 t^2\right\}^{3/2}} \exp\left\{-\dfrac{(x-ct)^2}{\alpha^2 + \left[\dfrac{2\lambda(dt)^{(2/D_F)-1}}{\alpha}\right]^2 t^2}\right\} \quad ; \qquad \text{Eq. (IV.83)}$$

ii) Fractal potential

$$Q(x,t) = -2\lambda^2(dt)^{(4/D_F)-2}\left\{\dfrac{x-ct}{\alpha^2 + \left[\dfrac{2\lambda(dt)^{(2/D_F)-1}}{\alpha}\right]^2 t^2}\right\}^2 \quad ; \qquad \text{Eq. (IV.84)}$$

iii) Fractal force

$$F(x,t) = -\partial_x Q = 4\lambda^2(dt)^{(4/D_F)-2} \dfrac{x-ct}{\left\{\alpha^2 + \left[\dfrac{2\lambda(dt)^{(2/D_F)-1}}{\alpha}\right]^2 t^2\right\}^2} \quad . \qquad \text{Eq. (IV.85)}$$

For any $t \neq 0$ the equations *(IV.81 – IV.85)* describing the dynamics of the fractal fluid are non-homogeneous in x and t. If we apply $x = ct$ these relationships become:

$$v(x = ct, t) \to c$$

$$\rho(x,t) = \dfrac{\pi^{-1/2}}{\left\{\alpha^2 + \left[\dfrac{2\lambda(dt)^{(2/D_F)-1}}{\alpha}\right]^2 t^2\right\}^{1/2}}$$

$$j(x,t) = v(x,y)\rho(x,t) = \dfrac{\pi^{-1/2}c}{\left\{\alpha^2 + \left[\dfrac{2\lambda(dt)^{(2/D_F)-1}}{\alpha}\right]^2 t^2\right\}^{3/2}} \quad . \qquad \text{Eq. (IV.86)}$$

$$Q(x = ct, t) \to 0$$

$$F(x = ct, t) \to 0$$

The above equations allow us to validate our model. Indeed, we have presented in the previous chapters (*II* and *III*) that the LPPs are described by a shifted Maxwellian distribution function. More precisely, the temporal trace of the ions/electrons can be described by the following function:

$$j(t) \sim \frac{1}{t^{3,4}} \exp\left[-\frac{m}{2kT_{ionic}} \left(\frac{d}{t} - v_{drift} \right)^2 \right].$$

Eq. (IV.87)

In the framework of our fractal approach, *Eq. (IV.86)* with the following conditions:

$$t \gg \frac{\alpha^2}{2\lambda(dt)^{\left(\frac{2}{D_F}\right)-1}}$$

$$x \gg \frac{c\alpha^2}{2\lambda(dt)^{\left(\frac{2}{D_F}\right)-1}}$$

Eq. (IV.88)

takes the approximate form:

$$j(x,t) \sim \pi^{-1} \frac{c}{\alpha} \left[\frac{\alpha^2}{2\lambda(dt)^{\left(\frac{2}{D_F}\right)-1}} \right]^2 \frac{1}{t^3} \exp\left\{ -\left[\frac{\alpha^2}{2\lambda(dt)^{\left(\frac{2}{D_F}\right)-1}} \right]^2 \left(\frac{x}{t} - c \right)^2 \right\}.$$

Eq. (IV.89)

We can observe that in *Eq. (IV.89)*, the current density of the fractal fluid depends also on the scale resolution, so that we obtain a fractal distribution describing the temporal traces of the ionic current. Assuming now that the plasma particle dynamics takes place on geodesics described by a fractal dimension $D_F = 2$ (Peano-type curves [*Mandelbrot*, 1982; *Nottale*, 1993, 2010; *Merches and Agop*, 2015]), we are able to eliminate the scale resolution dependence of the current density. Moreover, by means of correspondences:

$$x \equiv d, v_{drift} \equiv c, \frac{m}{2kT_{ion}} \equiv \left[\frac{\alpha^2}{2\lambda(dt)^{\left(\frac{2}{D_F}\right)-1}} \right]^2,$$

Eq. (IV.90)

where *d* is the target-probe distance, *v* is the drift particle velocity, *T* is the particle temperature, *m* is the rest mass of the ion and *k* is the Boltzmann constant, *Eq. (IV.89)* is reduced to *Eq. (IV.87)*.

In order to simplify the multi-functional dependences of the fractal dynamic variables (ρ, v, j, etc.) on parameters incorporating some of the external factors ($ex: \alpha, \lambda, (dt)^{\left(\frac{2}{D_F}\right)-1}$ etc.) we will choose to normalize these equations starting with the condition: $2\lambda = \alpha c$. These equations will be normalized by means of the variables:

$$\xi \to \frac{x}{\alpha}, \tau \to \frac{tc}{\alpha}, \mu \to 2\lambda(dt)^{\left(\frac{4}{D_F}\right)-2}.$$

Eq. (IV.91)

This normalization allows us to rewrite the dependences of the plasma variables on the fractalization degree which will now incorporate all the external influences to the plume evolution:

i)   Normalized velocity:

$$V(\xi,\tau,\mu) = \frac{1+\mu\xi\tau}{1+\mu\tau^2};$$

Eq. (IV.92)

ii)   Normalized particle density:

$$N(\xi,\tau,\mu) = [1+\mu\tau^2]^{-1/2} \exp\left[-\frac{(\xi-\tau)^2}{1+\mu\tau^2}\right];$$

Eq. (IV.93)

iii)   Normalized current density

$$J(\xi,\tau,\mu) = \frac{1+\mu\xi\tau}{[1+\mu\tau^2]^{-3/2}} \exp\left[-\frac{(\xi-\tau)^2}{1+\mu\tau^2}\right];$$

Eq. (IV.94)

iv)   Normalized fractal potential

$$q(\xi,\tau,\mu) = \mu\left[\frac{(\xi-\tau)^2}{1+\mu\tau^2}\right]^2;$$

Eq. (IV.95)

v)   Normalized fractal force

$$f(\xi,\tau,\mu) = \mu\frac{(\xi-\tau)^2}{\left[1+\mu\tau^2\right]^2};$$

Eq. (IV.96)

vi)   Normalized specific length

$$\Lambda(\xi,\tau,\mu) = \left[\frac{q(\xi,\tau,\mu)}{N(\xi,\tau,\mu)}\right]^{1/2} = \mu\frac{\xi-\tau}{[1+\mu\tau^2]^{-3/2}} \exp\left\{-\frac{1}{2}\frac{(\xi-\tau)^2}{\left[1+\mu\tau^2\right]}\right\}.$$

Eq. (IV.97)

IV.5.1   Numerical simulation

Using the system of equations defined above we will further investigate the spatial and temporal evolution of all these plasma dynamics variables in similar "external conditions" (for a constant value of μ). Also, we will explore the cumulative effect of the external parameters (fractal-non-fractal transition coefficient, λ, and scale resolution dt, and fractal dimension, D_F, of the movement curves), expressed through μ, on the dynamic variables evolution. We need also to consider that each temporal regime (ns, ps, fs) is defined by specific ablation mechanisms which were discussed in the previous chapters. Each mechanism is characterized by specific interaction time-scales to which we attributed specific fractal-non-fractal transition coefficients and scale resolutions. This aspect was an important part in understanding the results obtained in a stationary approximation and will be further taken into consideration. As such in accord with our previous results the electrostatic mechanisms, that manifest at a short evolution time (i.e. Coulomb explosion), will be defined by $\mu < 1$, while thermal mechanisms, which can be observed at longer evolution times, are defined by $\mu > 1$.

Before we discuss the results, it is important to make a good correlation between the variables describing the fractal fluid and the ones describing the LPP. Thus, the fractal particle density will describe the ionic/electronic density, the fractal current density will be related to the plasma ionic or electronic currents, the fractal velocity will be attributed to the thermal velocity. In the classical plasma physics the thermal velocity is used to describe the random movement of the particle outside the collecting space charge volume around the probe. Analogous, in the framework of our model, the fractal velocity defines the particle movement induced by the fractal field. Within the fractal model we do not have define a "fractal temperature", but the nature of the plasma temperature (a measure of the internal energy of the plume) is well described by the fractal potential, which is a measure of non-differentiability. Thus we can assume a proportionality relationship between the fractal potential and plasma temperature. Finally, the specific length of the fractal fluid, which defines fractal – non-fractal transition in the ablation plasma dynamics, is in good correspondence with the meaning of the Debye length from plasma physics, *i.e.* a characteristic length related to a minimum volume for which we can consider the plasma as being homogenous and neutral.

Once these connections are established, we can proceed to analyze the dynamics of a laser-produced plasma plume using the time-dependent solution of the compact fractal hydrodynamic model. Let us now study the qualitative dependences given by our model. The validity of the correlations presented above will be verified by using the theoretical function to fit the experimental data from all three ablation regimes. The comparison will be presented in the last part of the chapter, where it will be verified if our initial assumption is justified or not.

Figure IV.7 presents the space-time evolution of the previously mentioned dynamic variables determined by the equations (*IV.92 - IV.95)*. The simulations presented in this figure are

for a constant value of μ (= 5), characteristic for only one resolution scale describing a plasma plume produced mainly through thermal mechanisms. The particle density presents a quasi-exponential decrease in both time and space. Due to the mathematical relationship between the particle density and the current density, the latter will follow a similar evolution as the fluid expands in both space and time. These results are in good agreement with the predictions of other "differential" theoretical models [*Amoruso et al.,*, 1999] and are consistent with our experimental findings and other experimental studies [*Hansen et al.*, 1999; *Lunney et al.*, 2007; *Donnelly et al.*, 2010b]. *Figure V.7d* contains the spatial and temporal evolution of the plasma temperature. We can identify two maxima, one at short evolution times and a second one at longer evolution time. This particular result is in good agreement with the two-temperature model [*Zavestovskaya*, 2008; *Werner*, 2011; *Nica*, 2012], where the plume is presented as having two electron populations (hot and cold) having different temperatures.
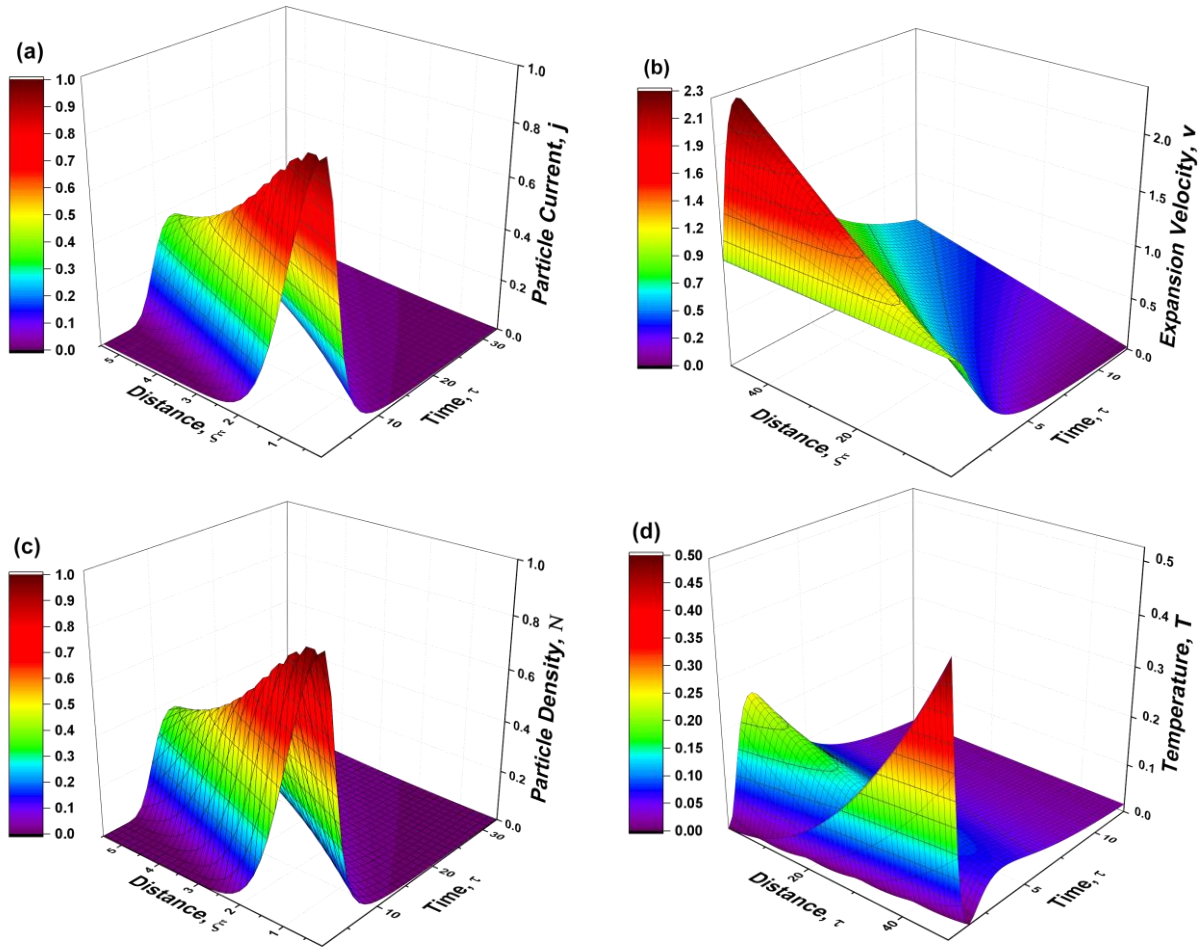
Figure IV.7   Space-time evolution of the following normalized plasma dynamics variables: particle current (a), expansion velocity (b), particle density (c) and temperature (d) for a fractalization degree $\mu = 5$.

Once these dependences given, in order to perform any comparison with our experimental data and with the ones given by differential theoretical models, we need to extract individual traces for all the plasma parameters. This can be achieved either for a fixed distance, where we follow temporal evolution, or for a constant moment of time following the spatial evolution. Thus, we represented the time dependence for a fixed value of spatial coordinate ($\xi = 5$) (*Figure IV.8a*) and the space dependence for a given value of temporal coordinate ($\tau = 5$), for the same plasma dynamics variables (*Figure IV.8b*). The evolution of some of the plasma parameters like particle current, density and temperature is in good agreement with the ones predicted by the theoretical models of Anisimov [*Anisimov et al.,* 1995,2002] and Murakami [*Murakami et al.,* 2005]. The decrease in temperature, velocity and particle density is also reflected in the evolution of the Debye length. Its increase is explained by the rarefaction of the plume which is also seen in the decrease of the particle density and plasma temperature presented in *Figure IV.8*.
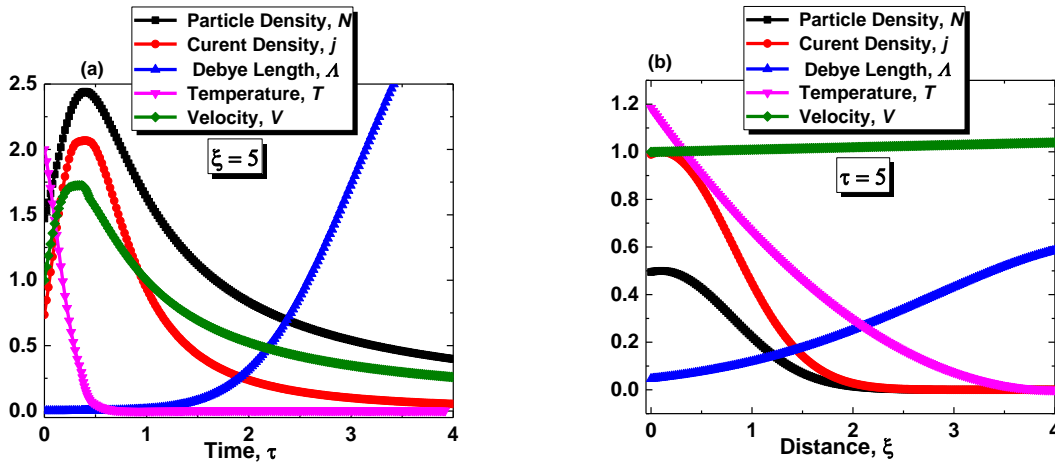
Figure IV.8   Normalized plasma dynamics variables (particle density, temperature, Debye length, velocity and current density) evolutions in time (a) and space (b) for a fractalization degree $\mu = 5$.

In the stationary case, we observed that the resolution scale plays an important role in the outcome of the expansion velocity field and thus on the shape of the plume. Once selected a resolution scale (in our case $\mu > 5$), let us investigate the effect of the increase of the fractalization degree on the evolution of the plasma parameters. Thus, all changes in temperature, density or velocity will affect the shape of the LPP. These changes are presented in *Figure IV.9* where we display the contour plot of the particle density in a (ξ, τ) plane. We observe that for smaller values ($\mu = 5 \div 10$) the plasma plume has a longer life-time, presents a higher density and has an elongated shape. With the increase of the fractalization degree, a decrease both of the particle density and of the plume life-time is observed. The decrease can be attributed to the effect induced by the properties of the expanding medium and can be correlated with strong scattering processes. The ejected cloud becomes confined for values higher than 50. The confinement of the plume is a

well-known phenomenon, being experimentally observed by other authors [*Harilal et al.*, 2014; *Amoruso et al., 2010*] when investigating the effect of the background pressure on the plume dynamics. In our opinion, the background pressure changes the mean free path and thus the fractal trajectories of the particles are modified (their geodesics), resulting in considerable changes in the plasma space-time evolution
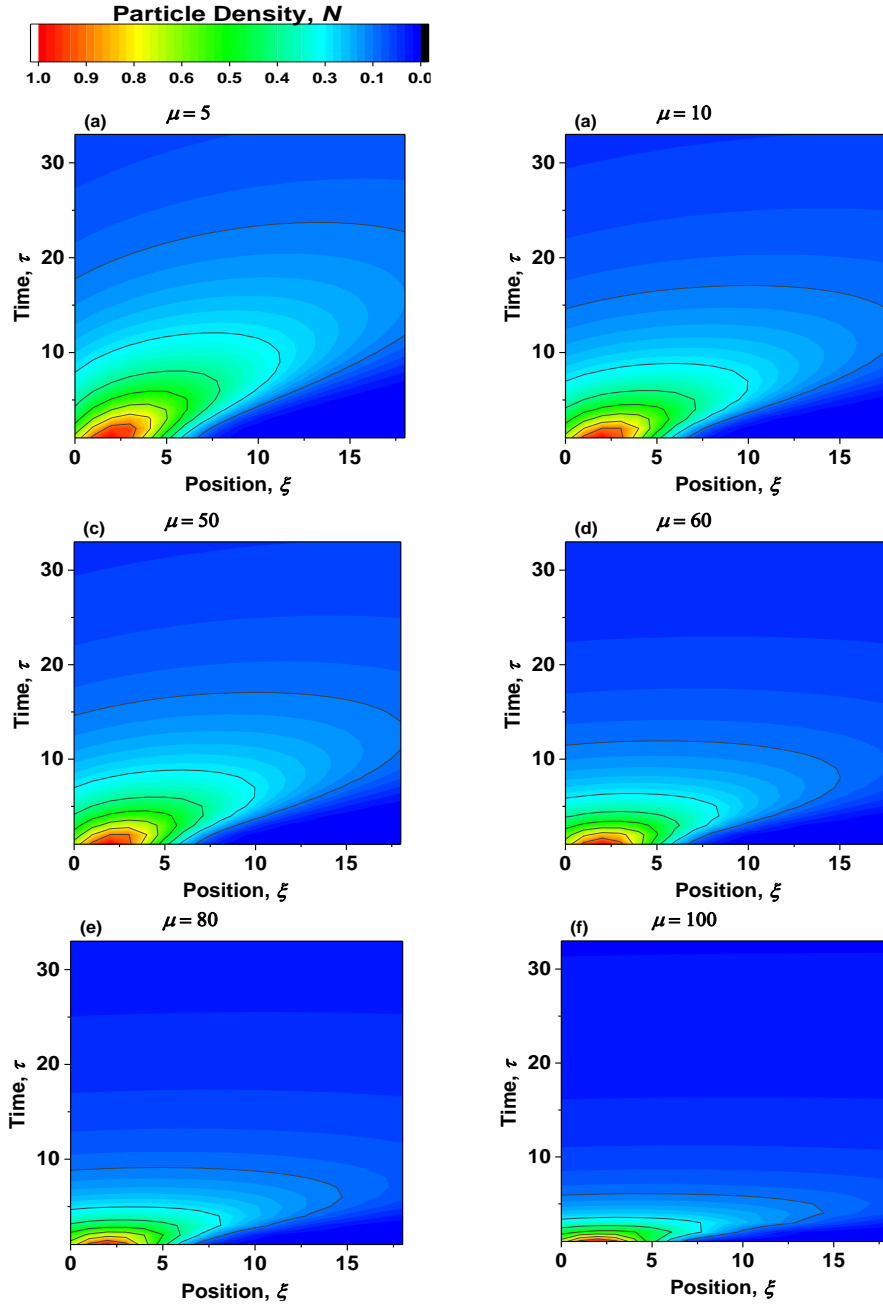
Figure IV.9   Contour plots displaying the space-time dependence of the normalized particle density for various fractalization degrees: $\mu = 5$ (a), $\mu = 10$ (b), $\mu = 50$ (c), $\mu = 60$ (d), $\mu = 80$ (e), $\mu = 100$ (f).

The change induced by the control parameter μ onto the pressure is not unique. Subsequently, due to the interconnectivity of all parameters, all the other plasma dynamics variables are affected by it. Let us focus now on the other plasma parameters (ρ, v, T, j) and to represent the contour plot on the (μ,τ) plane at a constant value of $\xi = 5$. The contour plot of the functions given in equations *(IV.92 - IV.95)* for a constant distance ($\xi = 5$) are represented in *Figure IV.10*. We observed that the plasma temperature presents two maxima as the value of μ is increased. The first one can be assimilated to the first plasma structure, since it is observed for values of $0 < \mu < 1$ and short evolution times. The second maximum is correlated with the second plasma structure, which is observed for $\mu > 1$ and longer evolution times. In literature, there are a series of plasma parameters which can have a direct influence on the fractalization degree, such as the background pressure [*Amoruso*, 2010], the laser pulse width [*Pandey et al.*, 2015] or the laser fluence [*Anoop et al.*, 2016], which may influence the structure and the shape of the plasma plume, but given the manner in which we defined μ, we cannot differentiate between them.
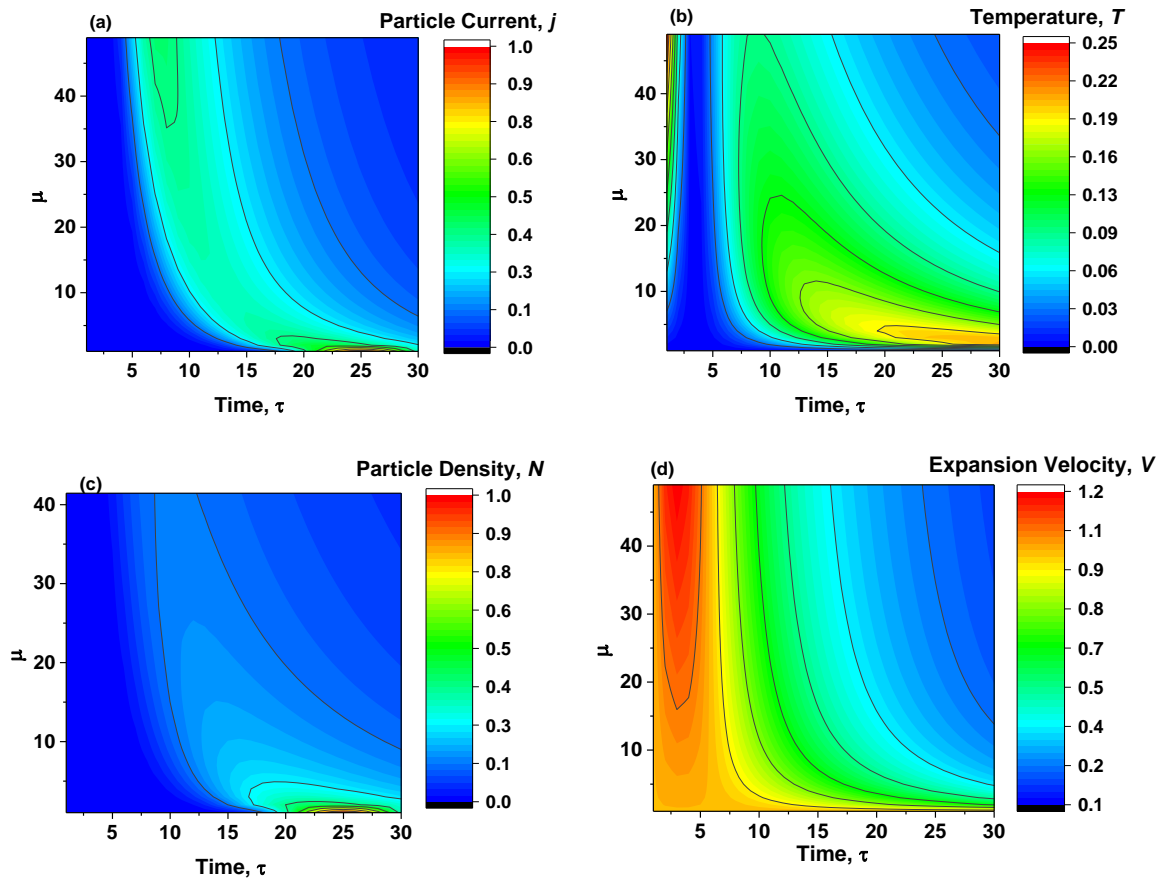
Figure IV.10   Contour plot of the following normalized plasma dynamic variables: current density (a), plasma temperature (b), particle density (c) and expansion velocity (d) for a constant normalized distance $\xi = 5$.

In both stationary and time-dependent studies, the simulation revealed different types of behaviors as a function of scale resolution. We would like to remind that the scale resolution has a 1/σ dependence and is proportional to μ. Thus, as a general remark, the overall plasma current, either ionic or electronic, will be a sum of all the individual contributions given by different plasma structures described by different scale resolution. The spatial and temporal distributions of the current density that describe the plasma plume for a constant value of $\mu = 0.5$ are plotted in *Figure IV.11(a-b)* and for $\mu = 5$ in *Figure IV.11(c-d)*. For the case of ns LPP we will have two resolution scales describing the two-structure plasma. Each structure is characterized by a specific particle density, expansion velocity and particle current density, and thus the global plasma can be described as a scale resolution superposition of individual current densities for $\mu = 5$ and $\mu = 0.5$ which is plotted in *Figure IV.11(e-f)*. This allows us to obtain a representation of the particle current that contains contributions from both types of ablation mechanisms.

From these representations, we find that the current density has a decrease in its amplitude and presents a shift towards higher space-time coordinates. This confirms the constant expansion velocity hypothesis used during the definition stage of the model. We obtained a space-time decrease of the current density as the plume expands, which is consistent with our experimental findings (i.e the case of ICCD fast camera imaging) and other similar dependences obtained through other differential theoretical approaches [*Mora et al.*, 2003; *Donnelly et al.*, 2010a; *Craxton et al.*, 2015]

The non-differential theoretical model through the two solutions (stationary and time-dependent) gives us the opportunity to thoroughly investigate the dynamics of a fractal fluid which then is attributed to the one real physical object - laser-produced plasma. The basic space-time evolutions of the plasma parameters are consistent with other theoretical models. The ability to vary the scale resolution allows us to investigate the dynamics of LPP generated through different ablation mechanisms. Although the results are promising they are mainly qualitative, for a quantitative approach we need to use the theoretical functions (*Eqs. (IV.92-97)*) to fit the experimental data and compare the parameters of the fractal fluid with those of the LPP.
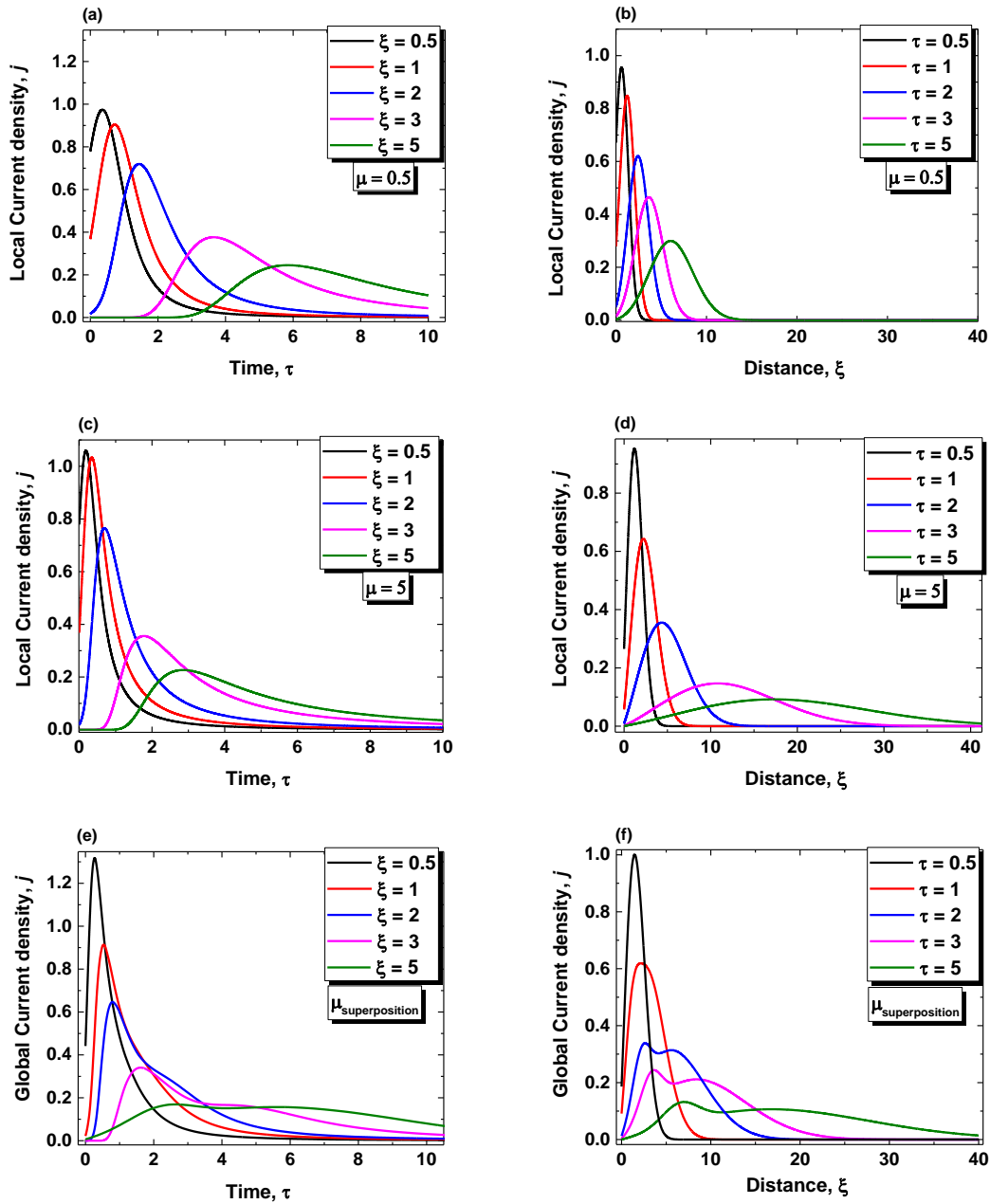
Figure IV.11   Spatial and temporal evolution of individual normalized current density for $\mu = 0.5$ (a-b), $\mu = 5$ (c-d), and total normalized current density for a scale resolution superposition $\mu = 5 \,/\, \mu = 0.5$ (e-f).

IV.5.2   Experimental confirmation of the model

The validation of any new theoretical model, or in our case the variation on a previously known model, can be achieved by confronting the simulated results to the physical reality of the phenomena, as seen from the experimental data. There are some qualitative and quantitative comparisons. From a qualitative perspective, the changes in the velocity field spatial distribution (*Figure IV.7*) with the variation of the resolution scale are similar to the ones obtained through experimental investigation regarding the shape of the expanding plume (*Figures III.15, III.25 and III.35*). From this qualitative "consistency" between the two methods, a good correlation can be made between the laser pulse width and the scale resolution parameter. This confirms our supposition that each ejection mechanism is described by a different sale resolution. Also, the increase of the lateral expansion (η axis, in the case of the theoretical model) is consistent with the spatial distribution of the plume observed through ICCD fast camera imaging, where we observed that the plasmas generated in ps and ns present a more significant lateral expansion with respect to the fs case. Moreover, given that the results presented in *Figures IV.7-11*, showcasing the spatial and temporal evolution of various plasma parameters, are dependent on normalized coordinates, the overall consensus will still be qualitative. The space-time evolution of fractal temperature, particle density, fractal velocity and specific length are consistent with those of their plasma physics equivalents (electron temperature, ionic/electronic density, thermal velocity and Debye length) determined by Langmuir probe measurements, for all three ablation regimes.

Aside the comparisons made above with other theoretical and experimental studies, let us validate our model by comparing it with experimental observations of some variables introduced in the previous sections (*II* and *III*). The temporal evolutions were fitted with the functions *Eq. (IV.92 - IV.95)* describing the corresponding normalized dynamic variables of our fractal fluid, presented in the previous sections, confirming that the model successfully reproduces the experimental data, with fitting parameters displayed in *Table IV.1* and discussed below. The experimental data confirm the decrease in electron temperature (*Figure IV.12a*), particle density (*Figure IV.12b*) and thermal velocity (*Figure IV.12.c*) and the increase of the specific length (Debye length, *Figure IV.12d),* as predicted by the theoretical model (*Figure IV.8*).
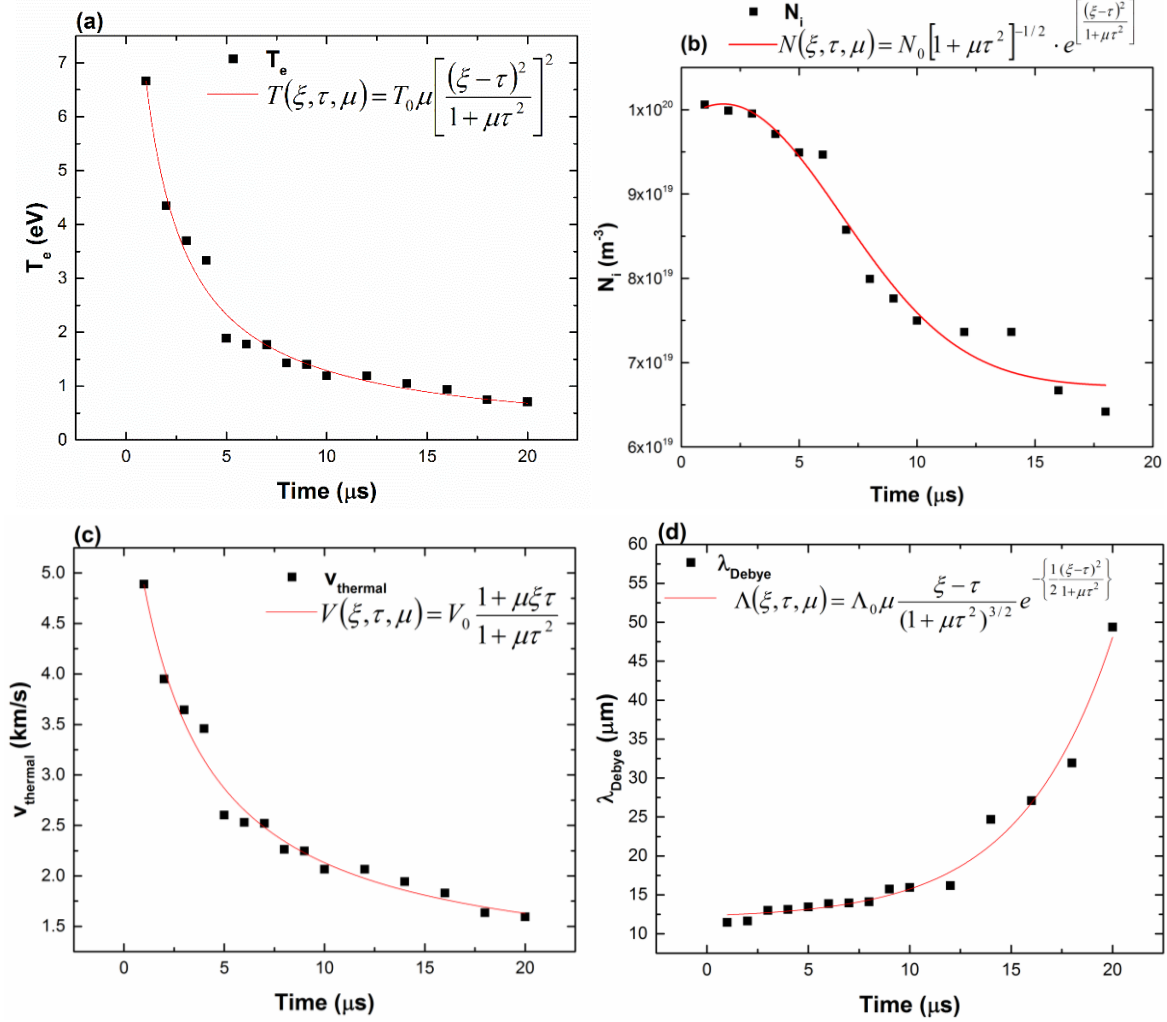
Figure IV.12   Temporal evolutions of the electron temperature (a), ion density (b), thermal velocity (c), Debye length (d) and individual fits using the relationships extracted from the compact fractal hydrodynamic model (see text and *Table IV.I* for details).

For fitting the experimental data with the theoretical model, they were first normalized with respect of the minimum recorded values (T_0, N_0, v_0, and Λ_0 - see *Table IV.I*). Also, the time was normalized with respect to the value $\tau_0 = 1$ µs (see above). From the numerical fit of the experimental data with the theoretical dependences given by our model (*Eqs. (IV.92 – 95))*, one can obtain the values of ξ and μ (see *Table IV.1*). The good agreement (within ~ 10%) obtained between their values derived from the four different fits confirms the validity of our model. Moreover, the values returned by the fits for the fractalization degree μ (in the range 2.6 – 2.95) correspond to the second plasma structure, result in good agreement with the evolution-times at which the experimental investigations were made (> 1 µs).

Table IV.1.   Correlations between the plasma parameters determined from the Langmuir Probe theory and the non-differential theoretical model variables.

Plasma variables given by the Langmuir Probe Method	Plasma variables as given by the compact fractal hydrodynamic model	Normalization and fitting values
Electron Temperature $$T_e = \frac{ln(\Delta I_e)}{\Delta V_{Probe}}$$	Normalized temperature by means of fractal potential $$q(\xi, \tau, \mu) = \mu \left[\frac{(\xi - \tau)^2}{1 + \mu\tau^2}\right]^2$$	$T_0 = 0.68$ eV $\xi \sim 11.5$ $\mu \sim 2.8$
Ion Density $$n_i = \frac{I_{i0}}{eA}\sqrt{\frac{2\pi m_i}{k_B T_i}}$$	Normalized density by means of non-differential state density $$N(\xi, \tau, \mu) = [1 + \mu\tau^2]^{-1/2} \cdot exp\left[-\frac{(\xi - \tau)^2}{1 + \mu\tau^2}\right]$$	$N_0 = 4.25 \cdot 10^{19} cm^{-3}$ $\xi \sim 11.8$ $\mu \sim 2.95$
Thermal Velocity $$v_{thermal} = \frac{1}{4}\sqrt{\frac{8k_B T_e}{\pi m_e}}$$	Normalized velocity by means of non-differentiable velocity $$V(\xi, \tau, \mu) = \frac{1 + \mu\xi\tau}{1 + \mu\tau^2}$$	$V_0 = 1.594$ km/s $\xi \sim 10.5$ $\mu \sim 2.6$
Debye Length $$\lambda_{Debye} = \sqrt{\frac{\varepsilon_0 k_B T_e}{e^2 n_e}}$$	Normalized specific length by means of ratio between the fractal potential and states density $$\Lambda(\xi, \tau, \mu) = \mu\frac{(\xi - \tau)}{[1 + \mu\tau^2]^{3/2}}exp\left\{-\frac{1}{2}\frac{(\xi - \tau)^2}{[1 + \mu\tau^2]}\right\}$$	$\Lambda_0 = 12.5$ μm $\xi \sim 10.7$ $\mu \sim 2.7$

In the previous chapter, we presented a broad space- and time-resolved investigation of laser-produced plasmas in various regimes. We can extend our theory-experiment comparisons towards various other sets of data representing the temporal evolution at various distances and the spatial evolution for different moments of time (see *Chapter III*). At this point we would like to remind that when a set of experimental data is compared with the theoretical functions we obtain a group of spatial and temporal coordinates characteristic to our fractal model and a specific value for the fractalization degree, defined for each experimental curve (*Table IV.1*). In the case of Al ns-LPP we extracted the theoretical values of the fractalization degree for each space-time coordinate (*Figure IV.13(a-b)*). Further we represented in *Figure IV.13(c-d)* a comparison between theoretical values with their experimental correspondences. We obtained a good correlation between the experimental and theoretical values, as the fractal model in its compact form manages to identify the spatial and temporal coordinates of the experimentally probed plasma volume.
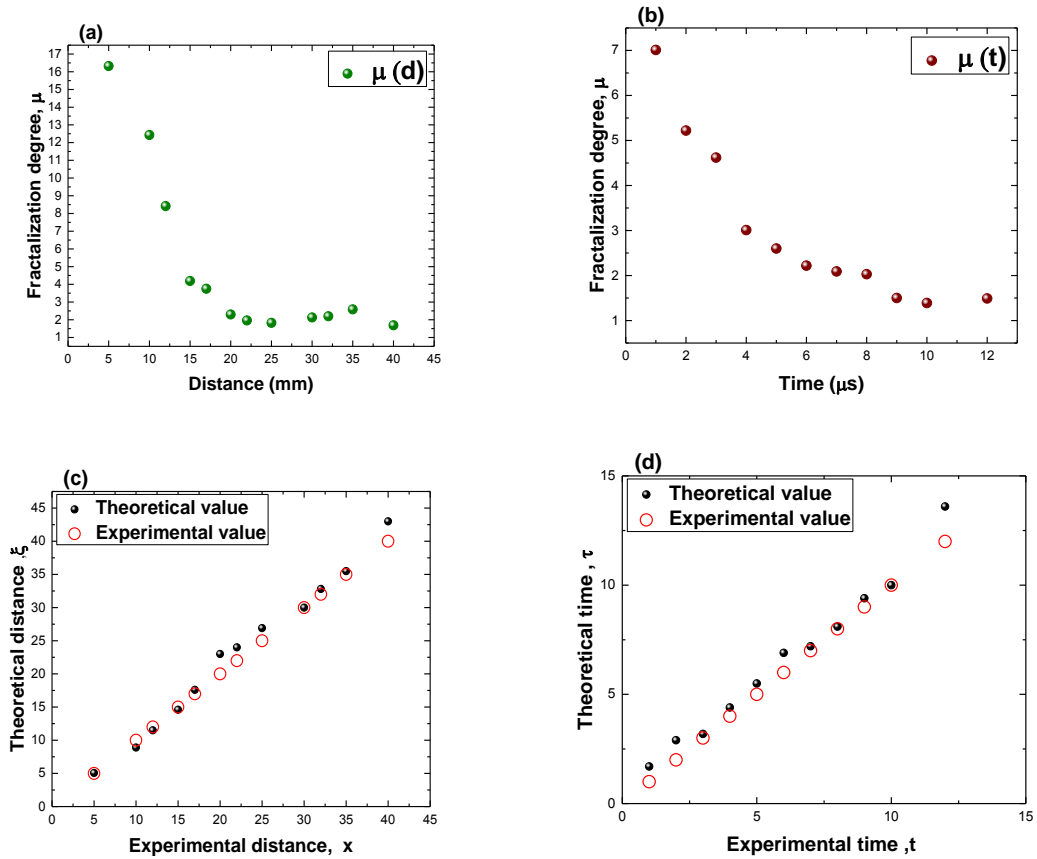
Figure IV.13 Space-time evolution of the fractalization degree determined for a ns laser-produced plasma on an Al target (a-b), and the comparison between the experimental and theoretical values of the probed plasma volume space-time coordinates (c-d).

We observe that the fractalization degree decreases at longer evolution times and at longer distances, result which is consistent with our experimental findings, where we observed that the particle concentration, thermal velocity and electron temperature all presented a similar evolution. As the plume evolves and it loses energy, the collisions between particles will be reduced and their trajectories will be less "broken", hence a decrease in the value of the fractalization degree. However, the values of the fractalization degree are higher than 1, thus we are still describing the component of the plume generated by thermal mechanism. The decrease does not suggest a possible transition towards electrostatic effects but simply "reflects" the decrease in thermal energy of the plume

Finally let us compare the results obtained from the fit of the experimental data extracted in different ablation regimes (ns, ps, fs). In *Figure IV.14* we plotted the evolution of the fractalization degree as a function of the pulse width. We observe that the results are in good agreement with our previous assumptions, when we attributed a resolution scale to a specific ablation mechanism. The fractalization degree, proportional with the scale resolution, has the smallest value for the case of fs laser ablation and as the pulse width increases and the thermal mechanism becomes predominant, the fractalization degree increases. Thus, we are able to extract from the experimental data the characteristic fractalization degree for each ablation regime, and confirm our assumption that each regime is described by a different resolution scale directly connected to the ablation mechanism involved in the particle ejection.
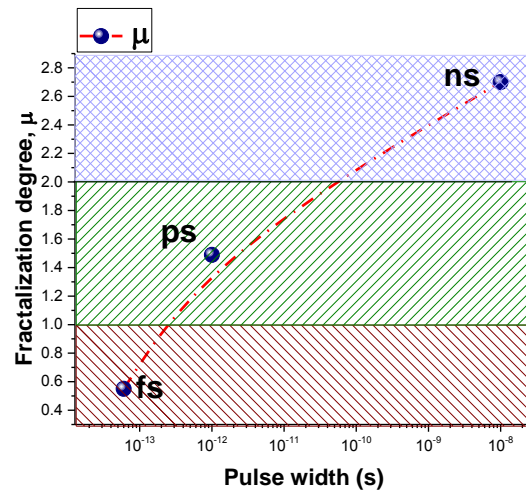
Figure IV.14   The evolution of the fractalization degree with the laser beam pulse width.

IV.6   Conclusions

We formulated two simplified versions of the fractal hydrodynamic model and used it to describe the dynamics of a fractal fluid, which is associated with a laser-produced plasma. The first approach involved the use of stationary solutions in order to make some global assessments on the expansion of a fractal fluid. The results were found to be in good agreement with the ICCD fast camera imaging performed on laser-produced plasmas in various ablation regimes, results discussed in *Chapter III*.

The second approach was to focus on the time-dependent solution. This led to the investigations of the space and time evolution of expansion velocity, particle current density and plasma temperature, and the results were in good agreement with other theoretical models. The model manages to simulate the formation and expansion of plasma plumes taking into account the scale differences between different ablation mechanisms.

The dynamics of the plumes revealed two contributions to plasma temperature and current density, which is consistent with the two plasma structures experimentally observed in the previous chapter. The particle current was reconstructed in order to showcase the contributions from the plasma structures, and the constant expansion velocity assumption was verified. The effect of the external conditions on the plasma dynamics was theoretically investigated, and a confinement of the fractal fluid was evidenced, consistent with the effect of the background pressure. The theoretical model was validated by experimental investigations performed on a nanosecond laser-produced Aluminum plasma. Good agreement was found between the temporal evolution of the plasma parameters determined through the Langmuir probe method and those found using the non-differentiable theoretical model.

The normalization of the plasma dynamic variables leads to a more compact form of the theoretical model, and thus allowed us to use a single control parameter that embodies the contributions of several external parameters on the dynamics of the ejected particles. Moreover, we present here for the first time clear associations between fractal model variables and specific plasma parameters (electron temperature, thermal velocity, particle density). Also for the first time we were able to attribute to each ablation regime a specific range of values of the fractalization degree. These results were achieved by fitting the experimental data acquired in each ablation regime.

The overall results presented in this chapter underline the practicality of the non-differential theoretical model for the study of laser–produced plasma dynamics. The experimental data confirm the predictions made by the fractal theoretical model and underline the utility of such an approach.

References for Chapter IV

Agop, M., P. Nica, S. Gurlui, C. Focsa, V. P. Paun, and M. Colotin (2009), Implications of an extended fractal hydrodynamic model, *Eur. Phys. J. D*, *56(3)*, 405–419.

Agop, M., P. Nica, S. Gurlui, and C. Focsa (2010), Fractal hydrodynamic model of high-fluence laser ablation plasma expansion*, AIP Conf. Proc., 64*, 482–491.

Amoruso, S. (1999), Modelling of laser produced plasma and time-of-flight experiments in UV laser ablation of aluminium targets, *Appl. Surf. Sci.*, *138–139*, 292–298.

Amoruso, S. (1999), Modeling of UV pulsed-laser ablation of metallic targets, *Appl. Phys. A, 69,* 323–332.

Amoruso, S., J. Schou, J. G. Lunney, and C. Phipps (2010), Ablation Plume Dynamics in a Background Gas, *AIP Conf. Proc.*, *1278(1)*, 665–676.

Anisimov, S. I., and B. S. Luk'yanchuk (2002), Selected problems of laser ablation theory, *Phys-Usp.*, *45(3)*, 293–324.

Anisimov, S. I., B. S. Luk'yanchuk, and A. Luches (1995), Dynamics of the three-dimensional expansion in a vapor produced by a laser pulse, Zh. Eksp. Teor. Fiz., *108(2)*, 240–257.

Anoop, K. K., M. P. Polek, R. Bruzzese, S. Amoruso, and S. S. Harilal (2015), Multidiagnostic analysis of ion dynamics in ultrafast laser ablation of metals over a large fluence range, *J. Appl. Phys.*, *117(8)*, 083108.

Anoop, K. K., S. S. Harilal, R. Philip, R. Bruzzese, and S. Amoruso (2016), Laser fluence dependence on emission dynamics of ultrafast laser induced copper plasma, *J. Appl. Phys.*, *120(18)*, 185901.

Badii, R., and A. Politi (1999), *Complexity: Hierarchical structures and scaling in physics*, Cambridge University Press, Cambridge.

Batchelor, G. K. (1999), *An introduction to fluid dynamics*, Cambridge University Press, Cambridge

Bogaerts, A. Z., Chen, R., Gijbels, and A. Vertes (2003), Laser ablation for analytical sampling: what can we learn from modeling?, *Spectrochem. Acta Part B, 58*, 1867–1893.

Boardman A. D., B. Cresswell, and J. Anderson (1996), An analytical model for the laser ablation of materials, *Appl. Surf. Sci., 55,* 96–98.

Bulgakova, N. M., and A. V. Bulgakov (1998), Gas-dynamic effects of the interaction between a pulsed laser-ablation plume and the ambient gas : analogy with an underexpanded jet, *J. Phys. D. Appl. Phys.*, *31*, 693–703.

Bulgakova, N. M., R. Stoian, A. Rosenfeld, I. V. Hertel, W. Marine, and E. E. B. Campbell (2005), A general continuum approach to describe fast electronic transport in pulsed laser irradiated materials: The problem of Coulomb explosion, *Appl. Phys. A-Mater., 81(2)*, 345–356.

Chen, F. F. (2003), *Lecture Notes on Langmuir Probe Diagnostics*, Academic, New York.

Craxton, R. S., K.S. Anderson, T. R. Boehly, V. N. Goncharov, D. R. Harding, J. P. Knauer, P. W. McKenty, J. F. Myatt, R. W. Short, S. Skupsky, W. Theobald, T. J. B. Collins, J. A. Delettrez, S. X. Hu, J. A. Marozas, A. V.

Maximov, D. T. Michel, P.B. Radha, S. P. Regan, and T. C. Sangster (2015), Direct-drive inertial confinement fusion: A review, *Phys. Plasmas, 22(11)*, 110501.

Cristescu, C. P. (2008), *Nonlinear Dynamics and Chaos in Science and Engineering*, Academy Publishing House, Bucharest.

Conde, J. C., F. Lusquinos , P. Gonzalez, J. Serra, B. Leon , A. Dima , L. Cultrera , D. Guid, A. Zocco, and A. Perrone (2004), Finite element analysis of the initial stages of the laser ablation process, *Thin Solid Films, 453–454*, 323–327.

Deville, M. O., and T. B. Gatski (2012), *MathematicalModeling For Complex Fluids And Flows*, Springer, New York.

Dimitriu, D. G., S. A. Irimiciuc, S. Popescu, M. Agop, C. Ionita, and R. W. Schrittwieser (2015), On the interaction between two fireballs in low-temperature plasma, *Phys. Plasmas*, *22(11)*, 113511.

Dabby F., and U. Paek (1972), High intensity laser-induced vaporization and explosion of solid material, *IEEE J. Quantum Electr., 8*, 106–111.

Dogar, A. H., B. Ilyas, S. Ullah, A. Nadeem, and A. Qayyum (2011), Langmuir probe measurements of Nd-YAG laser-produced copper plasmas, *IEEE T Plasma Sci.*, *39*, 897–900.

Doggett, B., C. Budtz-Joergensen, J. G. Lunney, P. Sheerin, and M. M. Turner (2005), Behaviour of a planar Langmuir probe in a laser ablation plasma, *Appl. Surf. Sci.*, *247(1–4)*, 134–138.

Donnelly, T., J. G. Lunney, S. Amoruso, R. Bruzzese, X. Wang, and X. Ni (2010a), Dynamics of the plumes produced by ultrafast laser ablation of metals, *J. Appl. Phys.*, *108(4)*, 0–13.

Donnelly, T., J. G. Lunney, S. Amoruso, R. Bruzzese, X. Wang, and C. Phipps (2010b), Plume dynamics in femtosecond laser ablation of metals, *AIP Conf. Proc.*, *643*, 643–655.

Falconer, K. J. (1985), *The geometry of fractal sets*, Cambridge University Press, Cambridge.

Fang R., D. Zhang, Z. Li, F. Yang, L. Li, X. Tan, F. Yang, and M. Sun (2008), Improved thermal model and its application in UV high-power pulsed laser ablation of metal target, *Solid State Commun., 145*, 556–560.

Federer, J., and A. Aharoner (1990), *Fractals in physics*, North Holland, Amsterdam.

Gilgenbach, R. M., H. L. Spindler, J. S. Lash, and S. D. Kovaleski (1937), Surface instability of multipulse laser ablation on a metallic target, *J. Appl. Phys.*, *83(8)*, 4466–4471.

Gouyet, J. F. (1992), *Physique et structures fractales*, Masson, Paris.

Gurlui, S., M. Agop, P. Nica, M. Ziskind, and C. Focsa (2008), Experimental and theoretical investigations of a laser-produced aluminum plasma, *Phys. Rev. E*, *78(2)*, 26405.

Haas, F. (2011), An Introduction to Quantum Plasmas, *Brazilian J. Phys.*, *41(4–6)*, 349–363.

Hansen, T. N., J. Schou, and J. G. Lunney (1999), Langmuir probe study of plasma expansion in pulsed laser ablation, *Appl. Phys. A-Mater., 5827,* 457-466.

Harilal, S. S., C. V. Bindhu, M. S. Tillack, F. Najmabadi, and A. C. Gaeris (2003), Internal structure and expansion dynamics of laser ablation plumes into ambient gases, *J. Appl. Phys.*, *93(5)*, 2380–2388.

Harilal, S. S., N. Farid, J. R. Freeman, P. K. Diwakar, N. L. LaHaye, and A. Hassanein (2014), Background gas collisional effects on expanding fs and ns laser ablation plumes, *Appl. Phys. A-Mater.*, *117(1)*, 319–326.

Ho, J. R., C. P. Grigoropoulos, and J. A. C. Humphrey (1996), Gas dynamics and radiation heat transfer in the vapor plume produced by pulsed laser irradiation of aluminum, *J. Appl. Phys.*, *79(9)*, 7205-7215.

Hou, T. Y., C. Liu, and J. G. Liu (2009), *Multi- Scale Phenomena in Complex Fluids*, World Scientific, Singapore.

Inogamov, N. A., V. V. Zhakhovskii, S. I. Ashitkov, V. A. Khokhlov, Y. V. Petrov, P. S. Komarov, M. B. Agranat, S. I. Anisimov, and K. Nishihara (2009), Two-temperature relaxation and melting after absorption of femtosecond laser pulse, *Appl. Surf. Sci.*, *255(24)*, 9712–9716.

Irimiciuc, S. A., M. Agop, P. Nica, S. Gurlui, D. Mihaileanu, S. Toma, and C. Focsa (2014a), Dispersive effects in laser ablation plasmas, *J. Appl. Phys.*, *53*, 116202.

Irimiciuc, S. A., I. Mihaila, and M. Agop (2014b), Experimental and theoretical aspects of a laser produced plasma, *Phys. Plasmas*, *21(9)*, 93509.

Irimiciuc, S. A., S. Gurlui, G. Bulai, P. Nica, M. Agop, and C. Focsa (2017b), Langmuir probe investigation of transient plasmas generated by femtosecond laser ablation of several metals: Influence of the target physical properties on the plume dynamics, *Appl. Surf. Sci.*, *417*, 108–118.

Irimiciuc, S. A., S. Gurlui, P. Nica, C. Focsa, and M. Agop (2017c), A compact non-differential approach for modeling laser ablation plasma dynamics, *J. Appl. Phys.*, *121(8)*, 083301.

Jeong S., R. Greif , and R. Russo (1998), Numerical modeling of pulsed laser evaporation of aluminum targets, *Appl. Surf. Sci., 127–129*, 177–183.

Jackson, E. A. (1978), Nonlinearity and irreversibility in lattice dynamics, *Rocky Mt. J. Math.*, *8(1–2)*, 127–196.

Koopman, D. W. (1971), Langmuir Probe and Microwave Measurements of the Properties of Streaming Plasmas Generated by Focused Laser Pulses, *Phys. Fluids*, *14(8)*, 1707-1717.

Landau, L. D, and E. M. Lifshits (1959), *Fluid mechanics*, Pergamon Press, London.

Leboeuf, J. N., K. R. Chen, J. M. Donato, D. B. Geohegan, C. L. Liu, A. A. Puretzky, and R. F. Wood (1996), Modeling of dynamical processes in laser ablation, *Appl. Surf. Sci.*, *96–98*, 14–23.

Lunney, J. G., B. Doggett, and Y. Kaufman (2007), Langmuir probe diagnosis of laser ablation plasmas, *J. Phys. Conf. Ser.*, *59*, 470–474.

Mandelbrot, B. B. (1982), *The fractal geometry of nature*, W.H. Freeman, New York.

Merches, I., and M. Agop (2015), *Differentiability and Fractality in Dynamics of Physical Systems*, World Scientific, Singapore.

Merlino, R. L. (2007), Understanding Langmuir probe current-voltage characteristics, *Am. J. Phys.*, *75*(12), 1078.

Mitchell, M. (2009), *Complexity: A Guided Tour*, Oxford University Press, Oxford.

Mora, P. (2003), Plasma Expansion into a Vacuum, *Phys. Rev. Lett.*, *90(18)*, 185002.

Murakami, M., Y. G. Kang, K. Nishihara, S. Fujioka, and H. Nishimura (2005), Ion energy spectrum of expanding laser-plasma with limited mass, *Phys. Plasmas*, *12(6)*, 62706.

El Naschie, M. S., O. E. Rössler, and I. Prigogine (1995), *Quantum mechanics, diffusion and chaotic fractals*, Pergamon, London.

Nica, P., P. Vizureanu, M. Agop, S. Gurlui, C. Focsa, N. Forna, P. D. Ioannou, and Z. Borsos (2009), Experimental and theoretical aspects of aluminum expanding laser plasma, *Jpn. J. Appl. Phys.*, *48*, 1–7.

Nica, P., M. Agop, S. Gurlui, C. Bejinariu, and C. Focsa (2012), Characterization of Aluminum Laser Produced Plasma by Target Current Measurements, *Jpn. J. Appl. Phys.*, *51(10R)*, 106102.

Nottale, L. (1993), *Fractal space-time and microphysics Towards a Theory of Scale Relativity*, World Scientific, Singapore.

Nottale, L. (2010), Scale relativity and fractal space-time: Theory and applications, *Found. Sci.*, *15(2)*, 101–152.

Pandey, P. K., S. L. Gupta, and R. K. Thareja (2015), Study of pulse width and magnetic field effect on laser ablated copper plasma in air, *Phys. Plasmas*, *22(7)*, 73301.

Peterlongo A., A. Miotello, and R. Kelly (1994), Laser-pulse sputtering of aluminum: Vaporization, boiling, superheating, and gas-dynamic effects, *Phys. Rev. E, 50,* 4716.

Rethfeld B., A. Kaiser, M. Vicanek, and G. Simon (2002), Ultrafast dynamics of non-equilibrium electrons in metals under femtosecond laser irradiation, *Phys. Rev. B, 65*, 214303.

Sappey, A. D., and T. K. Gamble (1991), Laser-fluorescence diagnostics for condensation in laser-ablated copper plasmas, *Appl. Phys. B Photo.*, *53(5–6)*, 353–361.

Shukla, P. K. (2009), Plasma physics: A new spin on quantum plasmas, *Nat. Phys.*, *5(2)*, 92–93.

Singh R. K., and J. Narayan (1989), A Novel Method for Simulating Laser-Solid Interactions in Semiconductors and Layered Structures, *Mat. Sci. Eng. B, 3*, 217.

Singh R. K., and J. Narayan (1990), Pulsed laser evaporation technique for depositing thin films: physics and theoretical model. *Phys. Rev. B, 41,* 8843–8859.

Stauffer, D., H. E. Stanley, and A. Lesne (2017), *From Newton to Mandelbrot*, Springer, Berlin.

Weibel, P., G. Ord, and O. E. Rössler (2005), *Space time physics and fractality,* Springer, Wien.

Werner, D., and S. Hashimoto (2011), Improved working model for interpreting the excitation wavelength- and fluence-dependent response in pulsed laser-induced size reduction of aqueous gold nanoparticles, *J. Phys. Chem. C*, *115(12)*, 5063–5072.

Wood R. F., and G. E. Giles (1981), Macroscopic theory of pulsed-laser annealing. I. Thermal transport and melting, *Phys. Rev. B, 25*, 2923.

Wu B., and Y. Shin (2006), Modelling of nanosecond laser ablation with vapor plasma formation, *J. Appl. Phys., 99*, 084310.

Zavestovskaya, I. N., O. A. Glazov, and N. N. Demchenko (2008), Threshold Characteristics of Ultrashort Laser Pulse Ablation of Metals., *Proc. 3rd Int. Conf. Front. Plasma Phys. Technol.*, *40(10)*, 10–18.

Chapter V   Conclusions and Perspectives

The main goal of this work was to use the core available investigation techniques for laser-produced plasma studies on a series of pure and complex targets. During the preparation of the thesis the work was divided into two directions. The first direction covered a series of fundamental investigations of laser-produced plasmas on metallic targets in various ablation regimes and similar experimental conditions regarding the background pressure and the laser fluence. The aim was, beside the comparison between the laser-produced plasmas in different ablation regimes, to investigate their dynamics at a fundamental level and understand how the dynamics of the ejected particles can be related to the fundamental ablation mechanism. This was followed by a similar treatment of LPP on chalcogenide targets. All the results led to the finding of empirical correlations between the properties of the-laser produced plasmas and the physical properties of the targets and to associate that to each specific ablation regime. The second direction was a theoretical study based on a fractal theoretical model for laser ablation plasma dynamics. The aim here was to correlate for the first time the parameters derived from the fractal model to the real experimental parameters given through Langmuir probe measurements and to explore the implications of such a complex mathematical approach for each ablation regime.

Experimental investigations of laser-produced plasmas

The experimental investigations were based on the previous work of C. Ursu during his PhD. Thesis [*Ursu*, 2010] and on all the advancements on the diagnostics part reported by our group in the recent years [*Gurlui et al.*, 2006; *Focsa et al.*, 2009, 2017, *Nica et al.*, 2009, 2010, 2012; *Pompilian et al.*, 2013]. In an attempt to step forward towards a unification between the information extracted from the laser ablation plasmas and the physical properties of the target and aid the overall pulsed laser deposition process, systematic space- and time-resolved optical and electrical investigations were performed on transient plasmas generated by nanosecond, picosecond and femtosecond laser ablation of a series of pure metallic targets (Cu, Mn, Ti, Al, Zn, Ni) and complex chalcogenide targets (($GeSe_2)_{100-x}(Sb_2Se_3)_x$).

The ICCD fast camera photography revealed the plume splitting in two plasma components. The splitting process was observed throughout all ablation regimes and for all investigated plasmas. The fast component, traveling with a velocity of a few tens of km/s, contains mainly ions and is generated through electrostatic mechanism (Coulomb explosion), while for the second one we found velocities one order of magnitude lower. The second structure was generated by thermal mechanisms and contains mainly neutral species. This is a results that was confirmed for ns, ps, and fs regimes and it is in good agreement with the actual understanding [*Chichkov et al.*, 1996; *Amoruso et al.*, 2004; *Gacek and Wang*, 2009; *Mao et al.*, 2013; *Focsa et al.*, 2017] of the splitting process during plasma expansion. The splitting phenomenon does not dependent on the properties of the target as similar results were obtained for the LPP generated on chalcogenide targets. A third plasma component was observed here, which is also of thermal nature and contains mainly nanoparticles and clusters [*Harilal et al.*, 2002], the same slow component can also be seen for pure targets in the ps and fs ablation regimes.

The studies were focused further on space- and time-resolved OES where the presence of neutral atoms, singly- and multiply-charged ions for each of the investigated plasmas was evidenced. The main differences here were observed in the ratio between the atomic and ionic lines in different ablation regimes, results consistent with other reports from literature [*Cremers and Radziemski*, 2006]. Using the Boltzmann plot method, the excitation temperature was estimated for each individual species. Nanosecond laser-produced plasmas showed a higher excitation temperature than the plasmas generated in shorter laser ablation regimes, result understood as a sign of the plume heating by the tail of the laser pulse. Consistent discrepancies were found at each ablation regimes between the excitation temperature corresponding to the ionized species and the neutrals one, result confirmed also in the case of chalcogenide plasmas.

The image offered by the optical methods consisted mainly in the study of the excited levels characteristic for each species present in the plasma. This was completed with space- and time-resolved electrical investigations based on the Langmuir probe method [*Doggett and Lunney*, 2009]. The electrical investigations were implemented on a wide range of spatial and temporal "coordinates" which allowed us to map the space-time evolution of all plasma parameters. The results revealed a "classical" behavior of all plasma parameters as the plume evolves in space and time: a decrease in particle density, plasma potential, ion and electron temperature and an increase of the Debye length. The study was extended to consider the drift movement of the ions by fitting with a shifted Maxwellian function the Langmuir probe time-of-flight signals [*Krása et al.*, 2008]. The wide range of targets used coupled with the three ablation regimes investigates offered a complete view on the dynamics of plasmas generated in different ablation regimes. What differentiates our studies of other similar approaches from the literature is the wide range of spatial and temporal points considered. We mapped the plasma parameters up to 4 cm from the target which is a usual distance at which the substrate is placed during pulsed laser deposition. Thus our results are most relevant to the PLD processes, where controlling the energy of the incoming particles is essential [*Miller*, 1994].

Transferring the diagnostic system (optical and electrical) to actual PLD conditions, we investigated the dynamics of the LPP in specific deposition conditions. The optical and electrical investigations of Al LPP in PLD conditions showcased peculiar behaviors of the global dynamics of the plume and of the individual charged particles. ICCD fast camera imaging evidenced the plume reflection phenomena in the vicinity of the substrate, this result is in good agreement with recent reports from Lippert's group [*Ojeda et al.*, 2017]. The rebound phenomenon was found to be strongly dependent on the background gas pressure and the PLD configuration, being more pronounced at high pressures and relatively short target-substrate distances. Also, the overall kinetic energy of the ejected particles was proven to be strongly affected by the PLD configuration, depending on the target - substrate distance and the background pressure. The LP measurement revealed an oscillatory behavior of the plasma ions, which was further confirmed also for atoms by OES measurements. The oscillations observed for the ionic current and the oscillation frequencies measured are consistent with previous reports of our group [*Gurlui et al.*, 2008; *Nica*

et al., 2010; *Focsa et al.*, 2017] and with recent reports of other groups [*Sunil et al.*, 2008; *Singh et al.*, 2014; *Anoop et al.*, 2015]. The main advancement made was based on performing space-resolved measurements which allowed the mapping of the oscillating frequency. We found here that in the vicinity of the target the ionic are oscillating on two frequencies (with one order of magnitude difference between them), while at longer distances only one oscillation frequency is noticeable.

An important milestone for our study was reached when the information extracted from the plasma was correlated with the physical properties of the target. The data derived from the optical measurements (velocities and excitation temperatures) were found to be linked to the atomic mass and the heat of vaporization of the target. Simultaneously, the data from the LP method mainly offers connections of the electron temperature, thermal velocity and plasma potential with the electrical and thermal conductivities of the targets. Based on the ideas exposed in theoretical studies made on the Coulomb explosion mechanism by the group of Bulgakova et al. [*Bulgakova et al.*, 2004, 2005], and on the Langmuir probe theory [*Mott-Smith and Langmuir*, 1926; *Hendron et al.*, 1997], we were able to explain the empirical dependences which connect the plasma parameters and the target physical properties, reported for the first time in our study. This was further confirmed through the investigation performed on the chalcogenide targets, where we evidenced the role played by the electrical conductivity of the target, in the same manner as for single-element metallic targets. Our data also confirmed some previous results by Schou et al. [*Thestrup et al.*, 2002], who correlated the ion density with the cohesive energy of the ions in the lattice. The empirical function connecting the properties of the plasma and the physical properties of the target are respected for every ablation regime giving our results a desirable generality.

These results show the utility of working with complementary experimental techniques for the spatial and temporal mapping of all plasma properties. In order to test the universality of our empirical relations, future work could be developed by extending the range of external parameters in terms of laser wavelength, fluence, background pressure, as well as an extension towards other investigation techniques like shadowgraphy, laser induced fluorescence or mass spectrometry. The important results obtained from the investigations performed in PLD conditions, can advocate for the implementation of complex diagnostic systems coupled with PLD machines and performing measurements during the deposition process in order to tackle in real-time problems of, e.g., non-stoichiometry or non-uniformity of the PLD technique.

Theoretical investigations of laser-produced plasmas dynamics

The theoretical investigations were based on the fractal theoretical model developed by our group [*Agop et al.*, 2009, 2010; *Nica et al.*, 2009]. We formulated two-simplified versions of the fractal model and used it to describe the dynamics of laser-produced plasmas. The first approach involved the use of a stationary solution in order to make some global assessments of the bi-dimensional expansion of a fractal fluid. The results were found to be in good agreement with the ICCD fast camera imaging performed on laser-produced plasmas in various ablation regime and

with the "clasical" theoretical understanding of the ablation processes [*Miller*, 1994; *Cremers and Radziemski*, 2006]. The second approach was focused on the time-dependent solution in a uni-dimensional case. This approach allowed the investigations of the space and time evolution of the expansion velocity, particle current density and plasma temperature, and the results were in good agreement with other differential theoretical models [*Anisimov and Luk'yanchuk*, 2002]. The model manages to simulate the formation and expansion of plasma plumes taking into account the scale differences between different ablation mechanisms.

The second milestone was reached when the results from simulations revealed two contributions to plasma temperature and current density, which is consistent with the dual component structure observed through experimental techniques. Moreover, we report here for the first-time clear associations between fractal model variables and specific plasma parameters (electron temperature, thermal velocity, particle density). By fitting the experimental data with the functions given by the fractal model, we defined specific ranges for the values of the fractalization degree in each ablation regime investigated. The theoretical studies and the comparison with the experimental data had a double role. The first one was to mimic the behavior of a laser-produced plasma, regardless of the ablation regime and to prove the practicality of a non-differential theoretical model. The second one was to understand more about the fractal parameters which define our model and how they translate to the real physical properties of the plasma.

The results given by the fractal approach are optimistic and can lead to the further development of the model transitioning towards more applicative research areas. Theoretical prediction regarding the deposition process could be the next step for our model. This would help control the deposition process, as predictions regarding the stoichiometry or the uniformity of the deposited film are critical for all possible technological applications.

References for Chapter V

Agop, M., P. Nica, S. Gurlui, C. Focsa, V. P. Paun, and M. Colotin (2009), Implications of an extended fractal hydrodynamic model, *Eur. Phys. J. D*, *56(3)*, 405–419.

Agop, M., P. Nica, S. Gurlui, and C. Focsa (2010), Fractal hydrodynamic model of high-fluence laser ablation plasma expansion*, AIP Conf. Proc., 64*, 482–491.

Amoruso, S., I. Unitá, S. Fisiche, N. Federico, M. S. Angelo, V. Cintia, I. Napoli, B. Toftmann, and J. Schou (2004), Thermalization of a UV laser ablation plume in a background gas: From a directed to a diffusionlike flow, *Phys. Rev. E*, *69(5)*, 56403.

Anisimov, S. I., and B. S. Luk'yanchuk (2002), Selected problems of laser ablation theory, *Physics-Usp.*, *45(3)*, 293–324.

Anoop, K. K., M. P. Polek, R. Bruzzese, S. Amoruso, and S. S. Harilal (2015), Multidiagnostic analysis of ion dynamics in ultrafast laser ablation of metals over a large fluence range, *J. Appl. Phys.*, *117(8)*, 083108.

Bulgakova, N. M., R. Stoian, A. Rosenfeld, I. V. Hertel, W. Marine, and E. E. B. Campbell (2005), A general continuum approach to describe fast electronic transport in pulsed laser irradiated materials: The problem of Coulomb explosion, *Appl. Phys. A-Mater.*, *81(2)*, 345–356.

Chichkov, B. N., C. Momma, S. Nolte, F. Alvensleben, and A. Tünnermann (1996), Femtosecond, picosecond and nanosecond laser ablation of solids, *Appl. Phys. A-Mater.*, *63(2)*, 109–115.

Cremers, D. A., and L. J. Radziemski (2006), *Handbook of Laser-Induced Breakdown Spectroscopy*, John Wiley & Sons Ltd, Oxford, UK.

Doggett, B., and J. G. Lunney (2009), Langmuir probe characterization of laser ablation plasmas, *J. Appl. Phys.*, *105(3)*, 33306.

Focsa, C., P. Nemec, M. Ziskind, C. Ursu, S. Gurlui, and V. Nazabal (2009), Laser ablation of As_xSe_{100-x} chalcogenide glasses: Plume investigations, *Appl. Surf. Sci.*, *255(10)*, 5307–5311.

Focsa, C., S. Gurlui, P. Nica, M. Agop, and M. Ziskind (2017), Plume splitting and oscillatory behavior in transient plasmas generated by high-fluence laser ablation in vacuum, *Appl. Surf. Sci.*, (in press).

Gacek, S., and X. Wang (2009), Plume splitting in pico-second laser material interaction under the influence of shock wave, *Phys. Lett. A*, *373(37)*, 3342–3349.

Gurlui, S., M. Sanduloviciu, M. Strat, G. Strat, C. Mihesan, M. Ziskind, and C. Focsa (2006), Dynamic space charge structures in high fluence laser ablation plumes, *J. Optoelectron. Adv. M.*, *8(1)*, 148–151.

Gurlui, S., M. Agop, P. Nica, M. Ziskind, and C. Focsa (2008), Experimental and theoretical investigations of a laser-produced aluminum plasma, *Phys. Rev. E*, *78(2)*, 26405.

Harilal, S. S., C. V. Bindhu, M. S. Tillack, F. Najmabadi, and A. C. Gaeris (2003a), Internal structure and expansion dynamics of laser ablation plumes into ambient gases, *J. Appl. Phys.*, *93(5)*, 2380–2388.

Hendron, J. M., C. M. O. Mahony, T. Morrow, and W. G. Graham (1997), Langmuir probe measurements of plasma parameters in the late stages of a laser ablated plume, *J. Appl. Phys.*, *81(5)*, 2131.

Krása, J., K. Jungwirth, S. Gammino, E. Krousky, L. Laska, A. Lorusso, V. Nassisi, M. Pfeifer, K. Rohlena, L. Torrisi, J. Ullschmied, and A. Velyhan (2008), Partial currents of ion species in an expanding laser-created plasma,

Vacuum, *83(1)*, 180–184.

Mao, X., J. Yoo, J. J. Gonzalez, and R. E. Russo (2013), Femtosecond vs. Nanosecond Laser Pulse Duration for Laser Ablation Chemical Analysis, *Spectroscopy*, *28(1),* 1-6.

Miller, C. J. (1994), *Laser Ablation*, Springer Heidelberg.

Mott-Smith, H. M., and I. Langmuir (1926), The theory of collectors in gaseous discharges, *Phys. Rev.*, *28*(4), 727–763.

Nica, P., P. Vizureanu, M. Agop, S. Gurlui, C. Focsa, N. Forna, P. D. Ioannou, and Z. Borsos (2009), Experimental and theoretical aspects of aluminum expanding laser plasma, *Jpn. J. Appl. Phys.*, *48*, 1–7.

Nica, P., M. Agop, S. Gurlui, and C. Focsa (2010), Oscillatory Langmuir probe ion current in laser-produced plasma expansion, *EPL - Europhys. Lett.*, *89(6)*, 65001.

Nica, P., M. Agop, S. Gurlui, C. Bejinariu, and C. Focsa (2012), Characterization of Aluminum Laser Produced Plasma by Target Current Measurements, *Jpn. J. Appl. Phys.*, *51(10R)*, 106102.

Ojeda-G-P, A., C. W. Schneider, M. Döbeli, T. Lippert, and A. Wokaun (2017), Plasma plume dynamics, rebound, and recoating of the ablation target in pulsed laser deposition, *J. Appl. Phys.*, *121(13)*, 135306.

Pompilian, O. G., S. Gurlui, P. Nemec, V. Nazabal, M. Ziskind, and C. Focsa (2013), Plasma diagnostics in pulsed laser deposition of GaLaS chalcogenides, *Appl. Surf. Sci.*, *278*, 352–356.

Singh, S. C., C. Fallon, P. Hayden, M. Mujawar, P. Yeates, and J. T. Costello (2014), Ion flux enhancements and oscillations in spatially confined laser produced aluminum plasmas, *Phys. Plasmas*, *21*(9), 93113.

Sunil, S., A. Kumar, R. K. Singh, and K. P. Subramanian (2008), Measurements of electron temperature and density of multi-component plasma plume formed by laser-blow-off of LiF-C film, *J. Phys. D. Appl. Phys.*, *41*(8), 85211.

Thestrup, B., B. Toftmann, J. Schou, B. Doggett, and J. G. Lunney (2002), Ion dynamics in laser ablation plumes from selected metals at 355 nm, *Appl. Surf. Sci.*, *197–198*, 175–180.

Ursu, C. (2010), Caracterisation par methodes optiques et electriques du plasma produit par ablation laser, PhD thesis, Université Lille 1 – Sciences Et Technologies.

Experimental and theoretical studies on the dynamics of transient plasmas generated by laser ablation in various temporal regimes

Abstract

Laser ablation methods exhibit a fast development in various application fields, as materials processing, medicine, nuclear fusion or analytical sciences. Despite important advances in the knowledge of the complex laser-matter interactions involved in this process, there is still need for better fundamental understanding and modeling. The aim of this work was to experimentally and theoretically investigate the dynamics of transient plasmas generated by laser ablation in various regimes (ns, ps, fs), and to try to correlate the observed behavior with the physical properties of the ablated materials We implemented space- and time-resolved optical, spectroscopic and electrical methods for the study of single-component metallic targets and of complex chalcogenide targets. This led to a space-time mapping of the main plasma parameters. The study performed in actual Pulsed Laser Deposition (PLD) conditions revealed some peculiar effects like ionic oscillations or plume reflection at the substrate. A compact fractal hydrodynamic model was developed to simulate the laser-produced plasma dynamics. The theoretical model accurately describes the spatial and temporal evolution of the main plasma parameters (electronic temperature, expansion velocities, particle number density, Debye length, plasma potential). We report for the first time empirical relations connecting these plasma parameters with the physical properties (electrical/thermal conductivity, atomic mass, heat of vaporization) of the target. These relationships transcend all three ablation regimes (ns, ps, fs).

Key words: laser ablation, low temperature plasma, fractal hydrodynamic model, optical emission spectroscopy, Langmuir probe, plasma oscillations, spatio-temporal dynamics.

Etudes expérimentales et théoriques sur la dynamique des plasmas transitoires générés par l'ablation laser dans différents régimes temporels

Resumé

Les applications de l'ablation laser connaissent un développement important, dans des domaines comme le micro-usinage, la médecine, le nucléaire ou les sciences analytiques. Malgré d'importantes avancées dans la connaissance des interactions complexes intervenant dans ce processus, on a encore besoin d'une meilleure compréhension fondamentale et de modélisation. Le but de ce travail a été d'étudier expérimentalement et théoriquement la dynamique des plasmas transitoires générés par ablation laser dans différents régimes temporels (ns, ps, fs) et d'essayer de corréler le comportement observé avec les propriétés physiques des matériaux ablatés. Nous avons mis en œuvre des méthodes optiques, spectroscopiques et électriques résolues spatialement et temporellement pour l'étude de cibles métalliques mono-éléments et de cibles plus complexes à base de chalcogénures. Cela nous a permis d'avoir une cartographie spatio-temporelle des principaux paramètres du plasma. L'étude en configuration PLD (Pulsed Laser Deposition) a révélé quelques effets particuliers, comme les oscillations ioniques ou la réflexion du plasma sur le substrat. Une version compacte du modèle hydrodynamique fractal a été développée pour simuler la dynamique du plasma. Le modèle théorique réussit à décrire l'évolution spatiale et temporelle des principaux paramètres du plasma (température électronique, vitesses d'expansion, concentration, longueur de Debye, potentiel du plasma). Nous proposons des relations empiriques reliant ces paramètres aux propriétés physiques (conductivités électrique/thermique, mass atomique, chaleur de vaporisation) de la cible. Ces relations transcendent les trois régimes d'ablation.

Mots-clés: ablation laser, plasmas froids, spectroscopie optique d'émission, sonde Langmuir, modélisation théorique, fractal, hydrodynamique, dynamique spatio-temporelle.